Nano- and micro-fabricated interfaces for in-vitro electrophysiology

A dissertation
submitted to the Faculty of Science of the University of Neuchâtel, in fulfilment of the requirements for the degree of "Docteur ès Sciences"

by

Berdondini Luca
Dipl. Microtech. Ing. EPFL

Institute of Microtechnology
University of Neuchâtel
Rue Jaquet-Droz 1, CH-2007 Neuchâtel
Switzerland

2003

IMPRIMATUR POUR LA THESE

Nano- and micro-fabricated interfaces for in-vitro electrophysiology

de M. Luca Berdondini

UNIVERSITE DE NEUCHATEL

FACULTE DES SCIENCES

La Faculté des sciences de l'Université de Neuchâtel, sur le rapport des membres du jury

Mme M. Koudelka-Hep (directrice de thèse),
MM. N. de Rooij, P. Seitz, N. Blanc (CSEM, Zürich)
et S. Martinoia (Gênes, I)

autorise l'impression de la présente thèse.

Neuchâtel, le 2 juillet 2003

Le doyen:

François Zwahlen

to Anja and
my parents

ABSTRACT

Microelectrode arrays (MEAs) allow the extracellular recording and stimulation of the in-vitro electrophysiological cellular activity. This thesis contributes to the development of MEAs with respect to the ever increasing demand of current research in in-vitro electrophysiology, i.e. better recording / stimulation performances, higher electrode densities, large active areas.

Thin-film and electrochemical technologies for fabricating and for modifying platinum and iridium microelectrode arrays, on silicon or pyrex substrates, are presented. The lift-off of platinum or iridium electrodes was improved with a two layers photoresist technique towards the process repeatability, the wafer homogeneity and solving the problem of metal wing tips. The microelectrodes behaviour for recording and stimulation is improved by platinum electrodeposition on planar MEAs and by the electrochemical oxidation of iridium electrodes.

The microelectrodes have been scaled down to nanometer dimensions with a mix-and-match approach (e-beam and conventional lithography). Such electrodes could allow the measurement in the nano-scale domain of cellular or sub-cellular physiology. The developed technologies are evaluated by fabricating and characterising nano-disk electrodes with diameters between 200 nm and 400 nm and nano-IDAs with gaps of about 260 nm. Additionally, the gap of nano-IDAs is additionally reduced to 100 nm using platinum electrodeposition. A collection efficiency of 99 % was achieved on nano-IDAs using ferrocyanide as the benchmark species.

The concept, the design and the first generation of an active pixel sensor (APS) based high density MEA (electrode pitch down to cellular dimensions) is presented and electrically evaluated in a phosphate solution and under culture conditions. The realised device features 64 x 64 pixels on a surface of 2.5 x 2.5 mm^2 and an electrode pitch of 20 μm. Each pixel (40 x 40 μm^2) integrates a microelectrode (20 x 20 μm^2) and an underneath pre-amplifier circuit. The analogue amplifier has been designed for providing different working modes for noise / signal trade-off.

An original gold electroless technique has been developed for rapidly post-processing the CMOS devices, since the standard CMOS aluminium alloy is not a suitable electrode material. The resulting gold electrodes show an excellent electrochemical behaviour and their biocompatibility has been confirmed with the preliminary tests on cardiomyocyte cultures.
In the context of the European project “Neurobit”, the final challenge is to develop a stand-alone, long-term mini-neurophysiological laboratory. The microsystem includes i) a microelectrode array with SU-8 clustering structures, and ii) a mini-incubator integrating Pt-RTD sensors, heating elements and pH IrOx sensors. The results achieved after one year are presented. SU-8 clustering structures of 350 μm and 550 μm have been fabricated improving the technology towards the biocompatibility, SU-8 adhesion in the culture media, and achieving thickness homogeneities of 2-3 %. In particular, an adhesion layer for promoting chemical bonding between the silicon nitride and the SU-8 has been developed, showing good adhesion for more than a month in PBS solution and a long-term good viability of rat hippocampal neurons.

The materials, techniques and methods developed during this thesis constitute a large basis for future developments in Bio-MEMS and neuro-electrical interfaces.

TABLE OF CONTENTS

PREFACE **3**

1 INTRODUCTION **5**

1.1 INTERFACING IN-VITRO NEURONAL NETWORKS – STATE-OF-THE ART 6

1.1.1 The neuron *6*

1.1.2 The action potential *9*

1.1.3 In-vitro culturing *16*

1.1.4 State-of-the art of recording / stimulation techniques *17*

The patch-clamp 19

Integrated patch-clamp 20

Microelectrode arrays (MEAs) 21

High-density electrode arrays 26

Field-effect-addressable potentiometric sensors (FAPS) 27

Light-addressable potentiometric sensor (LAPS) 28

The micro-action potential scanner (MAPS) 30

Biopatterning 31

Fluorescence recordings 32

1.2 BIBLIOGRAPHY 34

2 THE NEURONAL INTERFACE **45**

2.1 INTRODUCTION 45

2.2 ELECTRODE-ELECTROLYTE 46

2.2.1 Metals, semiconductors, insulators and electrolytes *46*

2.2.2 Metal-electrolyte interface *50*

At the equilibrium 50

Polarising the electrode 54

2.3 ELECTRODE-ELECTROLYTE-NEURON 56

2.3.1 Recording model *56*

2.3.2 Recording model *61*

2.3.3 Electrode characteristics for the recording *63*

2.4 STIMULATION CONSIDERATIONS 64
2.5 ARRAY OF METAL ELECTRODES 65
2.6 BIBLIOGRAPHY 67

3 FABRICATION AND CHARACTERISATION OF ELECTRODE ARRAYS AT THE MICRO- AND NANO-SCALE 69

3.1 INTRODUCTION 69
3.2 FABRICATION OF PLANAR MICROELECTRODES ARRAYS 70
3.2.1 Silicon substrate arrays 70
3.2.2 Pyrex substrate arrays 71
3.2.3 The lift-off process 73
3.2.4 Description of the realised planar MEAs 80
3.3 THREE DIMENSIONAL IRIDIUM TIPS ON SILICON 82
3.4 PLATINUM ELECTRODES MODIFICATION 84
3.5 IRIDIUM ELECTRODES OXIDATION 87
3.6 SCALING DOWN MICROELECTRODES TO NANOELECTRODES 89
3.6.1 Fabrication of nano-interdigitated electrodes (Nano-IDA) 90
3.6.2 Fabrication of nano-discs 93
3.6.3 Electrochemical behaviour of nano-disks and nano-IDAs 95
3.7 BIBLIOGRAPHY 100

4 AN APPROACH TO HIGH-DENSITY MICROELECTRODE ARRAYS 101

4.1 INTRODUCTION 101
4.2 IN-PIXEL PRE-AMPLIFIER 103
4.2.1 Choice of the pre-amplifier circuit 104
4.2.2 Design considerations of the 5 transistors OTA 106
4.2.3 Integrated pre-amplifier circuit 107
4.3 SPECIFICATIONS OF THE CMOS CHIP 109
4.3.1 Simulated results 110
4.3.2 Summary of the chip specifications 113
4.4 GOLD ELECTROLESS DEPOSITION 115
4.4.1 Electroless gold deposition on aluminium MEAs 116
4.4.2 Evaluation of the electroless gold layer 120
4.4.3 Gold electroless deposition on CMOS chips 122

4.5 ELECTRICAL CHARACTERISATION OF THE CMOS CHIP 124
4.5.1 Packaging 124
4.5.2 The electrical chip interface 126
4.5.3 Electrical tests in a phosphate solution 127
4.6 BIOLOGICAL EXPERIMENTS WITH CARDIOMYOCYTES 132
4.6.1 Cardiomyocytes culture preparation 132
4.6.2 Experimental and discussion 133
4.7 DISCUSSION AND FUTURE DEVELOPMENTS 137
4.8 BIBLIOGRAPHY 139

5 THE NEUROBIT PROJECT 141

5.1 INTRODUCTION – CONTEXT OF THE EU PROJECT 141
5.2 FUNCTIONAL BLOCK DIAGRAM OF THE NML MICROSYSTEM 142
5.3 THE MICRO-TRANSDUCER-ARRAY (MTA) 143
5.3.1 The clustering structure 144
Clustering structures based on SU-8 technology 146
300 μm thick SU-8 148
550 μm thick SU-8 148
Evaluation of the SU-8 clusters 149
5.3.2 The MEA 155
5.4 THE NEUROPHYSIOLOGICAL MINI-INCUBATOR 157
5.4.1 Heating and temperature sensors 158
The heating system 159
The temperature sensor 160
5.4.2 pH sensing 163
5.5 OUTLINE AND FUTURE WORK 164
5.6 BIBLIOGRAPHY 167

6 SUMMARY AND OUTLOOK 169

ANNEXE I 173

GAIN VERSUS TRANSISTOR DIMENSIONS 173

ANNEXE II 177

EVALUATION OF THE AMPLIFIER NOISE 177

ANNEXE III **181**

SIMULATION RESULTS 181

ANNEXE IV **187**

CHIP INTERFACE V.1.0 AND V.2.0 187

“Wonderful as are the laws and phenomena of electricity when made evident to us in inorganic or dead matter, their interest can bear scarcely any comparison with that which attaches to the same force when connected with the nervous system and with life …”

Michael Faraday
Philosophical Transactions of the Royal Society of London, 1839

PREFACE

Present research in biology is increasingly oriented towards developing high-resolution instruments for accessing the cellular or sub-cellular level. Instrumentation and materials are constantly improved and looking at this field with the eyes of a micro-engineer a wonderful word of stimulating developments is discovered. A recent example is the revolution of DNA chip arrays that allowed a faster decoding of the human genome. Genomics, proteomics and cellomics are today some of the fields needing the engineering of new tools for promoting research in biology.

This work focuses on applications for electrophysiology. In general terms, electrophysiology studies the electrical activity of living systems and correlates this activity with the physiology of the system. The Italian physician and physicist Luigi Galvani (1737-1798) with its interest in “animal electricity” and his famous experiment where he applied current to the nerves of a frog, observing the contractions of the muscles in their legs, can be considered as the first electrophysiologist. Today, electrocardiograms are measured routinely and pacemakers are implanted into human bodies showing the incredible results achieved in this field of R&D.

The electrophysiology at the cellular level or on networks of cells, e.g. neurons and cardiomyocytes, permits the study of the cellular behaviour in a simplified system compared to the in-vivo situation. Nowadays it is possible to culture networks of cells and keep them alive for several months up to years. Since the modelling of the physiological activity of single cells, or that of the even more complex network activity, is still far from the reality, the importance of in-vitro testing becomes understandable in order to learn how the cells grow, react and degenerate. This is the starting point for the development of new therapies and for a better understanding of the living systems. Prevention and treatment of diseases, like the disorders of the

nervous system as reported in Table 1.1, require the understanding of the normal brain functionality for which the in-vitro testing is an important tool. The devices developed during this thesis constitute a contribution to this research.

Disorder	**Description**
Alzheimer's disease	A progressive degenerative disease of the brain leading to senility and dementia.
Cerebral plasy	A motor disorder in children, caused by a damage to the cerebrum at the time of birth.
Depression	A serious disorder of mood characterised by insomnia, loss of appetite, and feelings of dejection.
Epilepsy	A condition characterised by periodic disturbances of brain electrical activity that can lead to seizures, loss of consciousness, and sensory disturbance.
Multiple sclerosis	A progressive disease that affects nerve conduction characterised by episodes of weakness, lack of coordination, and speech disturbances.
Parkinson's disease	A progressive disease of the brain that leads to difficulty in initiating voluntary movements.
Schizophrenia	A severe psychotic illness characterised by delusions, hallucinations, and bizarre behaviour.
Spinal paralysis	A loss of feeling and movement caused by traumatic damage to the spinal cord.
Stroke	A loss of brain function caused by disruption of blood supply, usually leading to permanent sensory, motor, or cognitive deficit.

Table 1.1: Disorders of the nervous system (modified from [Bear, 1996])

1 INTRODUCTION

Electrophysiology of in-vitro cellular cultures is playing an increasingly important role in both fundamental and applied research, for drug screening and the development of new therapies. In these fields, micromachining offers the most convenient technology for fabricating small dimension devices with increased resolution.

This work investigates the development of devices for interfacing in-vitro neuronal networks. Micromachining is here applied to fabricate microelectrode arrays (MEAs) allowing a long-term, multi-site stimulation and recording of the evoked or spontaneous cellular activity.

Due to the high multi-disciplinarity of this field, touching biology, micro-fabrication, electronics and computer-science, this thesis will begin with an introduction on some basic concepts of the neuronal physiology, in-vitro culturing and a description of the origin of the bioelectrical activity. The state-of-the art of the MEAs and a review of different approaches investigated up today for the extracellular electrophysiology, e.g. optical recordings and biopatterning will follow.

In order to understand the principles of the MEAs, it is necessary to focus on the modelling of the electrode-electrolyte and electrode-electrolyte-neuron interface. This is the subject of the second chapter, which will be followed, in chapter 3, by the microfabrication of the microelectrode arrays. Electrochemical methods for the platinum electrodeposition and iridium oxide formation will be investigated for modifying the electrode materials and for evaluating their quality.

The recent growing interest in higher resolution devices motivated the investigation of two approaches. These are nanometric electrodes, in order to reduce the inter-electrode separation and a completely new approach based on active pixel sensors (APS)

featuring a local preamplification directly behind the electrode and an on-chip digital addressing as will be described in chapter 4.
Finally, the last chapter will present the development of a mini-neurophysiological laboratory: a microsystem integrating an incubator and a microelectrode array. This last part concerns the IMT contribution to the ongoing European project NeuroBit.

1.1 Interfacing in-vitro neuronal networks – state-of-the art

Before entering into the technical aspects of developing instruments for studying the properties of the nervous systems, it is essential to understand some basic biological aspects involved in neuronal signals. This first chapter gives a background on neurophysiology by summarising the properties of the neuron, of its membrane and by describing the origin of the electrophysiological activity. More detailed descriptions can be found in excellent reference books [Bear, 1996; Kandel, 1991; Nicholls, 1992] as well as in the more recent special issue of Science [vol. 290, 2000].
The second part of this chapter describes the state-of-the art of the techniques used for studying in-vitro neuronal cultures and for monitoring their activity. The presented approaches offer to neurophysiology new ways to understand how the brain and the nervous system function by reducing their complexity into small networks of cells cultured in-vitro.

1.1.1 The neuron

The nervous system controls and regulates the functionalities of the human body. In common knowledge, it is considered to be essentially constituted of interconnected neurons but those are not the only type of cells present. Glia cells are the second main component. Both glia and neurons consist of a wide range of different cell types, differentiated by several criterions, e.g. shape, number of connections and functions.

A first classification based on their connections divide neurons between *sensory neurons* (neurons receiving stimuli from the external environment and thus connected to the sensory surface of the body), *motor neurons* (neurons connected to muscles) and *interneurons* (neurons interconnecting other neurons).
Before pursuing with the classification of neurons, called *histology*, it is necessary to describe the main components of a *prototypical neuron*[1]. It consists of a cell body, *the soma*, and of two types of extensions: the *dendrites* and the *axons* (Figure 1.1).

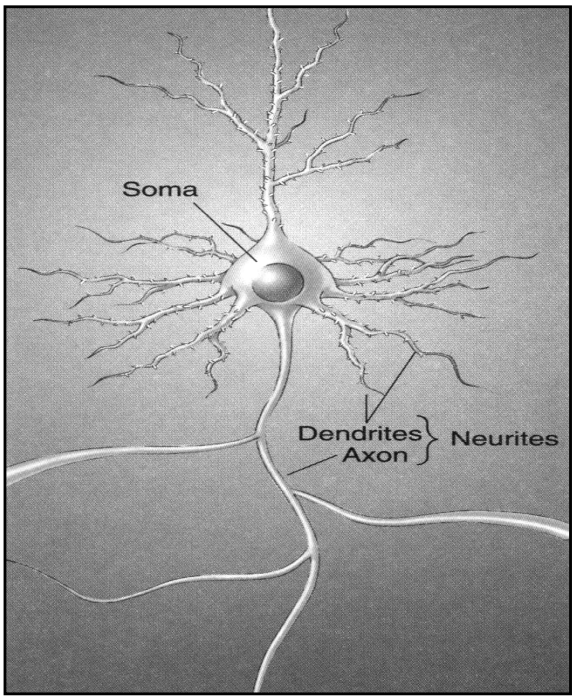

Figure 1.1: The neuron (modified from [Bear, 1996])

The intracellular and extracellular environments are separated by the *neuronal membrane*. The soma contains the *cytosol*, a salty and potassium-rich solution embedding a wide range of functional structures called *organelles* and the cellular *nucleus*. The dendrites consist of a short arborisation around the soma and act as "antennas" of the cell, receiving signals from connected neurons.

[1] A prototypical neuron is a simplified neuron showing its main components extrapolated from the wide range of different neuronal cell types.

The long arborisation (up to several dm) starting from the soma and acting as output connection is called the axon. Its width varies greatly among species: the diameter of a squid axon is about 500 μm, lobster nerve and frog muscle axons are about 75 μm, and mammalian motor neurons average ~10 μm. The total number of axons and dendrites, the *neurites*, extending from the soma allows distinguishing three types of neurons: *unipolar* if there is just one neurite, *bipolar* for two neurites and *multipolar* for three or more neurites. Neurons are also classified by the shape of the dendrite trees (e.g. pyramidal cells and stellate cells) or by the axon length (Golgi type I for long axons, and Golgi type II for shorter axons).
The initial part of the axon connecting the soma is called *axon hillock*. The *axon terminal* is the site where the axon connects the dendrites of another cell. The point of contact is the *synapse*, which is divided in two sides: the *presynaptic* (axonal terminal side) and *postsynaptic* (dendrite or soma side). The space between the pre and postsynaptic sides is the *synaptic cleft*, ranging from 1 to 100 nm [Clark, 1997]. The importance of the synapses is the *synaptic transmission* of the signals. Electrical impulses travelling along the axons are here converted into chemical signals, the *neurotransmitters*, released by vesicles on the presynaptic side and bonded on receptors on the postsynaptic side. At the synapses, the signals are thus transformed from electrical to chemical and from chemical to electrical signals. The resulting particular properties of this transformation, discussed in 1.1.4, are the central aspects involved in the brain information treatment and are also involved in capacities like memory and learning.
Glia cells are the second most important cell type in the nervous system, but their functions are not yet well understood. They are considered to act as supporting cells for neurons and to guide axons to their targets areas during development of the nervous system. However, it is still not known whether glia cells promote the formation of synapses and how precisely they are involved in cellular communication. Glias are divided into *astrocytes*, *oligodendroglia* and *Schwann cells*. Astrocytes are glias filling the space between

neurons (about 20 nm wide) and regulate the chemical content of the extracellular space. They also affect the neurotransmitter release in the synaptic cleft and possess neurotransmitter receptors for triggering biochemical and electrical activity inside the glia [Fields, 2002]. Oligodendroglia (present only in the central nervous system) and Schwann cells (in the peripheral one) provide the *myelin* wrapping of axons for their insulation.
Neuron dimensions depend on the cell type and vary in different living systems. This work focuses on hippocampal[2] rat neurons, having typical in-vitro cells dimensions between 10-40 μm.

1.1.2 The action potential

In order to describe the biophysical origin of the electrical neuronal signals, it is necessary to get into the properties of the neuronal membrane.

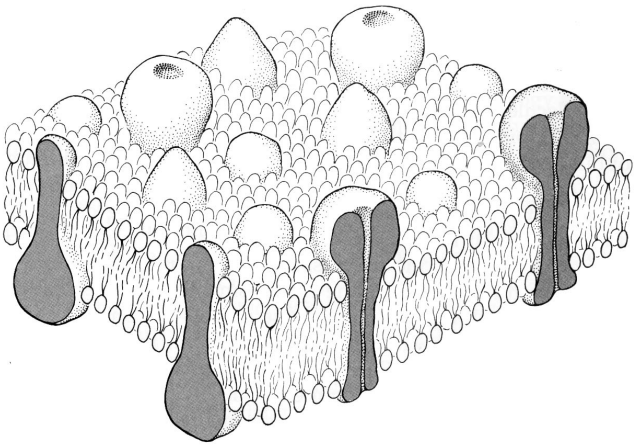

Figure 1.2: The neuronal membrane (modified from [Nicholls, 1992])

It is a phospholipid membrane (Figure 1.2) less than 5 nm thick, dividing the intracellular and extracellular fluid. It incorporates essentially three basic structures to control and transport specific

[2] The hippocampus is a region of the cerebral cortex lying adjacent and medial to the olfactory cortex where all the cortical activities are converging. In humans, it is situated in the temporal lobe and may play a special role in learning and memory.

ions across the membrane*: selective ion channels*, *voltage gated channels* (channels depending on the trans-membrane potential) and *ion pumps*. All those structures consist of membrane spanning protein and are the key structures involved in the electrophysiological activity. In fact, the ionic concentration differences between the inside and the outside of the cell result in a charge difference causing a potential drop across the membrane called *membrane potential*[3].

A first model used to describe the membrane potential has been proposed in 1952 by Hodgkin and Huxley [Hodgkin, 1952] and is called the *H-H model*. It considers a model neuron with a phospholipid membrane and selective ion channels. The concentrations of the major ions inside and outside the cell are reported in the following table (Table 1.2).

ion	extracellular	intracellular
Na^+ [mM]	150	15
K^+ [mM]	5	100
Cl^- [mM]	150	13
Ca^{2+} [mM]	2	0.0002
other ions [mM]	0	116

Table 1.2: Model neuron showing the concentration in mM of the major ions at the resting equilibrium inside and outside of the cell (modified from [Bear, 1996] and [Nicholls, 1992]).

As indicated in the same Table by the arrows, a concentration gradient for each species exists between the inside and the outside of the cell. This gradient tends to equalise the ionic concentrations.

[3] By convention the membrane potential is measured from the inside versus the outside of the cell.

But this does not happen, since at the same time an electrical gradient acting in the opposite direction would be established due to the presence of non-diffusible ions in the cell. For this reason, at this electrochemical equilibrium, called *resting equilibrium*, no net current flows across the membrane and a potential difference, the *resting potential*, can be measured across the membrane.
The equilibrium potential for a single species M separated by the membrane can be calculated using the *Nernst equation*:

$$E_M = \frac{RT}{zF} \ln\left(\frac{[M]_o}{[M]_i}\right) \tag{1.1}$$

where $[M]_o$ and $[M]_i$ are the molar concentration outside and inside the cell, R is the thermodynamic gas constant (8.34151 $J.K^{-1}.mol^{-1}$), T the temperature in K, z the valence of the ion and F the Faraday constant (96485 $C.mol^{-1}$).
Knowing the ion permeabilities g_M through the membrane for each ionic species, it is possible to estimate the resting potential V_m by using the *Goldman-Hodgkin-Katz (GHK) equation (*also known as the *constant field equation*[4]*)* [Nicholls, 1992]:

$$V_m = \frac{kT}{q} \ln\left(\frac{g_K[K^+]_o + g_{Na}[Na^+]_o}{g_K[K^+]_i + g_{Na}[Na^+]_i}\right) \tag{1.2}$$

where k is the Boltzmann constant (1.38×10^{-23} J/K), T is the temperature in K, q is the elementary charge (1.6022×10^{-19} C), g_M the ion permeabilities for the species M and $[M]_o$, $[M]_i$ respectively represent the outside and inside concentrations. The contributions across the membrane of Cl^- and Ca^{2+} are negligible since the membrane is essentially permeable to sodium and potassium.

[4] The GHK equation is also called constant field equation since one assumption is a uniform field across the membrane.

Assuming g_{Na}/g_K = 0.04 at 37°C [Nicholls, 1992], the GHK equation can be written as:

$$V_m = \frac{kT}{q} \ln \left(\frac{[K^+]_o + \frac{g_{Na}}{g_K}[Na^+]_o}{[K^+]_i + \frac{g_{Na}}{g_K}[Na^+]_i} \right) \tag{1.3}$$

which gives the resting potential V_m = *-65 mV*. However, the GHK equation shows a limit since it does not consider ion pumps modifying the ion permeabilities. For example the sodium-potassium pump is the active mechanism allowing to maintain a given concentration of these two ions. Consequently, in practice the measured resting membrane potential V_m is in the order of –73 mV [Nicholls, 1992].

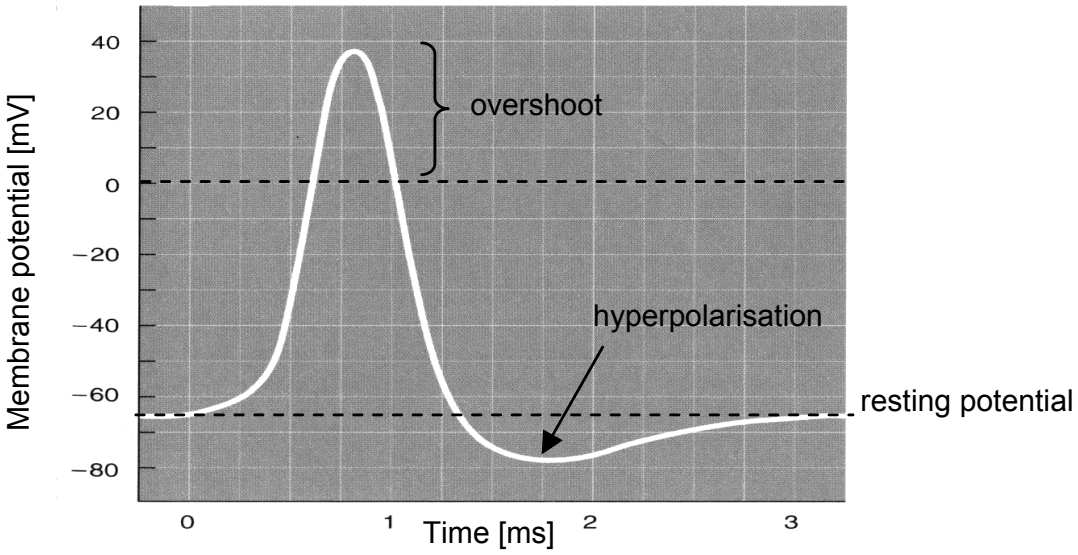

Figure 1.3: The action potential is composed by a rising phase, a falling phase and a hyperpolarisation (modified from [Bear, 1996])

The *action potential* or *spike* (Figure 1.3) is a transitory (few milliseconds) non-linear change of the membrane potential (up to 100 mV potential change). It is composed of a *rising phase* (*depolarisation),* followed by a *falling phase* bringing the membrane potential down to a *hyperpolarisation* or *undershoot*. This shape is due to the activity of the voltage controlled channels of the membrane that modify the ion permeabilities as a function of the membrane potential. For the same reason, the membrane fires an action potential only when it is depolarised up to a critical *threshold*. This depolarisation is due to the entering of Na^+ into the cell through specialised ions channels sensitive for example to membrane stretching, or to neurotransmitters (in interneurons). However, it is also possible to depolarise the membrane artificially using microelectrodes as described in section 1.1.4.
At the threshold level (about 20 mV), extra sodium channels are opened and the depolarisation rapidly increases in a nonlinear avalanche like way. The repolarisation is the result of a potassium efflux due to voltage-activated potassium channels (Figure 1.4). The potential falls down under the resting potential and during this short period no extra action potentials can be fired. This is called the *refractory period*. The propagation of the action potentials along an axon is the result of a chain of events. Once a segment of the axon is depolarised up to the threshold, the voltage-controlled ion channels open and the influx of positive charges will depolarise the successive axon segment, which will activate the firing of the next one, and so on. The refractory period impedes the backward travelling of the action potential along the axon and thus only one direction of propagation is possible. The rate of propagation for mammalian motor neurons is around 10-120 m/s, while for non-myelinated sensory neurons it is about 5-25 m/s.
Once the action potential reaches a synapse at the axon terminal, the vesicles of the presynaptic neuron release the neurotransmitters.

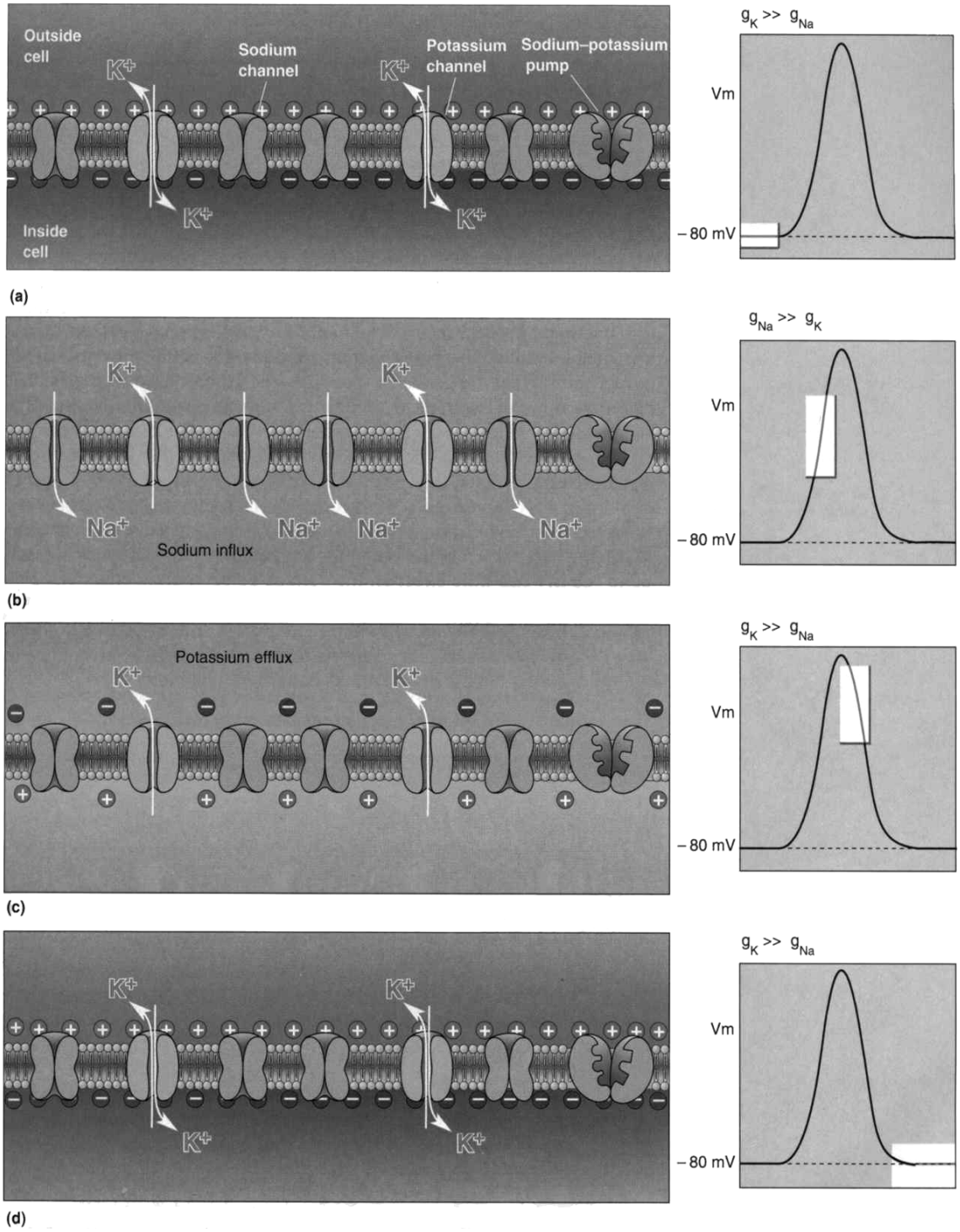

Figure 1.4: The action potential is modulated by the changing of the relative ionic permeability of the membrane. (a) Membrane permeable only to K^+ and $V_m = E_K$. (b) Sodium channels open. (c) Sodium channels close and additional potassium channels open. (d) The resting potential is restored. (modified from [Bear, 1996])

After diffusing into the synaptic cleft, they reach the post-synaptic side, where their binding to specific receptors modify the membrane ionic permeability. If this modification allows the membrane to reach the threshold, a post-synaptic action potential is fired. The magnitude of the post-synaptic signal depends on the amount of released neurotransmitter, resulting in an excitatory (EPSP: excitatory post-synaptic potential) or inhibitory action potential (IPSP: inhibitory post-synaptic potential). The integration of all signals from the synapses on the post-synaptic neuron will determine whether or not this neuron will initiate the action potential to the next cells. A key feature of synaptic transmission is its plasticity: the organisation of synaptic connections is modified by neuronal network activity, creating and eliminating synapses. This property is postulated to drive the formation of durable memory [Balley, 1993; Geinisman, 2000].

Cholinergic	
Acetylcholine	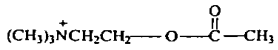
Adrenergic (Catecholaminergic)	
Dopamine	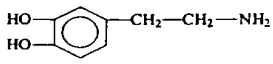
Norepinephrine	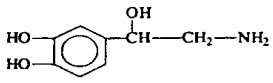
Epinephrine	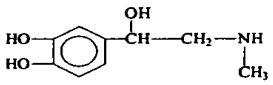
Serotonergic (Tryptaminergic)	
5-Hydroxytryptamine or serotonin	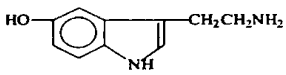
Amino Acidic	
γ-Aminobutyric acid (GABA)	$NH_2CH_2CH_2CH_2COOH$
Glutamate	$HOOC—CH_2CH_2CH(NH_2)—COOH$
Glycine	NH_2CH_2COOH
Peptidic	
Met-enkephalin	

Table 1.3: General classes of neurotransmitters (modified from [Clark, 1997])

The general classes of neurotransmitters include acetylcholine, catecholamines, indoleamines, amino acids and peptides. Table 1.3 shows typical neurotransmitters [Clark, 1997]. As mentioned, the role of these substances is essential for the brain activity. For example dopamine plays an important role for the regulation of motor functions, for the control of mood and emotion and its study is essential for Parkinson's disease, schizophrenia and depression [Clark, 1997].

1.1.3 In-vitro culturing

The human body is made of about 10^{13} cells of which about 10^{11} cells are neurons. On average each neuron makes 10^3 - 10^4 contacts with other neurons [Grattarola, 1998]. These values give an idea of the complexity in analysing in-vivo the chemical and electrical signals involved in the nervous system. As will be presented next, in-vitro testing allows investigating smaller networks.

In in-vitro studies the cells are maintained alive outside the body facilitating their accessibility and decreasing the complexity of the system. This technique has seen its first developments with tissue of a chicken at the beginning of the last century, in the laboratory of Ross Granville Harrison. At present the reference for culturing nerve cells is the book of G. Banker and K. Goslin [Banker, 1998] where different methods and cell culture-types are exhaustively described.

Neuronal cultures are called *primary cultures*, since they are prepared from cells taken directly from the animal. In-vitro culturing techniques are constantly improved, and different methods exist. Summarizing the culture preparation, mammalian neurons are extracted from the animal, mechanically and enzymatically dissociated and put in suspension in a culture medium. The obtained suspension is then placed on an appropriate substrate (typically a Petri dish) and, with time, the cells sediment on the surface. This step is called *cell* or *culture plating*. Under favourable conditions, i.e. sterility, temperature, pH, osmolarity, oxygenation and supply of nutrients/growth factors, the neurons fix themselves on the substrate

and start to grow. An interconnected neuronal network is in this way obtained [Corner, 1994; Habets, 1987]. This type of culture is called *dissociated*. It is also possible to culture brain slices, either *acute slices* (freshly cut) [Borkholder, 1997; Jimbo, 2000; Oka, 1999; Yeung, 2001] or maintained in an *organotypic* culture [Stoppini, 1997; Egert, 1998; Jahnsen, 1999; Thiébaud, 1997; Thiébaud, 1999; Tscherter, 2001]. The brain slices are interesting while they have a pre-defined in-vivo cell organisation and thus are similar to the real in-vivo morphology. However, similarities between slice cultures and dissociated cultures have been observed. For example, the rhythmic activity in organotypic and randomised networks of spinal cord seems to be controlled by the intrinsic neuronal activity with no need of a specific architecture [Streit, 2001].
Dissociated or slice cultures can be performed on appropriate micromachined surfaces and kept alive up to years. In this way, Bio-MEMS devices can be employed to study the electrical or chemical signalling as well as other physiological aspects in small networks.

1.1.4 State-of-the art of recording / stimulation techniques

Different techniques exist for measuring and evoking the electrophysiological activity of in-vitro neuronal networks. As described next, it is possible to distinguish between intracellular and extracellular techniques.
Previously, the membrane potential has been described considering the ionic phenomena across the cellular membrane. The measurement of this potential difference needs two measuring points, one in the cell and the second outside. This kind of electrophysiological measurement is called an *intracellular technique* and requires the breaking of the membrane. Another category, the *extracellular technique*, places one measuring point outside the cell, close to the membrane and a second one, the reference, far away from the cell. As described above, when an action potential occurs, the intracellular and the extracellular ionic concentrations are both

modified by the membrane transport properties. The extracellular changes are localised near the membrane. Thus, currents entering or leaving a neuron generate voltage signals at the electrode nearby. This results from a resistive drop in the medium between the reference electrode and the recording electrode.
The recorded action potential measuring directly the membrane potential or measuring the extracellular change are different. Figure 1.5 shows a simultaneous intracellular and extracellular recording [Claverol-Tinture, 2002].

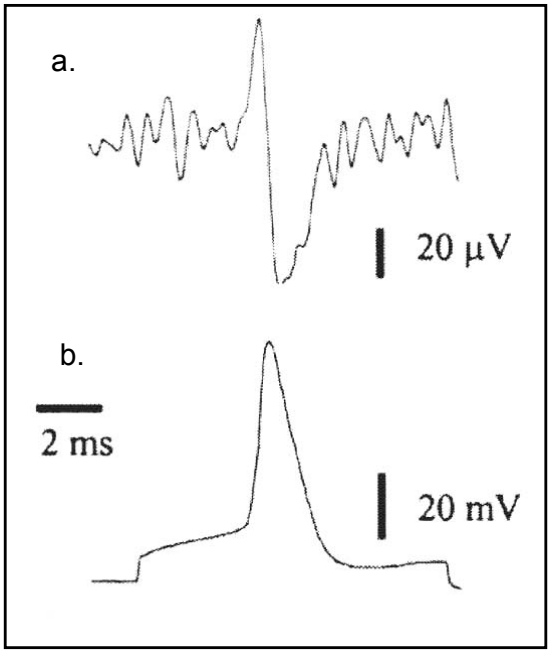

Figure 1.5: Simultaneous (a) extracellular recording and (b) intracellular recording (modified from [Claverol-Tinture, 2002])

Additionally, extracellularly recorded signals show lower amplitude. Instead of action potentials up to 100 mV_{pp} measured intracellularly, the extracellularly recorded signals are typically in the range of 20 to 500 μV_{pp}. This range is additionally lowered to 20-200 μV_{pp} for vertebrate's neurons. The significant advantage compared to intracellular techniques is an increased lifetime of the culture and the possibility to perform multiple measurements.

The *extracellular stimulation* of the membrane can be realised by applying a potential or a current to the extracellular electrode. If the membrane is depolarised up to the threshold, the neuron will initiate an action potential.
By stimulating and recording the cellular activity, it is possible to bidirectionally interface the network. Moreover, for a non-invasive technique it is possible to routinely study the network for long-term. This is particularly interesting for studying the network plasticity allowing the understanding of how the network "encode" and "processes" the information [Clement, 1999; Hua, 2000; DeMarse, 2001; Jimbo, 1998; Sokolov, 1999]. Those aspects are the topic of the ongoing Neurobit project, which will be discussed in chapter 5 of this work.

The patch-clamp

Until now, in-vitro electrophysiology has seen the majority of its development using glass pipette electrodes. Neurophysiologists have studied single-cell properties, ion-channels, drugs effects and synaptic signalling with these electrodes [Misgeld, 1998]. The electrodes are made by pulling a glass tube into a fine capillary at one end (less than 1 μm in diameter) and filling it with a saline solution. Finally an electrode, typically platinum or silver / silver chloride, electrically contacts the solution to the measuring circuit.
Glass pipettes are used in different configurations: intracellular, whole-cell patch[5], cell-attached patch and extracellular. In intracellular and whole-cell-patch techniques the cellular membrane is broken after aspiring it into the glass pipette. Thus, the electrode solution is in direct contact with the cytoplasm. The membrane binds itself to the glass forming a tight electrical seal. The whole-cell-patch is less damaging than the intracellular technique, but the osmotic equilibrium between the intracellular medium and the electrode

[5] B. Sakmann and E. Neher were awarded the Nobel price for the discovery of this technique in 1991.

solution is a critical point to avoid swelling or shrinkage of the cell. In the cell-attached patch the procedure is similar to the whole-cell patch, with the difference that the membrane is not broken. Only part of the membrane is sucked into the pipette. However, vibrations present a risk to break the attached membrane.
Finally, extracellular recording or stimulation can also be performed by placing the glass pipettes near the membrane. But like other glass pipette techniques, their individual manipulation limits the number of electrode-cell couplings. It is in fact extremely difficult to manipulate and work with more than four electrodes at the same time.

Integrated patch-clamp

The patch-clamp offers several interesting properties, e.g. high signal amplitude, for studying membrane ionic channels. Unfortunately, the classical method is mainly limited by the laborious process of manipulating the pipettes, and thus in the number of patched cells. Additionally, the patched cell is not easily accessible for optical, fluorescence or scanning probe observations.
In recent years, the integrated approach for parallel patches has been developed [Farre, 2001; Guia, 2002; Fertig, 2001; Pantoja, 2001; Fertig, 2001; Klemic, 2002; Lehnert, 2002; Fertig, 2002; Sigworth, 2002; Fertig, 2002]. A hole or an array of holes of a few microns in diameter are provided in a substrate and are electrically contacted to the electrolyte (Figure 1.6). The cellular membrane is sucked into the hole to form a tight electrical seal and is than broken. In this way the backside electrolyte is in contact with the intracellular cytoplasm allowing the monitoring of the ion channels activity. Several devices have been reported: using a quartz membrane of 20 μm with a hole of 1 μm in diameter [Fertig, 2002]; using a poly(dimethylsiloxane) (PDMS) substrate with a hole of 10 μm in diameter [Klemic, 2002]; or using silicon substrates like the

commercial system of AVIVA Bioscience[6] in collaboration with Axon Instruments.

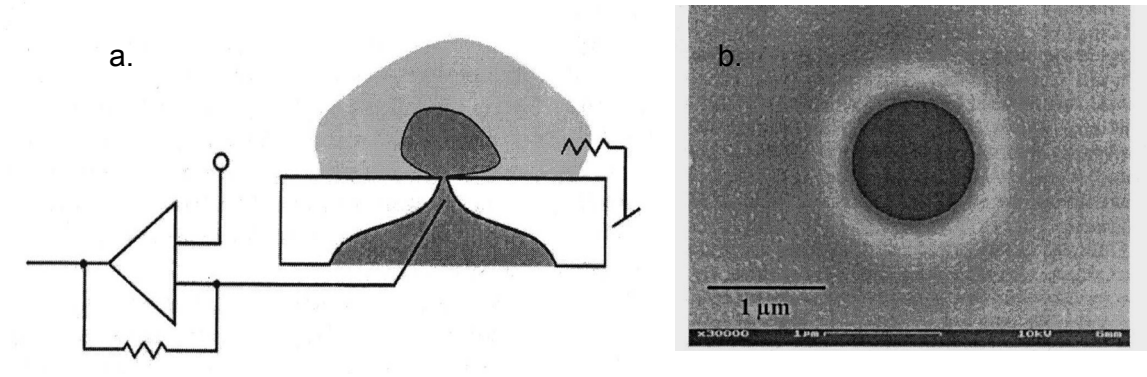

Figure 1.6: The integrated patch clamp. (a) Principle, (b) SEM picture of the etched glass (modified from [Fertig, 2001])

One of the main difficulties of this approach is to achieve a stable sealing of the cellular membrane on the substrate. This can be partially solved by modifying the chip surface with adhesion promoters in a similar way to the bio-patterning approach (see below). For this reason and for the ones previously reported for the standard approach, this technique does not allow long-term measurements. The integrated patches are certainly interesting for simplifying the classical glass pipettes method.

Microelectrode arrays (MEAs)

Considerable effort has been devoted during the last twenty years to develop microelectrodes arrays (MEAs) for the non-invasive monitoring and stimulation of the electrophysiological activity of in-vitro neuronal networks. The concept consists in plating the cell culture on top of a micromachined surface, where an array of microelectrodes has been defined. Long-term, multi-sites recording/stimulation are the most interesting properties of the MEAs technology.

[6] http://www.avivabio.com/About/scientific.html

The development of MEAs began in 1972 by recording field potentials from spontaneously contracting sheets of chick cardiac myocites [Thomas, 1972]. On cultured neuronal networks the firsts results have been presented at the beginning of the eighties [Pine, 1980; Gross, 1982]. Many experiments in the early 1990s have demonstrated the potential of this technique, increasing the neurobiologists interest [Israel, 1990; Najafi, 1990; Grattarola, 1991; Regehr, 1989; Stevens, 1993; Bove, 1995; Breckenridge, 1995; Grattarola, 1995]. Thus, while single unit recording technology, e.g. patch-clamp, still remains the standard approach to study neuronal cells, microelectrodes arrays are becoming a valuable research tool in both fundamental and applied neurophysiology.

Today, several MEAs of different materials (TiN, Pt, ITO, IrO_x, Au) and geometry have been developed [Blau, 1997; Boppart, 1992; Hoogerwerf, 1994; Breckenridge, 1995; Bucher, 1999; Cunningham, 2001; Gonzalez, 1997; Hammerle, 1994; He, 2000; Keefer, 2001; Maher, 1999; Maher, 1999; Owens, 1995; Regehr, 1989; Regehr, 1988] and a few of them are also commercialised [Multichannel Systems[7], Panasonic[8], Ayanda-biosystems[9], G. Gross[10]]. Figure 1.7 shows some of those devices.

They typically integrate, on glass, silicon or plastic substrates, an array of 30 up to 128 planar electrodes. The substrate surface is insulated by a biocompatible material (PA, Si_xN_y, EPON SU-8). Electrode diameters range between 10 μm to 100 μm with an inter-electrode spacing between 100 μm and 500 μm organised in a regular matrix (4 x 4, 5 x 5, 6 x 6, 8 x 8), regular hexagonal grids, double ellipses or circles.

---

[7] http://www.multichannelsystems.com/

[8] http://www.med64.com/

[9] http://www.ayanda-biosys.com/

[10] http://www.cnns.org/

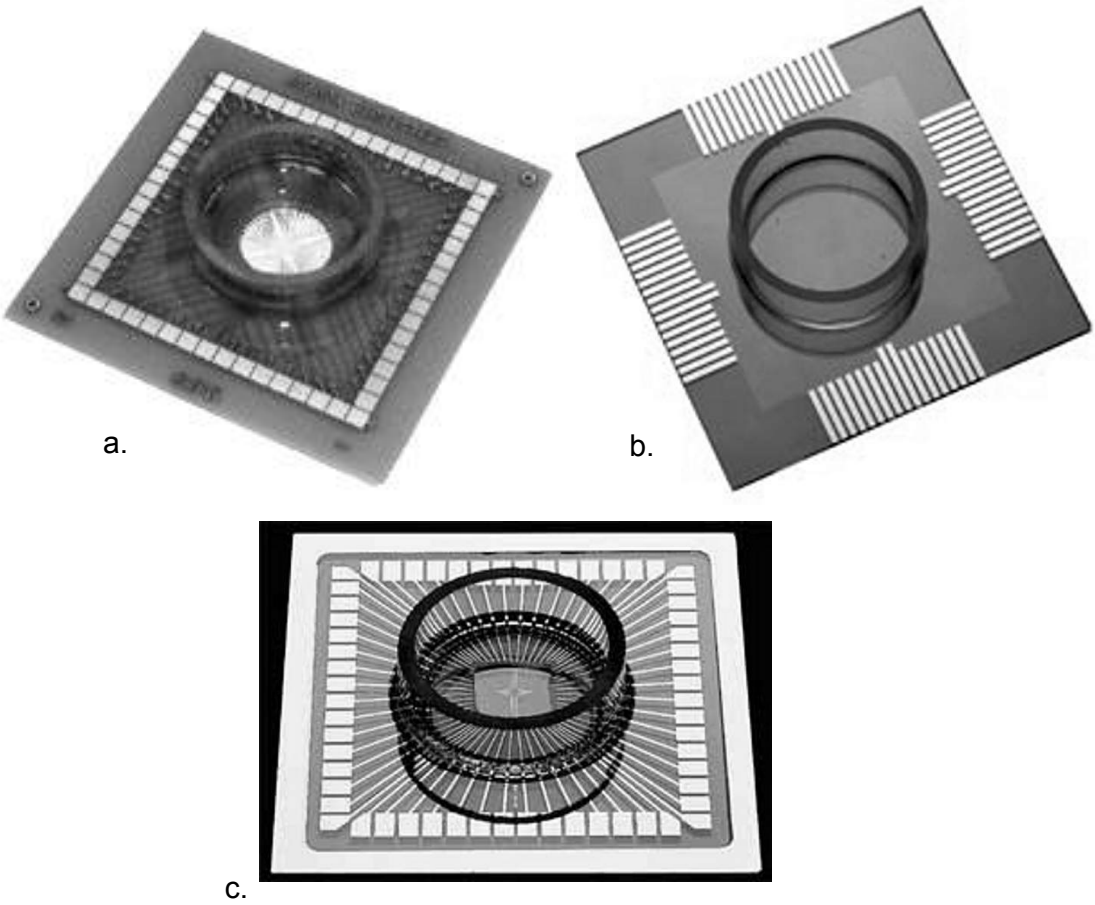

Figure 1.7: Commercially available MEAs: (a) Ayanda-biosystems, , (b) Panasonic, (c) Multichannel Systems.

Each electrode is connected with an individual pad by patterned metal leads. The typical MEA set-up (Figure 1.8), connects each pad to an external measuring system for amplifying the potential difference between each microelectrode and a reference in the solution [Pine, 1980; Martinoia, 1993]. Table 1.4 summarises the specifications of two commercially available systems.

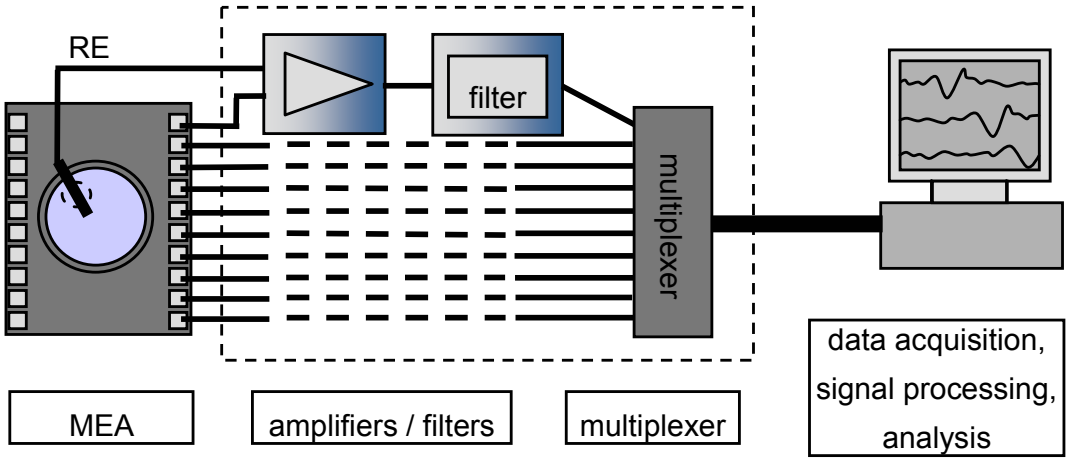

Figure 1.8: Schematics of a typical MEA set-up. The signals from the microelectrodes are individually amplified / filtered referred to the reference electrode (RE).

In order to reduce noise contributions due to the distance between the electrodes and the external amplification stage and to simplify the overall electronic set-up, MEAs with an on-chip CMOS amplifier circuit placed on the sides of the chip have been developed in particular for in-vivo applications [Buttler, 1991; Najafi, 1986; Najafi, 1994; Schwarz, 2000; Kovacs, 1994; Kovacs, 1992; Pancrazio, 1998].

The material choices for the device and for the packaging are limited. The employed materials have to satisfy the biocompatibility, the durability and resist to the sterilisation conditions such as conventional autoclave method (120°C in high pressure humid environment), ethylene, or UV light exposure. Moreover the electrodes should have an impedance lower than 500 kΩ at 1 kHz to allow the recording [Potter, 2001]. To limit the electrode impedance, platinum black is widely used. However, the resulting electrodes are rather fragile, restricting the re-usability of those devices. This has been improved by sputtering iridium oxide [Blau, 1997] or titanium nitride [Egert, 1998]. For brain slices, the electrode impedance has been lowered by increasing the electrode surface with micromachined or electroplated three dimensional electrode array [Thiébaud, 1999; Heuschkel, 2002].

	Multichannel system	Panasonic system
Array		
Number of electrodes	64 or 128	64
Electrode diameter	10 or 30 μm	50 μm
Electrode separation	100 or 200 μm	150 μm
Active area	1.5 x 1.5 mm^2	1 x 1 mm^2
Acquisition Unit		
Number of acquisition channels	8, 16, 32, 128	8
Dynamic range	60 dB (1:10000)	61 dB (1: 10100)
Sampling rate	25 kHz / channel	20 kHz / channel
Resolution	12 bits ADC	?
Max. band width	0.1 Hz – 10 kHz	0.1 Hz – 20 kHz
Noise level	<< 20 μV	100 μV

Table 1.4: Specifications of two commercially available MEAs systems.

In another approach, the silicon-oxide transistor gate of *field-effect-transistors (FET)* is used as electrode [Baumann, 1997; Baumann, 1999; Besl, 2001; Bove, 1996; Fromherz, 1991; Fromherz, 1993; Fromherz, 1994; Fromherz, 1996; Fromherz, 1999; Offenhausser, 1997; Offenhausser, 2001; Offenhausser, 1995; Owens, 1995; Sprossler, 1998; Sprossler, 1999; Vassanelli, 1997; Vassanelli, 1998; Vassanelli, 1998; Yeung, 2000; Zeck, 2001]. Changes in the cell's membrane voltage cause a variation of the gate voltage, which can be recorded as a difference in the source-drain current. However, this approach suffers from the transistor thermal noise contribution (100 μV_{rms} at a bandwidth of 10 kHz, [Vassanelli, 1998]). Additionally, extrinsic noise acts on the interconnecting wires superimposing an important noise contribution to the recorded signals. This limits the detectable signals to signals larger than 200 μV [Sprossler, 1999].

High-density electrode arrays

There is an increasing interest in higher density devices, which could provide higher spatial resolution [Potter, 2001; Eichenbaum, 1998]. This interest is related to the growing use of MEAs for studying network properties and modifications. In fact, following the Hebb's proposal (1949), it is generally believed that the information is processed by distributed neuronal networks and not by the features of single cells. To enable the interpretation of underlying cellular events, high spatial/temporal resolution devices with a large number of recording points are necessary. Additionally, high density arrays would also solve some other practical issues. Firstly, it has to be remembered that neurons cultured on MEAs can move. This impedes the long time recording from the same cell. Actually, the distance between microelectrodes (between 70 and 200 μm) is relatively large compared to the dimensions of the studied neurons (soma diameter between 10-40 μm for in-vitro hippocampal rat neurons). If a neuron will move to an area between two microelectrodes, it will not be possible to clearly record its activity. Secondly, a high density MEA would be a powerful tool for a variety of experiments, without needing the development of specific MEAs geometries.

In both MEAs and FETs technologies, the increase of the electrode density on large active areas is limited by the necessity to connect each active site by one individual lead. Thus, for reasons of the space requirement and the lead impedance, the density of measuring points is limited. Other ways to overcome this problem have been suggested: the field-effect-addressable potentiometric sensor (FAPS) and the light-addressable potentiometric sensor (LAPS). A review of those approaches has been discussed by M. George in [George, 2000]. A third approach has been described very recently, the micro-action potential scanner MAPS concept [Gill, 2002], but is still at an early development stage.

Field-effect-addressable potentiometric sensors (FAPS)

The field-effect-addressable potentiometric sensor/stimulator (FAPS) devices permit a large number of individually addressable, densely packed active sites [Parak, 1999; Böhm, 1999; Böhm, 2000]. The geometry of the FAPS is presented in figure 1.9. It consists of two perpendicular grid-structures of field-effect channels and gate electrodes. Similar to FETs, applying a bias voltage to one gate electrode to deplete the channel and a constant current between the source and the drain, it is possible to detect the resistance variation of the channel generated by a surface potential.

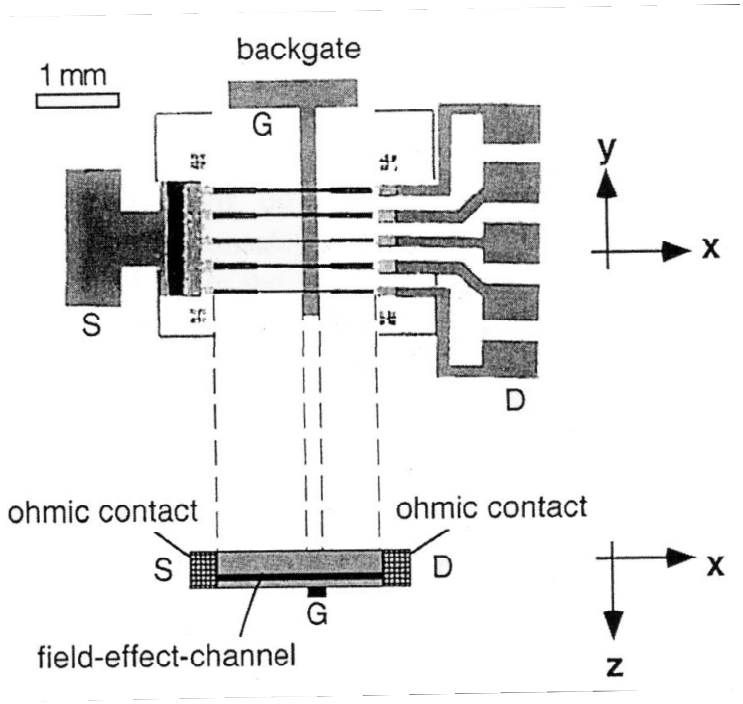

Figure 1.9: Principle of the field-effect-addressable potentiometric sensor (FAPS) (modified from [Böhm, 2000])

The sensitive region is selected at the intersection of the measured channel and the biased gate. The advantage of this concept compared with conventional FET arrays is the sharing of the field-effect channels allowing a drastic reduction of connecting leads: only 100 leads against 10'000 for 10'000 active sites [George, 2000]. The

spatial resolution is limited by the size and the separation of the active sites.
A test structure with five parallel field-effect channels, 65 μm wide and 2 mm long, has been presented [Böhm, 1999; Böhm, 2000]. At a 3 kHz time resolution, a potential sensitivity between 100-150 μV has been reported. However, if more addressable points would be realised adding back-gate electrodes and the respective front-gate electrodes, the length of the field-effect channels, and thus their resistance will increase. At constant time resolution this increment involves a loss in the potential sensitivity [Böhm, 2000]. Thus, the gain in number of active sites has to be paid for by a loss of the sensitivity.

Light-addressable potentiometric sensor (LAPS)

A completely different approach is the MEC3600 presented by Bucher et al., [Bucher, 2001]. It is a light-addressable microelectrode chip with 3600 electrodes (60 x 60) on a surface of 1.8 x 1.8 mm^2. The chip is realised by patterning indium-tin oxide leads on a transparent glass substrate (49 x 49 mm^2). Then, amorphous silicon is deposited on the top side (150 nm thick) and insulated with a silicon nitride layer. Finally, gold or titanium nitride electrodes are structured on the silicon nitride (Figure 1.10).
Utilising the increase in photoconductivity of the amorphous silicon layer upon backside illumination by a focussed laser (Ar-laser 488 nm, diameter 1.6 μm, P_{spot} = 1.6 mW), it is possible to opto-electrically connect the electrodes with the corresponding metal lead. Each metal lead, 20 μm wide with a separation of 10 μm to each other, is externally connected to an amplification circuit and light addressing is used to select the electrode to record from. Recordings of spontaneously active cardiac myocytes using LAPS have been reported.
A second optically switched microelectrode array (OSMA) providing 10^4 electrodes of 50 μm in diameter is described by Manuccia et al., [Manuccia, 1998]. Even though the electrode density is drastically

increased with this approach, the spatial electrode resolution and thus its use for electrophysiological measurements is still limited. Firstly, the lateral resolution in the electrolyte is limited by light scattering in the transparent glass substrate [Bucher, 2001]. This is responsible for signal contributions from neighbouring electrodes.

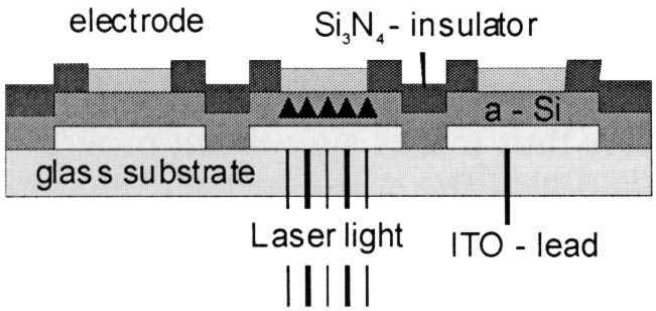

Figure 1.10: Principle of a light addressable potentiometric sensor (LAPS) (MEC3600, modified from [Bucher, 2001])

Secondly, investigations of the spatial resolution and potential sensitivity of LAPS reported by M. George in [George, 2000] have shown that even using highly doped semiconductors to improve the spatial resolution, there is a loss of sensitivity. In fact, in the limiting case of using a metal instead of a semiconductor, no space charge region would be created and thus no photocurrent would flow. Also with LAPS as it has been shown with FAPS, the gain in integration density has to be paid with loss of sensitivity. The resulting characteristics are a potential sensitivity of approximately 100 μV at a 0.3 ms time resolution and a limiting spatial resolution of 10 μm. Additionally, a practical limit in the spatial resolution is given by the size of the focus and separation of the light-pointer.

Finally, a time delay up to several μs between each electrode's recording is the result of the optical addressing by mechanical displacement of the light source and of the activation time of the optoelectrical connection between electrodes and leads. George reports an example of a device with 250 active sites of 20 x 20 μm^2 with an assumed sensitivity of 100 μV and a spatial resolution of 20

μm. He shows that with a light modulation of 25 kHz, it would take 10 s to get an image of the whole surface potential. This delay is too long to study the cell-to-cell communication with a large number of active sites. The advantage of this system is however the freedom in choosing the measuring sites.
Unfortunately, an additional important problem in some biological applications is the phototoxicity effect of the addressing light on cells like neurons, rendering this method unsuitable for long-term recordings [Sprossler, 1998].

The micro-action potential scanner (MAPS)

The MAPS concept has recently been presented by P. R. Gill at the EMBS conference 2002 [Gill, 2002]. It is based on the novel use of a p-n junction (Figure 1.11).
The n-side of the structure is in direct contact with the cultured cells (signal sources). It is known that only if the p-n voltage exceeds a certain value V_r, all the n-type material will be in the conductive zone. The p-side acts as a resistive material, providing a potential gradient upon potential application. By controlling the amplitude (AC signal) of the applied potential (V) and by defining the potential of the solution, it should be possible to control the size of the conductive area. Scanning the surface, and measuring the signal between the n-type layer and a reference electrode in the solution, allows adding or subtracting signal sources from the observed signal.
With continuous spatial scanning it should be possible to reconstruct all the signals of the sources. Theoretically a typical probe with a square receptive field of 200 μm would have a spatial resolution of about 7 μm, but the recording capabilities of the MAPS still have to be proven, and, as discussed by the authors, this device “should be treated with a cautious enthusiasm”.

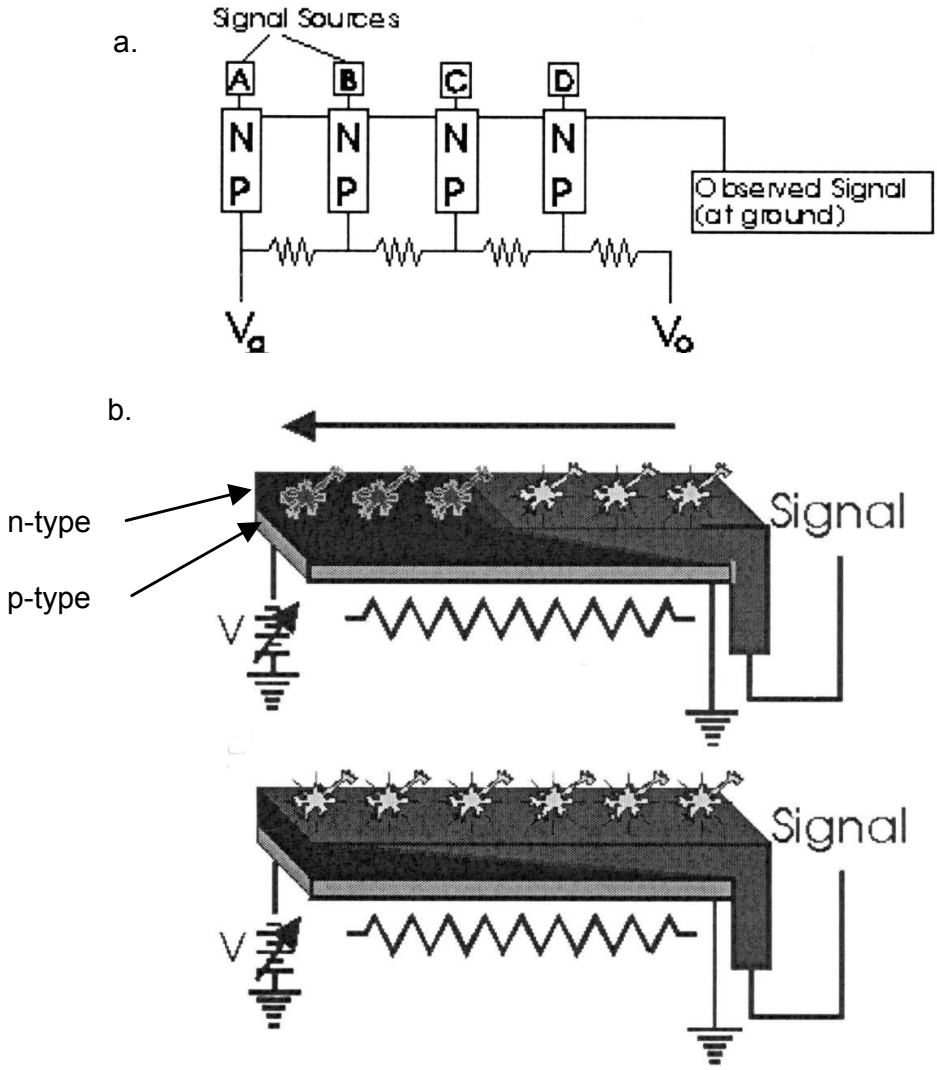

Figure 1.11: Principle of the micro-action potential scanner (MAPS). (a) a series of p-n junctions can act as a multiplexer. (b) continuous version of the discrete mulltiplexer. (modified from [Gill, 2002])

Biopatterning

An alternative to overcome the limited density of electrodes and also for solving the problem of the random positioning of the cells in dissociated cultures, is the biopatterning. The cell positioning and thus a geometrically defined network is obtained by defining areas with favoured or inhibited adhesion. A review of these techniques is presented in [Blawas, 1998; Kane, 1999; Ito, 1999]. Patterns of

functional molecules can be obtained by ink-jet techniques, microfluidics [Martinoia, 1999], photochemical structuring [Morigaki, 2001; Nicolau, 1999; Chang, 2001; Lee, 1994], by deep UV lithography [Lom, 1997], or by soft printing. This last technique is the most popular [Griscom, 2002]. A polymer printing stamp, e.g. PDMS [Xia, 1998], or SU-8 [Griscom, 2001] is used to stamp the adhesion proteins like polylysine on the substrate [James, 2000; Heiduschka, 2001]. Used adhesion promoters/inhibitors include amines (adhesion promoter) and alkanes (adhesion inhibitor), patterns of silanes with different hydrophilicity [Kleinfeld, 1988; Corey, 1991] or cell adhesion molecules like laminin covalently bonded on glass substrates [Tai, 1998].

Techniques for network patterning are constantly investigated [Sorribas, 2002; Saneinejad, 2000], including the use of silicon wells structures [Maher, 1999; Maher, 1999; Heiduschka, 2001]. Another recent technique exploits the use of dielectrophoretic forces for defining the pattern [Matsue, 1997; Heida, 2001; Heida, 2002].

The fascinating aspect of biopatterning is the possibility in defining simple geometrically controlled networks, which are of large interest in modelling and neuroinformatics. However, it has to be remembered that “natural” growth of the cultured cells is modified. The pros and cons of the biopatterning are subject of controversy.

Fluorescence recordings

Instead of using electrical recordings, the cellular or network activity can also be monitored by using optical dyes [Salzberg, 1977; Kawaguchi, 1996]. The fluorescence dye is introduced into the culture and photoemission is stimulated by a light flash of a few hundreds of milli-seconds at the specific wavelength. A photodiode array typically with 10 x 10 or 25 x 25 pixels is used [Chien, 1991; Chien, 1991; Neunlist, 1999]. Higher resolution has been achieved with the high-speed (1000 frames/s) CCD camera of 64 x 64 pixels developed by Pine and Potter in 1997 [Pine, 1997]. Laser beam rapid scanning systems based on acusto-optic deflectors have also

been reported [Bullen, 1999; Saggau, 1998; Bullen, 1997]. Calcium-sensitive dyes, e.g. Fluo-3, allow the recording of bursts of activity, but its temporal resolution is not fast enough to see the individual action potentials [Jimbo, 1993; Voigt, 1997]. Better temporal resolution and detection of subthreshold events or inhibitory potentials have been achieved using voltage-sensitive dyes. These have been successfully used to monitor the membrane potential in invertebrate ganglia [Wu, 1998] and in vertebrate monolayer networks [Obaid, 1999] or cultured hippocampal neurons [Bullen, 1999]. This technique is mainly limited by the phototoxic effects of the high illuminating dose required for the photoemission [Obaid, 1999]. Recent developments of new dyes may reduce phototoxic and photobleaching effects as well as enhance the signal-to-noise ratio [Siegel, 1997]. Developments of techniques for cell labelling with specific dyes, e.g. lyophilic dyes [Blau, 1999; Siegel, 2000; Siegel, 1997], or virus transfection of cells with different colored fluorescent proteins [Guerrero, 2002; Okada, 1999] could also be used to monitor and track specific structures in the culture. The combination of optical recordings techniques with MEAs could be an interesting topic for a future development.

1.2 Bibliography

Balley, C.H. and E.R. Kandel, Structurral changes accompanying memory storage. Annual Review in Physiology, 1993. **55**: p. 397-426.

Banker, G. and K. Goslin, Culturing nerve cells. 2nd ed. 1998, Cambridge, Massachusetts: MIT Press.

Baumann, W.H., et al., Measurement of cellular signals with chemical sensitive field effect transistors. Abstracts of Papers of the American Chemical Society, 1997. **213**: p. 51-BTEC.

Baumann, W.H., et al., Microelectronic sensor system for microphysiological application on living cells. Sensors and Actuators B-Chemical, 1999. **55**(1): p. 77-89.

Bear, M.F., B.W. Connors, and M.A. Paradiso, Neuroscience: exploring the brain. 1st ed. 1996, Baltimore: Williams & Wilkins.

Besl, B.J. and P. Fromherz, Brain chip: Transistor array for extracellular recording of hippocampal slices. Biophysical Journal, 2001. **80**(1): p. 450.

Blau, A., Bioelectronical neuronal networks. 1999, University of Tuebingen: Tuebingen.

Blau, A., et al., Characterization and optimization of microelectrode arrays for in vivo nerve signal recording and stimulation. Biosensors & Bioelectronics, 1997. **12**(9-10): p. 883-892.

Blawas, A.S. and W.M. Reichert, Protein patterning. Biomaterials, 1998. **19**: p. 595-609.

Böhm, S., et al. The Field-Effect-Adressable Potentiometric Sensor/Stimulator (FAPS): Fabrication and Characterization. in Eurosensors XIII. 1999. The Hague.

Böhm, S., et al., Characterization of the field-effect addressable potentiometric sensor (FAPS). Sensors and Actuators B-Chemical, 2000. **68**(1-3): p. 266-273.

Boppart, S.A., B.C. Wheeler, and C.S. Wallace, A Flexible Perforated Microelectrode Array for Extended Neuronal Recordings. IEEE Transactions on Biomedical Engineering, 1992. **39**(1): p. 37-42.

Borkholder, D.A., et al., Microelectrode arrays for stimulation of neural slice preparations. Journal of Neuroscience Methods, 1997. **77**(1): p. 61-6.

Bove, M., et al., Interfacing Cultured Neurons to Planar Substrate Microelectrodes - Characterization of the Neuron-to- Microelectrode Junction. Bioelectrochemistry and Bioenergetics, 1995. **38**(2): p. 255-265.

Bove, M., et al., The neuron-transistor junction: Linking equivalent electric circuit models to microscopic descriptions. Thin Solid Films, 1996. **285**: p. 772-775.

Breckenridge, L.J., et al., Advantages of using microfabricated extracellular electrodes for in vitro neuronal recording. Journal of Neuroscience Research, 1995. **42**(2): p. 266-76.

Bucher, V., et al., Low-impedance thin-film polycrystalline silicon microelectrodes for extracellular stimulation and recording. Biosensors & Bioelectronics, 1999. **14**(7): p. 639-649.

Bucher, V., et al., Electrical properties of a light-addressable microelectrode chip with high electrode density for extracellular stimulation and recording of exciTable cells. Biosensors & Bioelectronics, 2001. **16**(3): p. 205-210.

Bucher, V., et al., Light-addressed sub-μm electrodes for extracellular recording and stimulation of exciTable cells. Microelectronic Engineering, 2001. **57-8**: p. 705-712.

Bucher, V., et al., Electrical properties of light-addressed sub-μm electrodes fabricated by use of nanostencil-technology. Microelectronic Engineering, 2002. **61-2**: p. 971-980.

Bullen, A., S.S. Patel, and P. Saggau, High-speed, random-access fluorescence microscopy .1. High- resolution optical recording with voltage-sensitive dyes and ion indicators. Biophysical Journal, 1997. **73**(1): p. 477-491.

Bullen, A. and P. Saggau, High-speed, random-access fluorescence microscopy: II. Fast quantitative measurements with voltage-sensitive dyes. Biophysical Journal, 1999. **76**(4): p. 2272-2287.

Buttler, W., et al., JFET-PMOS Technology in the design of Monolithic Preamplifier Systems for Multielectrode Detectors. IEEE Transactions on Biomedical Engineering, 1991. **38**(2): p. 69-75.

Chang, J.C., G.J. Brewer, and B.C. Wheeler, Modulation of neural network activity by patterning. Biosensors & Bioelectronics, 2001. **16**(7-8): p. 527-533.

Chien, C.B. and J. Pine, An Apparatus for Recording Synaptic Potentials from Neuronal Cultures Using Voltage-Sensitive Fluorescent Dyes. Journal of Neuroscience Methods, 1991. **38**(2-3): p. 93-105.

Chien, C.B. and J. Pine, Voltage-Sensitive Dye Recording of Action-Potentials and Synaptic Potentials from Sympathetic Microcultures. Biophysical Journal, 1991. **60**(3): p. 697-711.

Clark, R.A., S.E. Zerby, and A.E. Ewing, Electrochemistry in neuronal microenvironments, in Electroanalytical chemistry, A.J. Bard and I. Rubinstein, Editors. p. 227-295.

Claverol-Tinture, E. and J. Pine, Extracellular potentials in low-density dissociated neuronal cultures. J. of Neuroscience Methods, 2002. **117**: p. 13-21.

Clement, R.S., et al., Functional connectivity in auditory cortex using chronic, multichannel unit recordings. Neurocomputing, 1999. **26-7**: p. 347-354.

Corey, J.M., B.C. Wheeler, and G.J. Brewer, Compliance of Hippocampal-Neurons to Patterned Substrate Networks. Journal of Neuroscience Research, 1991. **30**(2): p. 300-307.

Corner, M.A., Reciprocity of structure-function relations in developing neuronal networks - the odissey of a self-organizing brain through research fads, fallacies and prospects. Prog. Brain Res., 1994. **102**: p. 3-31.

Cunningham, W., et al., Fabrication of microelectrode arrays for neural measurements from retinal tissue. Journal of Physics D-Applied Physics, 2001. **34**(18): p. 2804-2809.

DeMarse, T.B., et al., The Neurally Controlled Animat: Biological brains acting with simulated bodies. Autonomous Robots, 2001. **11**(3): p. 305-310.

Egert, U., et al., A novel organotypic long-term culture of the rat hippocampus on substrate-integrated multielectrode arrays. Brain Res Brain Res Protoc, 1998. **2**(4): p. 229-42.

Eichenbaum, H.B. and J.L. Davis, Neuronal ensembles. Strategies for recording and decoding. 1998, New York: Wiley-Liss.

Farre, C., et al., Whole-cell patch clamp recordings performed on a chip. Biophysical Journal, 2001. **80**(1): p. 1414.

Fertig, N., R.H. Blick, and J.C. Behrends, Whole cell patch clamp recording performed on a planar glass chip. Biophysical Journal, 2002. **82**(6): p. 3056-3062.

Fertig, N., et al., Activity of single ion channel proteins detected with a planar microstructure. Applied Physics Letters, 2002. **81**(25): p. 4865-4867.

Fertig, N., et al., A microstructured chip electrode for low noise single channel recording. Biophysical Journal, 2001. **80**(1): p. 1413.

Fertig, N., et al., Microstructured glass chip for ion-channel electrophysiology. Physical Review E, 2001. **6404**(4): p. art. no.-040901.

Fields, R.D. and B. Stevens-Graham, New insights into neuron-glia communication. Science, 2002. **298**(October): p. 556-562.

Fromherz, P., Interfacing neurons and silicon by electrical induction. Berichte Der Bunsen-Gesellschaft-Physical-Chemie, Chemical Physics, 1996. **100**(7): p. 1093-1102.

Fromherz, P., Extracellular recording with transistors and the distribution of ionic conductances in a cell membrane. European Biophysics Journal with Biophysics Letters, 1999. **28**(3): p. 254-258.

Fromherz, P., C.O. Muller, and R. Weis, Neuron Transistor - Electrical Transfer-Function Measured by the Patch-Clamp Technique. Physical Review Letters, 1993. **71**(24): p. 4079-4082.

Fromherz, P., et al., A Neuron-Silicon Junction - a Retzius Cell of the Leech on an Insulated-Gate Field-Effect Transistor. Science, 1991. **252**(5010): p. 1290-1293.

Fromherz, P. and H. Schaden, Defined Neuronal Arborizations by Guided Outgrowth of Leech Neurons in Culture. European Journal of Neuroscience, 1994. **6**(9): p. 1500-1504.

Geinisman, Y., Structural synaptic modifications associated with hippocampal LPT and behavioral learning. Cerebal Cortex, 2000. **10**: p. 952-962.

George, M., W.J. Parak, and H.E. Gaub, Highly integrated surface potential sensors. Sensors and Actuators B-Chemical, 2000. **69**(3): p. 266-275.

George, M., et al., Investigation of the spatial resolution of the light- addressable potentiometric sensor. Sensors and Actuators a-Physical, 2000. **86**(3): p. 187-196.

Gill, P.R. and L.P. Lee. MAPS: the micro action potential scanner. in EMBS. 2002. Madison.

Gonzalez, C. and M. Rodriguez, A flexible perforated microelectrode array probe for action potential recording in nerve and muscle tissues. Journal of Neuroscience Methods, 1997. **72**(2): p. 189-95.

Grattarola, M., et al., The Engineered Petri Dish - a New Tool for Biotechnology. Minerva Biotecnologica, 1995. **7**(3): p. 228-233.

Grattarola, M., et al., Cell-Metabolism Measurements in Culture Via Microelectronic Biosensors. Cytotechnology, 1991. **5**: p. 57-58.

Grattarola, M. and G. Massobrio, Bioelectronics handbook: MOSFETs, biosensors, and neurons. 1998, New York: McGraw-Hill.

Griscom, L., et al., Cell placement and neural guidance using a three-dimensional microfluidic array. Japanese Journal of Applied Physics Part 1-Regular Papers Short Notes & Review Papers, 2001. **40**(9A): p. 5485-5490.

Griscom, L., et al., Techniques for patterning and guidance of primary culture neurons on micro-electrode arrays. Sensors and Actuators B-Chemical, 2002. **83**(1-3): p. 15-21.

Gross, G.W., A.N. Williams, and J.H. Lucas, Recording of spontaneous activity with photoetched microelectrode surfaces from mouse spinal neurons in culture. Journal of Neuroscience Methods, 1982. **5**: p. 13-22.

Guerrero, G., et al., Tuning FlaSh: Redesign of the dynamics, voltage range, and color of the genetically encoded optical sensor of membrane potential. Biophysical Journal, 2002. **83**(6): p. 3607-3618.

Guia, A., et al., Micro-positioning enabled patch clamp recordings on a chip. Biophysical Journal, 2002. **82**(1): p. 787.

Habets, A., et al., Spontaneous neuronal firing patterns in fetal-rat cortical networks during development in vitro - a quantitative analysis. Exp. Brain Res., 1987. **69**: p. 43-52.

Hammerle, H., et al., Extracellular recording in neuronal networks with substrate integrated microelectrode arrays. Biosensors and Bioelectronics, 1994. **9**(9-10): p. 691-6.

He, H.X., et al., Fabrication of microelectrode arrays using microcontact printing. Langmuir, 2000. **16**(25): p. 9683-9686.

Heida, T., W.L.C. Rutten, and E. Marani, Understanding dielectrophoretic trapping of neuronal cells: modelling electric field, electrode-liquid interface and fluid flow. Journal of Physics D-Applied Physics, 2002. **35**(13): p. 1592-1602.

Heida, T., et al., Viability of dielectrophoretically trapped neural cortical cells in culture. Journal of Neuroscience Methods, 2001. **110**(1-2): p. 37-44.

Heiduschka, P., et al., Defined adhesion and growth of neurons on artificial structured substrates. Electrochimica Acta, 2001. **47**(1-2): p. 299-307.

Heuschkel, M.O., et al., A three dimensional multi-electrode array for multi-site stimulation and recording in acute brain slices. Journal of Neuroscience Methods, 2002. **114**: p. 135-148.

Hodgkin, A.L. and A.F. Huxley, A Quantitative Description of Membrane Current and its Application to Conduction and Excitation in Nerve. Journal of Physiology, 1952. **117**: p. 500-544.

Hoogerwerf, A.C. and K.D. Wise A Three-Dimensional Microelectrode Array for Chronic Neural Recording. IEEE Transactions on Biomedical Engineering, 1994. **41**(12): p. 1136-1146.

Hua, S.E., et al., Microelectrode studies of normal organization and plasticity of human somatosensory thalamus. Journal of Clinical Neurophysiology, 2000. **17**(6): p. 559-574.

Israel, D.A., D.J. Edell, and R.G. Mark, Time delays in propagation of cardiac action potential. American Journal of Physiology, 1990. **258**(6 Pt 2): p. H1906-17.

Ito, Y., Surface micropatterning to regulate cell functions. Biomaterials, 1999. **20**: p. 2333-2342.

Jahnsen, H., et al., Coupling of Organotypic Brain Slice Cultures to Silicon-Based Arrays of Electrodes. Methods in Enzymology, 1999. **18**: p. 160-172.

James, C.D., et al., Aligned microcontact printing of micrometer-scale poly-L-lysine structures for controlled growth of cultured neurons on planar microelectrode arrays. IEEE Transactions On Biomedical Engineering, 2000. **47**(1): p. 17-21.

Jimbo, Y., H.P. Robinson, and A. Kawana, Strengthening of synchronized activity by tetanic stimulation in cortical cultures: application of planar electrode arrays. IEEE Transactions On Biomedical Engineering, 1998. **45**(11): p. 1297-304.

Jimbo, Y. and H.P.C. Robinson, Propagation of spontaneous synchronized activity in cortical slice cultures recorded by planar electrode arrays. Bioelectrochemistry, 2000. **51**: p. 107-115.

Jimbo, Y., H.P.C. Robinson, and A. Kawana, Simultaneous Measurement of Intracellular Calcium and Electrical-Activity from Patterned Neural Networks in Culture. IEEE Transactions on Biomedical Engineering, 1993. **40**(8): p. 804-810.

Kandel, E.R., J.H. Schwartz, and T.M. Jessell, Principles of neural science. 3rd ed. 1991, New York: Elsevier Science.

Kane, R.S., et al., Patterning proteins and cells using soft lithography. Biomaterials, 1999. **20**: p. 2363-2376.

Kawaguchi, H., et al., Multichannel optical recording of neuronal network activity and synaptic potentiation in dissociated cultures from rat hippocampus. Neuroscience Letters, 1996. **205**(3): p. 177-180.

Keefer, E.W., et al., Characterization of acute neurotoxic effects of trimethylolpropane phosphate via neuronal network biosensors. Biosensors & Bioelectronics, 2001. **16**(7-8): p. 513-525.

Kleinfeld, D., K.H. Kahler, and P.E. Hockberger, Controlled Outgrowth of Dissociated Neurons on Patterned Substrates. Journal of Neuroscience, 1988. **8**(11): p. 4098-4120.

Klemic, K.G., et al., Micromolded PDMS planar electrode allows patch clamp electrical recordings from cells. Biosensors & Bioelectronics, 2002. **17**(6-7): p. 597-604.

Kovacs, G.T., C.W. Storment, and J.M. Rosen, Regeneration microelectrode array for peripheral nerve recording and stimulation. IEEE Transactions On Biomedical Engineering, 1992. **39**(9): p. 893-902.

Kovacs, G.T.A., et al., Silicon-Substrate Microelectrode Arrays for Parallel Recording of Neural Activity in Peripheral and Cranial Nerves. IEEE Transactions on Biomedical Engineering, 1994. **41**(6): p. 567-577.

Lee, J.S., et al., Micropatterning of Cultured-Cells on Polystyrene Surface by Using an Excimer-Laser. Applied Physics Letters, 1994. **65**(4): p. 400-402.

Lehnert, T., et al., Realization of hollow SiO2 micronozzles for electrical measurements on living cells. Applied Physics Letters, 2002. **81**(26): p. 5063-5065.

Lom, B., K.E. Healy, and P.E. Hochberger, A versatile technique for patterning biomolecules onto glass coverslips. Journal of Neuroscience Methods, 1997. **50**: p. 385-397.

Maher, M.P., et al., Microstructures for studies of cultured neural networks. Medical & Biological Engineering & Computing, 1999. **37**(1): p. 110-118.

Maher, M.P., et al., The neurochip: a new multielectrode device for stimulating and recording from cultured neurons. Journal of Neuroscience Methods, 1999. **87**(1): p. 45-56.

Manuccia, T.J. and L.M. Dobbs. The optically switched microelectrode arrays (OSMA). in Substrate-integrated Microelectrode Arrays: Technology and Applications. 1998. Reutlingen.

Martinoia, S., et al., A General-Purpose System for Long-Term Recording from a Microelectrode Array Coupled to ExciTable Cells. Journal of Neuroscience Methods, 1993. **48**(1-2): p. 115-121.

Martinoia, S., et al., A simple microfluidic system for patterning populations of neurons on silicon micromachined substrates. Journal of Neuroscience Methods, 1999. **87**(1): p. 35-44.

Matsue, T., N. Matsumoto, and I. Uchida, Rapid micropatterning of living cells by repulsive dielectrophoretic force. Electrochimica Acta, 1997. **42**(20-22): p. 3251-3256.

Misgeld, U., H.U. Zeilhofer, and D. Swandulla, Synaptic modulation of oscillatory activity of hypothalamic neuronal networks in vitro. Cell. Mol. Neurobiology, 1998. **18**: p. 29-43.

Morigaki, K., et al., Patterning solid-supported lipid bilayer membranes by lithographic polymerization of a diacetylene lipid. Angewandte Chemie-International Edition, 2001. **40**(1): p. 172-174.

Najafi, K., Integrated Sensors in Biological Environments. Sensors and Actuators B-Chemical, 1990. **1**(1-6): p. 453-459.

Najafi, K. and K.D. Wise, An ImplanTable Multielectrode array with On-Chip Signal Processing. Journal of Solid-State Circuits, 1986. **sc-21**(6): p. 1035-1044.

Najafi, K. and K.D. Wise, A low-noise demultiplexing system for active multichannel microelectrode arrays. IEEE Transactions on Biomedical Engineering, 1994. **38**(1): p. 75-81.

Neunlist, M., S. Peters, and M. Schemann, Multisite optical recording of excitability in the enteric nervous system. Neurogastroenterology and Motility, 1999. **11**(5): p. 393-402.

Nicholls, J.C., A.R. Martin, and B.G. Wallace, From neuron to brain. 3rd ed. 1992, Sunderland, Mass.: Sinauer Associates.

Nicolau, D.V., et al., Patterning neuronal and glia cells on light-assisted functionalised photoresists. Biosensors & Bioelectronics, 1999. **14**: p. 317-325.

Obaid, A.L., et al., Spatiotemporal patterns of activity in an intact mammalian network with single-cell resolution: Optical studies of nicotinic activity in an enteric plexus. Journal of Neuroscience, 1999. **19**(8): p. 3073-3093.

O'Connor, S.M., et al., Immobilization of neural cells in three-dimensional matrices for biosensor applications. Biosensors & Bioelectronics, 2000. **14**(10-11): p. 871-881.

Offenhausser, A. and W. Knoll, Cell-transistor hybrid systems and their potential applications. Trends in Biotechnology, 2001. **19**(2): p. 62-66.

Offenhausser, A., J. Ruhe, and W. Knoll, Neuronal Cells Cultured on Modified Microelectronic Device Surfaces. Journal of Vacuum Science & Technology a-Vacuum Surfaces and Films, 1995. **13**(5): p. 2606-2612.

Offenhausser, A., et al., Field-effect transistor array for monitoring electrical activity from mammalian neurons in culture. Biosensors & Bioelectronics, 1997. **12**(8): p. 819-826.

Oka, H., et al., A new planar multielectrode array for extracellular recording: application to hippocampal acute slice. Journal of Neuroscience Methods, 1999. **93**: p. 61-67.

Okada, A., et al., Imaging cells in the developing nervous system with retrovirus expressing modified green fluorescent protein. Experimental Neurology, 1999. **156**(2): p. 394-406.

Owens, A.L., et al., Multi-electrode array for measuring evoked potentials from surface of ferret primary auditory cortex. Journal of Neuroscience Methods, 1995. **58**(1-2): p. 209-20.

Pancrazio, J.J., et al., Description and demonstration of a CMOS amplifier-based-system with measurement and stimulation capability for bioelectrical signal transduction. Biosensors & Bioelectronics, 1998. **13**(9): p. 971-979.

Pantoja, R., et al., Bilayer reconstitution of voltage-dependent ion channels using a microfabricated silicon chip. Biophysical Journal, 2001. **81**(4): p. 2389-2394.

Parak, W.J., et al., Can the light-addressable potentiometric sensor (LAPS) detect extracellular potentials of cardiac myocytes? IEEE Transactions on Biomedical Engineering, 2000. **47**(8): p. 1106-1113.

Parak, W.J., et al., The field-effect-addressable potentiometric sensor/stimulator (FAPS) - a new concept for a surface potential sensor and stimulator with spatial resolution. Sensors and Actuators B, 1999. **58**(1-3): p. 497-504.

Pfrieger, F.W. and B.A. Barres, Synaptic efficacy enhanced by glia cells in vitro. Science, 1997. **277**(September): p. 1684-1687.

Pine, J., Recording Action-Potentials from Cultured Neurons with Extracellular Micro-Circuit Electrodes. Journal of Neuroscience Methods, 1980. **2**(1): p. 19-31.

Pine, J. and S.M. Potter. A high-speed CCD camera for optical recording of neuronal activity. in Soc. Neuroscience. 1997.

Potter, S.M., Distributed processing in cultured neuronal networks. Progress in Brain Research, 2001. **130**: p. 49-62.

Regehr, W.G., et al., Sealing Cultured Invertebrate Neurons to Embedded Dish Electrodes Facilitates Long-Term Stimulation and Recording. Journal of Neuroscience Methods, 1989. **30**(2): p. 91-106.

Regehr, W.G., J. Pine, and D.B. Rutledge, A Long-Term In-vitro Silicon-Based Microelectrode-Neuron Connection. IEEE Transactions on Biomedical Engineering, 1988. **35**(12): p. 1023-1032.

Rutten, W., et al., Neuroelectronic interfacing with cultured multielectrode arrays toward a cultured probe. Proceedings of the IEEE, 2001. **89**(7): p. 1013-1029.

Saggau, P., A. Bullen, and S.S. Patel, Acousto-optic random-access laser scanning microscopy: Fundamentals and applications to optical recording of neuronal activity. Cellular and Molecular Biology, 1998. **44**(5): p. 827-846.

Salzberg, B.M., et al., Optical Recording of Neuronal-Activity in an Invertebrate Central Nervous-System - Simultaneous Monitoring of Several Neurons. Journal of Neurophysiology, 1977. **40**(6): p. 1281-1291.

Saneinejad, S. and M.S. Shoichet, Patterned poly(chlorotrifluoroethylene) guides primary nerve cell adhesion and neurite outgrowth. Journal of Biomedical Materials Research, 2000. **50**(4): p. 465-474.

Schwarz, M., et al., Single chip CMOS imagers and flexible microelectronic stimulators for a retina implant system. Sensors and Actuators B, 2000. **83**: p. 40-46.

Science, Beatuful, complex, and diverse specialists., 2000. **290**(October).

Siegel, M.S. and E.Y. Isacoff, A genetically encoded optical probe of membrane voltage. Neuron, 1997. **19**(4): p. 735-741.

Siegel, M.S. and E.Y. Isacoff, Green fluorescent protein-based sensors for detecting signal transduction and monitoring ion channel function, In Methods in Enzymology. J., Abelson, S. Emr, and J. Thorner Eds., Academic Press, in press.

Sigworth, F.J. and K.G. Klemic, Patch clamp on a chip. Biophysical Journal, 2002. **82**(6): p. 2831-2832.

Sokolov, E.N. and T.A. Palikhova, Elementary and compound postsynaptic potentials in the defensive command neurons of Helix lucorum. Acta Biologica Hungarica, 1999. **50**(1-3): p. 235-245.

Sorribas, H., C. Padeste, and L. Tiefenauer, Photolithographic generation of protein micropatterns for neuron culture applications. Biomaterials, 2002. **23**(3): p. 893-900.

Sprossler, C., et al., Electrical recordings from rat cardiac muscle cells using field-effect transistors. Physical Review E, 1999. **60**(2): p. 2171-2176.

Sprossler, C., et al., Long-term recording system based on field-effect transistor arrays for monitoring electrogenic cells in culture. Biosensors & Bioelectronics, 1998. **13**(6): p. 613-618.

Stevens, R.H. and K. Najafi, Artificial Neural Networks as Adjuncts for Assessing Medical- Students Problem-Solving Performances on Computer-Based Simulations. Computers and Biomedical Research, 1993. **26**(2): p. 172-187.

Stoppini, L., S. Duport, and P. Carreges, A new extracellular multirecording system for electrophysiological studies: application to hippocampal organotypic culltures. J. Neuroscience Methods, 1997. **72**: p. 23-33.

Streit, J., et al., The generation of rhythmic activity in dissociated cultures of rat spinal cord. European Journal of Neuroscience, 2001. **14**(2): p. 191-202.

Tai, H.C. and H.M. Buettner, Neurite outgrowth and growth cone morphology on micropatterned surfaces. Biotechnology Progress, 1998. **14**(3): p. 364-370.

Thiébaud, P., et al., An array of Pt-tip microelectrodes for extracellular monitoring of activity of brain slices. Biosensors & Bioelectronics, 1999. **14**: p. 61-65.

Thiébaud, P., et al., Microelectrode Arrays for Electrophysiological Monitoring of Hippocampal Organotypic Slice Cultures. IEEE Transaction on Biomedical Engineering, 1997. **44**(11): p. 1159-1163.

Thomas, C.A., et al., A miniature microelectrode array to monitor the bioelectric activity of cultured cells. Exp. Cell Research, 1972. **74**(61-66).

Tscherter, A., et al., Spatiotemporal characterization of rhythmic activity in rat spinal cord slice cultures. European Journal of Neuroscience, 2001. **14**(2): p. 179-190.

Vassanelli, S. and P. Fromherz, Neurons from rat brain coupled to transistors. Applied Physics Materials Science & Processing, 1997. **65**(2): p. 85-88.

Vassanelli, S. and P. Fromherz, Transistor records of rat hippocampal neurons. European Journal of Neuroscience, 1998. **10**: p. 2838.

Vassanelli, S. and P. Fromherz, Transistor records of exciTable neurons from rat brain. Applied Physics Materials Science & Processing, 1998. **66**(4): p. 459-463.

Voigt, T., H. Baier, and A.D. deLima, Synchronization of neuronal activity promotes survival of individual rat neocortical neurons in early development. European Journal of Neuroscience, 1997. **9**(5): p. 990-999.

Wu, J.Y., et al., Voltage-sensitive dyes for monitoring multineuronal activity in the intact central nervous system. Histochemical Journal, 1998. **30**(3): p. 169-187.

Xia, Y. and G.M. Whitesides, Soft lithography. Annual Revue of Material Science, 1998. **28**: p. 153-184.

Yeung, C.K., et al., Investigations into the use of miniaturised field effect transistors (FETs) as a novel electrophysiological tool in pharmacological research. British Journal of Pharmacology, 2000. **131**: p. 217P.

Yeung, C.K., et al., Modulation of the growth and guidance of rat brain stem neurons using patterned extracellular matrix proteins. Neuroscience Letters, 2001. **301**(2): p. 147-150.

Yeung, C.K., et al., Modulation of the growth and guidance of rat brain stem neurons using patterned extracellular matrix proteins. Neuroscience Letters, 2001. **301**: p. 147-150.

Zeck, G. and P. Fromherz, Noninvasive neuroelectronic interfacing with synaptically connected snail neurons immobilized on a semiconductor chip. Proceedings of the National Academy of Sciences of the United States of America, 2001. **98**(18): p. 10457-10462.

2 THE NEURONAL INTERFACE

2.1 Introduction

The aim of this second chapter is to provide some basic considerations for designing microelectrode arrays for extracellular recording and stimulation.

At first, the electrode-electrolyte interface is described. This part begins with a few remarks about the differences in the conductivity phenomena in metals, semiconductors and electrolytes. The interface is described in terms of the electrode impedance. However, it has to be pointed out that in electrochemistry this is a very complex subject and several models, specific to particular cases, have been developed. An exhaustive description of the electrode impedance model is not the aim of this work. Nevertheless, for the engineering of MEA systems (microelectrode arrays and amplifier circuit) this element has to be taken into account in order to design an amplifier with sufficiently high input impedance (or the opposite: to adapt the electrode impedance to an existing measuring circuit). If the electrode impedance is higher or equivalent to the amplifier input one, the circuit will function as a voltage divider with the consequence of loosing part of the signal. Excellent electrochemical references for describing the interface are the books of Bard and Girault [Girault, 2001; Bard, 2001].

Secondly, the interface electrode-electrolyte-neuron is described considering the simplified case of recording from a single neuron on a metal microelectrode. This provides the basics for understanding the technique and the involved phenomena. A more detailed reference about this subject is the bio-electronics handbook of M. Grattarola [Grattarola, 1998] where the modelling is extensively described.

Finally, some considerations for the case of stimulating the electrophysiological activity with a microelectrode are reported. Two

aspects involved in stimulation have to be highlighted: the behaviour of the microelectrode under stimulation (current or voltage applied to the electrode with respect to a reference electrode); and the stimulation of the neuronal network activity (biological side). Due to their complexity, both sides are not yet completely described in the literature. The first one, the electrode-electrolyte interface behaviour, depends on the stimulation signal, the electrode material and on the electrolyte. Its complete modelling is, as in the case of recording, difficult. The second one, the modelling on the neuronal network side, sees its complexity rising from the large number of interconnected neurons. Models based on the Hodgkin and Huxley model (H-H), described in chapter one, have been reported in the literature [Grattarola, 1998, Bove, 1996, Buitenweg, 2001, Rutten, 2001].
In the last part of this chapter the electrode material properties for the stimulation will be discussed. In practice, stimulation is realised by applying relatively high voltages with respect to physiological signals (up to a few volts) or by applying currents (up to a few mA). This might result in electrochemical reactions with the consequence of toxic effects on the neuronal culture.

2.2 Electrode-electrolyte

2.2.1 Metals, semiconductors, insulators and electrolytes

Before entering into the modelling of the electrode-electrolyte interface it is useful to briefly discuss the basic differences in conduction between metals, semiconductors and electrolytes.
Conduction in metals is the result of the displacement of electrons, considered as a “gas”, in the metal crystal lattice. The Fermi-Dirac equation describes the statistic distribution of their energy (Figure 2.1). The higher energy level filled by an electron is the *valence band* and the lower empty energy level is called the *conduction band*. In the case of metals both conduction and valence bands overlap. At

the absolute zero, 0 K, all energy levels up to the Fermi level (E_F) are filled by electrons. At room temperature, their kinetic energy is increased by the thermal energy and contributes in bringing them in conduction.

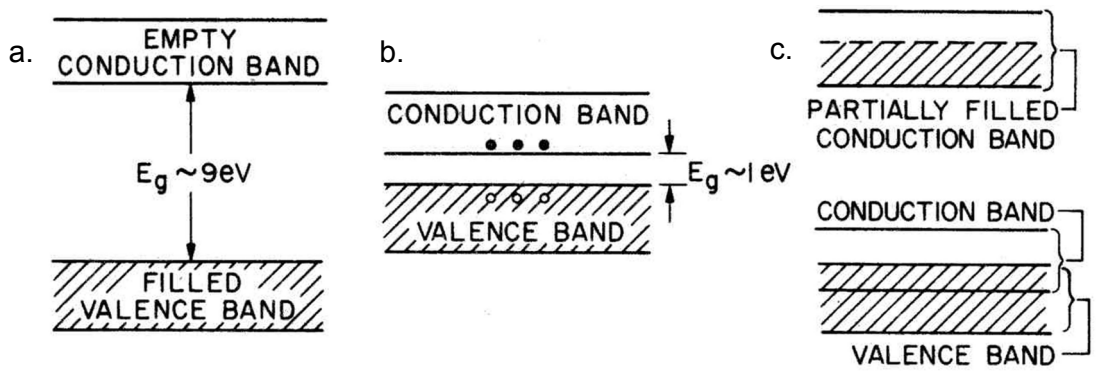

Figure 2.1: Energy band diagram for (a) an insulator, (b) a semiconductor and (c) a metal (modified from [Sze, 1985])

In the case of a *semiconductor*, the conduction and valence band are separated by an energy gap E_G (1.17 eV for silicon and 1.52 eV for gallium arsenide at 0 K). For a pure semiconductor crystal, any energy level in this gap (forbidden gap or energy gap) cannot be occupied by the electrons. Two kinds of charges are distinguished for semiconductors: negatives ones, the electrons, and positives ones, the holes. Both can contribute to the conduction, and the current density J_c as function of an electric field E can be described as:

$$J_c = \sigma . E \tag{2.1}$$

where the conductivity is defined as

$$\sigma = q.n.\mu_n + q.p.\mu_p \tag{2.2}$$

and where q is the unitary charge (1,602177.10^{-19} C) and n and p the electron and hole densities with their respective mobilities μ_n and μ_p. By doping the semiconductor with impurities, additional energy levels in the band gap are introduced. A donor ion will introduce additional

electrons in the conduction band and the semiconductor becomes *n-type*. Similarly, an acceptor ion will "accept" an additional electron and the semiconductor become *p-type*. In terms of conduction this modifies the n and p densities and thus the conductivity σ.
Insulators are materials showing an energy gap higher than 5 eV. In this case, a simple thermal excitation is not enough to bring an electron from the valence band to the conduction one.
Metals, semiconductors and insulators are well described in quantum physics, but the case of electrolytes is more complicated. An electrolyte is constituted by ions in a solvent like water. Consider the $M_{aq}^{(z+1)+}$/ M_{aq}^{z+} redox couple in solution. The ions $M_{aq}^{(z+1)+}$ introduce unoccupied energy levels for electrons and M_{aq}^{z+} occupied ones. The main problem in describing the energy levels in an electrolyte is that they are not constant as in the case of a metal, but fluctuate with the fluctuation of the polarisation of the solvent. In fact, there are important interactions between the ions and their environment (the solvent), which constantly modify the energy levels. Considering the hypothesis of a gaussian distribution centred on the most probable value, it is possible to describe the energy levels in the system. This is reported in Figure 2.2.
By definition the Fermi level of the electron in solution corresponds to the electrochemical potential E_F^{sol}, which is the half of the sum of the more probable oxidation and reduction energies of the redox couple. Note that in terms of scales, the Fermi level is normally expressed in physics in electron-volts (eV) referred to the energy of the electrons in vacuum (vacuum level). In electrochemistry, the electrochemical potential of the redox couple in solution is expressed in volts referred to the normal hydrogen reference electrode (NHE). To link the two scales it is necessary to define the potential of the hydrogen reference electrode in the physical scale. This has been defined thermodynamically by Lohmann [Lohmann, 1967] and it is $E_{H^+/H2}$ = –4.5 eV vs. the vacuum energy level.

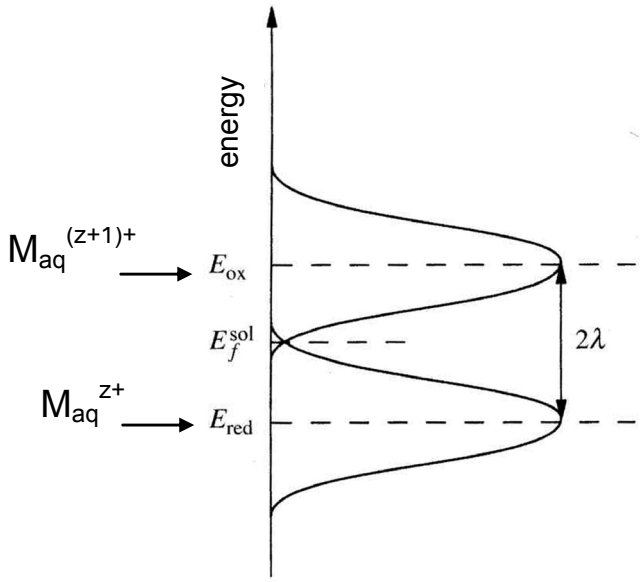

Figure 2.2: Energy levels of an electron in an electrolyte containing a single $M_{aq}^{(z+1)+}$/ M_{aq}^{z+} redox couple. (modified from [Girault, 2001])

The quantum physics description of the conduction in electrolytes is extremely complicated since all the redox couples in solution should be considered. Another model describes conduction in an electrolyte as the sum of the contributions of all positive and negative ions present in the solution, considered, in a first approximation, as punctual charges. Under an electric field E, the current density for each species can thus be described as:

$$J_i = \sigma_i . E \tag{2.3}$$

with the ionic conductivity σ_I given by:

$$\sigma_i = z_i^{\,2} \cdot F^2 \cdot \frac{D_i c_i}{RT} \tag{2.4}$$

where F is the Faraday constant (96485 $C.mol^{-1}$); D_i the diffusion coefficient for the species i; c_i the concentration for the specie i; R is the thermodynamic gas constant (8.34151 $J.K^{-1}.mol^{-1}$); z_i the valence of the ion and T the temperature in Kelvins.

In electrochemistry it is quite common to use molar ionic conductivity i.e. the conductivity per molar unit [$S \cdot mol^{-1} \cdot cm^2$]:

$$\lambda_i = \frac{\sigma_i}{c_i} \tag{2.5}$$

2.2.2 Metal-electrolyte interface

At the equilibrium

Placing a metallic electrode into an electrolyte solution, a thermodynamical equilibrium between the two phases is established. Without any polarisation of the electrode (referred to a reference electrode in the electrolyte), a potential difference between the two phases is generated at the interface. This is due to several reasons: the electron transfer between the electrode and the ions in the solution, the solvent dipole orientations and the ion adsorptions on the electrode surface [Pletcher, 1991]. The exhaustive modelling of these phenomena is difficult and is beyond the aim of this chapter. However, for understanding the electrode interface and thus the electrode impedance, some of them will be considered.
Intuitively, considering the energy model of the metal-electrolyte interface, the energy of the Fermi level in the metal and in the electrolyte must be identical at the equilibrium potential. The exchange current density is determined by the degree of overlap between the distribution functions of oxidised and reduced species (Figure 2.3). On the metal side, the high number of charge carriers (10^{22} cm^{-3}) and their high mobility will prevent any charge accumulation. However, on the electrolyte side, due to the lower number of charge carriers and their lower mobility, the charge (given by the ions) will be distributed as a function of the distance to the electrode. The direct consequence is that the potential difference will essentially be distributed on the electrolyte side. Several models have been developed in electrochemistry to describe this charge distribution with the assumption that ions are punctual charges. This

simplification is due to the difficulties in a quantum-physics approach, where it would be necessary to consider the energies levels distributions of all redox couples in the electrolyte.
The *Goüy-Chapman theory* (1910-1913) allows modelling of the potential distribution at the interface, with the following assumptions:

- the interactions are only electrostatic.
- the ions are considered as punctual charges and their polarisability is neglected.
- the metal is represented as an infinite planar surface with a surface charge σ.
- the ions distribution follows the Boltzmann distribution:

$$N_i(x) = N_i^{\infty} e^{-z_i e(\phi(x)-\phi^{\infty})/kT} \tag{2.6}$$

where ϕ^{∞} is the internal solution potential when $x \rightarrow \infty$; $N_i(x)$ is the ions density for the elementary volume defined between x and x + dx; and k is the Boltzmann constant (1.3807×10^{-23} $J.K^{-1}$).
The development of the equations is performed by Girault [Girault, 2001], considering that the interface must be electrically neutral (charge on the metal = - ionic charge in solution). The resulting potential distribution across the interface calculated for different concentrations is given in Figure 2.4. This figure shows that the potential drop is localised on a few tens of nanometers on the electrolyte side. Its distribution is similar to the one between a metal and a dielectric and it is thus possible to define an equivalent capacitor C_{GC} corresponding to the ionic distribution. However, due to the numerous approximations of the theory, this value of the interfacial capacitor is only valid near the potential of zero charge (pzc) (electrode potential for which the electrode charge is zero).

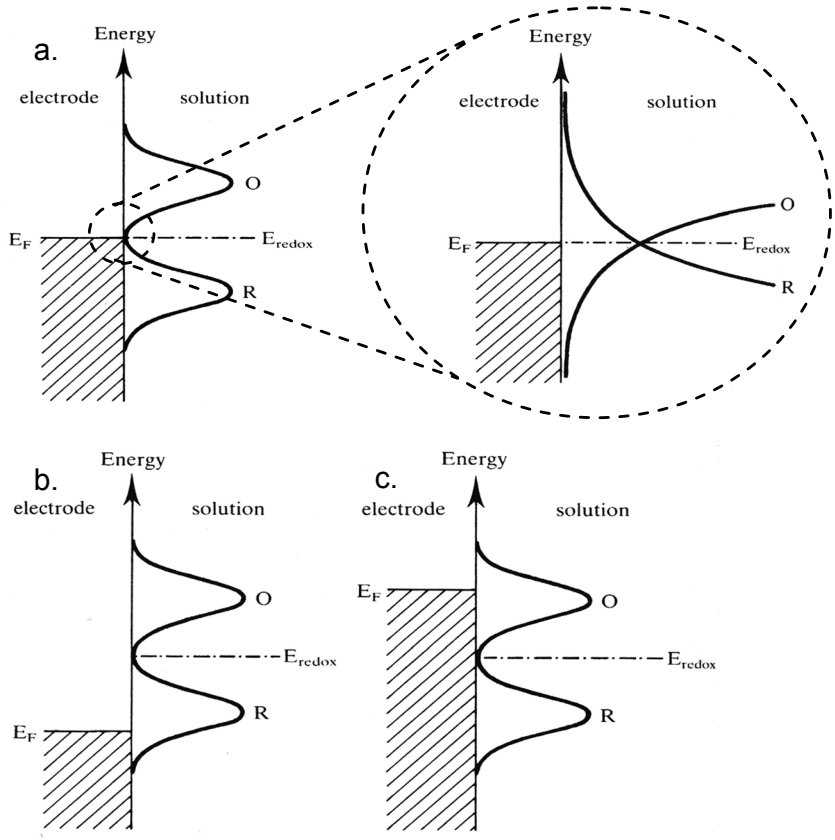

Figure 2.3: Energy level diagrams for (a) the equilibrium potential, (b) at a positive overpotential, (c) at negative overpotential (modified from [Pletcher, 1991])

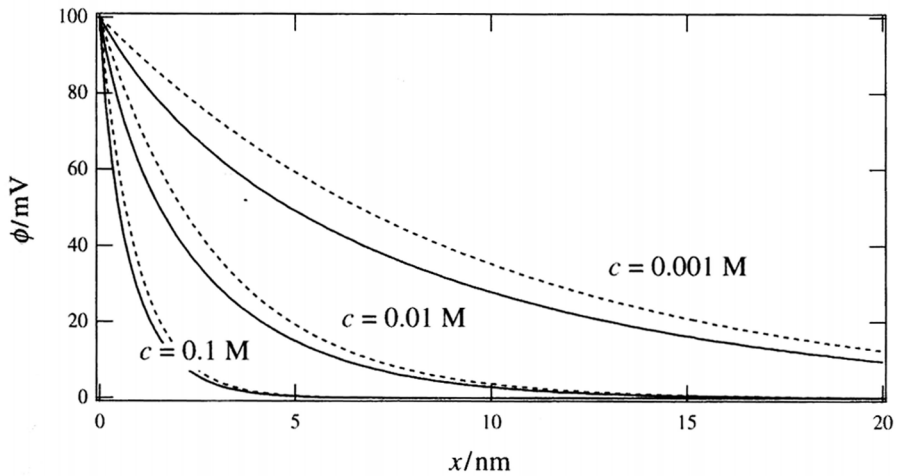

Figure 2.4: Simulation of the potential distribution across the metal electrode-electrolyte interface for different electrolyte concentrations. Electrode potential of 100 mV.(modified from [Girault, 2001])

At first instance, to overcome this limitation, the total capacitor, called double layer capacitor C_{dl}, could be defined by two capacitors in series: the first, the Helmholtz capacitor C_H, due to a monolayer of water and specifically adsorbed ions on the electrode (Stern layer, 300 pm thick), and the second, the previously described Goüy-Chapman capacitor C_{GC} (Figure 2.5). Thus, it results,

$$\frac{1}{C_{dl}} = \frac{1}{C_H} + \frac{1}{C_{GC}} \tag{2.7}$$

However, the Helmholtz capacitor is dominant at high electrolyte concentrations (>1M) or when the dielectric constant of the solvent is large (like in the case of water) [Girault, 2001]. Thus, for the culture media as electrolyte, it is possible to approximate the double layer capacitor with the Helmholtz capacitor. In practice the Helmholtz capacitor is usually in the order of 10-40 μF/cm^2 [Bard, 2001] depending on the electrode material.

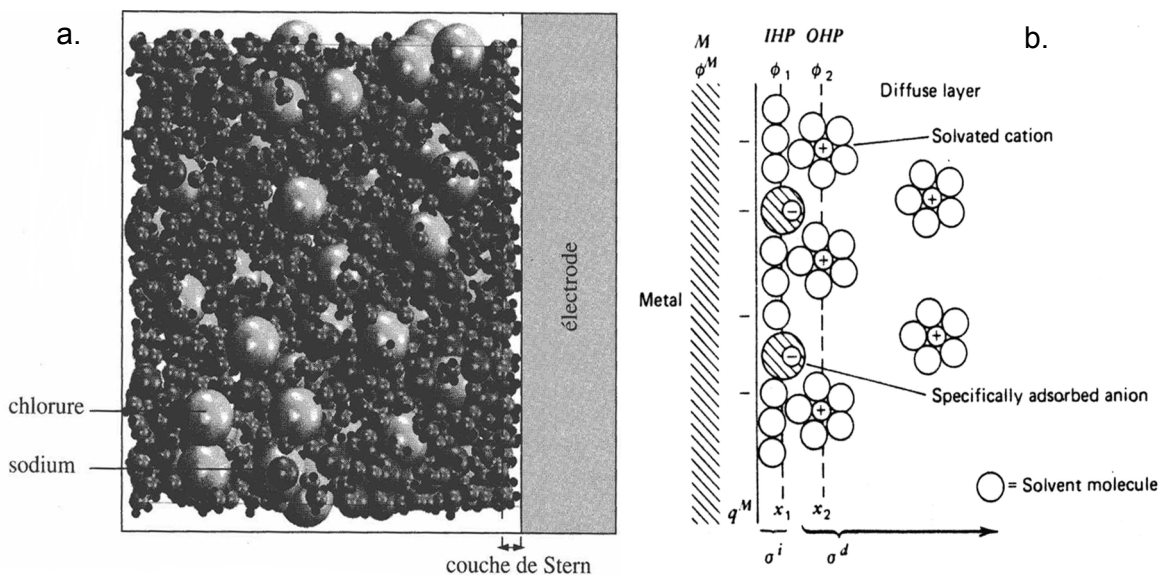

Figure 2.5: (a) Simulation of the interface metal / solution 3 M of sodium chloride, charge on the electrode -1μC. The hydrated sodium ions cannot reach the electrode (Stern layer) (modified from Girault, 2001). (b) Model of the electrode-solution, double-layer region (modified from Bard 1980). IHP : internal Helmholz plane (Stern layer); OHP : outer Helmholz plane (Helmholz layer).

Polarising the electrode

When a polarisation is applied to the electrode-electrolyte interface, two limiting, ideal cases are distinguished:

- the *ideally polarisable* electrode
- the *ideally non-polarisable* electrode

In the case of an ideally polarisable electrode, only a charge separation at the interface appears without any charge transfer across the metal-electrolyte interface. The external polarisation will only modify the charging of this interface. The equivalent circuit model can thus be represented as the double layer capacitor, resulting from the previously described charge distribution, in parallel with an infinite resistor (Figure 2.6). An example of such electrode is the mercury in a inert salt solution.
An ideally non-polarisable electrode is characterised by the fact that the potential difference across the interface is virtually fixed. The equivalent circuit model of this interface is defined by the double layer capacitor in parallel with a low resistor. Any attempt to modify the interface potential will be compensated by a charge-transfer current through the resistor called charge-transfer resistor, R_{CT}. An example of electrodes showing this behaviour are the *reference electrodes*, i.e. the hydrogen electrode, the calomel or the silver / silver chloride electrodes.

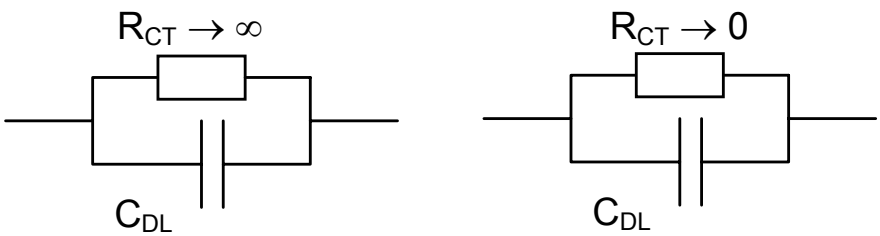

Figure 2.6: RC model of (a) an ideally polarisable electrode (mercury) and (b) an ideally non-polarisable electrode (reference electrodes).

In addition to those two limiting cases, all the other electrodes always present a leakage current resulting from the electrons transfer due to oxidation/reduction reactions generated by the applied potential. In this context, the interface equivalent electric circuit contains additional non-linear elements depending on specific phenomena, i.e. diffusion, kinetics of the reaction.
For the case of a microelectrode polarised with respect to the culture media by the electrophysiological activity (in case of recording), a simple model of the interface reported in the literature considers a charge transfer resistor in parallel to the double layer capacitor [Buitenweg, 2001]. The charge transfer resistor is defined by the equation 2.8 (from [Girault, 2001]), where I_0 is the exchange current (equation 2.9).

$$R_{CT} = \frac{RT}{nFI_0} \tag{2.8}$$

$$I_0 = zFAk^{\theta}[c_R(\infty)]^{1-\alpha}[c_O(\infty)]^{\alpha} \tag{2.9}$$

where R is the thermodynamic gas constant (8.34151 $J.K^{-1}.mol^{-1}$), T the temperature in Kelvin, F the Faraday constant (96485 $C.mol^{-1}$), n the exchanged electrons, z the valence of the ion; A the electrode surface (m^2), c_R, c_O are the respective interfacial reduced and oxidised species concentrations (mol), k^{Θ} is the standard speed constant ($m.s^{-1}$) and α is the charge transfer coefficient.
In reality it has to be considered that the microelectrode impedance is not a simple RC circuit with constant elements. The frequency contributes in modifying both R and C. In low-frequency (<10 kHz) this results in an electrode impedance rising up to several MΩ with a mainly capacitive phase.

In the MEA field, it is common to compare the microelectrode impedance at a frequency of 1 kHz, considering that an impedance lower than 1 MΩ should allow recording.

2.3 Electrode-electrolyte-neuron

The electrode-neuron interface is described in order to provide a simple equivalent circuit for evaluating the MEAs design requirements for recording and stimulation. Based on the H-H model described in chapter one a model is developed, considering only one neuron on a microelectrode. This is a limited model since in practice each neuron is connected in a network and is randomly placed with respect to the electrode. More detailed models have been reported in the literature [Bove,1995, Buitenweg 2001, Rutten 2001]
For the stimulation, remarks concerning the safe stimulation and on the electrode material are reported.

2.3.1 Recording model

Consider the cross-section of the system (Figure 2.7) constituted by a single neuron on a microelectrode. The reference electrode (RE) is placed in the culture medium, and the voltage V is measured between the reference and the recording electrode. As described in chapter one, the electrophysiological properties of the neuron are determined by the electrical properties of the membrane and, in second instance, by the neuronal morphology. Here only the membrane properties are considered.

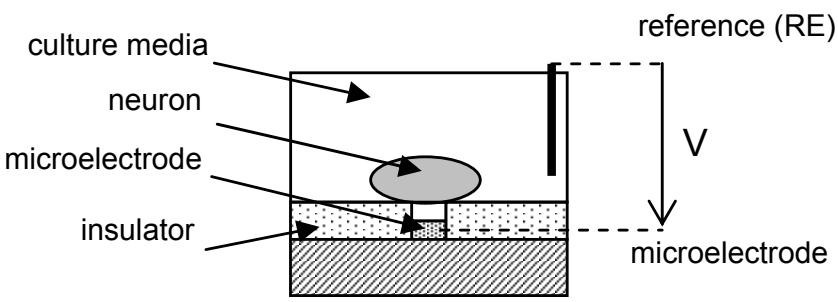

Figure 2.7: Cross-section of the system constituted by a single neuron on a microelectrode. V is the measured extracellular potential.

The membrane properties can be represented by the Hodgkin and Huxley (H-H) model considering the current contributions of the specific voltage-gated channels. An equivalent circuit is represented in Figure 2.8, considering the ions specific membrane conductivity (g_M), the ionic voltage drop through the membrane (V_M), a leak current I_l (which also include the chloride contribution), and the cellular membrane capacitance (C_{mem}).

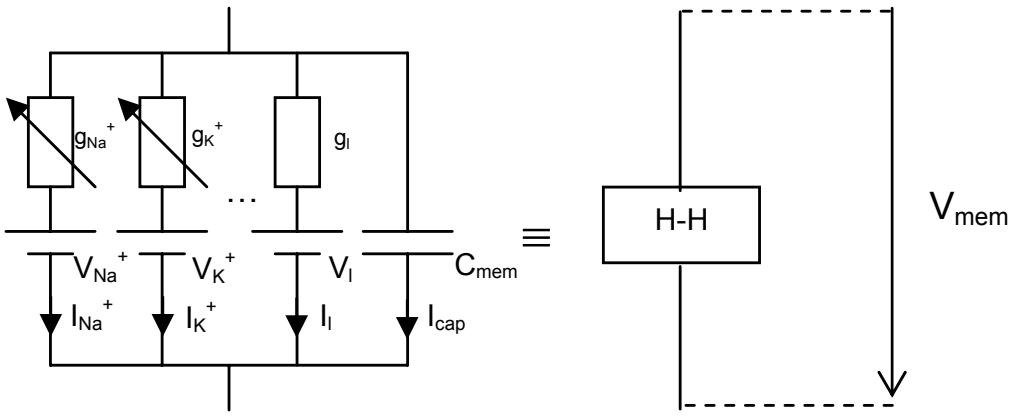

Figure 2.8: Hodgkin and Huxley (H-H) model of the membrane. g_M: ions specific membrane conductivity, V_M: ionic voltage drop through the membrane, I_l: leak current and C_{mem} the cellular membrane capacitance.

According to this model, each ionic channel is modelled by a membrane potential dependent conductivity (g_m) in series with the equilibrium ionic potential (E_i) that can be evaluated using the Nernst equation (equation 1.1). The membrane capacitance, C_{mem}, is estimated at 1 μF/cm^2 [Regehr, 1989].
With this equivalent circuit, the resulting total membrane current is the sum of all ionic and capacitive contributions, which results in:

$$I_{tot}(V_{mem},t)=C_m\frac{dV_{mem}}{dt}+g_K(V_{mem}-E_K)+g_{Na}(V_{mem}-E_{Na})+g_L(V_{mem}-E_L) \qquad (2.10)$$

In order to take into account the active ion transport through the membrane the potassium and sodium conductivities cannot be considered as constant. They have to be considered being functions

of the membrane potential [Grattarola, 1998]. Thus, an approach is to express them using an average value G_M modulated by an activation / inactivation factor [Buitenweg, 2001].

Extracellularly, the generated ionic current provides a voltage drop through the RC circuit between the reference electrode and the recording electrode. Figure 2.9 reports a model of the system considering the electrode interface model, the membrane H-H model and the parasitic elements of the microelectrode, i.e. the insulator capacitor $C_{insulator}$, the lead resistor R_{lead}, as well as the resistive drops in the culture media (R_{sol}).

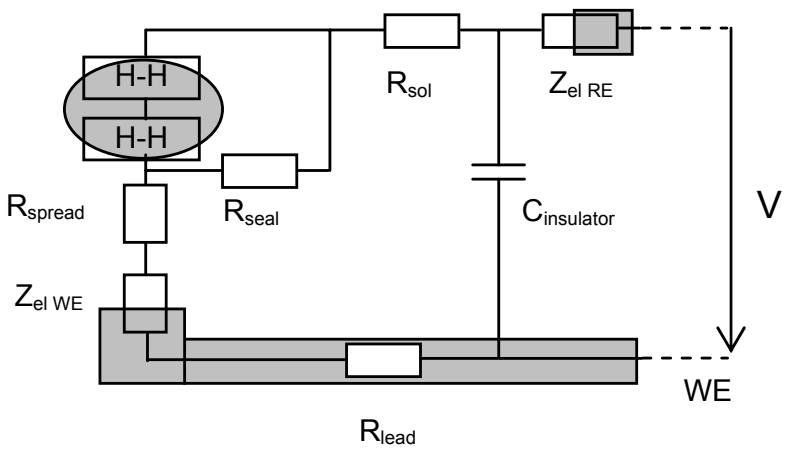

Figure 2.9: Model of the microelectrode-electrolyte-neuron.

Additionally, two other elements are considered: the spread resistor (R_{spread}) and the seal resistor (R_{seal}). They are described next as well as each element of the model.

- the spread resistor (R_{spread})

The spreading resistance is due to the spreading current from the electrode in the electrolyte between the electrode surface and the neuron. Its value is proportional to the electrolyte resistivity (typical culture media resistivity ρ_s = 0,7 Ωm) and determined by the electrode geometry. For a square electrode with a side length *a*, it can be estimated with:

$$R_{spread} = \frac{\rho_s \ln(4)}{\pi a} \tag{2.11}$$

and for a circular electrode of radius *r* [Regehr, 1989]:

$$R_{spread} = \frac{\rho_s}{4\pi r} \tag{2.12}$$

Considering a circular microelectrode of 10 μm in diameter, the spread resistor is 11 kΩ.

- the seal resistor (R_{seal})

The sealing resistor represents the resistive drop due to the electrolyte between the neuronal membrane and the insulator. It is calculated with the relation:

$$R_{seal} = \frac{\rho_{seal}}{d}\frac{l}{w} \tag{2.13}$$

where ρ_{seal} is the sealing resistivity, d the average neuronal membrane to insulator distance, i.e. 50 nm [Buitenweg, 2001], and l and w the respective length and width of the portion of the insulator covered by the neuronal membrane.

Grattarola reports values for the sealing resistivity ρ_{seal} depending on the strength of the seal. For a weak seal it is possible to consider its value equal to the electrolyte solution resistivity. For a tight seal a higher value between 1 to 5 Ωm should be considered.
In practice the value of the sealing resistor is difficult to estimate because it depends on the strength of the seal and on the dimensions of the plated chip area. Widely different R_{seal} can be found in the literature [Bove, 1996] ranging from a few of kΩ up to several MΩ.

- parasitic electrode elements (R_{lead}, $C_{insulator}$)

The parasitic electrode contribution can be estimated considering the lead resistor R_{lead} (connecting the microelectrode to the pad) and the capacitor $C_{insulator}$. For a rectangular lead of width w_m, length l_m, thickness h, resistivity ρ_m, and an insulating layer of thickness t with a relative permeability ε_r (ε_0 = 8.854x10^{-12} AsV^{-1}m^{-1}), it results:

$$R_{lead} = \frac{\rho_m}{h}\frac{l_m}{w_m} \tag{2.14}$$

$$C_{insulator} = \varepsilon_r \varepsilon_0 \frac{l_m w_m}{t} \tag{2.15}$$

Evaluating those elements per millimetre square for a platinum lead 1500 Å thick ($\rho_{m,Pt}$ = 10.10^{-10} Ωcm) and for a millimetre square of silicon nitride 4000 Å thick (ε_r = 7.5), R_{lead} = 6.6 mΩ/mm and $C_{insulator}$ = 166 pF/mm are obtained.

- the recording electrode impedance ($Z_{el\ WE}$)

The electrode impedance model has been previously described. As first approximation it is determined by the R_{CT}, C_{DL} elements as shown in Figure 2.10.

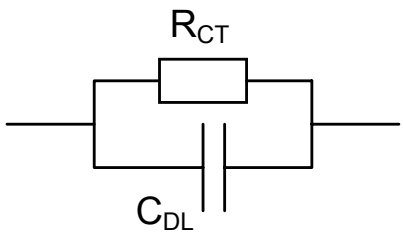

Figure 2.10: Simplified model of a microelectrode interface considering only the double layer capacitor and the charge transfer resistor.

In practice, the R_{CT} and C_{DL} are estimated considering the electrode area (A_{el}) and for R_{CT} an exchange current density J_0 (ranging between 10^{-2} to 10^{-18} A/cm^2 [Ives, 1961, p.17], for Au J_0 = 3.98x10^{-6} A.cm^{-2}, for Pt J_0 = 7.94x10^{-6} A.cm^{-2} [Kovacs, 1996]). The double layer

capacitance is estimated with the value c_{dl} expressed in $\mu F/cm^2$ (between 10 – 40 $\mu F/cm^2$ depending on the electrode material [Bard, 2001]).

$$R_{CT} = \frac{RT}{nFJ_0 A_{el}} \tag{2.16}$$

$$C_{DL} = c_{dl} A_{el} \tag{2.17}$$

Calculating at 37°C the R_{CT} and C_{DL} at 1.1 KHz[11] for a platinum electrode of 10 μm in diameter, the values of R_{CT} = 430 kΩ and C_{DL} = 7.85 pF (c_{dl} = 0.1 F/m^2) are obtained. The calculated total impedance is $|Z_{eq}|$ = 425 kΩ. This is a rough estimation allowing to evaluate and compare microelectrodes. However, for lower frequencies much higher values are observed, with a mainly capacitive behaviour.

- the reference electrode impedance ($Z_{el\ RE}$)

In the case of using a “real” reference electrode, i.e. Ag/AgCl, the equivalent circuit will see the R_{CT} component tending to zero (ideally non-polarisable electrode). The resulting impedance can thus be considered as purely capacitive.

On the other hand if the reference electrode is a pseudo-reference, noble metal electrode, the R_{CT} component should be considered and estimated using equations 2.17 and 2.18.

2.3.2 Recording model

The extracellular recorded signals are commonly measured as potentials. However, it has to be highlighted that the voltage between the microelectrode and the reference electrode is the result of the extracellular membrane currents through the ohmic circuit R_{seal}, R_{spread} and R_{sol}. Additionally, as previously described, these resistors depend on the network sealing and culture media resistivity, and are

[11] In the field of MEAs the microelectrode impedance is evaluated and compared at 1.1 kHz.

thus difficult to control. Therefore, a further simplification of the model considers that the extracellular recorded potential is mainly determined by the current generated on the electrode side of the neuron through the sealing resistor. It is convenient to substitute $I(V_{mem},t)$ and R_{seal} with an equivalent voltage source as described in Figure 2.11. An additional impedance Z_{in} has been introduced representing the amplifier input impedance connected between the reference and the working electrode.

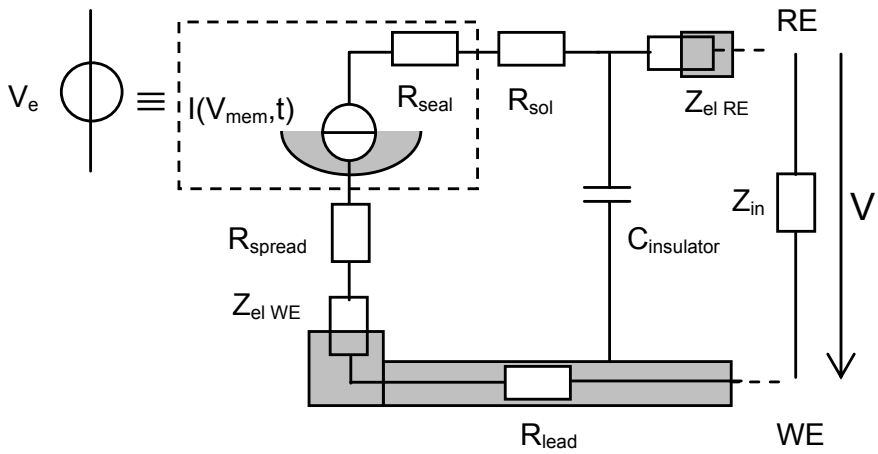

Figure 2.11: Simplified voltage recording model. Z_{in} is the input impedance of the recording amplifier (WE represents the microelectrode and RE the reference electrode).

2.3.3 Electrode characteristics for the recording

In terms of noise, the system is mainly influenced by Johnson noise [Garyantes, 1992] given by the total resistor R_{tot}.

$$V_{noise,rms} = \sqrt{4kTBR_{tot}} \tag{2.18}$$

where k is the Boltzmann constant (1.38×10^{-23} J/K), T is the temperature in K, and B is the frequency bandwidth.

Considering that the resistance R_{tot} is mainly due to the electrode impedance, it is necessary to reduce its value (under the MΩ) in order to achieve a higher signal-to-noise ratio (SNR). The calculated noise on bandwidth of 10 kHz for a 1 MΩ electrode impedance, yields 12.8 μV_{rms}.

In this sense, reported works showed how to decrease the electrode impedance by increasing the electrode surface, with the widely used platinum black deposition, Pt-electrodeposition techniques (hillocks-shaped three dimensional electrodes) [Thiébaud, 1997], or with tip-shaped electrodes. [Thiébaud, 1999; Heuschkel, 2002]. Also a high electrode roughness is preferable for the recording since it allows to increase the real electrode surface area.

Additionally, the SNR is reduced by the environmental noise and by the noise of the amplifying electronics. The minimisation of those noise sources has to be taken into account with particular care when engineering the recording system.

2.4 Stimulation considerations

For an injection current I_{ext} (at the membrane) the resulting membrane potential can be described by:

$$\frac{dV_m}{dt} = \frac{1}{C_m}\left[I_{ext} - g_{Na}(V_{mem} - E_{Na}) - g_K(V_{mem} - E_K) - g_L(V_{mem} - E_L)\right] \quad (2.19)$$

This modifies the membrane potential (and the ions conductivities g_M) and depending on the amplitude, an action potential can be fired (see chapter one).

Empirically it has been described that to stimulate an action potential, a microelectrode close to the membrane has to depolarise the membrane by –15 mV referred to the culture media potential [Garyantes, 1992] for a time sufficiently long to open the voltage-activated channels: approximately 200 μs [Hille, 1992]. As a first approximation, it can be considered that the spread resistor as well as the seal one provide the resistive divider in the circuit and can be used to estimate the potential to be applied to the electrode. However, the variability of the sealing resistor from culture to culture makes this theoretical evaluation difficult.

Nevertheless, some considerations can be formulated. During the recording, the processes at the electrode interface are mainly of a capacitive nature (electrode polarisation given by the electrophysiological activity), whereas during stimulation other reactions may occur. Faradaic reactions, i.e. electrolysis, resulting from an applied potential to the electrode have to be avoided in order to limit any toxic effect on the culture.

To limit toxic effects two aspects are considered:

- the choice of the electrode material is important in order to maximise the charge that can be applied to the microelectrode.
- the use of biphasic stimulation signals for reversing the oxidation/reduction reactions and limit the microelectrode degradation.

An important material property is the charge injection limit (Q_{inj}), which represents the maximal charge that can be injected before observing faradaic currents. For a safe stimulation, materials with high Q_{inj} have thus to be preferred. Electrodeposited platinum- black has been one of the first materials to be used, followed by iridium-oxide and titanium-nitride. For platinum and black-platinum values of 75 $\mu C/cm^2$ up to 0.4 mC/cm^2 have been reported [Ziaie, 1991; Blau, 1997; Brummer, 1983] and this material is therefore widely used for the long-term stimulation. Recently, higher values have been reported for titanium-nitride, 0.87 mC/cm^2 up to 22 mC/cm^2 and for iridium-oxide, 4 mC/cm^2 up to 400 mC/cm^2 [Weiland, 2002; Blau, 1997]. Based on the Q_{inj} values it is possible to identify iridium-oxide as a preferred choice for stimulation.

2.5 Array of metal electrodes

In the previous paragraphs, the electrical model of a single electrode has been described. However, in the case of an array of electrodes, the additional parasitic capacitive coupling between the leads should be taken into account. Sakurai and Tamaru [Sakurai, 1983] proposed an approximation considering the interaction of one electrode lead with the two nearest neighbours.

The resulting electrode coupling capacitor C_c and the insulator capacitor $C_{insulator}$ result in:

$$C_c = 2\varepsilon_0\varepsilon_r l.\left[0.03.\left(\frac{w}{d}\right) + 0.83.\left(\frac{t}{d}\right) - 0.07.\left(\frac{t}{d}\right)^{0.222}\right].\left(\frac{s}{d}\right)^{-1.34} \quad (2.20)$$

$$C_{insulator} = \frac{1.15\varepsilon_0\varepsilon_r lw}{d} + 2.8\varepsilon_0\varepsilon_r l.\left(\frac{t}{d}\right) \quad (2.21)$$

where ε_r is the relative permeability of the insulator, ε_0 is the permeability constant, and w are the length and width of the lead, t is the thickness of the lead, d the insulator thickness and s is the spacing between the leads.

Additionally, in the case of a network of neurons, it has to be considered that in principle every electrode will record the activity of all the neurons, modulated by the relative sealing resistor. This contributes to additional signal sources on the recording electrode. However, the modelling of these effects has not been reported up to now, and the simple approximation previously described is normally considered.

2.6 Bibliography

Bard, J. and L.R. Faulkner, *Electrochemical Methods, Fundamentals and Applications*. 2nd. ed. 2001, New York: Wiley.

Blau, A., et al., *Characterization and optimization of microelectrode arrays for in vivo nerve signaling recording and stimulation.* Biosensors & Bielectronics, 1997. **12**(9-10): pp. 883-892.

Bove, M., Grattarola, M., Martinoia, S., and Verreschi, G., *Interfacing cultured neurons to planar substrate microelectrodes - characterization of the neuron-to- microelectrode junction*, Bioelectrochemistry and Bioenergetics, vol. 38, pp. 255-265, 1995.

Bove, M., Martinoia, S. Grattarola, M., and Ricci, D., *The neuron-transistor junction: linking equivalent circuit models to microscopic descriptions*, Thin solid films, vol. 284-285, pp. 772-775, 1996.

Brummer, S.B., L.S. Robblee, and F.T. Hambrecht, *Criteria for selecting electrodes for electrical stimulation: theoretical and practical considerations*, Ann. N.Y. Acad. Sci., 1983. **405**: p. 159-171.

Buitenweg, J.R., *Electrical behaviour of the neuron-electrode interface*, 2001, Twente University Press, Twente.

Garyantes, T.K., *The effect of electrical stimulation on neuronal outgrowth and the development of a new method for chronic long-term stimulation and recording from group's of neurons in culture*, 1992, Caltech: Pasadena.

Girault, H.H., *Electrochimie physique et analytique*. 2001, Lausanne: Presses polytechniques et universitaires romandes.

Grattarola, M., G. Massobrio, and P. Antognetti, *Bioelectronics Handbook: MOSFETs, Biosensors, and Neurons*. 1998: McGraw-Hill.

Heuschkel, M.O., et al., *A three dimensional multi-electrode array for multi-site stimulation and recording in acute brain slices.* Journal of Neuroscience Methods, 2002. **114**: p. 135-148.

Hille, B., *Ionic channels excitables neurons*. 1992, Sunderland: Sinauer ass. inc.

Ives, D.J.G. and G. Janz, *Reference electrodes: theory and practice*. 1961, New York: Academic press.

Lohmann, F., Z. Naturforshung, 1967. **22a**(843).

Pletcher, D., *A first course in electrode processes*. 1991, Southampton: ECC.

Regehr, W.G., et al., *Sealing cultured invertebrate neurons to embedded dish electrodes facilitating long-term stimulation and recording*, Journal of Neuroscience Methods, 1989. **30**: p. 91-106.

Rutten, W., et al., *Neuroelectronic interfacing with cultured multielectrode arrays toward a cultured probe.* Proceedings of the Ieee, 2001. **89**(7): p. 1013-1029.

Sakurai, T. and K. Tamaru, *Simple formulas for two- and three-dimensional capacitances.* IEEE Transactions on electron devices, 1983. **ED-30**(2): p. 183-185.

Stalder, C., *Etude des electrodes polycristallines à base de TiO_2 destinees à la conversion d'energie solaire en energie chimique*, Faculté des Sciences, 1981, Université de Genève: Genève.

Sze, S.M., *Semiconductor devices: physics and technology*. 1985, New Jersey: Wiley.

Thiébaud, P., et al., *An array of Pt-tip microelectrodes for extracellular monitoring of activity of brain slice,* Biosensors & Bioelectronics, 1999. **14**: p. 61-65.

Thiébaud, P., et al., *Microelectrode Arrays for Electrophysiological Monitoring of Hippocampal Organotypic Slice Cultures,* IEEE Transaction on Biomedical Engineering, 1997. **44**(11): p. 1159-1163.

Weiland, J.D., D.J. Anderson, and M.S. Humayun, *In vitro electrical properties for iridium oxide versus titanium nitride stimulating electrodes,* IEEE Transactions on biomedical eng., 2002. **49**(12): p. 1574-1579.

Ziaie, B., Y. Gianchandani, and K. Najafi, *A high current IrOx thin-film neuromuscular microstimulator,* IEEE Sensors & Actuators Transducers, 1991. **6**: p. 124-127.Sensors & Actuators Transducers, 1991. **6**: p. 124-127.

3 FABRICATION AND CHARACTERISATION OF ELECTRODE ARRAYS AT THE MICRO- AND NANO-SCALE

3.1 Introduction

The enabling technologies for the fabrication of microelectrode arrays have seen an incredible development during the last twenty years. As described in chapter 1 several MEAs of different materials and geometry are today available and some of them also commercialised (Multichannel, Panasonic). They typically consist of an array of 30 up to 128 microelectrodes: planar or three-dimensional (Au, Pt, ITO, TiN) or (FETs) electrodes, integrated on a glass or silicon substrates. The electrode diameter ranges between 10 μm to 100 μm, with a typical electrodes separation of 70 μm to 200 μm.

The aim of this chapter is to discuss the microfabrication of metallic microelectrode arrays in order improve the technology, evaluate the electrode materials and the resolution that can be currently achieved. Devices on silicon and pyrex substrates, with platinum and iridium oxide as electrode materials, with planar and three dimensional electrodes are presented.

A commonly used technology to define metal leads is the lift-off technique. This technological choice allows to pattern the electrode arrays using the same mask for different metals, i.e. platinum, gold and iridium. However this technique still shows several limitations in term of resolution. For this reason, the conventional single layer photoresist lift-off technique has been improved by using a two layers photoresist technique. This allows to overcome the problem of the metal wing tips, which introduce inhomogeneities in the top insulation layer, and to improve the patterning resolution.

In the second part two techniques for modifying the thin-film platinum and iridium electrodes are presented. The impedance of platinum electrodes is reduced by bright platinum electrodeposition, due to the increase of the electrode surface. Secondly, iridium electrodes are electrochemically oxidised to iridium oxide in order to increase the charge injection limit for the stimulation.
In the last part of this chapter, the fabrication of nanoelectrodes by e-beam writing is investigated. The smaller dimension of these electrodes would allow measurements in the nano-scale domain of cellular or sub-cellular physiology. Here the technology is demonstrated by fabricating nano-disk electrodes and nano-interdigitated electrodes. Preliminary electrochemical tests of those devices show the functionality of both types of nano-electrodes.

3.2 Fabrication of planar microelectrodes arrays

3.2.1 Silicon substrate arrays

Silicon wafers 525 μm thick and with a 4'' diameter are used. A standard cleaning is performed in:

1) fuming HNO_3, 10 min., for removing the organic contaminants
2) buffered hydrofluoric acid (BHF), 1 min., for removing the native silicon oxide layer
3) 70% HNO_3 at 115°C, 10 min., to re-oxidise the silicon surface

The wafers are rinsed in deionised (DI) water between each step and dried with N_2 at the end of the process.
In order to avoid electrical cross-talk between the electrodes through the silicon substrate a bottom insulating layer of 2000 Å thick silicon nitride is deposited by low pressure chemical vapour deposition (LPCVD). Metal electrodes are defined by lift-off resist (see 3.2.3) followed by the metal evaporation (pressure 10^{-6} mTorr, deposition rate 5-10 Å/s). The top insulating layer, 2000 Å thick LPCVD silicon

nitride, is deposited and the electrodes as well as the contacting pads are defined by photolithography (AZ1518 from Shipley, 1.8 μm thick), and opened by SF_6/O_2 plasma etching. The photoresist is stripped in acetone and the wafer rinsed with isopropanol. Finally, the wafer is cleaned in a *piranha* solution (5 min. in H_2SO_4 and 5 min. adding a drop of H_2O_2). The choice of this cleaning compared to an oxygen plasma stripping is motivated by the lower degree of oxidation of the electrodes. The fabrication steps are reported in Figure 3.1.

3.2.2 Pyrex substrate arrays

Pyrex, 7740, wafers 500 μm thick (Sensor Prep Services, Elburn) with a 4'' diameter are used. The cleaning of the pyrex wafers is realised in:

1) fuming HNO_3, 10 min., for removing organic contaminants
2) buffered hydrofluoric acid (BHF), 1 min.

Also in this case, the wafers are rinsed in deionised (DI) water between each step and dried with N_2 at the end of the process.
Due to the insulating properties of the pyrex it is not necessary to deposit a bottom passivation layer, therefore the metal electrodes are directly defined by lift-off on the pyrex surface. By using pyrex substrates it is not possible to deposit the top passivation layer by LPCVD since the deposition temperature (800°C) is higher than the fusion temperature of the substrate. For this reason, a plasma enhanced chemical vapour deposition (PECVD) at 300°C is performed for depositing the silicon nitride layer. The resulting insulating layer shows a lower density than the LPCVD one, but its stability and insulating properties are nevertheless adequate (dielectric constant $\varepsilon_r = 7.5$ and resistivity $\rho = 1.10^{14}$ Ωcm).
Also in this case a photolithography step is used for patterning the openings of the electrodes and of the contact pads. The silicon nitride is opened with plasma etching. Finally, the stripping and the

cleaning of the wafers are performed like in the case of the silicon substrates in piranha solution. The process of fabrication of planar MEAs on Pyrex is summarised in Figure 3.1.

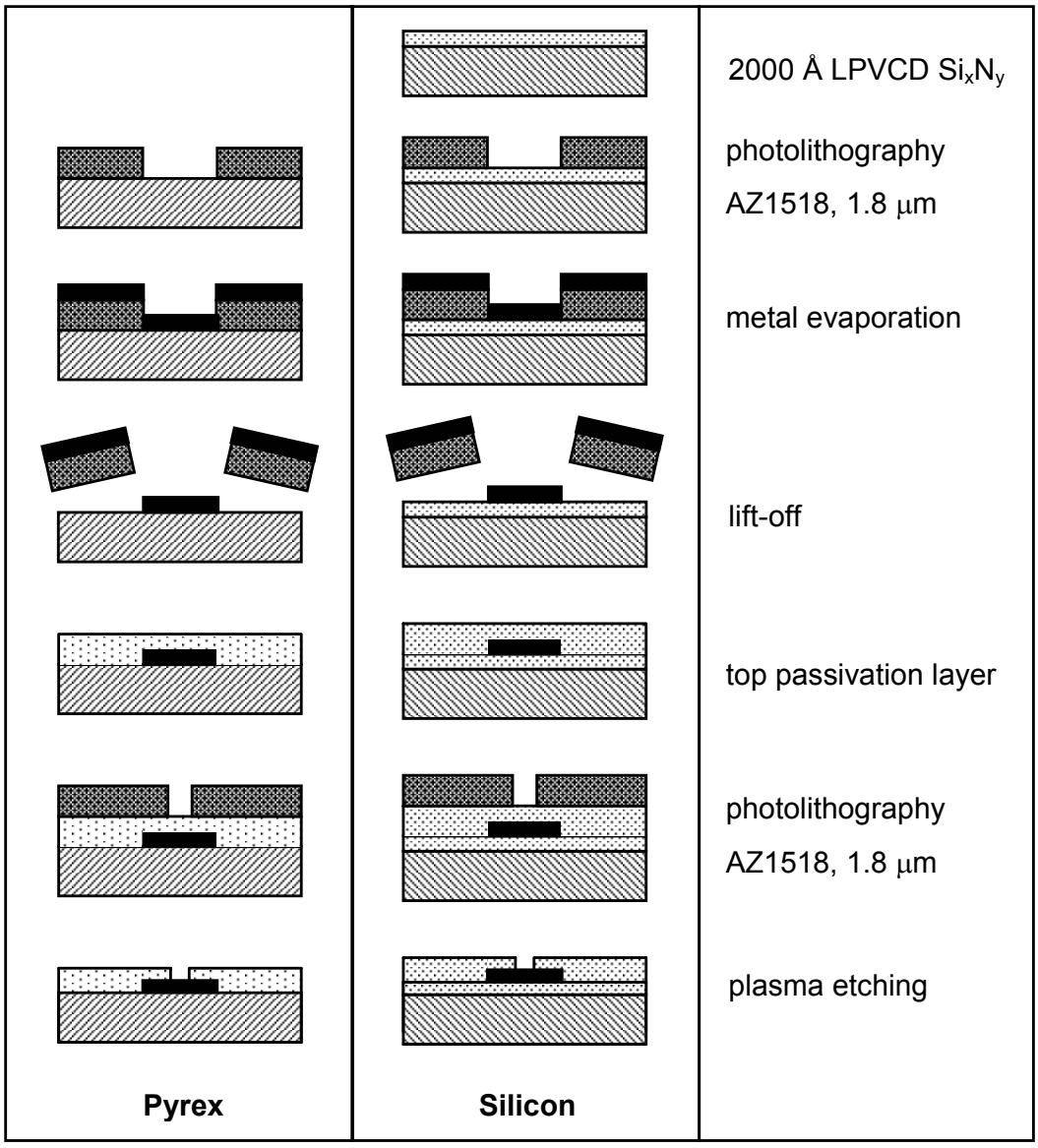

Figure 3.1: Fabrication process for planar MEAs on pyrex and on silicon substrates.

3.2.3 The lift-off process

The conventional lift-off is realised by patterning a positive photoresist layer followed by the evaporation of the metal. The metal structures are then realised by lifting-off the photoresist in acetone. In this way only the metal deposited in the developed photoresist structures remains on the wafer.
A platinum lift-off process starts by patterning a positive photoresist layer (AZ1518). A layer 1.8 μm thick of photoresist is spinned (spinner Karl-Süss 152) on the dehydrated (30 min. at 200°C) and HMDS treated substrate. After pre-baking (1 min. at 100°C) on hot-plate (hot-plate Karl-Suss 152), the photoresist is then exposed in vacuum-contact mode to UV-light at 365 nm (Ma-6 from Karl-Süss). The development is performed in a 1:4 solution of AZ351B (from Shipley) and deionised water (DI) for 60 seconds. Successively 200 Å of titanium on pyrex wafers or 200 Å of tantalum on silicon wafers are evaporated as adhesion layers for the 1300 Å of platinum. Finally the photoresist is removed in acetone and the substrate is rinsed with isopropanol.
The closely spaced interdigitated electrodes geometry is one of the most demanding ones and has therefore been used for illustrating the technology (Figure 3.2).
Some practical issues affecting this technique are the following:

1. the side walls of the photoresist structures have to be as vertical as possible (controlling the exposure dose and the development). If the profile is too positive (Figure 3.3) the sidewall will be covered by a continuous metal layer. This results in the difficult removal of the excessive metal, in metal wing tips, and in bad resolution.
2. the structuring of thick metal leads needs a thicker photoresist layer. This results in a lower resolution photolithography due to the light diffraction.

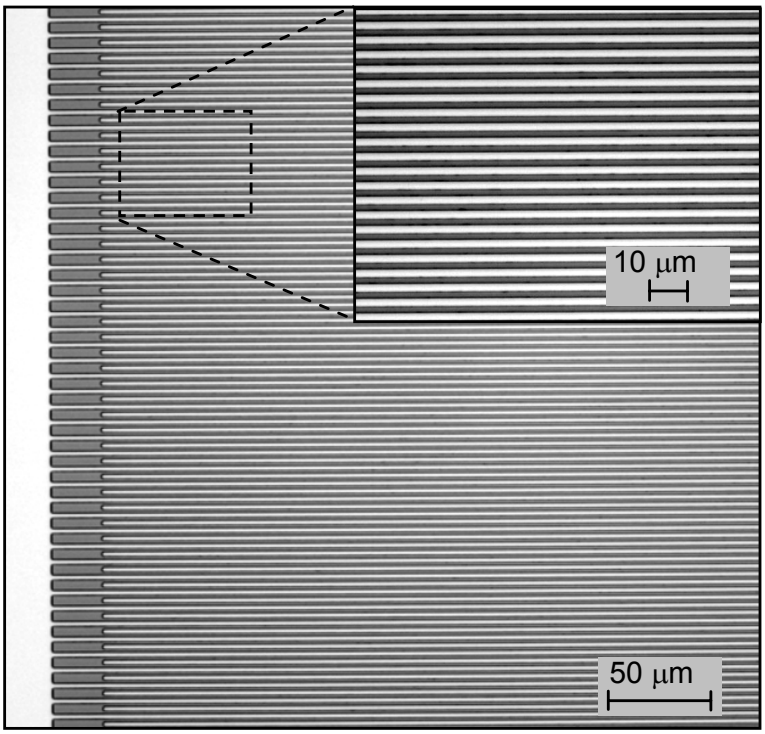

Figure 3.2: 2 μm IDAs after Pt lift-off (AZ1518).

3. soft metals such as aluminium and gold are delicate to lift-off since it is not possible to mechanically accelerate the process, e.g. using sonication (US). This would result in metal cracks and irregularities.
4. noble metals with a high evaporation temperature are difficult to deposit. The higher e-beam energy may increase the deposition temperature in the chamber. For example, for iridium, temperatures up to 100°C have been measured during the evaporation. It is thus necessary that the patterned photoresist withstands these temperatures. If this is not the case, the evaporation will cause the cracking of the photoresist layer.

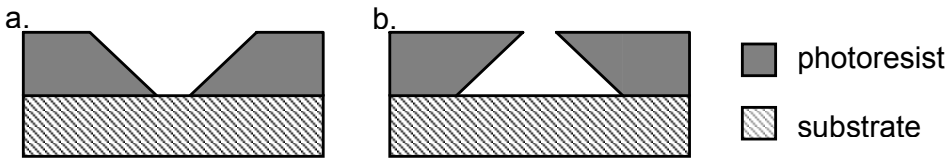

Figure 3.3: (a) positive photoresist profile, (b) negative photoresist profile (exaggerated)

In the past a chlorobenzene treatment of the positive photoresist after exposure was used in order to stress the top of the photoresist layer and achieve negative profiles after development. However, the high toxicity of this product motivated the research of alternative processes.
An alternative is the use of negative photoresists, i.e. Ma-N 410, Ma-N 420 (Microresist Resist Technology). These photoresists offer the advantage of negative profiles when developed. This allows to overcome the metal wing tips problem, but practically the homogeneity of the process on the wafer it is not always satisfying. This is mainly due to the difficulties in developing the photoresist (in particular for the thicker Ma-N 420) and residues that may affect the lift-off.
In order to improve the lift-off technique, in collaboration with the colleagues D. Briand, O. Guenat and E. Milotte, a two layer photoresist technique has recently been developed. It consists in spinning and baking of a first photoresist layer (LOR from Microchem), which is 2-3 times thicker than the metal that has to be deposited. Successively, a positive resist (AZ1813 from Shipley) is patterned on the first layer. The development of the exposed second layer will underetch the first one, resulting in a structure as shown in Figure 3.4.(b) This allows to ensure the access of the photoresist removing solution (remover PG from Microchem) and thus well-defined metal structures contours.

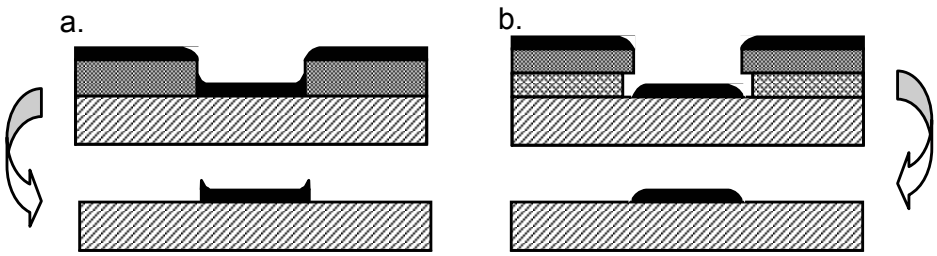

Figure 3.4: Comparison between (a) positive single layer photoresist lift-off and (b) the two layer photoresist lift-off (LOR resist + AZ1813). The new method allows to avoid metal wing tips and ensure the top passivation of the metal leads.

For patterning a metal layer 1500 Å thick, a dehydrated pyrex substrate (200°C for 30 min.) is coated with 4000 Å of LOR3B. Different baking temperatures and times have been tested in order to evaluate (by optical inspection) the resulting underetching (table 3.1).

LOR3B bake temperature	LOR3B bake time	underetching
150°C	5 min.	> 10 μm
170°C	5 min.	2.5 μm
170°C	10 min.	~ 1 μm
190°C	5 min.	< 1 μm

Table 3.1: Evaluation by optical inspection of the underetching for different bake temperatures and times of a layer of 4000 Å of LOR3B and 1.3 μm of AZ1813 as second photoresist layer.

Then a 1.3 μm thick layer of AZ1813 is deposited and prebaked at 110°C for 1 min. on a hot-plate. The exposure of the photoresist is realised in vacuum-contact mode on a Ma-6 mask aligner (365 nm wavelength) with an exposure dose of 45 mJ/cm^2. Finally, without a post-bake, the exposed layer is developed for 60 s in diluted 1:4 AZ400K:DI water solution.

The development of the exposed photoresist layer results in the underetching of the first one. Figure 3.5 shows the result after development. After the photolithography, 1500 Å of metal (200 Å of Ti and 1300 Å of Pt) are evaporated and the lift-off is realised in a solution of Remover PG at 60°C, for 1 hour. The resulting structures are shown in Figure 3.6.

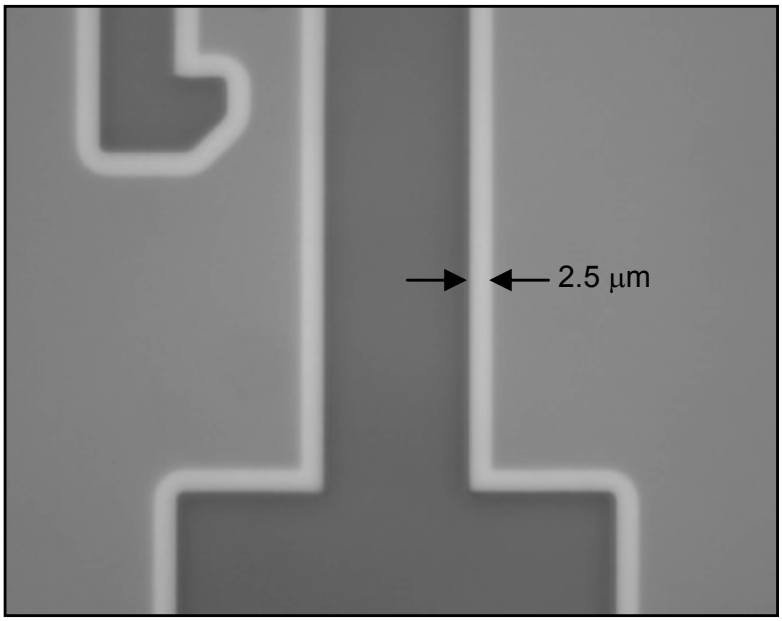

Figure 3.5: Optical image of the developed LOR3B (4000 Å) on pyrex. Baking at 170°C, 5min + 1.3 μm of AZ1813. An underetching of 2.5 μm has been obtained after development in AZ400K 1:4 for 60 s.

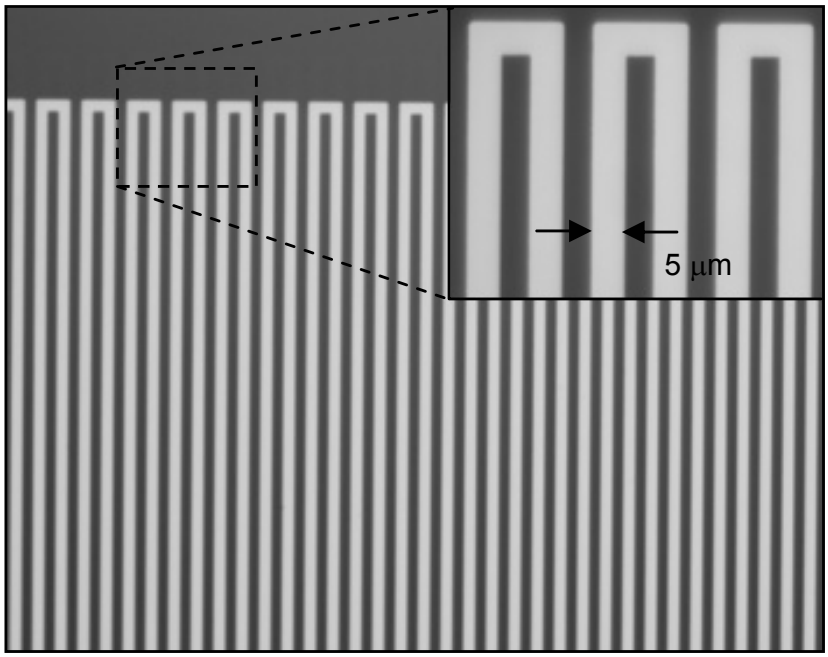

Figure 3.6: Optical image of a 5 μm structure fabricated with the two layers technique. (Ti-Pt 1500 Å, pyrex substrate)

There are several advantages of this technique:

1. the second photoresist layer (AZ1813) is the one defining the resolution and its thickness is independent of the metal thickness.
2. several viscosities of the first photoresist layer (LOR) exists allowing layer thicknesses ranging between 500 Å (LOR 0.5A) and 60'000 Å (LOR 30B). This allows a metal thickness up to 3 μm (from LOR technical specifications).
3. the underetch of the first layer is controlled by its baking conditions (temperature and time).

On pyrex substrates, baking the LOR layer at 190°C for 5 min., underetching lower than 1 μm has been obtained. This allowed the fabrication of devices with interlines separation down to 5 μm and structures down to 2 μm should be possible.

A comparison between the structures (1500 Å Ti-Pt, with 5 μm lines and 5 μm spacing) realised with the lift-off of one layer (Figure 3.7) and two layers technique respectively (Figure 3.7) has been performed by optical and AFM imaging. Even though the optical images of both structures show good resolution, the metal wing tips are clearly visible by AFM on the positive resist lift-off structure. On the other hand, the structure obtained with the two layer technique shows lines with rounded profile and excellent resolution.

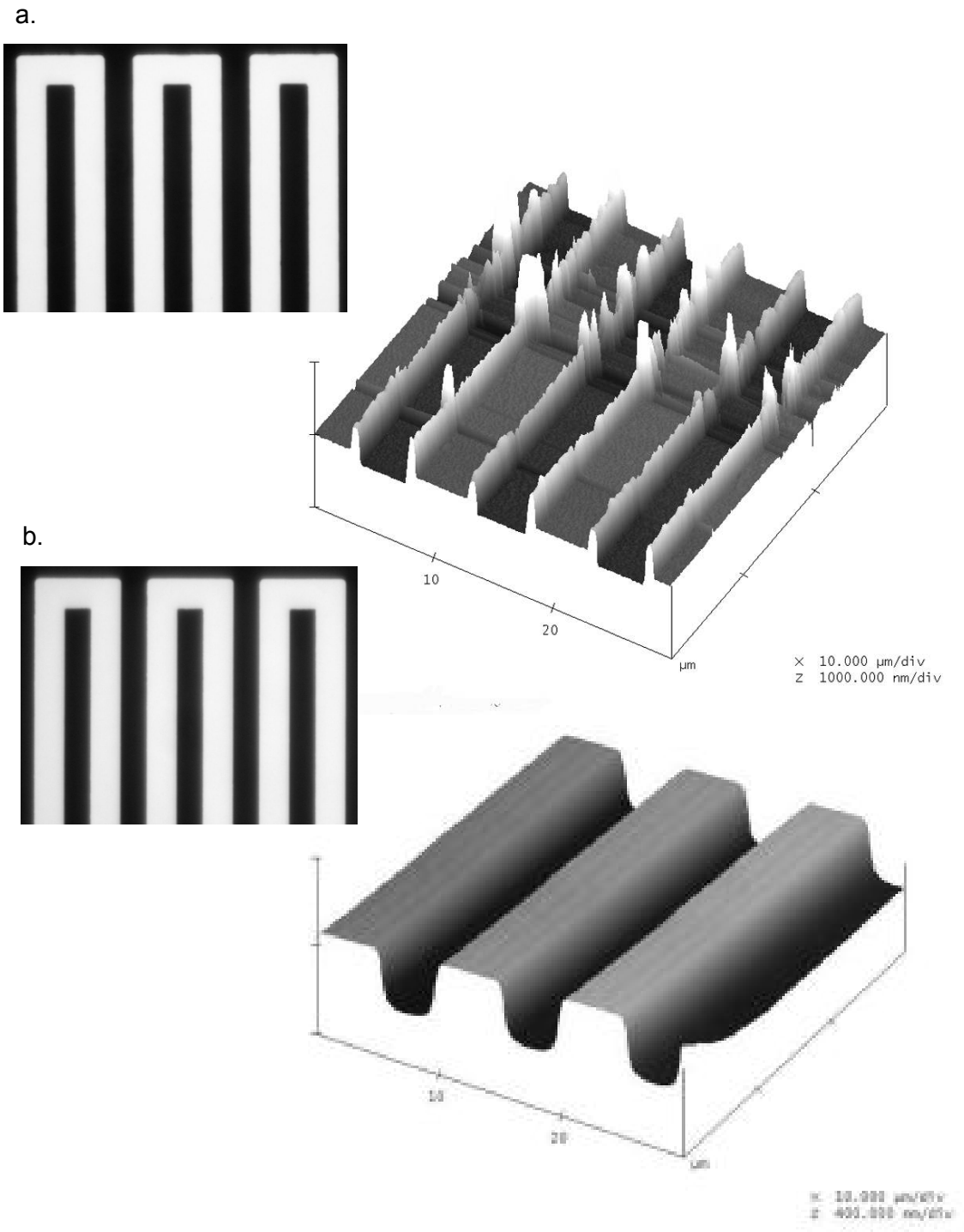

Figure 3.7: Optical and AFM images of 5 µm metal lines realised (a) with one layer of positive resist, (b) with the two layers technology. Metal wing tips are clearly visible on the AFM image (a). This is not the case for the LOR device.

3.2.4 Description of the realised planar MEAs

The previously described technology has been used to fabricate MEAs on silicon and pyrex substrates. Table 3.2 summarises the realised planar devices.

substrate material	electrode material	top passivation material
525 μm thick Si	200 Å Ta + 1300 Å Pt	2000 Å LPVCD Si_xN_y
525 μm thick Si	200 Å Ta + 1100 Å Ir	2000 Å LPVCD Si_xN_y
500 μm thick Pyrex 7740	200 Å Ti + 1300 Å Pt	4000 Å PECVD Si_xN_y
500 μm thick Pyrex 7740	200 Å Ti + 1100 Å Ir	4000 Å PECVD Si_xN_y

Table 3.2: Summary of the realised planar devices on silicon and pyrex substrates.

All these devices were realised with the same design, integrating 30 microelectrodes (rectangular geometry) of 10 μm in diameter and 4 pseudo-references (Figure 3.8). The active area is 2.4 x 0.7 mm^2 and the inter-electrode separation is 300 μm horizontally and 180 μm vertically.

After dicing the devices (6 x 8 mm^2) are packaged on a printed-circuit-board (PCB) providing compatibility with the Multi-Channel recording system (MCS, Reutlingen). The packaging is realised by gluing the chip on the PCB, wire-bonding of the contact pads and insulating them with an epoxy. Finally, a glass chamber is glued on the PCB defining a reservoir for the culture media (Figure 3.9).

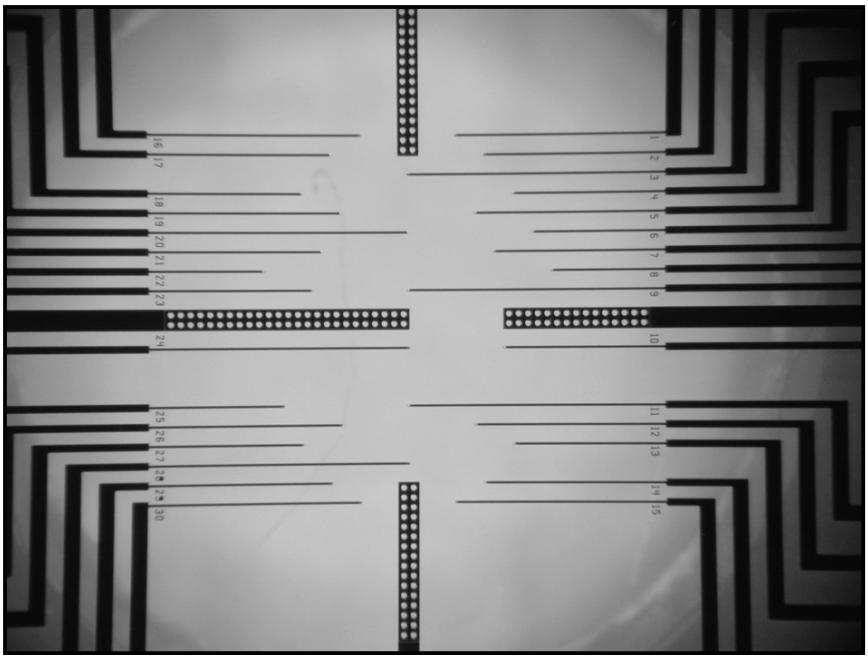

Figure 3.8: MEAs on a pyrex substrate (30 microelectrodes of 10 μm, active area 2.4 x 0.7 mm, 4 pseudo-references).

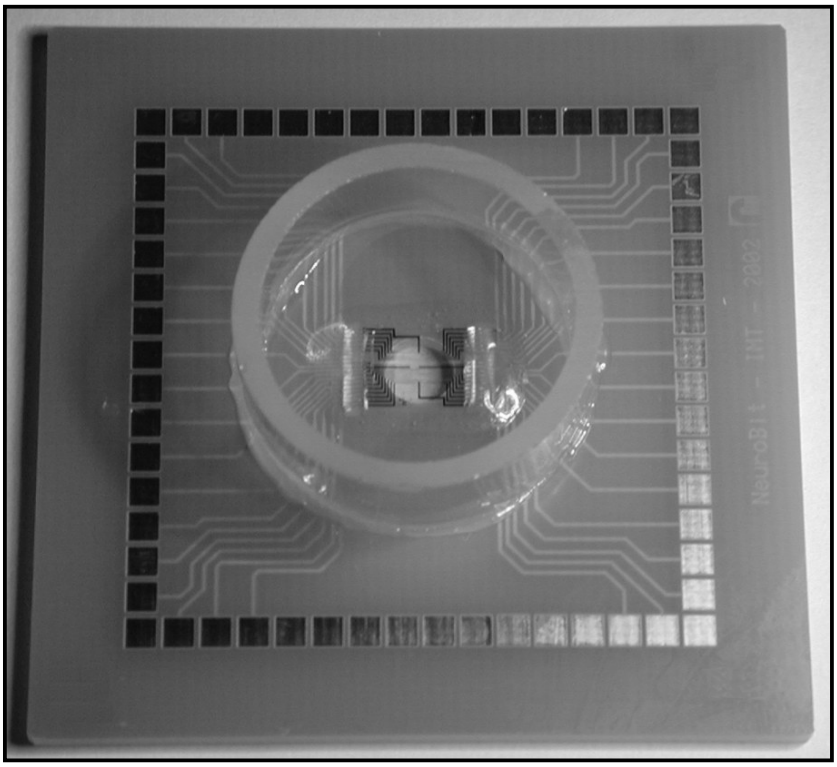

Figure 3.9: Packaged device on a MCS compatible PCB. A glass chamber defines the culture media reservoir.

3.3 Three dimensional iridium tips on silicon

Based on the platinum-tip technology reported by P. Thiébaud [Thiébaud 1999], an array of 32 iridium tip shaped electrodes (47 μm) was realised on silicon. The technology has been modified evaporating a 200 Å thick layer of tantalum (adhesion layer), followed by a 1000 Å thick layer of iridium. The lift-off was realised using a negative photoresist (Ma-N 420). A 2000 Å thick LPCVD silicon nitride layer was used as the top passivation. Finally, the tips (47 μm in height) were opened by the etching of the silicon nitride layer (SF_6/O_2 plasma) using a 38 μm thick photoresist (AZ4562 from Shipley, [Roth, 1999]). The resulting tip opening is a cone with a base of 10 to 15 μm and a height of 15 to 20 μm (Figure 3.10).
The three dimensional iridium tips were electrochemically oxidised as presented next in section 3.5.

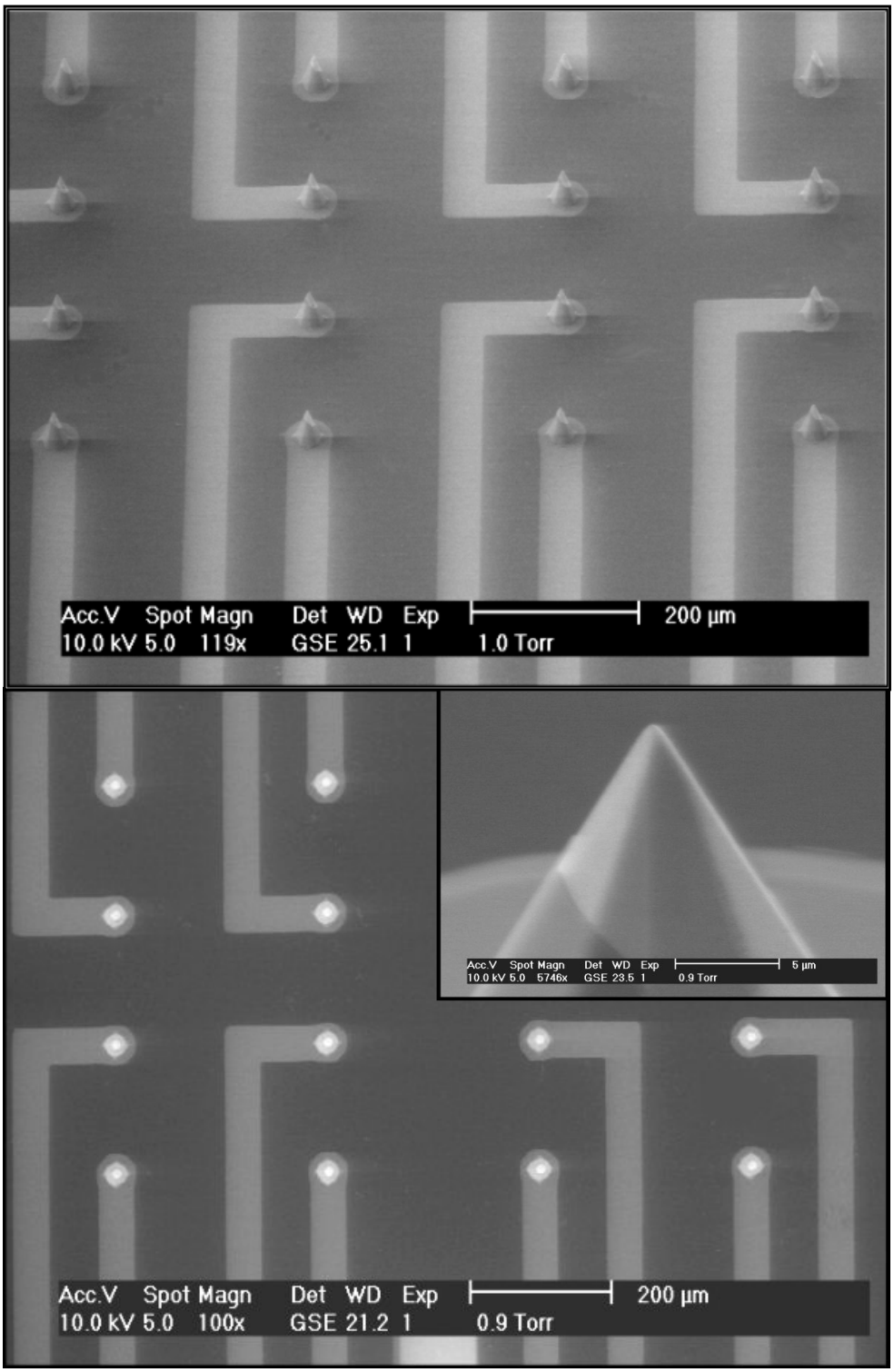

Figure 3.10: Part of an array of 32 Ir tip-shaped electrodes.

3.4 Platinum electrodes modification

In order to improve the microelectrode impedance, a small platinum hillock was grown by electrodeposition on the planar platinum electrodes.

The device is packaged and the contact pads are connected in a sandwich structure where gold Zebra Strips (from Fulipoly, Jp) provide the electrical contacts. This allows an easy mounting and dismounting of the devices. The microelectrodes are pre-treated by cyclic-voltammetry (IBM Voltammetric Analyser EC/225) in a 1M H_2SO_4 solution. The applied potential ramp is between –0.25 V and 1.55 V versus Ag/AgCl reference electrode (100 mV/s). A platinum wire counter-electrode was used.

Figure 3.11: Cyclic voltammograms of Pt electrodeposition on 10 μm in diameter Pt microelectrodes (Ag/AgCl reference electrode, Pt counter electrode, scan rate 50 mV/s).

The platinum electrodeposition is realised in a commercially available platinum solution (3745 from Engelhard) by cyclic-voltammetry. The potential range varies from 0 V to –0.725 V versus Ag/AgCl reference electrode (50 mV/s). Figure 3.11 shows the cyclic voltammograms during the electrodeposition on 11 microelectrodes. Performing 10 scans, small platinum hillocks of a few μm have been obtained on microelectrodes of 10 μm diameter (Figure 3.12).

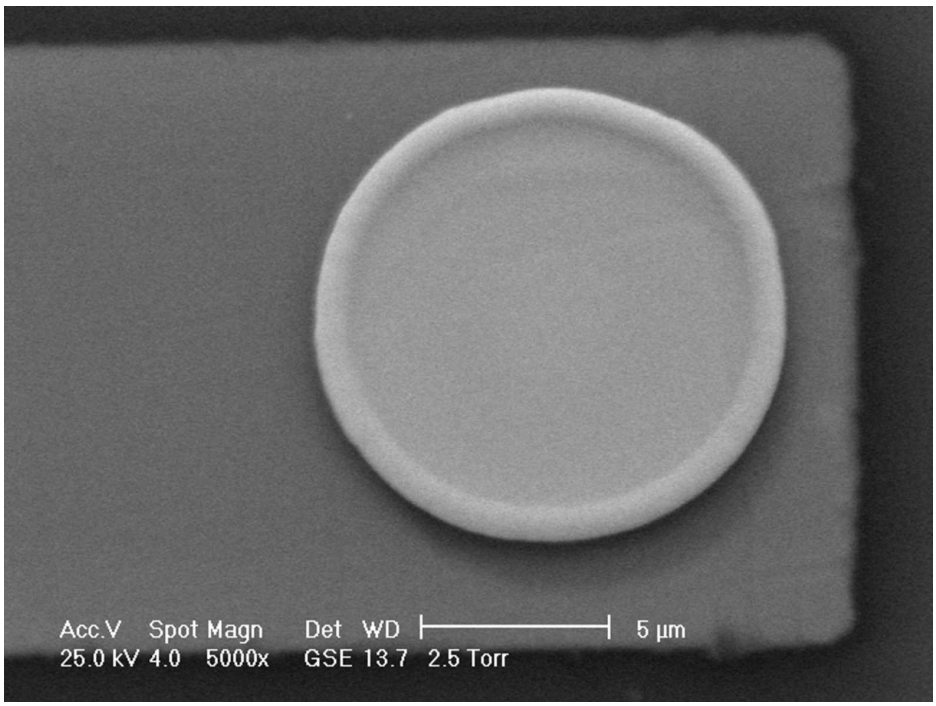

Figure 3.12: SEM image of one electrodeposited Pt electrode.

The resulting real radius of the microelectrodes has been calculated with the equation[12] [Bard, 2001]:

$$r_{real} = \frac{I_{oxidation}}{4nFDC} \tag{3.1}$$

[12] The real radius is calculated from the oxidation current reporting the three dimensional shape to a planar electrode of equivalent area.

with *n* the number of exchanged electrons, *F* the Faraday constant (96484.6 $C.mol^{-1}$), *D* the diffusion constant, and *C* the concentration in $mol.cm^{-3}$.

The oxidation current $I_{oxidation}$ has been measured at 0.6 V in a 1M KCl / 100mM ferrocyanide solution. The voltammograms are given in Figure 3.13 and the resulting calculated real electrode radii versus the number of scanning cycles are reported in Table 3.3 (with D = 6.30 10^{-6} cm^2s^{-1} and C = 100.10^{-3} $mol.cm^{-3}$).

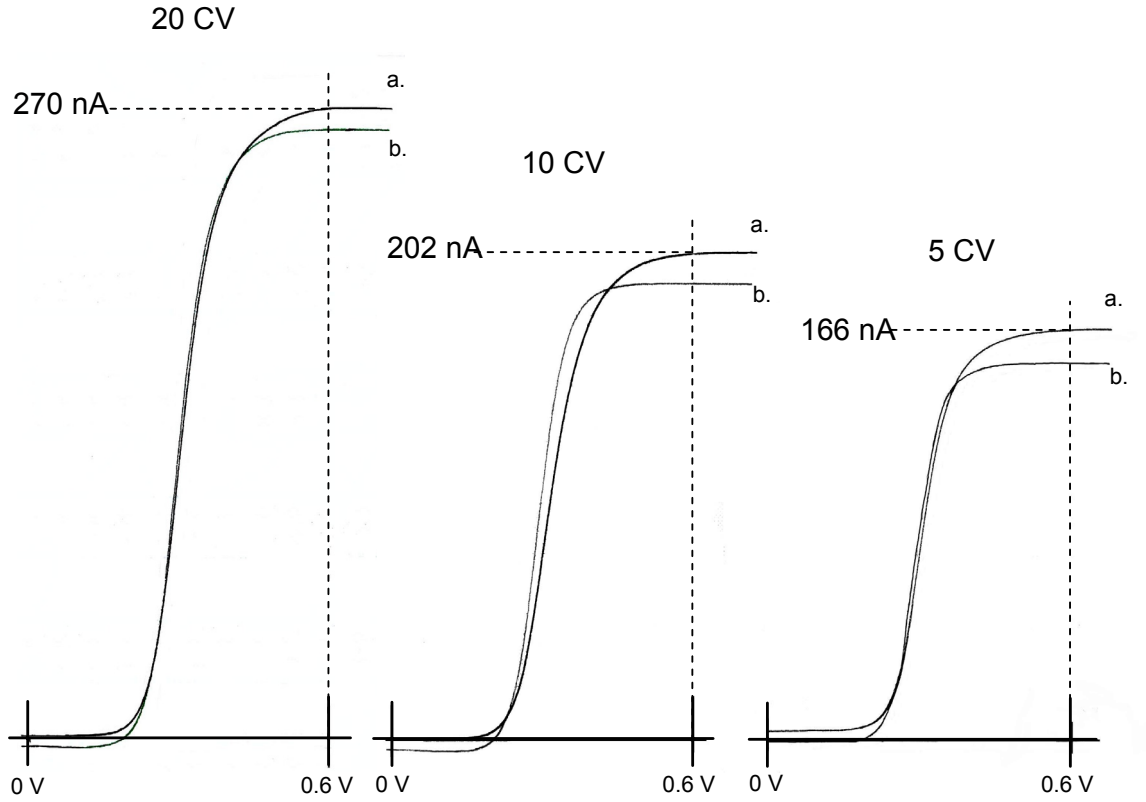

Figure 3.13: Voltammograms of Pt hillock microelectrodes in a 1M KCl / 100mM ferro-CN solution (Ag/AgCl reference electrode, Pt counter electrode, potential range from 0.1 V to 0.7 V; scan rates of (a) 100mV/s and (b) 50 mV/s). The oxidation current, $I_{oxidation}$, has been measured at 0.6 V (plateau).

	at 100 mV/s	at 100 mV/s	at 50 mV/s	
No. CV	**I_{base} [nA]**	**$I_{oxidation,1}$ [nA]**	**$I_{oxidation,2}$ [nA]**	**r_{real} [μm]**
5	0.4	166	158	6.81
10	1.6	202	194	8.24
20	5.0	270	256	10.90

Table 3.3: Real electrode radius versus the number of electrodeposition cycles. Solution: 1M KCl / 100mM ferro-CN. The initial microelectrode radius was 5 μm.

From the Table 3.3 it can be observed that starting from an electrode geometry of 5 μm in radius, the real electrode radius is doubled with 20 cycles.
As described in chapter 2, the electrode impedance is proportional to the inverse of the electrode area. Previously reported measurements [P. Thiebaud, 1999] showed a decrease of the impedance (at 1.1 KHz) for planar platinum electrodes, 10 μm in diameter, from 0.5 MΩ with a phase angle of -75 degrees to 0.2 MΩ with a phase angle of –67 degrees, by electroplating platinum hillocks (40 μm x 40 μm x 20 μm). Thus, for shorter electrodeposition times, the electrode impedance will be in the expected range.

3.5 Iridium electrodes oxidation

The iridium MEAs have been packaged and interconnected like the platinum devices on a MCS compatible PCB. The electrochemical oxidation of the iridium microelectrodes was realised in a 1M H_2SO_4 solution by cyclic voltammetry between –0.2 V and 1.3 V. A total of 50 cycles at a scan rate of 100 mV/s are typically used.
The cyclic voltammograms for twelve planar electrodes in parallel are shown in Figure 3.14.(a). Similarly, tip shaped iridium electrodes have also been oxidised and their voltammograms are reported in Figure 3-14 (b).
As expected, SEM imaging of the modified microelectrodes does not show a visible changing of the electrode surface. However, the

increase of the area under the IrO_x CV peaks is representative for the increase of the charge storage capacity of the iridium oxide.

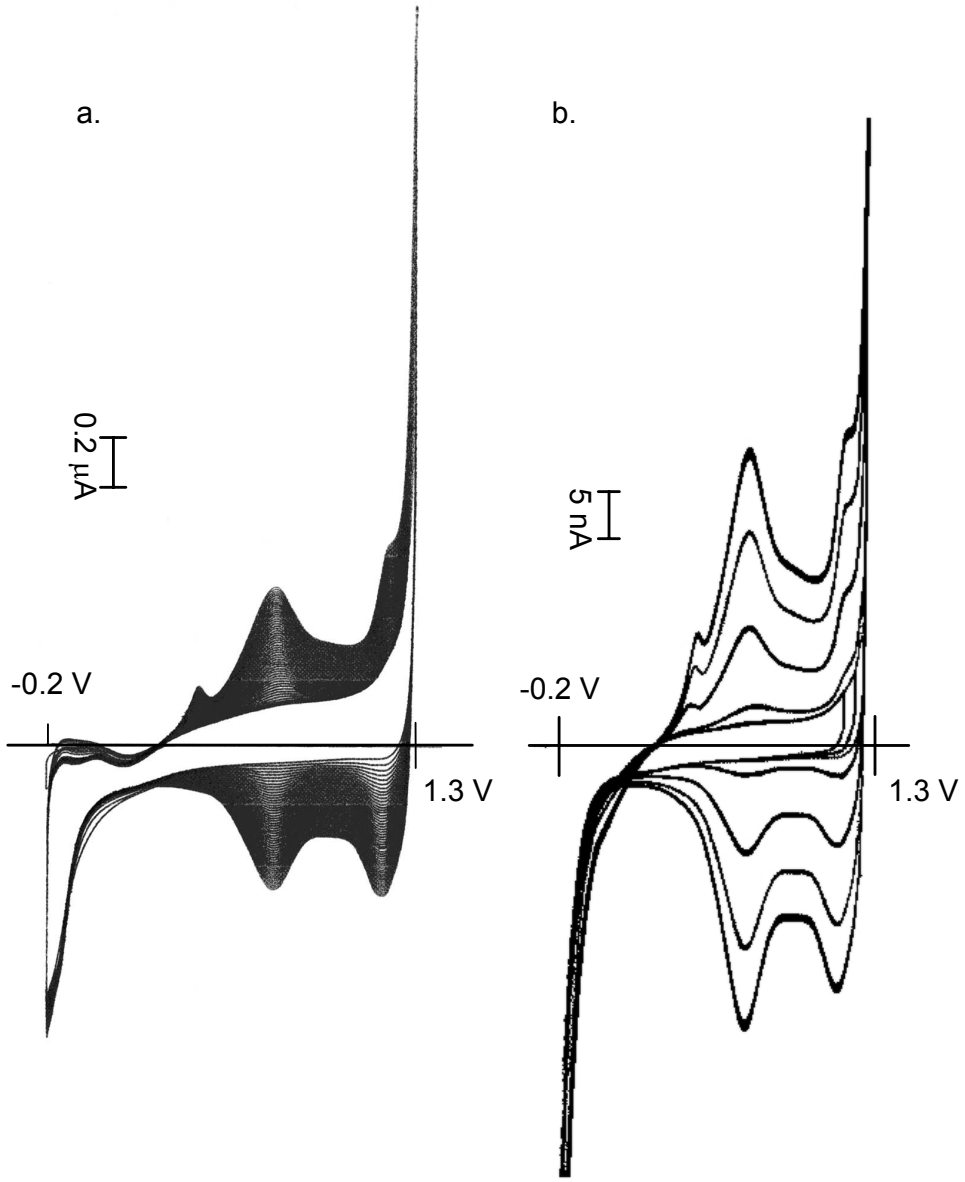

Figure 3.14: Ir oxidation in 1M H_2SO_4 of (a) 12 planar microelectrodes of 10 µm in diameter (25 min.) and (b) 1 tip shaped electrode (3 hours) (–0.2 V and 1.3 V., scan rate of 100 mV/s).

3.6 Scaling down microelectrodes to nanoelectrodes

The electrodes and electrode arrays with dimensions down to the nanometer domain would enable measurements in extremely small environments and nanometer scale investigations. Additionally, a lower electrode separation could be achieved, resulting in a higher resolution monitoring of cellular or sub-cellular physiology.

Electrodes defined by photolithographic techniques show dimensions and separations limited by the lift-off resolution, which is itself limited by the photolithography resolution. Theoretically with a 365 nm wavelength UV light source and considering the light diffraction, a minimal resolution line of 0.6 μm can be calculated. In practice, depending on the photoresist thickness, a line resolution of 0.8 μm (Ma-6 aligner from Karl-Süss) or 1 μm (AL-6 aligner from Electronic Vision) could be possible. However, for lift-off, these minimal line dimensions are increased as function of the metal thickness. For a typical metal layer thickness of 1500 Å, and a 1.8 μm thick photoresist layer, the pattern resolution is ~2 μm. Thus, a higher resolution lift-off can be achieved with a lower light wavelength and a thinner metal layer.

To scale down the electrodes to the nanoscale, the standard technologies based on photolithography have to be adapted, combined and /or substituted with other techniques. Different types of techniques, such as deep-UV, e-beam lithography, focused ion-beam milling, nano-imprint and direct writing by STM can be used for the fabrication of nanoelectrodes. In this context, for investigating the fabrication capabilities, e-beam writing has been used for fabricating nanodisk electrodes and interdigitated electrodes (IDAs) with sub-micrometer dimensions and gaps. The e-beam fabrication of IDAs with gaps ranging from 1 μm to 300 nm has been reported [M. Paeschke, 1995]. In another more recent work, nano-IDAs with electrode widths and spacings ranging from 550 nm down to 250 nm have been realised [P. van Gerwen, 1998, W. Laureyn, 2001]. The latter approach was based on e-beam lithography while the former

combined e-beam lithography, isotropic etching and standard lithography.
In order to render the e-beam technology more convenient i.e. to reduce the e-beam writing time (about 2 minutes for writing 100 x 100 μm^2), our approach combines the e-beam lithography for the realisation of the nano-structures with a standard photolithography used for the patterning of the interconnections. Lift-off has been used for both nano- and micro-scale metal structuring. The realised devices are characterised by AFM, SEM and evaluated by electrochemical techniques. The e-beam writing was performed in collaboration with S. Gautch. The realised devices demonstrate the feasibility of this technology.

3.6.1 Fabrication of nano-interdigitated electrodes (Nano-IDA)

Interdigitated nanoelectrodes were fabricated on a 525 μm thick <100> silicon wafer. A limited e-beam writing time has been achieved by combining e-beam technology for the nanoelectrodes' patterning and standard i-line (365 nm wavelength) photolithography for the interconnections. The nano-IDAs and the alignment marks were designed to fit in the e-beam writing window of 100 x 100 μm^2. Placing step by step each pattern using the x-y positioning table it was possible to process the wafer sequentially.
The fabrication process is shown in Figure 3.15. After wafer cleaning, the bottom passivation layer, 2000 Å of silicon nitride, was deposited by LPCVD. The e-beam photoresist layer, 2000 Å thick PMMA 950k (4%, Anisol) was coated by spinning and pre-baked on a hot-plate for 30 min. at 170°C. The nano-electrodes as well as the wafer alignment marks were written with a Raith200 e-beamer (10kV e-beam, photoresist sensibility of 115 $\mu C/cm^2$). After development of the positive resist (30 s in 1:3 MIBK, IPA), and metal evaporation of a 150 Å thick adhesion layer of Ta and a 350 Å thick layer of Pt, the PMMA lift-off was realised in acetone.

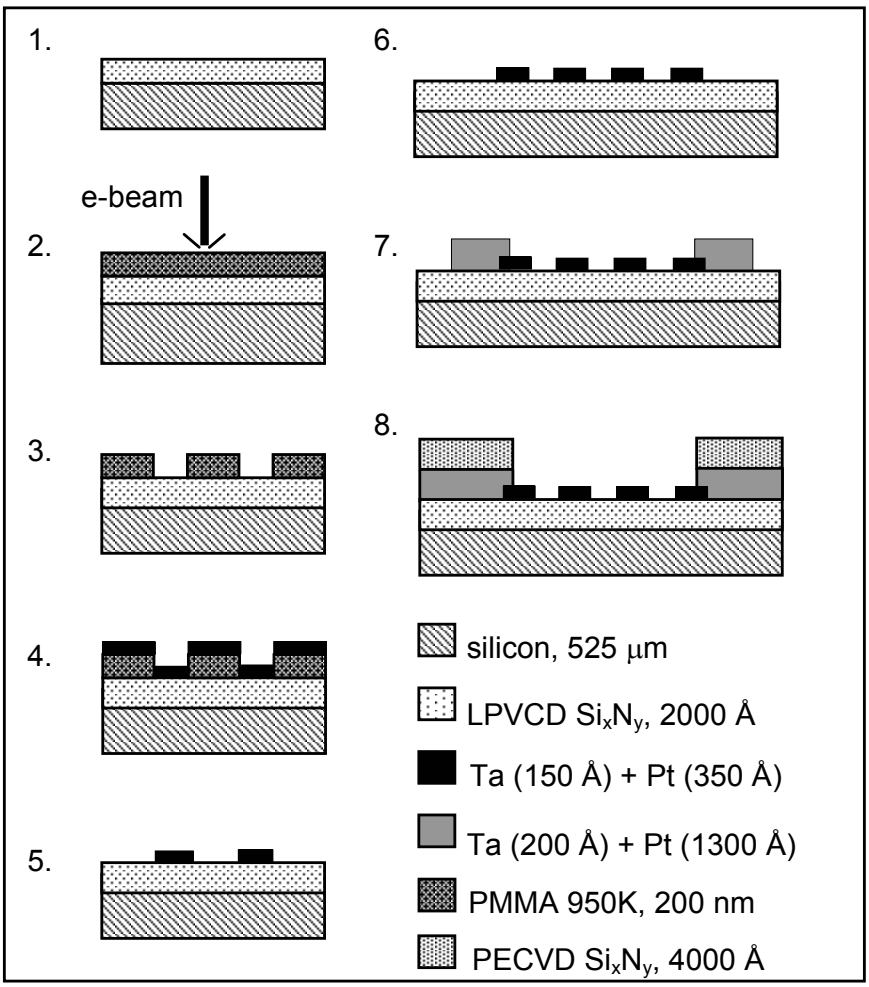

Figure 3.15: Fabrication process of nano-IDA electrodes. 1. Bottom passivation; 2. e-beam writing of the PMMA; 3-5 Development and lift-off of the nano structures; 6-7 conventional lift-off for the contacts; 8. top passivation and opening.

The electrodes interconnections, 200 Å tantalum and 1300 Å platinum were patterned by i-line (365 nm) photolithography with a second lift-off process (AZ1518 photoresist, 1.8 μm thick).
Finally, the top passivation layer consisting of 4000 Å silicon nitride was deposited by PECVD and etched by a SF_6/O_2 RIE plasma, opening the contact pads and the active area on the nano-interdigitated electrodes.
The resulting nano-interdigitated electrodes have an active area of 76 x 100 μm^2, an electrode pitch of 785 nm and a gap of 261 nm. By over-exposing the PMMA it is possible to reduce the electrode gap.

Structures with a pitch down to 100 nm are possible with this technology (Figure 3.16).

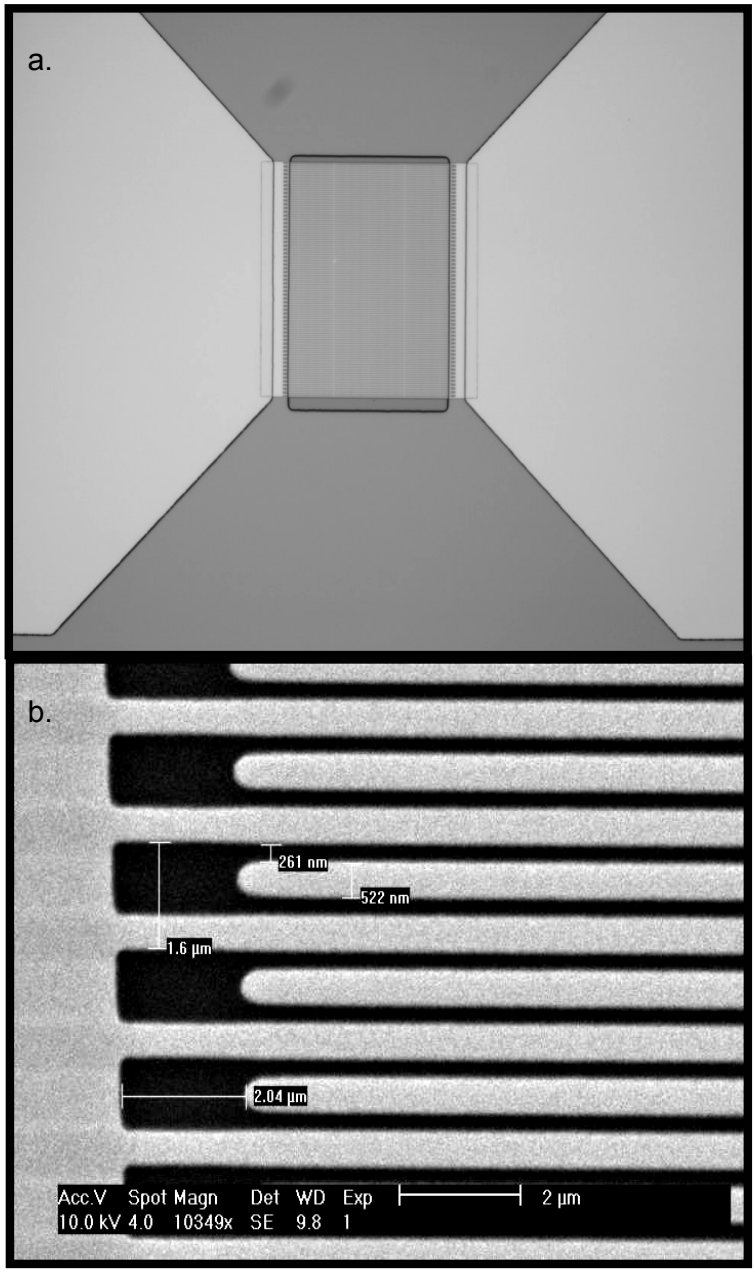

Figure 3.16: (a) Optical view of the fabricated nano-IDA, (b) SEM image (line width 522 nm, separation 261 nm).

3.6.2 Fabrication of nano-discs

Nanodisk electrodes were fabricated on 525 μm thick silicon wafers (Figure 3.17). After cleaning the wafers (see 3.2.1), a bottom passivation layer of 2000 Å thick silicon nitride was deposited by LPCVD. The metal lines, 200 Å of tantalum and 1300 Å of platinum, were patterned by lift-off with one layer photolithography (AZ1518 photoresist from Shipley, 1.8 μm thick). The same device has also been realised by evaporating 200 Å of tantalum and 1000 Å of iridium. After lift-off in acetone and cleaning in piranha, 2000 Å of silicon nitride were deposited by LPCVD as top insulation layer. The nano-electrodes were patterned by e-beam (Raith200 e-beamer, 10kV e-beam) using a photoresist layer of 200 nm thick PMMA 950k (4%, Anisol), which was pre-baked on hot-plate for 30 min. at 170°C.

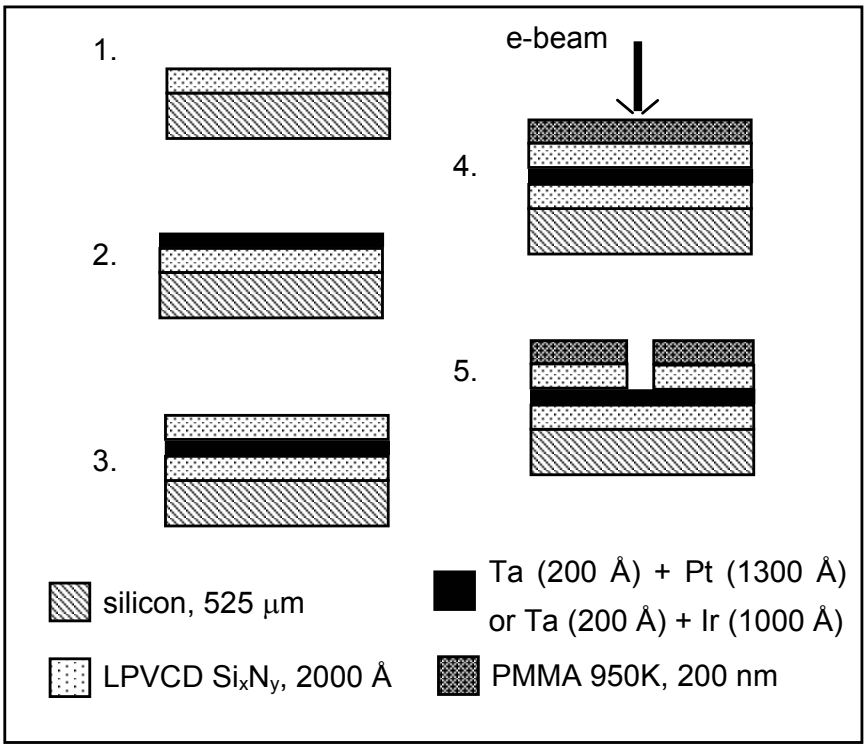

Figure 3.17: Fabrication process for nano-disks electrodes. 1. Bottom passivation; 2. conventional lift-off of the metal (Ir or Pt); 3. top passivation; 4. e-beam writing of the PMMA; 5. plasma etching and opening of the nano-disks.

A plasma etching (SF_6/O_2 RIE plasma) was used to open the nano-electrodes through the silicon nitride layer. The contact pads were patterned by standard photolithography (AZ1518 photoresist, 1.8 μm thick) and the top insulation layer was etched in SF_6/O_2 RIE plasma. Modifying the e-beam exposition dose, nanoelectrode diameters between 200 nm and 400 nm were obtained after plasma etching of the top insulation layer. The electrode dimensions were measured by AFM imaging (Figure 3.18).

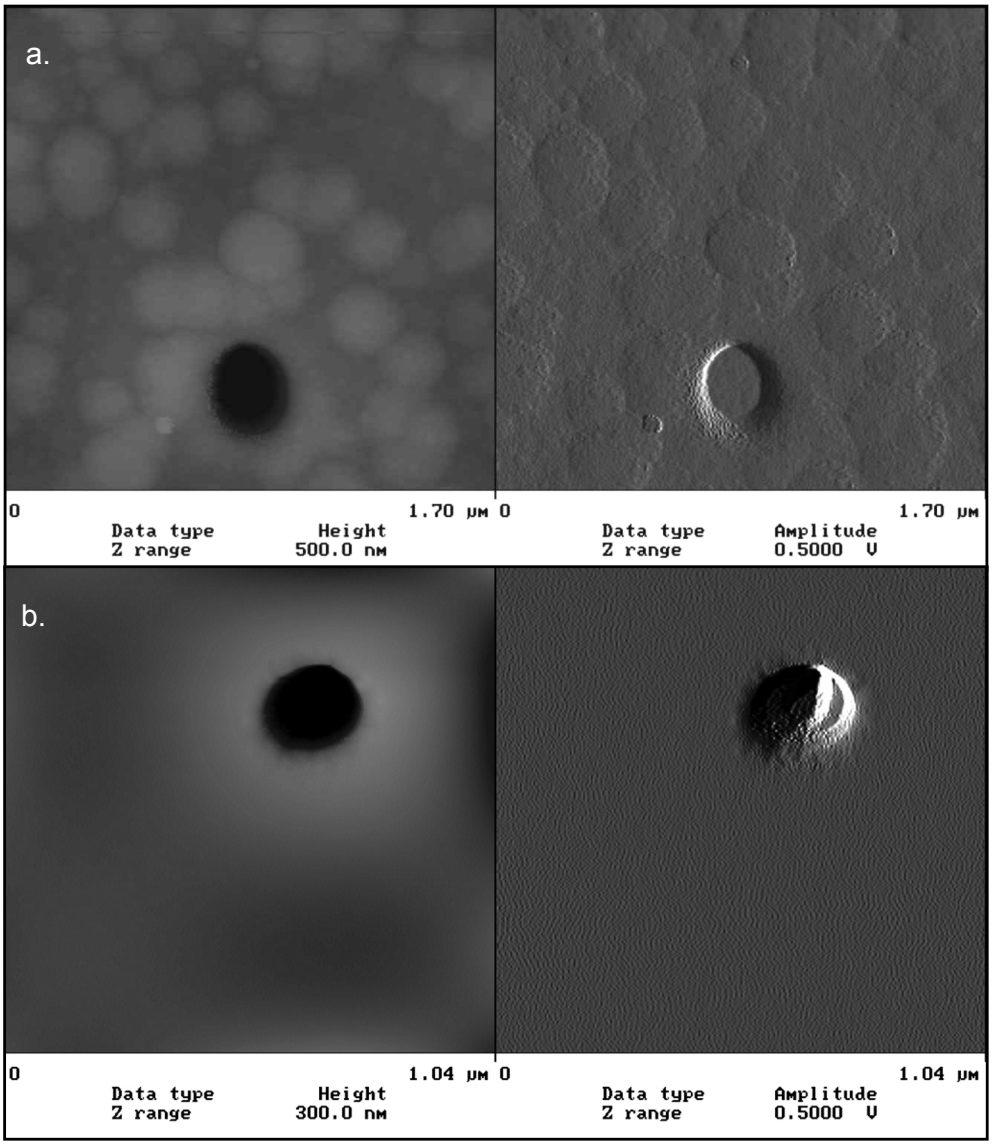

Figure 3.18: AFM image of (a) an Ir nano-disk electrode (diameter 281 nm) and (b) a Pt nano-disk electrode (diameter 252 nm). (left: topology; right: error image)

3.6.3 Electrochemical behaviour of nano-disks and nano-IDAs

A preliminary characterisation of the electrochemical behaviour of the realised nano-structures was performed. Due to the limited number of tests, these results should be taken with precautions.

Nano-disk electrodes were evaluated by cyclic voltammetry in a KCl 1M / 100mM ferrocyanide solution (Ag/AgCl reference electrode, Pt counter electrode) by scanning the potential between 0 V and 0.9 V at different scan rates. The resulting voltammograms (Figure 3.19) show the independence of the diffusion limited current towards the scan rate, representative of the micro-, or in this case, nano-electrode behaviour.

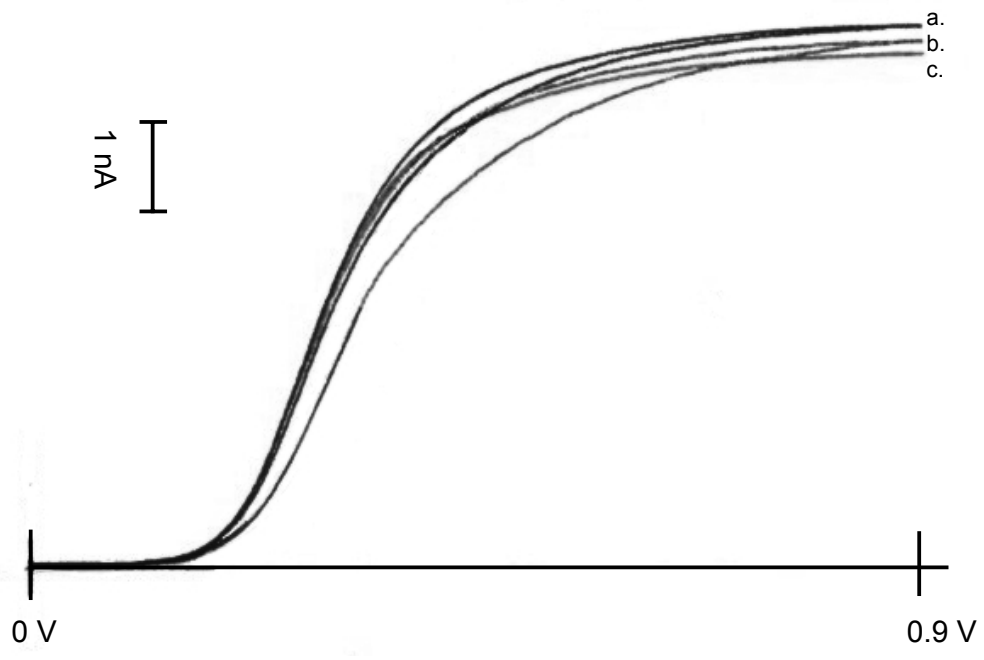

Figure 3.19: Nano-disk voltammograms in KCl 1M / 100mM ferro-CN. (a) 100 mV/s, (b) 25 mV/s, (c) 5 mV/s. (Ag/AgCl reference electrode, Pt counter electrode, 0 V to 0.9 V).

After background current correction a steady-state diffusion limited current I_{dl} between 5 nA to 6 nA has been measured. Based on the diffusion limited current it is possible to calculate the real radius of the recessed electrodes using the following equation [J. Bard, 2001]:

$$I_{dL} = 4nFDCr \frac{1}{\frac{4h}{\pi r} + 1} \tag{3.2}$$

where *n* is the number of exchanged electrons (n = 1), *F* the Faraday constant (96484.6 C.mol^{-1}), *D* the diffusion coefficient (D = 6.30 10^{-6} cm^{2}s^{-1}), *C* the concentration (C = 100 mmol.cm^{-3}), r the real electrode radius and h the passivation layer thickness (h = 2.10^{-5} cm).

Nanoelectrode diameters of 0.71 μm and 0.81 μm have been calculated for I_{dl} = 5 nA and I_{dl} = 6 nA respectively.
According to equation 3.2 the recessed geometry has a higher influence on the diffusion limited current for nanoelectrodes than for microelectrodes (Figure 3.20). In fact, calculating the diffusion limited current as a function of the electrode diameter and using different insulator thicknesses (h = 2000 Å and h = 0 Å) it can be observed (Figure 3.20) that the percentage ratio $I_{dl,h=2000Å}$ / $I_{dl,h=0Å}$ rises from 90% for an electrode diameter of 5 μm to 66.6% for a diameter of 1 μm and to 44% for a diameter of 0.4 μm. Thus, when the electrode diameter approaches the thickness of the passivation layer, the theory predicts that the diffusion limited current decreases, meaning that the influence of the recessed geometry is more important. However, the measurements on nanoelectrodes show a higher I_{dl} then the theoretical one, which results in a calculated electrode diameter about 2 times larger than the one measured by AFM. Certainly more measurements have to be done to confirm this observation, especially ensuring the absence of pinholes in the passivation layer.

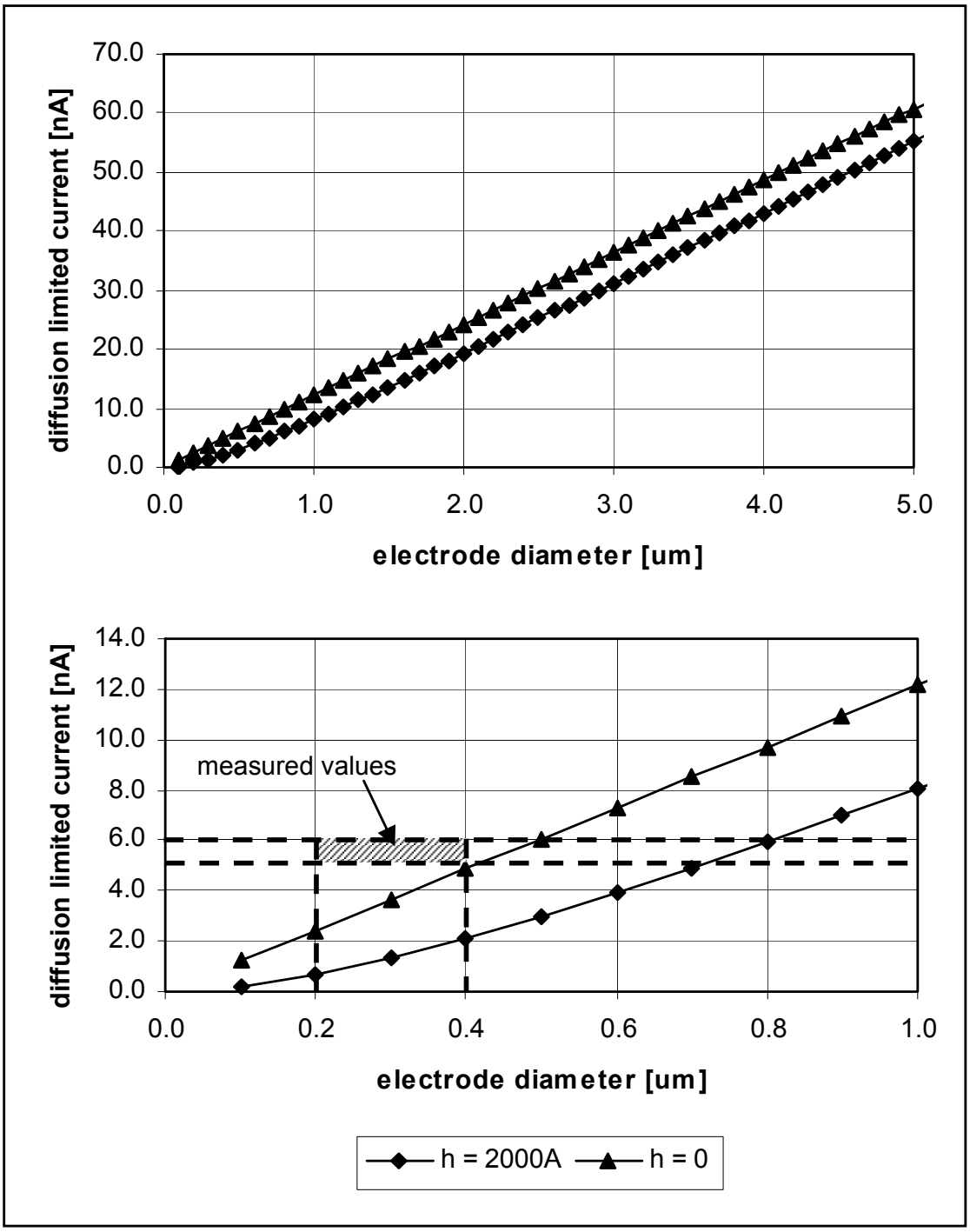

Figure 3.20: Calculated I_{dl} versus the microelectrode diameter and passivation thicknesses of 0 and 2000 Å. For diameters lower than 1 μm the diffusion current is mainly limited by the passivation thickness. The measured values are reported considering the determined diameter (AFM) and the experimental I_{dl}. These values are higher than the theoretical ones.

Nano-IDAs were characterised by measuring the collection efficiency [Bard, 2001], using ferrocyanide as the benchmark species. Applying a potential to one electrode and scanning the potential of the second one, a collection efficiency of 99 % has been found (Figure 3.21). As expected by previous results on micro-IDAs [J-C. Fiaccabrino, 1996] the collection efficiency is increased by reducing the gap between the IDAs.

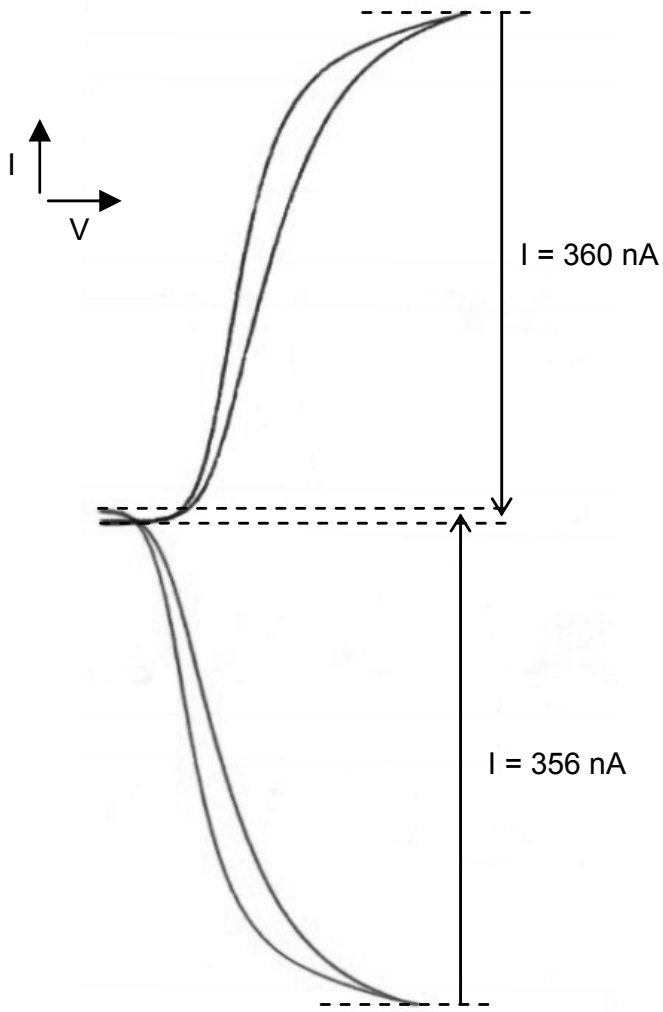

Figure 3.21: Nano-IDA (pitch 785 nm, gap of 250 nm) collection efficiency measurement in 1M KCl / 100 mM ferro-CN (Ag/AgCl reference electrode, Pt counter electrode, 0 V to 0.9 V, 25 mV/s).

Further reducing of the separation gap was possible by the electroplating of platinum on the electrodes, following the same method reported in 3.4. Figure 3.22 shows the electrodeposited platinum on one electrode. Controlling the lateral growth it would be in principle possible to reduce the gap to a few nanometers.

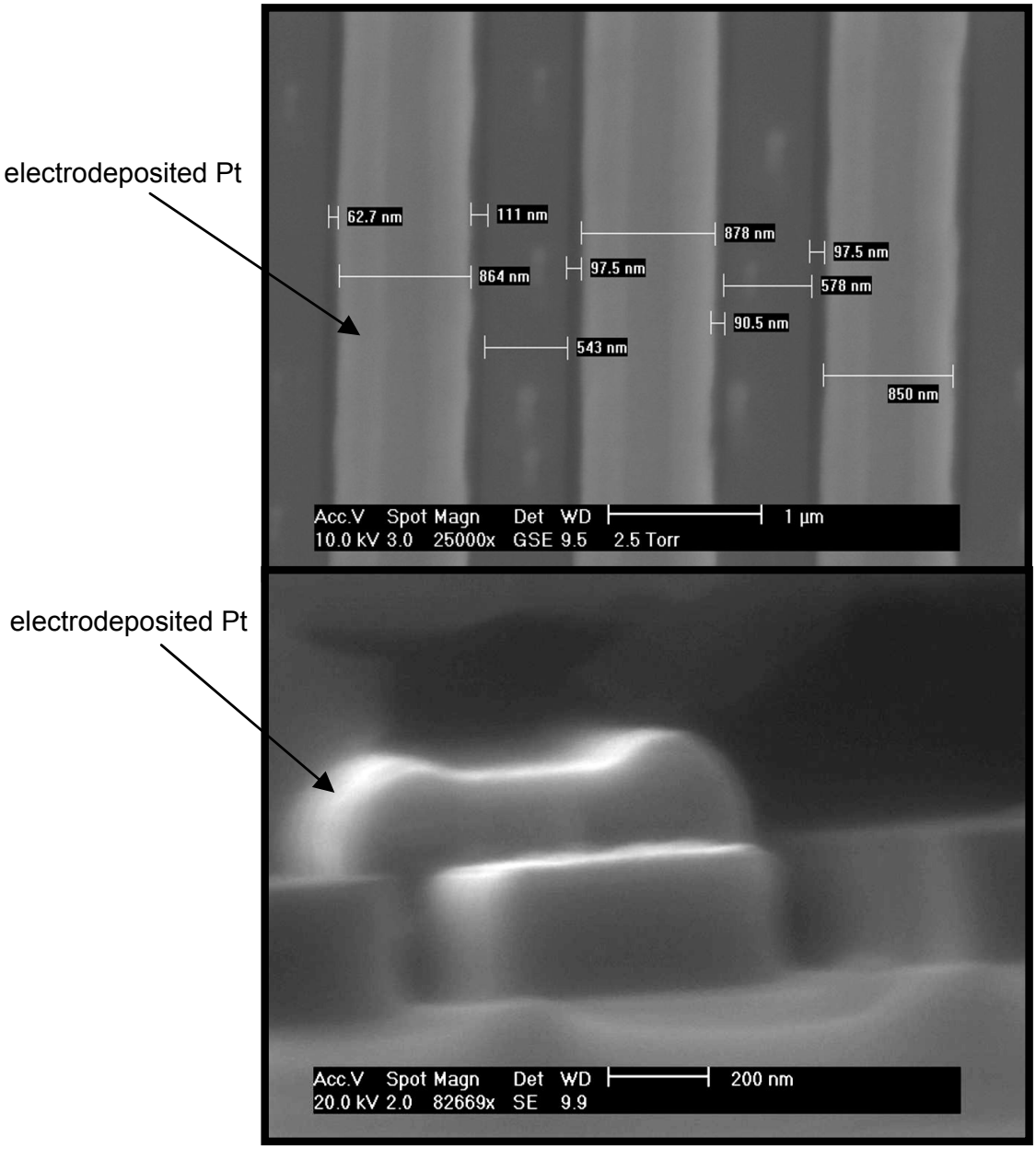

Figure 3.22: Nano-IDA with Pt electrodeposited electrodes. This technique allows the reduction of the nanoelectrode gaps.

3.7 Bibliography

Bard, J. and L.R. Faulkner, *Electrochemical Methods, Fundamentals and Applications*. 2nd. ed. 2001, New York: Wiley.

Fiaccabrino, G.-C., *Thin-film microelectrode arrays: materials & design*, *Inst. of Microtechnology*. 1996, University of Neuchâtel: Neuchâtel.

Laureyn, P., et al., *Characterisation of nanoscale interdigitated palladium electrodes of various dimensions in KCl solutions.* Electroanalysis, 2001, **13**(3): p. 204-211.

Roth, S., et al., *High aspect ratio UV photolithography for electroplated structures*, J. Micromechanical Microeng., 1999, **9**: p. 105-108.

Paeschke, M., et al., *Properties of Interdigital Electrode Arrays with Different Geometries.* Analytica Chimica Acta, 1995. **305**(1-3): p. 126-136.

Thiébaud, P., *Fabrication of microelectrode arrays for electrophysiological monitoring of hippocampal organotypic slice cultures by interface*, in *Inst. of Microtechnology*. 1999, University of Neuchâtel: Neuchâtel.

Van Gerwen, P., et al., *Nanoscaled interdigitated electrode arrays for biochemical sensors.* Sensors & Actuators B, 1998, **49**: p. 73-80.

4 AN APPROACH TO HIGH-DENSITY MICROELECTRODE ARRAYS

4.1 Introduction

In chapter three the technologies for fabricating planar or three dimensional microelectrode arrays have been presented and electrodes with dimensions down to the nanometre scale have been fabricated. In parallel to further improving the recording / stimulation performances of the substrate integrated MEAs, i.e reduction of the electrode impedance, increase of the injection charge, another emerging research topic is the development of high density microelectrode arrays on large active areas. The final aim would be to obtain at least one electrode close to each neuron, meaning an inter-electrode separation comparable to the cellular dimensions.

The motivations are:

1. the random positioning of the neurons on the MEAs reduces today the number of effective electrode-neuron couplings. The increasing interest in studying the network activity and its plasticity would benefit from the increase of the array spatial resolution.
2. the neurons cultured on MEAs are not fixed on the microelectrodes and can move. This impedes the long time monitoring from the same neurons.
3. today, MEAs with a particular geometric layout of the microelectrodes are developed specific to the experiments. A high density MEA would be a universal tool for a variety of experiments.

This list is certainly not exhaustive, but only representative of the biological problems encountered with current MEAs technology. The question is if it would be possible to fabricate higher density electrode arrays on large active areas with the current technology.

Several reasons justify the need of investigating another approach:

1. at the chip level, the individual wiring of each electrode to a pad by patterning metal leads, limits the electrode density, the active area, and thus the spatial resolution. In fact, leads connecting the centre array's electrodes have to pass between the external electrodes. For an electrode array of x columns and y lines, x * y leads are necessary as well as x * y pads, resulting in a totally inadequate technology for thousands, densely packed, electrodes.
2. externally, an amplification and filtering circuit for each electrode is needed in order to achieve a high temporal resolution and synchronous signal recordings. This is not adapted for thousands, densely integrated, microelectrodes.

Different alternative approaches dealing with the problem of addressing a large number of closely spaced electrodes, have been developed and reviewed in chapter 1, i.e. LAPS, FAPS, MAPS.
In this work, in collaboration with the CSEM, an approach based on the solid-state active pixel sensor (APS) technology has been investigated. The APS technology was developed for image sensors and is produced by the commercially available complementary metal-oxide-semiconductor (CMOS) process [Willemin, 2001; Seitz, 1995]. This allows the on-chip integration of photo-detector array elements, on-pixel amplifiers, timing and control circuits, high-speed analogue signal chain circuits and multiplexers as well as analogue-to-digital converters (ADC).
The aim is to design and evaluate a first prototype of high density array, integrating a local pre-amplifier behind each electrode and replacing the on-pixel photosensitive elements of conventional APS

with metallic microelectrodes. The in-pixel integration of an amplifier circuit would allow to locally pre-amplify the signal and prevent the signal degradation from extrinsic noise sources, i.e. electromagnetic interferences, acting on leads as for traditional MEAs.
The choice of focusing on the recording instead of both recording and stimulation features is motivated by the need of evaluating this technology and the feasibility of the approach. Thus a flexible (in terms of working modes) circuit has been investigated.

4.2 In-pixel pre-amplifier

The choice and the design of the in-pixel pre-amplifying circuit has to take into account:

1. a typical electrophysiological signal range between 20 μV_{p-p} and 200 μV_{p-p} (for vertebrate neurons) and a maximal signal bandwidth between a few Hz and 4 kHz.
2. the electrode impedance, which has to be compensated by the input impedance of the amplifier in order to avoid signal reduction by the resulting voltage divider circuit.
3. the place needed for the integration of the circuit in order to be included in a pixel with dimensions corresponding to the neuronal ones.

The first design has been realized in 0.5 μm CMOS technology with pixel dimensions of 40 μm x 40 μm, and targeting a gain of 100 times. The design and the choices of the pre-amplifier circuit satisfying these constraints are described in next paragraphs. These aspects have been developed during a diploma work [T. Overstolz, 2000] at the Image Sensing Section of the CSEM (CSEM SA, Zürich, Switzerland).

4.2.1 Choice of the pre-amplifier circuit

Given by the small pixel dimensions, a simple, low number of transistors pre-amplifier circuit is investigated. Two single stage amplifier circuits, i.e. the inverter and the differential amplifier, could be integrated. The inverter amplifier (Figure 4.1) is a simple circuit acting as amplifier in the linear region where both transistors T1 and T2 are saturated.

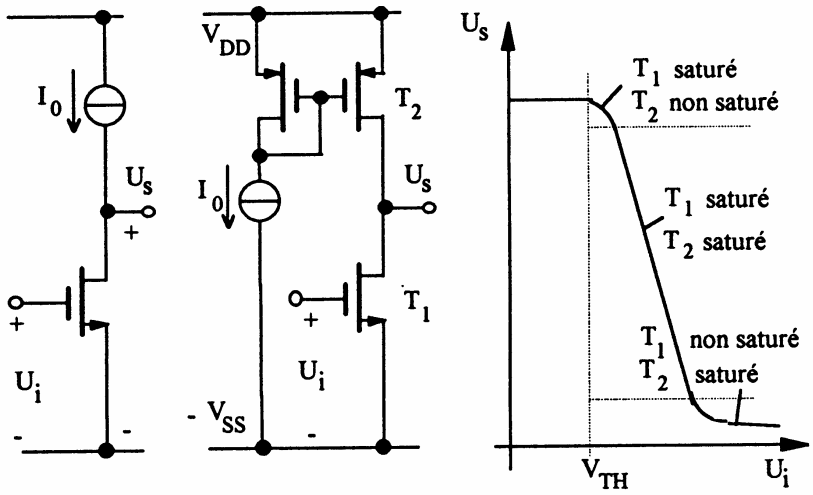

Figure 4.1: The inverter acts as an amplifier in the linear region (T_1, T2 saturated). It is realised with a single MOS transistor and a current source.

Notwithstanding its simplicity, high gain, low slew rate distortion and low noise (low number of transistors needed), this circuit suffers a major drawback due to its extreme sensitivity to bias voltage variations. Its integration would introduce different ideal biasing voltages for each pixel due to variations in the threshold voltages and variations in the physical geometries between each pixel.

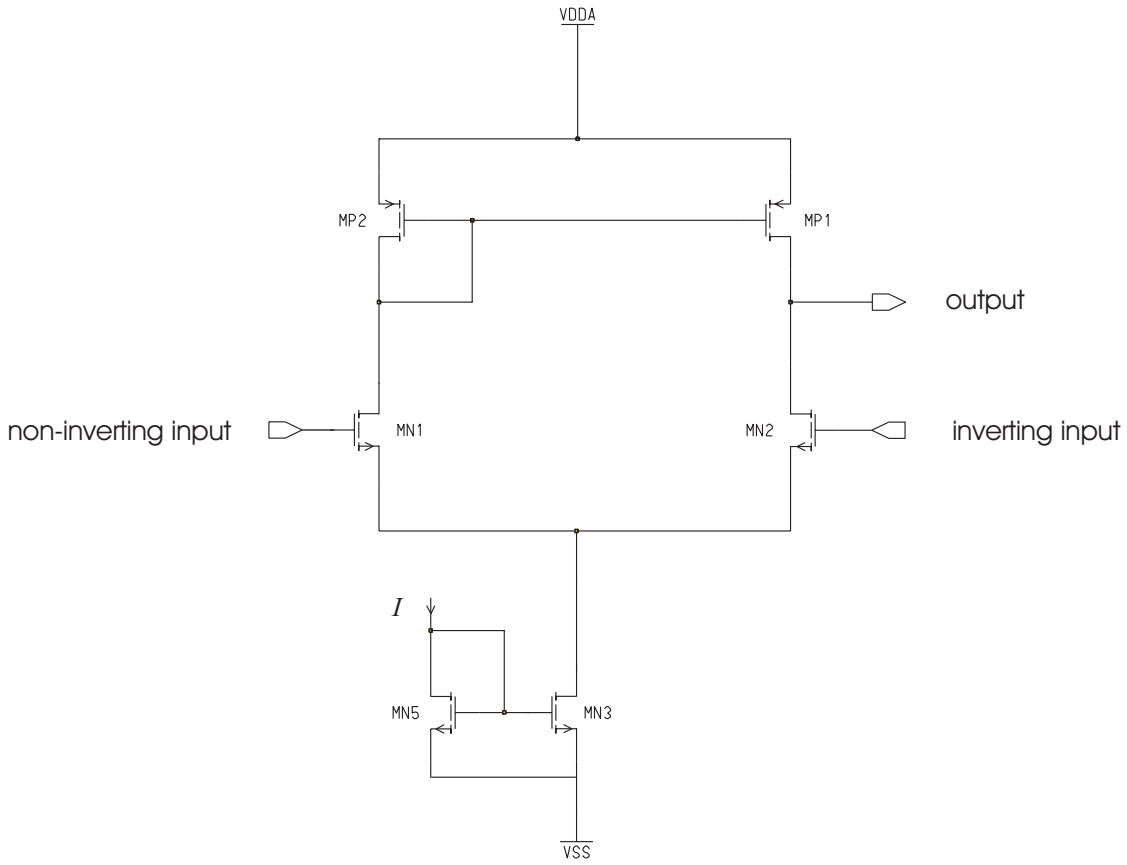

Figure 4.2: The 5 transistors operational transconductance amplifier (OTA). This differential amplifier (AC + DC) is constituted by the n-MOS transistors MN1 and MN2. The p-MOS transistors MP1 and MP2 and the n-MOS transistors MN3 and MN5 form two current mirrors.

Alternatively, a differential amplifier, the 5 transistor operational transconductance amplifier (OTA) (Figure 4.2), has been investigated. This is a widely used stage in analogue circuits where it is integrated as input stage for operational amplifiers (OP). It amplifies both continuous (DC) and alternating (AC) signals applied on the differential pair, constituted by the n-MOS transistors MN1 and MN2. The p-MOS transistors MP1 and MP2 and the n-MOS transistors MN3 and MN5 form two current mirrors.
This circuit shows a high gain and better stability to bias voltage when operated in common-mode, and was a preferable choice for this first design.

4.2.2 Design considerations of the 5 transistors OTA

The 5 transistors OTA could be integrated in the inverting (Figure 4.3 a.) and non-inverting (Figure 4.3 b.) configurations. However, both configurations require the integration of high value resistors in order to increase the gain, which in CMOS technology is difficult and surface consuming.

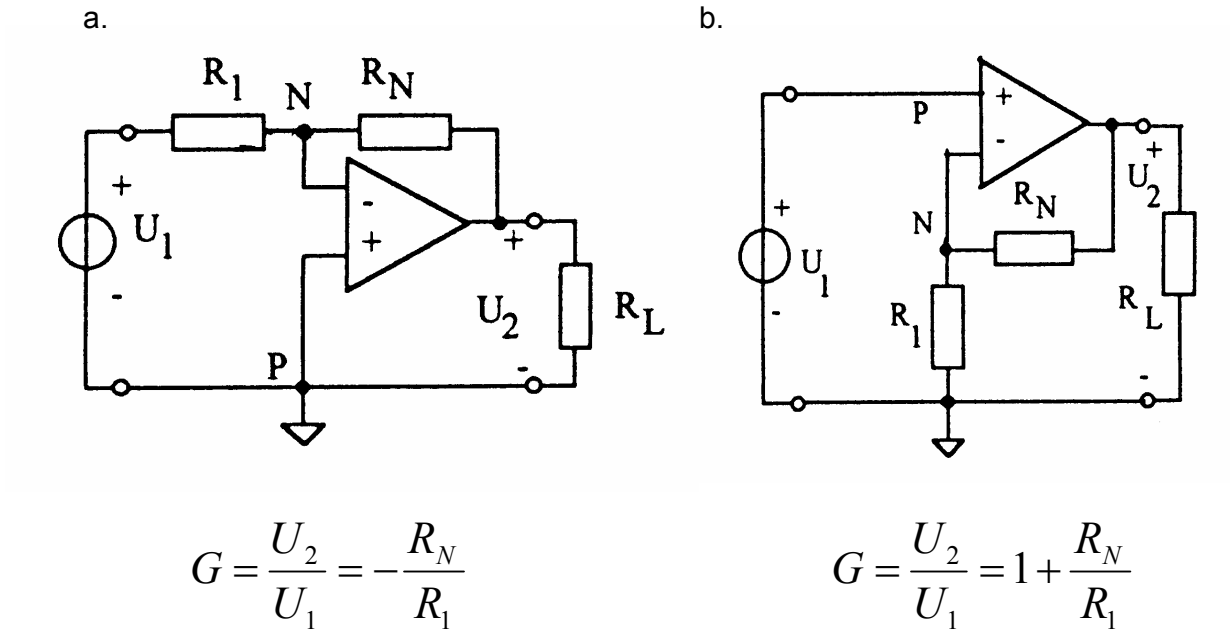

$$G = \frac{U_2}{U_1} = -\frac{R_N}{R_1} \qquad G = \frac{U_2}{U_1} = 1 + \frac{R_N}{R_1}$$

Figure 4.3: The (a) inverting and (b) non-inverting close-loop configurations. The gains (G) are defined by the resistors ratio.

An alternative is to take advantage of the high open-loop gain, which can be defined with the width and length of the input transistors (MN1 and MN2 of Figure 4.2).

Analytically, considering the model of strong inversion of a MOS transistor, it can be found that (Annexe I):

- the gain increases by the square root of the width of the input transistors (MN1,2).
- the gain increases when the transistors in the current mirror (MP1,2) are longer compared to the length of the transistors in the differential pair (MN1,2).
- the gain increases by the square root of decreasing drain-source current.

Simulations of the input transistor dimensions toward gain and drain-source current have been carried out in order to achieve a higher gain and a lower noise. The noise has been simulated considering thermal noise, shot noise and flicker noise (1/f noise) contributions, calculating the referred input noise as the sum of the noise sources referred to the transistors input (Annexe II). The noise has been reduced by design optimisation considering that the transistors of the differential pair must be wide to increase their transconductances whereas the transistors in the current mirror must be long to decrease their transconductances. The final dimensions and simulation results are reported later in paragraph 4.3.2.

4.2.3 Integrated pre-amplifier circuit

In open-loop, connecting one input of the 5 transistors OTA to a microelectrode and the second input to a reference electrode, the differential amplifier is sensitive to DC-offsets on the input pair. There is thus the risk of saturating the amplifier. Therefore, an additional (optional) unity-gain, feedback mode, has been included. In this configuration the offsets are compensated by the feedback itself. The final integrated pre-amplifier circuit is shown in Figure 4.4. The OP amplifier in the schematics is constituted by the previously described 5 transistors OTA.

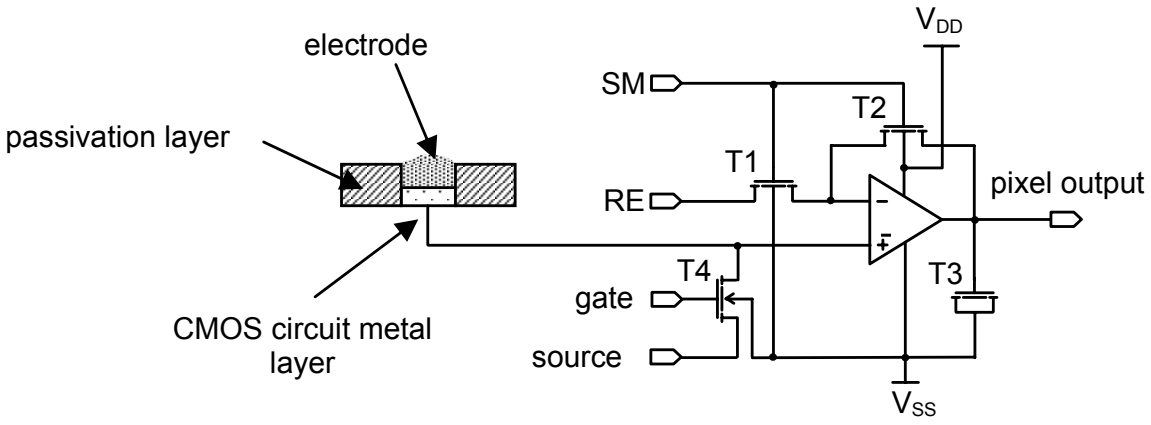

Figure 4.4: Final integrated in-pixel circuit. The non-inverting input is directly connected to the electrode; the inverting input is connected to a reference electrode in open-loop. T_1 and T_2 act as voltage controlled switches allowing the selection of the feed-back unity gain mode. Transistor T_4 can be used as voltage controlled resistor for current measurements; transistor T_3 acts a output capacitor.

The non-inverting input is directly connected to the electrode, while the reference electrode (RE), common to all electrodes, is externally connected to the inverting one. Transistors T_1 (n-MOS) and T_2 (p-MOS) functions as voltage controlled resistors. Applying V_{SS} or V_{DD} on their gates (SM), it is possible to select, respectively, the close-loop ($T_1 \rightarrow \infty$ and $T_2 \rightarrow 0$) or the open-loop ($T_1 \rightarrow 0$ and $T_2 \rightarrow \infty$) amplification. The open-loop gain is programmable and is controlled by the DC polarisation on both inputs. The close-loop (feedback) mode has a gain of one and acts as an impedance transformer having a high input impedance and a low output one.
Transistor T_3 is a MOS output capacitance characterised by a 10 x 10 μm^2 gate surface and values 400 fF, allowing to lower the signal bandwidth. Additionally, for current instead of voltage measurements, transistor T_4 can act as a resistor by controlling its gate voltage and connecting its source to the ground.

4.3 Specifications of the CMOS chip

The first prototype (using ALCATEL 0.5 μm standard technology) integrates 64 x 64 pixels, on a surface of 2.56 x 2.56 mm^2. Each pixel, Figure 4.5, has a dimension of 40 x 40 μm^2, a microelectrode of 20 x 20 μm^2 and a pre-amplifier. This results in an electrode separation of 20 μm (40 μm centre to centre). The addressing logic was previously developed at the CSEM for high-speed digital cameras and is constituted by a row decoder and a column decoder. It is integrated on the sides of the chip as described in the block diagram of Figure 4.6. By digital addressing (6 bits for the rows and 6 bits for the columns) it allows to randomly select each pixel individually and output the recorded signal to the single chip output, enabling the sequential read-out at high sampling rate (maximal frame rate reading one pixel of 10 MHz). It is thus possible to image the electrophysiological activity from the whole active area or from limited regions of the network.

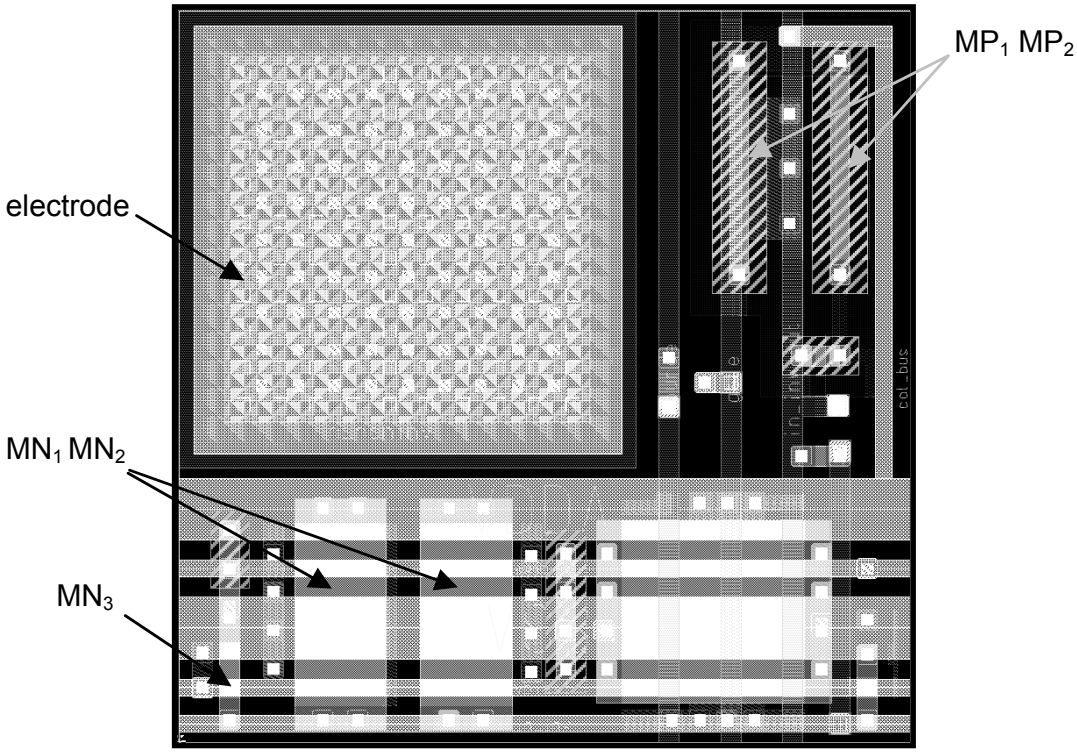

Figure 4.5: Pixel layout. Dimensions 40 x 40 μm, electrode 20 x 20 μm. The amplifier circuit is integrated on the side of the electrode.

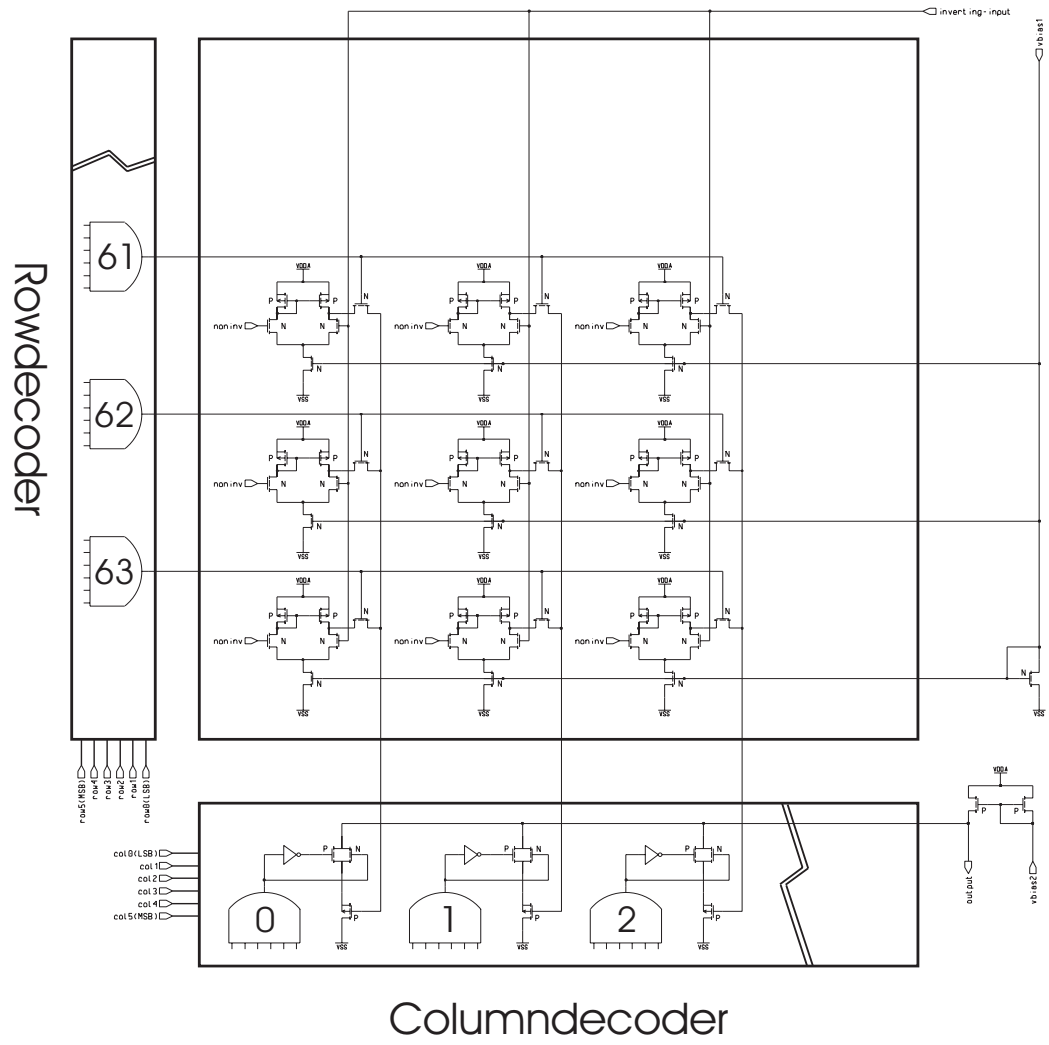

Figure 4.6: Block-diagram showing 6 pixels and the row / column decoders on the sides. The addressed pixel output the electrode signal on the column bus, and the column decoder on the chip output.

4.3.1 Simulated results

In order to optimise the circuit design, simulations with Accusim (simulation package of Mentor Graphics) have been performed modifying the channels length and width of transistors MN1,2 (input transistors), MP1,2 (current mirror in the differential pair) and MN3,4 (current mirror for the biasing). The dc-gain, the bandwidth and the referred input noise have been simulated towards transistors

geometries (Annexe III). The final dimensions and characteristics are summarised in Table 4.1.

MN1,2	width [μm]	5
	length [μm]	10
MP1,2	width [μm]	1
	length [μm]	10
MN3,4	width [μm]	1.1
	length [μm]	3
Gain*	[db]	40.6
Bandwidth*	[kHz]	39.8
Noise	[μV] rms	79.6

Table 4.1: The final transistors dimensions and amplifier characteristics after circuit optimisation by simulations. (*) Values calculated for a DC polarisation of 1.5 V.

Once the geometries fixed, the open-loop gain and the DC-bandwidth have been simulated for bias voltages (on the input signal) between 1.4 V and 1.6 V. Gains from 23 dB up to 50 dB with frequency bandwidth of 270 kHz to 14 kHz respectively are obtained (Figure 4.7). This allows the programming of the gain and the filtering of the pre-amplifier by modifying the DC component on the input pair. The simulated amplifier referred input noise results in 79.6 μV rms. The resulting noise is still rather high for the measurement of neuronal signals. However, the achieved performances should allow the circuit evaluation and preliminary biological tests with cardiomyocytes, where the electrophysiological signals are much higher (up to 1 mV_{p-p}). These aspects are discussed later in 4.5 and 4.6.

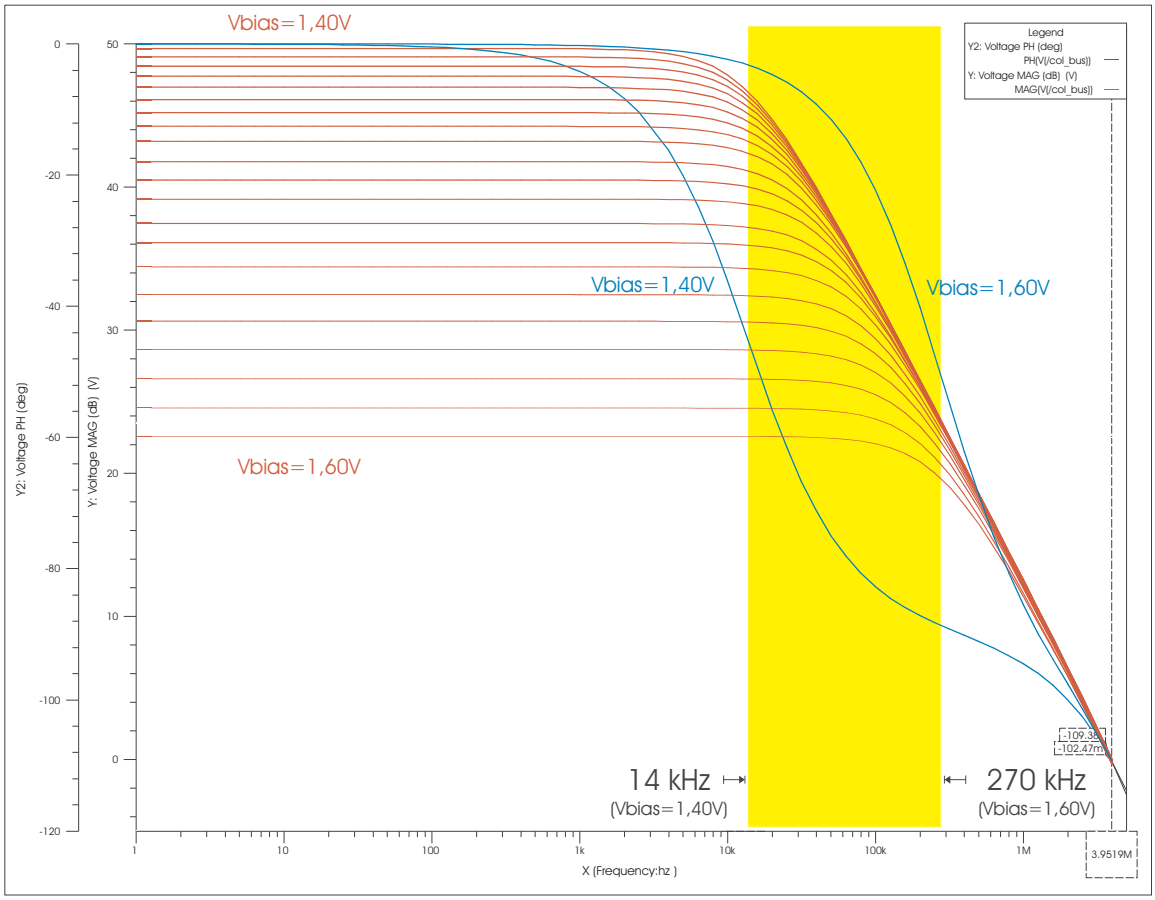

Figure 4.7: Simulated open-loop behaviour. The DC polarisation of the input pair programs different gains and bandwidth.

As discussed in chapter 2, the electrode impedance for the recording is mainly capacitive (increases at low frequencies) and a high input impedance amplifier is thus necessary. In the designed circuit the input impedance is essentially given by the input parasitic capacitance (gate capacitance of the non-inverting input), which results in about 200 fF (C).

The resulting impedance is then given by (f is the frequency):

$$Z_{in} = \frac{1}{2\pi f C} \tag{4.1}$$

At a frequency f = 1.1 kHz, the impedance rises to about 723 MΩ which is much higher than the electrode impedance (lower than 1 MΩ at 1.1 kHz, see chapter 2).

4.3.2 Summary of the chip specifications

The specifications of the realised CMOS chip are reported in Figure 4.8 and in next page.

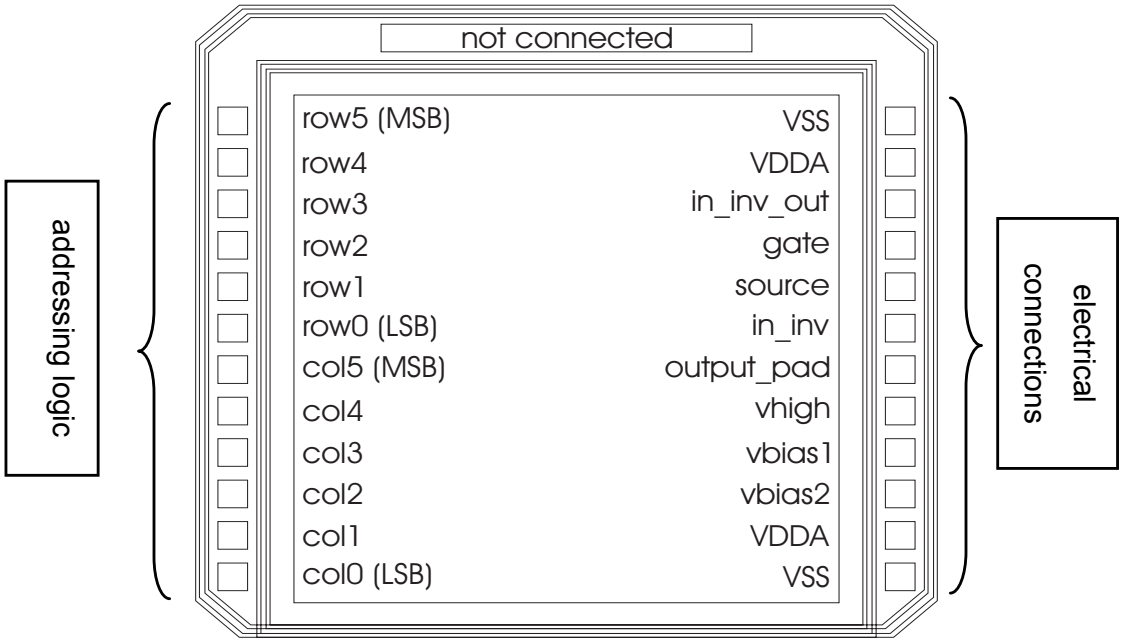

Figure 4.8: Schematics of the CMOS first prototype. The left-side connections constitute the digital pixel addressing. The right-side provides the device powering and the output pixel signal (output_pad).

<u>Chip dimensions</u>

Pixel dimensions:	40 x 40 μm^2
Electrode dimensions:	20 x 20 μm^2
Electrode separation:	20 μm
Pixel number:	64 x 64 (= 4096)
Active area surface:	2.56 x 2.56 mm^2
Total chip dimensions:	3.16 x 3.43 mm^2
Bonding pads	24 with dimensions 100 x 100 μm^2

<u>In pixel pre-amplifier</u>

Referred input noise (simulation)	79 µV
Voltage range (output):	0 – 3.3 V
Open-loop differential amplifier programmable gain:	23 – 50 dB
Bandwidth	270 – 14 kHz
Closed loop (feed-back)	unity gain
Input impedance at 1.1 kHz (calculated)	723 MΩ

<u>On-chip addressing logic</u>

Sampling:	up to 10 MHz
Maximal frame rate at 10 MHz:	2.4 kHz (64x64 pixels)
Frame rate of 25 kHz:	400 randomly selected electrodes
Logic 0:	0 V (10 MΩ – 100 MΩ)
Logic 1:	4.5V
At 25 kHz frame rate:	400 electrodes -> 800 x 800 μm^2

<u>Power connections</u>

Vss:	to ground (0 V)	
VDDA:	+3.3 V	
In_inv_out:	+4.5 V	-> differential amplifier
	0 V	-> feedback unity gain
Gate:	to ground (0 V)	
Source:	to ground (0 V)	
In_inv:	DC bias (reference) with 1.4V – 1.6V DC	
Output_pad:	Addressed pixel output	
Vhigh:	+4.5V	
Vbias1:	connected to a current source of 10 µA	
Vbias2:	connected to a current source ranging between 500 µA –2 mA	

4.4 Gold electroless deposition

The drawback of the commercially available CMOS standard technology is that it uses aluminium alloy layers for electrical contacts. Aluminium and its alloys show unfortunately poor electrochemical stability in physiological media and a poor biocompatibility. For these reasons a post-processing is necessary to deposit a more noble metal on the aluminium electrodes.
Essentially three techniques could be used for this purpose: a photolithographic lift-off post-processing, an electrodeposition or an electroless deposition.
The photolithographic process (using lift-off or wet-etching) is not adapted for prototyping since it needs an alignment to the CMOS chip and should be thus performed in the case of working at the wafer level. In fact, in practice, a first CMOS prototype is typically produced in small series of a few chips. Moreover, it is known that the evaporated gold shows a poor adhesion on aluminium due to the aluminium oxide inter-layer.
The drawback of the electrodeposition is that it requires a direct contact to the electrode in order to polarise the electrode at the deposition potential. This is not the case of the electroless plating, making this technique particularly interesting for this application.
Modifications of aluminium electrodes by electroless have been reported by Pournaghi-Azar and Krasopoulo [Pournaghi-Azar M.H., 1998; Krasopoulo A.V., 1997] describing the electroless deposition of nickel and nickel/gold. In particular Krasopoulos showed a rapid technique to modify an array of integrated microelectrodes for solid-state chemical multisensor chips. Gold shows interesting chemical and electrical properties and plating solutions for Au deposition on Ni, Cu, Au, and Pd substrates are commercially available. Electroless of nickel/gold is also largely described in the literature for solder bumping and wire bonding [Strandjord, 2002; Honma, 2001; Okinaka, 1998; Okinaka 2000].
In this work an original technique is developed for depositing gold directly on aluminium without using inter-layers, on MEAs and on the

integrated CMOS circuit. In our knowledge, no direct gold electroless deposition on aluminium microelectrodes has been previously reported.
Several deposition tests have been carried out on aluminium MEAs in order to obtain a rough and compact layer. Roughness is interesting in order to decrease the electrode impedance and thus the thermal noise of the recording electrodes. Depositions have been characterised by ESEM microscopy, cyclic voltammetry (CV) and x-ray spectroscopy (XPS).

4.4.1 Electroless gold deposition on aluminium MEAs

Microelectrode arrays with aluminium electrodes have been fabricated for testing the electroless gold deposition. The same design as the one described for planar Pt and Ir MEAs in chapter 3 was used. The arrays were fabricated on 4 inches, 525 μm thick silicon wafers insulated at first with a 2000 Å thick layer of silicon nitride deposited by low-pressure chemical vapour deposition (LPCVD). Secondly, the metal leads were patterned photolithographically with a lift-off process, evaporating an adhesion layer of 250 Å of Ta and 1 μm layer of Al. A 4000 Å top insulation layer of silicon nitride was then deposited by plasma enhanced chemical vapour deposition (PECVD). Finally, the electrodes as well as the contact pads were opened by a photolithographic process followed by a SF_6/O_2 dry plasma etching (Figure 4.9).
The electroless gold deposition was performed in two steps using commercially available plating solution. A first gold deposition by displacement is performed by immersion in Atomex solution (Engelhard), diluted in DI water in order to obtain a gold concentration of 3.4 g/L. Then, the electroless gold deposition is realised by immersion in Cathagold solution (Engelhard), which is a gold cyanide solution with pH 13.7 at room temperature.

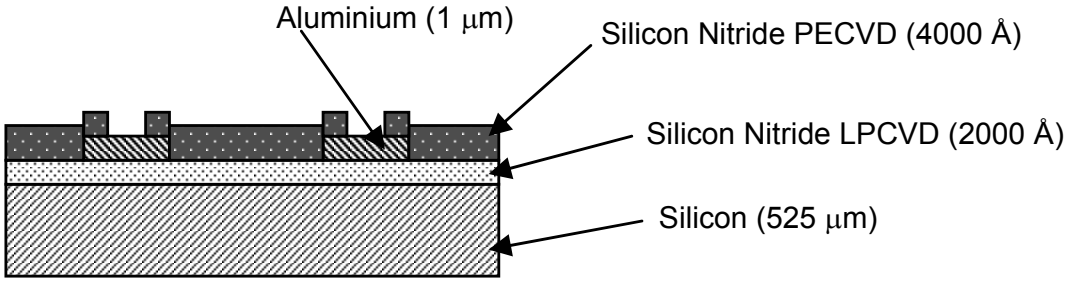

Figure 4.9: Cross-section of the test device for developing the gold electroless deposition.

The solution provider specifies a typical working temperature between 45-75°C for the Atomex solution and of 75°C for the Catagold. Typical deposition rates are about 10^{-2} μm/min. for the first solution and 2 μm/hour for the second one. Treating the chip under those conditions for several hours, no evidence of deposition was observed.

However, reducing the deposition time and the working temperature, a deposition on the aluminium electrode has been achieved. The ESEM picture (Figure 4.10) shows the deposition on a pseudo-reference and on two microelectrodes after 16 hours in Atomex solution at 57°C followed by 5 min. in Catagold at the same temperature.

A single microelectrode image is shown in Figure 4.11(a). The resulting dendritic deposition has a maximal height of about 20 μm, meaning an estimated deposition rate of 4 μm/min. This means a deposition rate 120 times higher than that specified by the solution provider.

This first result motivated the test of different depositions times and temperatures in order to slow down the deposition rate and achieve a compact and rough electrode surface.

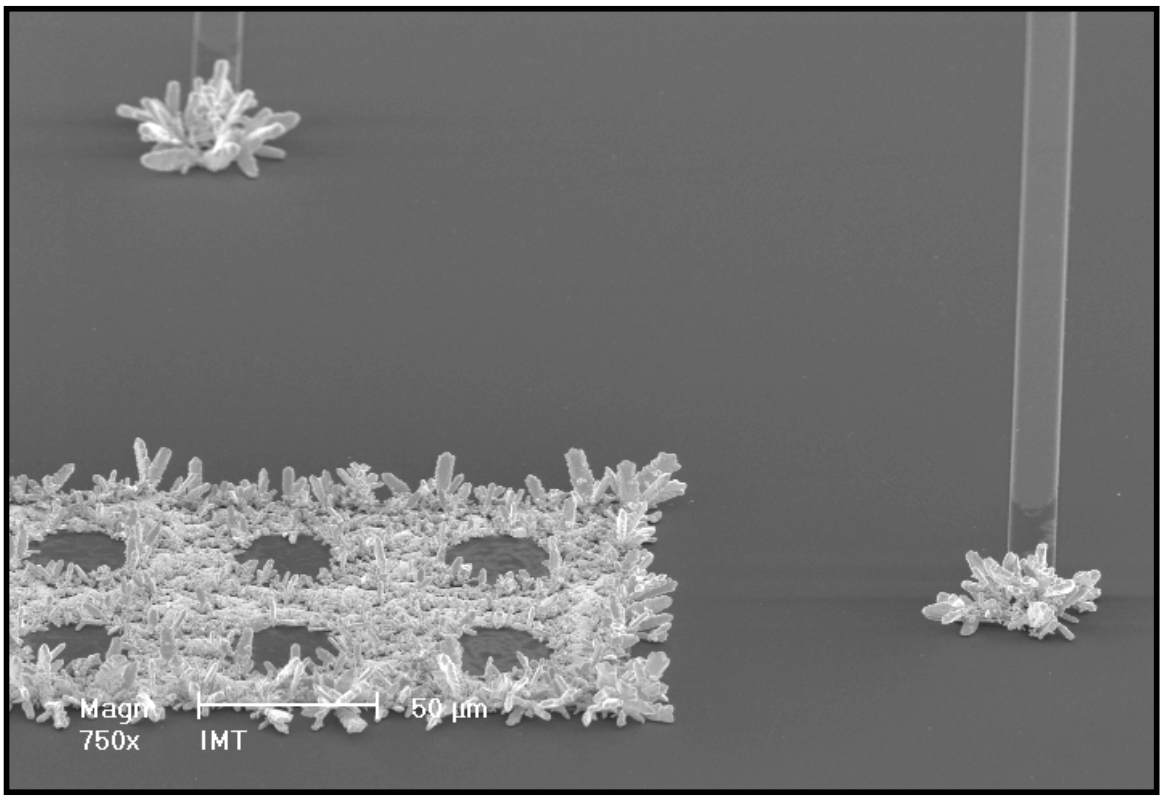

Figure 4.10: ESEM picture of the Au electroless deposition on Al electrodes (16 hours in Atomex solution, 5 min. in Catagold, T = 57°C)

Reducing the temperature down to 23°C and immerging the chip 5min. in the first bath and 1min. in the second one, the deposit of Figure 4.11(b) has been obtained. The height of the deposit is reduced as well as the lateral growth. At a temperature of –9°C of the Cathagold bath, after 1 min. of treatment, the deposited layer is shown in Figure 4.11(c).

The temperature is one of the parameters that can be modified to affect the deposition. A second one is the solution concentration and in particular the $KAu(CN)_2$ concentration. Figure 4.11(d) shows the result of a deposition upon diluting 1 part of Cathagold solution in 20 parts of DI water and performing the electroless deposition for 15min. at 23°C.

This last result is particularly interesting because it yields in a rather compact layer and because the deposition can be performed at room temperature and at low $KAu(CN)_2$ concentration.

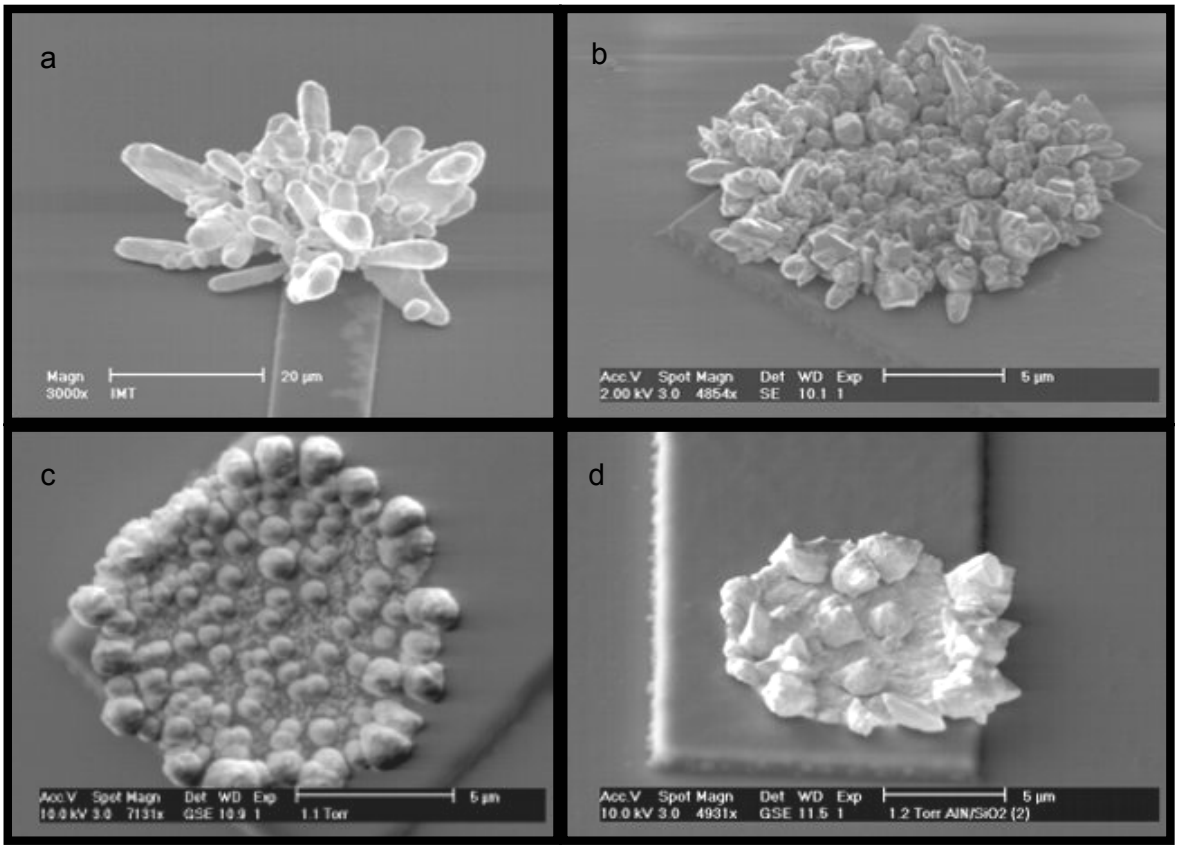

Figure 4.11: Au electroless deposition on Al microelectrodes.
(a) 16 hours Atomex + 5 min. Catagold, T = at 57°C, (b) 5 min. Atomex + 1 min. Catagold, T = 23 °C, (c) 5 min. Atomex, T = 23°C + 1 min. Catagold, T = -9 °C, (d) 5 min. Atomex + 1 min. 1:20 Catagold : DI water, T = 25 °C.

The homogeneity of the deposit on the 32 electrodes is satisfactory even though the deposit on the larger pseudo-references was less compact. This is probably due to the influence of the geometry on the electroless deposition as reported in the work of Vanderputten for nickel electroless [Vanderputten, 1993].

4.4.2 Evaluation of the electroless gold layer

The electrochemical behaviour of the deposited gold on aluminium microelectrodes has been evaluated by cyclic voltammetry (CV).
Cyclic voltammetry (Figure 4.12) of a gold wire and an aluminium microelectrode covered by electroless gold has been performed in a 1M H_2SO_4/N_2 solution.

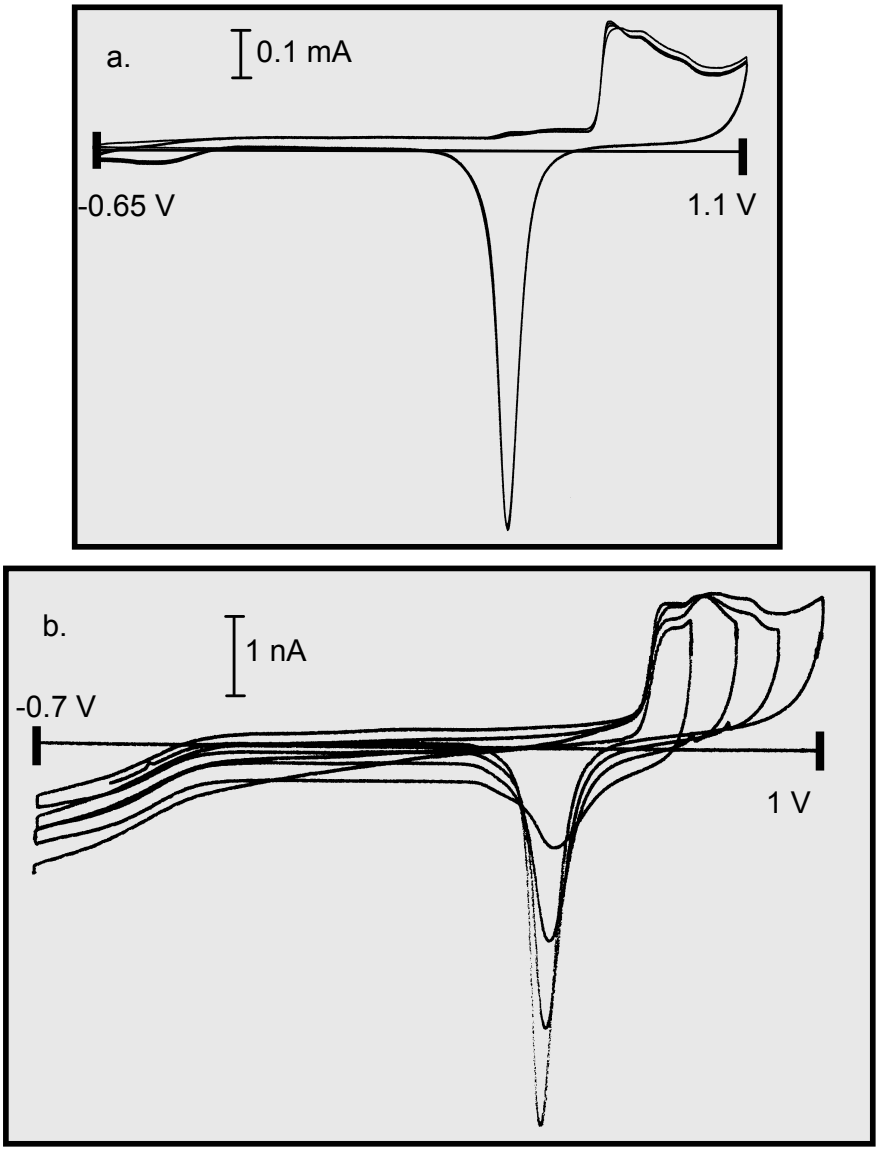

Figure 4.12: CV in 1M H_2SO_4 / N_2 of a (a) gold wire, (b) electroless Au on Al (anodic potential sequentially increased). The same behaviour is observed. (Ag/AgCl reference electrode, Pt counter electrode, potential range from –0.7 V to 1 V; scan rate of 100 mV/s).

Comparing the two CVs, identical oxidation-reduction behaviour is observed. This is a first indication of the good quality and purity of the electroless gold. Moreover, the electrical interface between aluminium and gold do not introduce resistive or capacitive components.

Assessment of the deposited material was performed by high resolution XPS spectra analysis on Kratos Axis Ultra spectrometer (LMCH, EPFL, Lausanne). The base pressure of the system was 1.1 10^{-6} Torr and charge neutralisation was applied in order to compensate for surface charging. Due to the small electrodes diameter the x-ray spot of 50 μm in diameter was focused on the contact pads instead of the electrodes. The spectra (Figure 4.13) were collected over a binding energy range between 0 and 1100 eV with a pass energy of 80 eV and an acquisition time of 480 s.

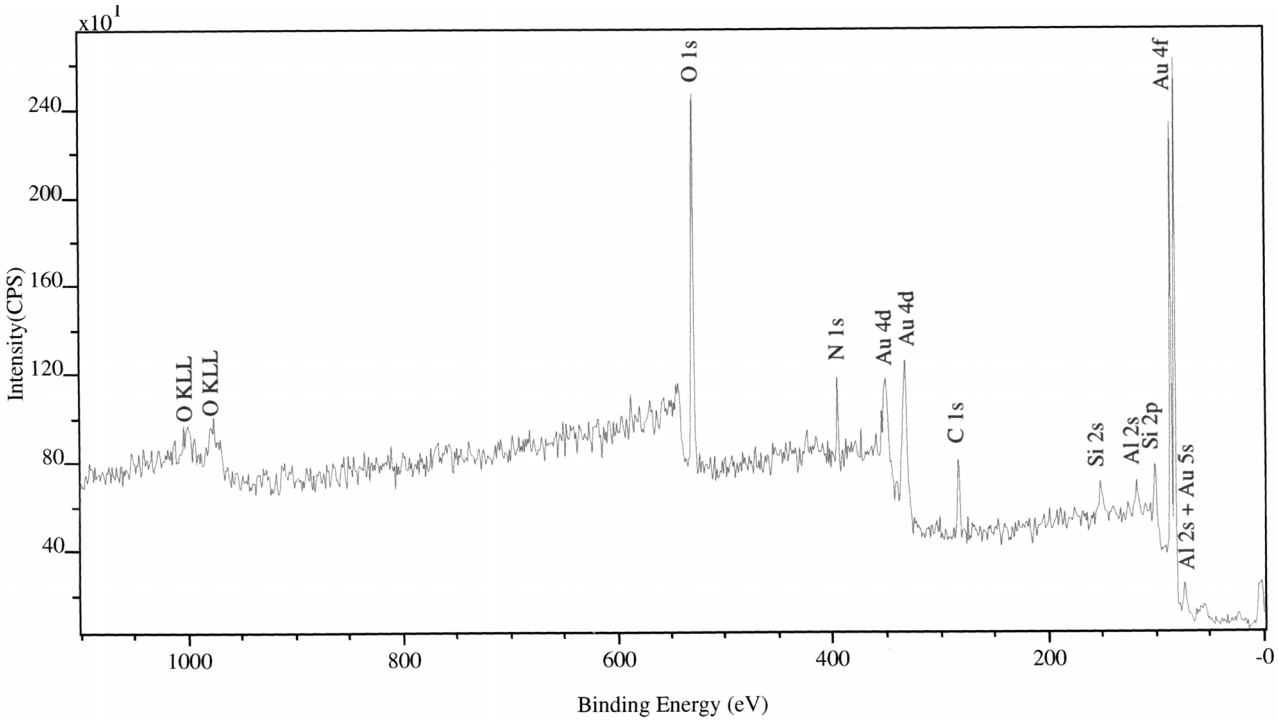

Figure 4.13: XPS survey spectra of the electroless Au showing clear evidence of the gold deposition, in particular in form 4f. (Kratos Axis Ultra spectrometer, base pressure 1.1 10^{-6} Torr, x-ray spot size 50 μm).

The XPS spectrum shows a clear evidence of gold deposition (in particular in form 4f). However, while the deposition on the microelectrodes results in compact layers, the pseudo-references show slightly less dense deposited layers. Therefore the contributions from the underneath Al can be seen on the spectrum. Due to the difficulties in placing the x-ray spot on the structures, contributions from the surrounding nitride insulation layer are also visible.

4.4.3 Gold electroless deposition on CMOS chips

The CMOS chip was at first wire-bonded on a PCB and wires protected with an epoxy (see 4.5.1). For the CMOS chip, instead of immersing the chip in the Au electroless solution as described previously, the deposition was performed with a drop of Cathagold solution. The process is summarised in Table 4.2. Figure 4.14(a) shows 4 pixels before and Figure 4.14(b) after the process. The deposition is well localised on the aluminium electrodes and the homogeneity on the whole active area is very satisfying (Figure 4.15). Unfortunately, an electrochemical evaluation of the deposited gold on the CMOS chip could not be realised, since it was not possible to directly contact the electrodes and perform cyclic-voltammetry measurements.

Gold displacement in Atomex	
temperature	25 °C
time	5 min.
Gold electroless in Cathagold	
dilution in DI water	1:20
temperature	25 °C
time	15 min.

Table 4.2: Au electroless process for the CMOS device.

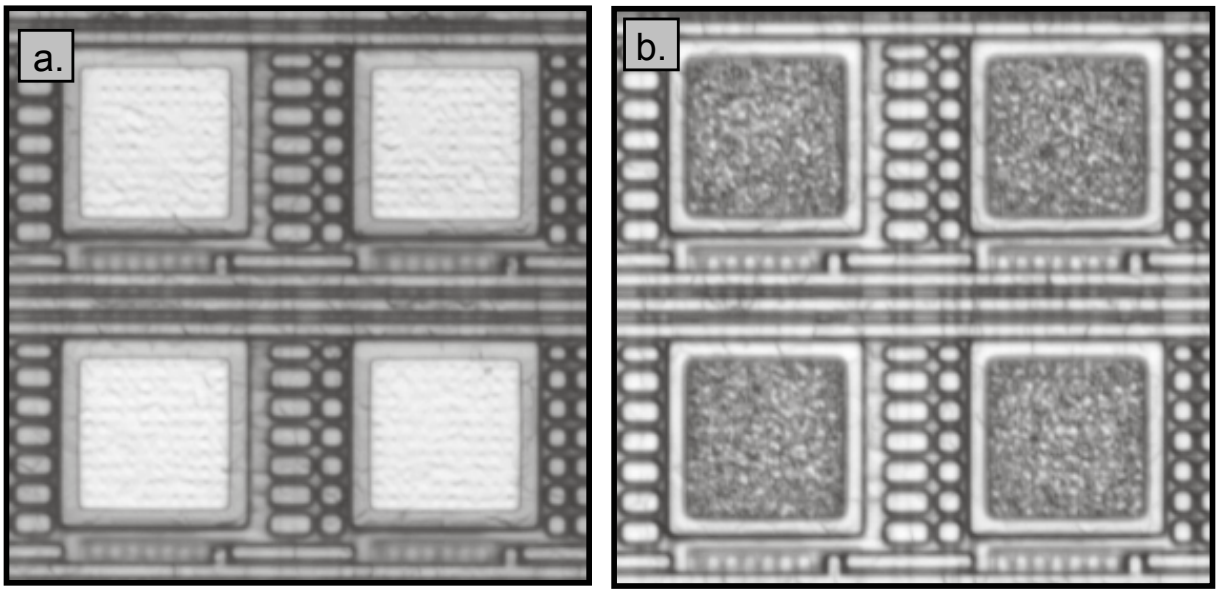

Figure 4.14: Optical image of 4 pixels (a) before the electroless Au deposition and (b) after the deposition of Au. A rough and compact layer is achieved.

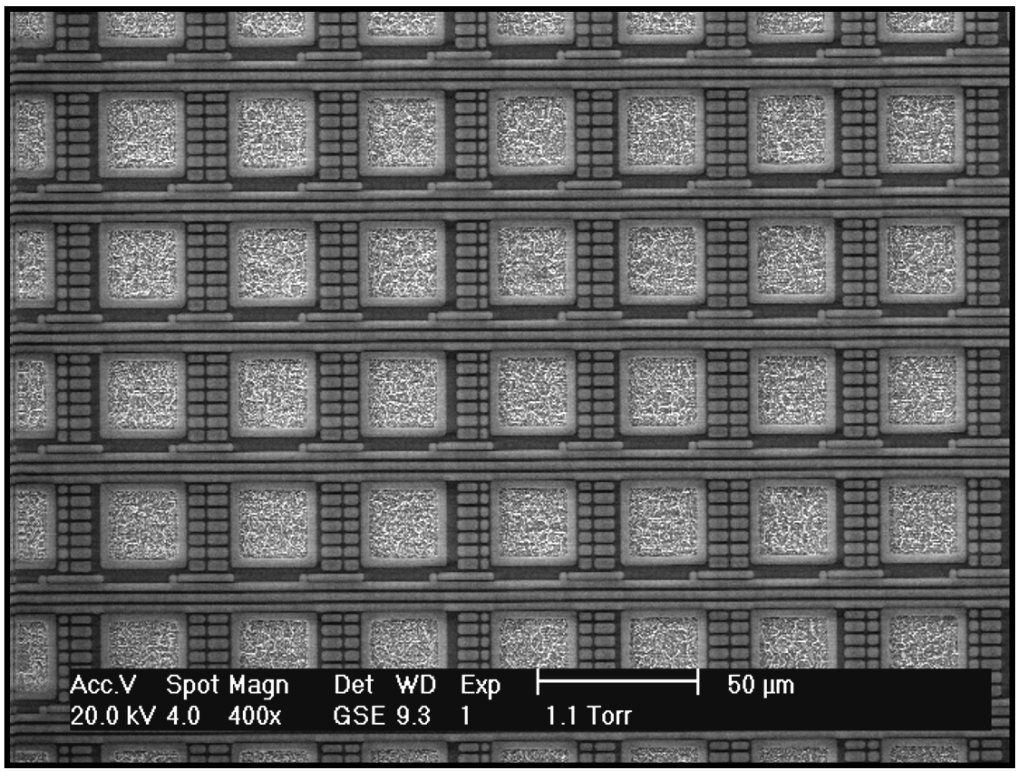

Figure 4.15: ESEM of the deposited Au on the CMOS device.

4.5 Electrical characterisation of the CMOS chip

A total of 20 CMOS chips have been fabricated in Alcatel 0.5 μm technology. The packaging, the design of an electrical interface card as well as the electrical tests performed on the chips are reported below.

4.5.1 Packaging

For the electrical and biological evaluation of the first high density array prototype, a simple packaging solution has been developed. This provides the electrical contacts as well as a culture chamber.
The chip is wire-bonded on a PCB providing a DIP24 socket connector, and wires protected with an epoxy. A Plexiglas spacer is glued on the PCB and a polystyrene (PS) reservoir mounted (Figure 4.16). Figure 4.17 shows the packaged device, and Figure 4.18 the active area.

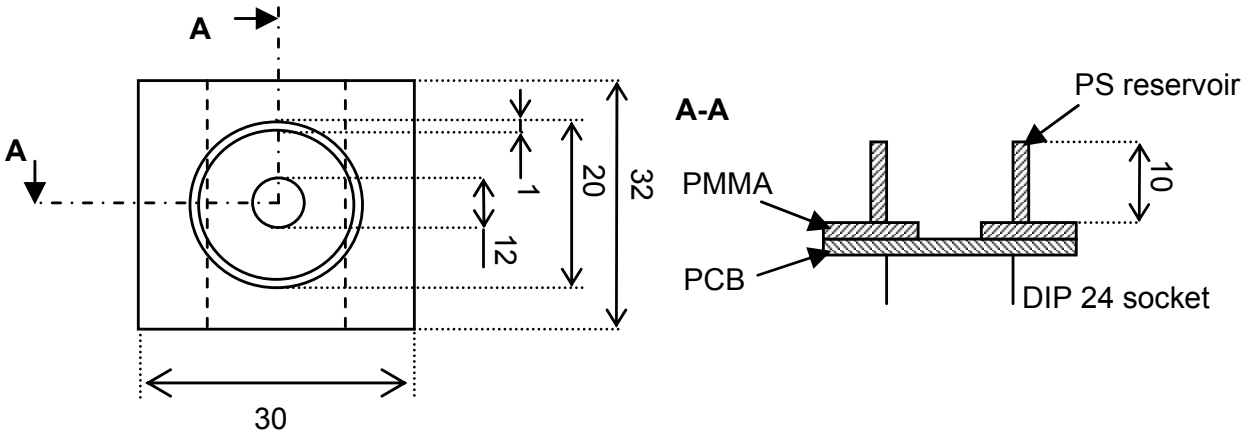

Figure 4.16: Design of the device package. The chip is glued and wire-bonded on a PCB providing a DIP24 connector and a PS reservoir.

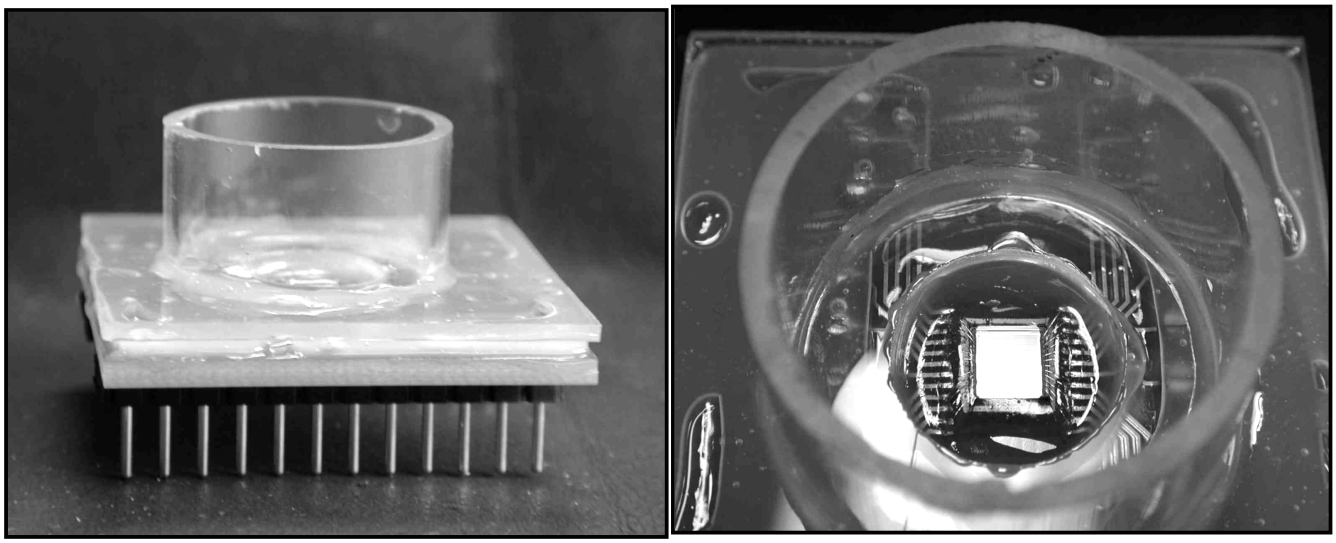

Figure 4.17: The packaged device.

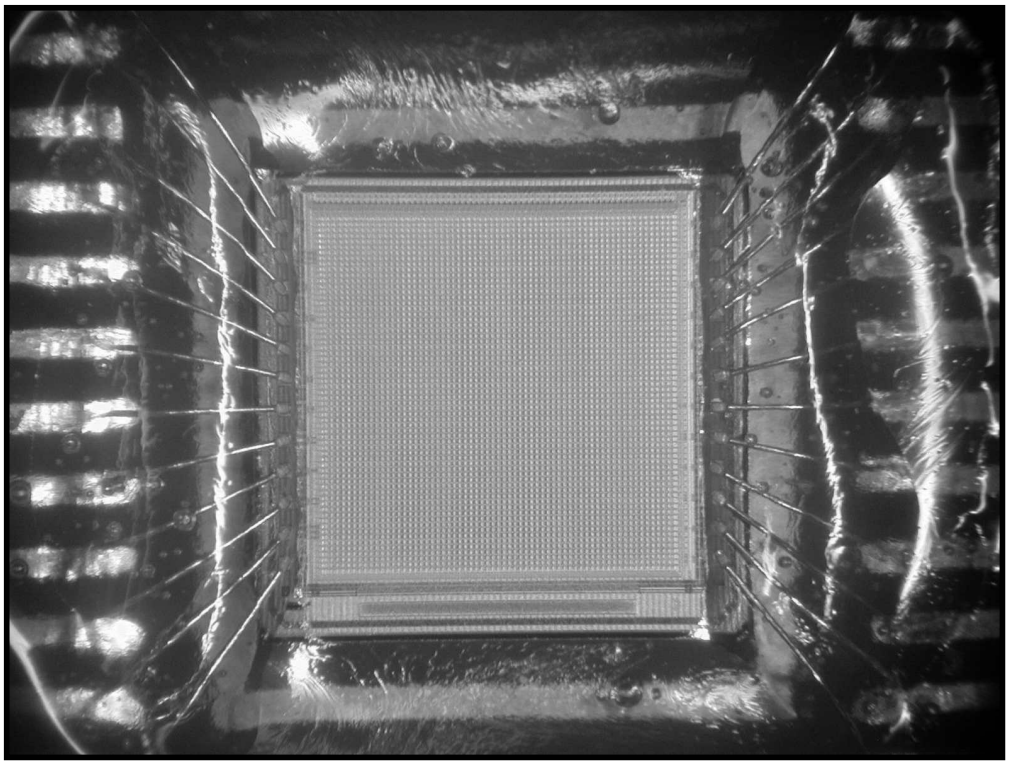

Figure 4.18: Optical image of the the active area after packaging and gold electroless deposition.

4.5.2 The electrical chip interface

A home-built electrical chip interface has been developed in order to provide:

- a stable support and the electrical contacts
- the power supplies (3.3 V, 5 V)
- the current sources for $V_{bias1,2}$ (10 μA and 500 μA – 2 mA)
- manual addressing
- chip output signal amplification (1, 100 x) and optional filtering

The circuit schematic is reported in Annexe IV
For the electrical tests in a phosphate solution, the interface gain was set to 1 (voltage follower) without filtering. The 100 times amplifier has been added for the biological tests as well as a RC filtering at 1 KHz.
The chip pads were connected as reported in the Table 4.3. In order to reduce the noise, the whole system has been placed in a Faraday cage and coaxial cables have been used.

VSS = Ground = 0V
VDD = 5V
VDDA = 3.3V
Vhigh = VDD = 5V
Gate = Source = ground
Vbias1 = 10.3 μA
Vbias2 = 1.8 mA
Addressing by manual switch (Logic 1 = 3.3V, Logic 0 = 0V)
In_inv = DC polarisation (open-loop mode) or 0 V (close-loop mode)
In_Inv_out = 3.3 V (open-loop mode) or 0 V (close-loop mode)
Reading pixel 32,32

Table 4.3: Device pad connections on the chip interface.

4.5.3 Electrical tests in a phosphate solution

Electrical tests have been carried out in a phosphate solution in order to evaluate the integrated pre-amplifier characteristics of a single pixel in open and close-loop configurations. The chip reservoir was filled with a 150 mM phosphate solution (pH adjusted to 7.3 with H_3PO_4). For testing, an AC signal generator (HP 30120A) was used. The sinusoidal signal amplitude has been reduced from 100 mV_{p-p} to 2 mV_{p-p} using an attenuator (HP 355D VHF Attenuator).
To operate the pre-amplifier in open-loop, the same DC polarisation with respect to the electrical ground must be applied on the input pair: on the recording microelectrode and on the inverting amplifier input (reference). As reported in Figure 4.19 (a), the polarisation ($V_{DC,In}$) of the microelectrode is carried out via a Pt wire directly dipped into the solution. This wire is connected to an external DC voltage generator (HP E3632A DC power supply) in series with the AC signal generator ($V_{AC,In}$). The same DC voltage generator ($V_{DC,In}$) is used to polarise the inverting amplifier input.

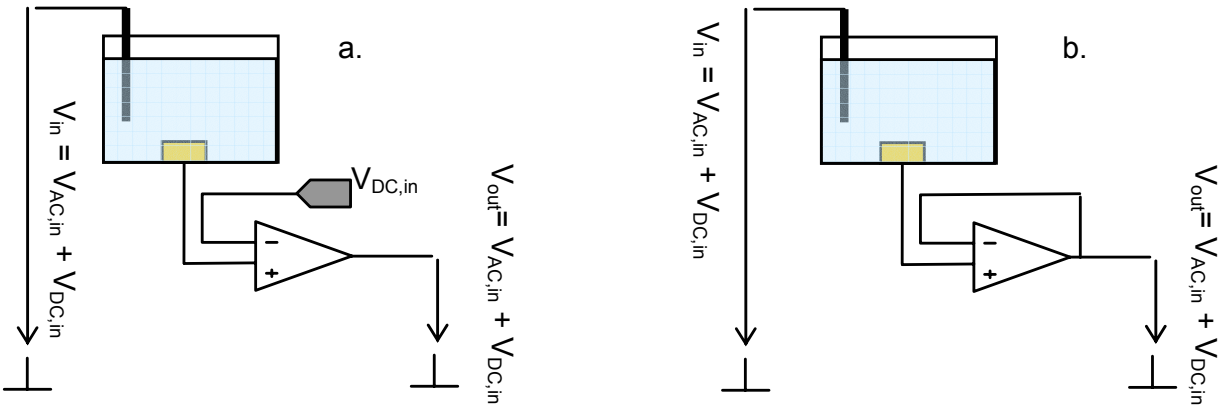

Figure 4.19: Set-up for the device testing in (a) open-loop mode and (b) in feed-back unity gain mode. The reservoir is filled with a phosphate solution and a small AC signal is applied. The DC signal is used for polarising the amplifier.

The DC polarisation is applied with respect to the electrical ground. Thus, since the microelectrodes are at a floating potential, no potential drop is established in the solution by the polarisation.

The open-loop gain has been measured by addressing a single pixel and applying an AC signal with frequencies ranging between 50 Hz and 60 kHz. The maximal gain has been measured for a DC polarisation of 0.7 V (Figure 4.20) and ranges between 29.5 dB and 30.8 dB for a bandwidth of 10 kHz. The gain was difficult to stabilize due to the high sensitivity of the differential pair to the noise acting on the polarisation. The sources of this noise are mainly given by the solution resistor, introducing differences between the polarisation of the two amplifier inputs, by the electrode-electrolyte interfaces (platinum wire - electrolyte, microelectrode - electrolyte), and by an additional noise source introduced by the DC voltage generator.

The contribution of the noise (DC + AC) on the input pair has at least three direct consequences for the open-loop mode:

1. the risk of saturating the amplifier (offset).
2. an additional AC-noise source is added to the output amplified signal.
3. the stability of the amplifier gain (programmed with the DC polarisation) is affected within the bandwidth and vs. time.

For these reasons, i.e. gain stability due to the noise acting on the polarisation, the open-loop mode seems not being well adapted for our application.

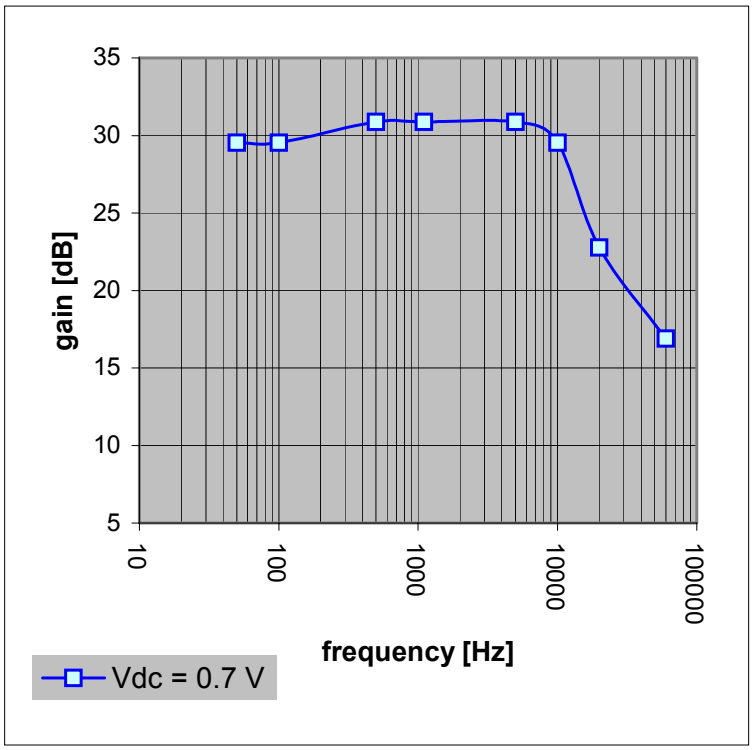

Figure 4.20: Gain ($V_{AC,out}$ / $V_{AC,in}$) versus frequency of the open-loop mode (applied AC signal: sinusoidal, 2 mV_{PP}, 50 Hz - 60 kHz; DC polarisation of 0.7 V).

The close-loop mode (unity-gain amplifier) acts as an impedance transformer (high input impedance and low output one) and amplifies the signals in respect to the electrical ground. Nevertheless, in this configuration, a polarisation of the amplifier between V_{SS} (electrical ground) and V_{DD} (3.3 V) is also necessary. In practice, this was realised similarly as in the case of the open-loop mode, i.e. with a platinum wire immersed in the solution.

A 2 mV_{p-p} sinusoidal signal, offset by a DC polarisation, was applied in the solution via the platinum wire (Figure 4.19(b)). The gain ($V_{AC,out}$ / $V_{AC,in}$) was measured vs. the polarisation signal for an input AC signal with a frequency of 1 kHz (Figure 4.22). In the same conditions, the output offset was measured vs. the input polarisation and is reported in Figure 4.21.

From these curves it can be observed that at 1.6 V polarisation, the gain starts to be reduced since the amplifier reaches its saturation

($V_{DC,out}$ = 2.8 V). For this reason, a maximal polarisation of 1.5 V has to be used.
The frequency analysis of the gain was performed between 5 Hz and 6 MHz with a polarisation of 1.5 V (Figure 4.23). The results show that the amplifier has a unity gain and a cut-off frequency of 1 MHz.
Compared to the open-loop mode, this configuration is easier to operate, i.e. the feedback compensates the instabilities of the polarisation. Therefore, the close-loop mode seems being a preferable choice for our application.
In terms of noise the output signal is affected by the intrinsic amplifier noise (Annexe II), and by extrinsic noise, which is generated by the chip interface (external circuits, noise from the input signals) as well as the environmental noise (50 Hz). In this configuration, the overall noise was smaller than 500 μV_{p-p}.

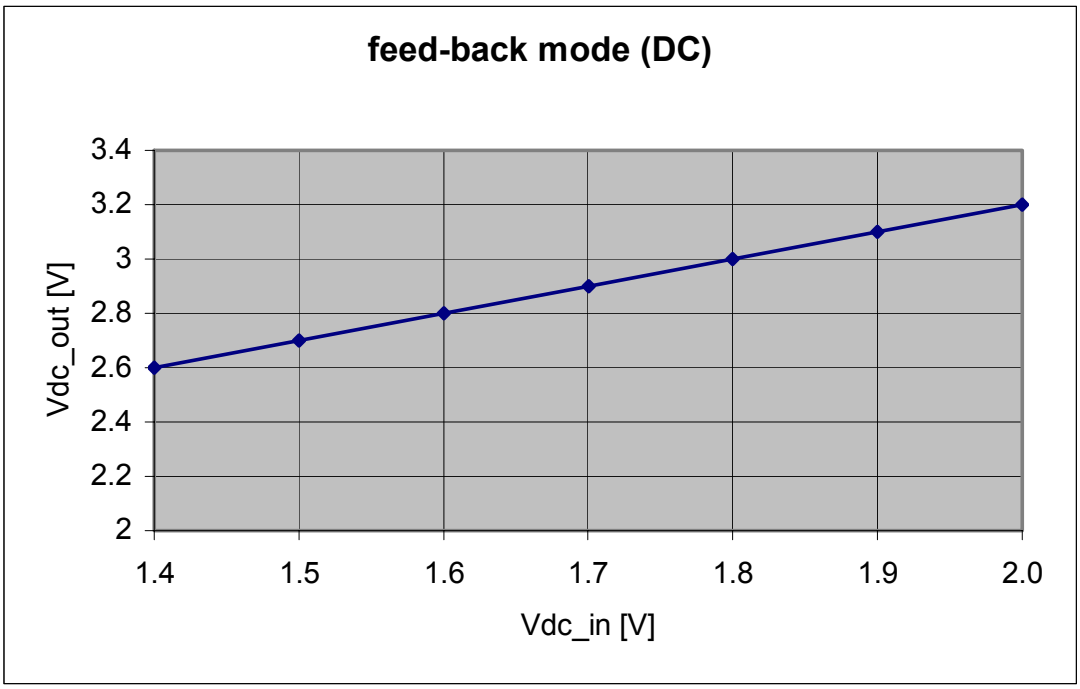

Figure 4.21: Output DC signal versus input DC signal in unity-gain mode.

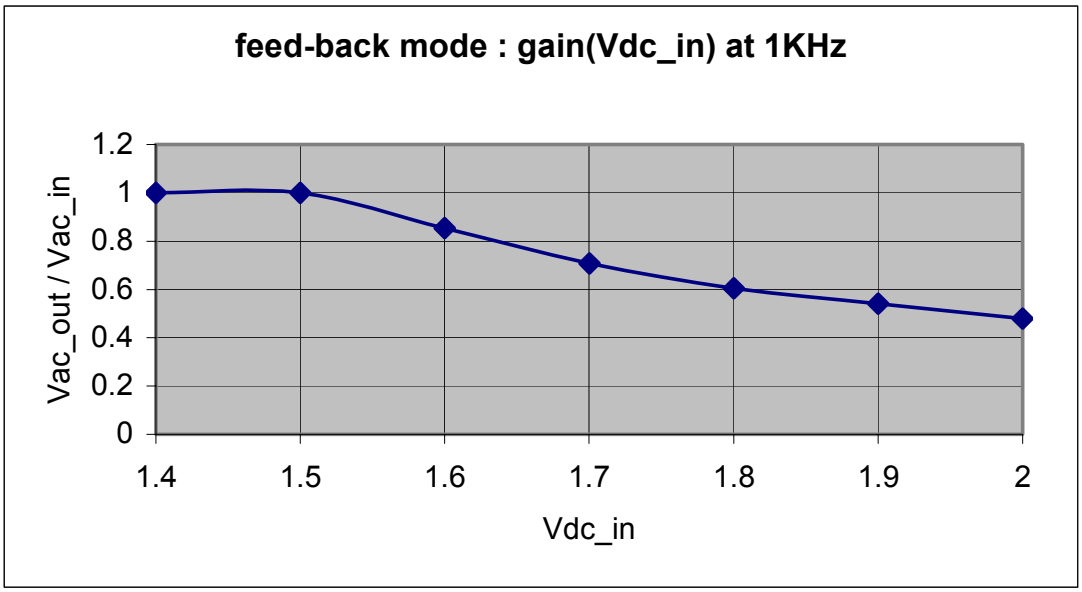

Figure 4.22: Gain in unity-gain mode versus polarization (AC signal of 2 mV_{pp}, 1kHz)

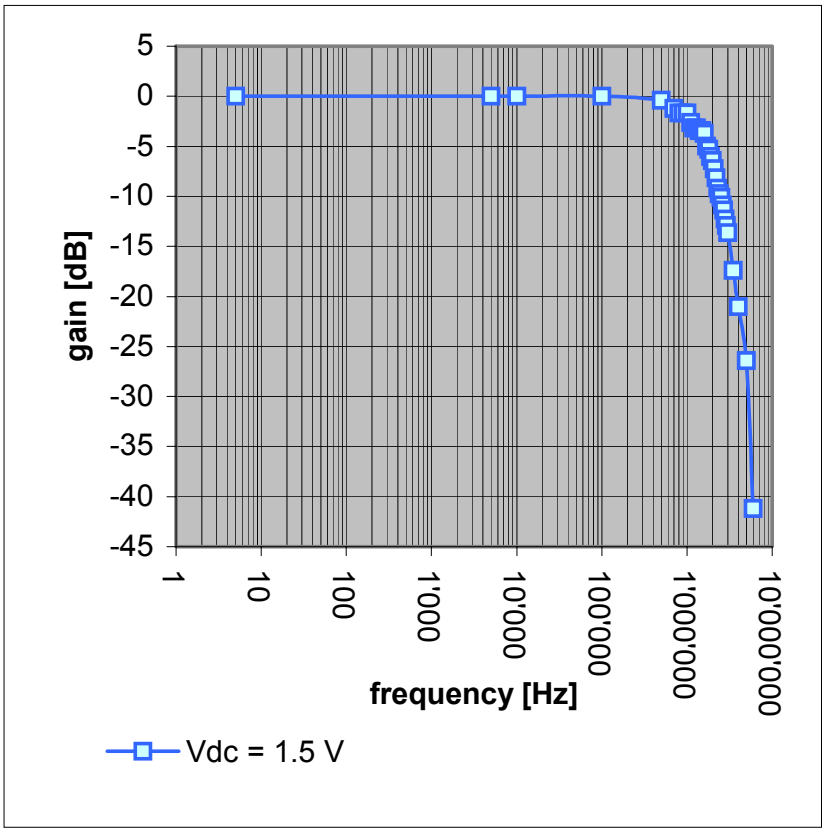

Figure 4.23: Gain vs. frequency in the unity-gain mode. (applied AC signal: sinusoidal, 2 mV_{PP}, 50 Hz - 6 MHz; DC polarisation of 1.5 V)

4.6 Biological experiments with cardiomyocytes

The previously reported electrical tests demonstrated the functionality of the integrated pre-amplifier in a phosphate solution. The results, in particular in the close-loop mode, encouraged preliminary tests with cellular cultures. Cardiomyocytes have been chosen for these preliminary tests since they are easier to culture than neurons, show a spontaneous activity after 2 days in-vitro, and extracellular electrophysiological signals up to 1 mV_{p-p} have been reported [Kucera et al., 2000]. These tests were performed at the Physiologisches Institut of the University of Bern, in collaboration with Prof. S. Rohr.
The aim of these tests was to ascertain the biocompatibility of the post-processed CMOS device. The electrophysiological activity recordings have been attempted in both open- and close-loop modes and are discussed next.

4.6.1 Cardiomyocytes culture preparation

The high density MEAs were prepared for culturing as follows:

1. rinsed in DI water.
2. coated for 30 s with collagen (human placenta, type VI)
3. rinsed 3 times with DI water
4. sterilised under UV light for 90 minutes (reservoir filled with the culture media)

Primary cultures of neonatal rat ventricular cardiomyocytes were obtained using previously published procedures. [Rohr et al., 1991]. The cell suspension was preplated in large culture flasks in order to reduce the fibroblast content and the myocytes remaining in suspension were seeded at a density of 1.9 x 10^3 cells/mm^2 on the high density MEA. The cultures were kept in an incubator at 35°C in a humidified atmosphere containing 1.2 % CO_2. Medium exchanges were performed on the first day after seeding and every other day

thereafter with supplemented medium M199 (Gibco, Basel, Switzerland) containing a reduced concentration of serum (5%). Experiments started at least after 2 days of culturing.

4.6.2 Experimental and discussion

The resulting dense monolayer cultures could not be imaged on the non-transparent CMOS device since an inverted microscope is required. However, this has been realised on a pyrex substrate MEA with cultures plated in the same conditions (Figure 4.24).

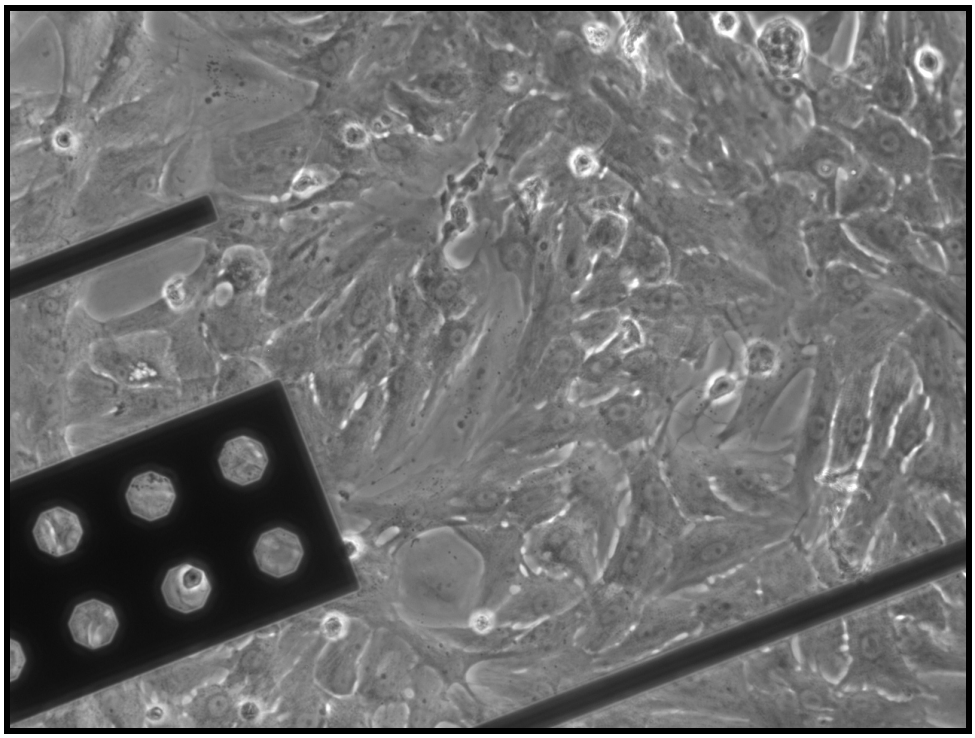

Figure 4.24: Neonatal rat ventricular cardiomyocytes on pyrex MEA (optical picture performed at the University of Bern).

On all the tested CMOS devices, the cardiomyocyte monolayer showed after 2 days in culture spontaneous cellular contractions with a beat rate of few Hz (by optical observations). This confirms the health of the culture on the realised device and corresponds to previously reported experiments on conventional MEAs [Kucera et al., 2000]. Electrophysiological experiments have been realised between the third and fifth day after plating. The CMOS devices could be reused by cleaning them with isopropanol and rinsing in DI water. A first interesting result is that the electroless gold electrodes resisted the cleaning.

One of the risks working with these MEAs is given by the need of powering the chip with voltages up to 5 V (V_{high}). This may result in an electrolysis on the chip surface due to the voltage drops through the CMOS passivation layer. This was not the case on the developed device demonstrating the good quality of the top insulator (2 μm silicon nitride and silicon oxide).

Recordings of the electrophysiological activity have been tried in a similar set-up as the one presented for the electrical tests, i.e. removing the AC waveform generator (Figure 4.19). The chip and its home-built electrical interface were placed in the incubator in order to keep the culture temperature at 35 °C. The recording pixels were randomly selected on the active area covered by the culture, and the output signal monitored on an oscilloscope.

In open-loop mode several tests have been carried out modifying the DC polarisation up to 1.6 V, setting the interface gain to 1 and to 100, and adding an RC filtering at 1 kHz. In the close-loop mode, modifying the set-up as described for the electrical tests, similar experiences were performed. Examples of the recorded signals are reported in Figures 4.25 and 4.26. Unfortunately, in both open- and close-loop mode no evidence of physiological activity could be observed up our days.

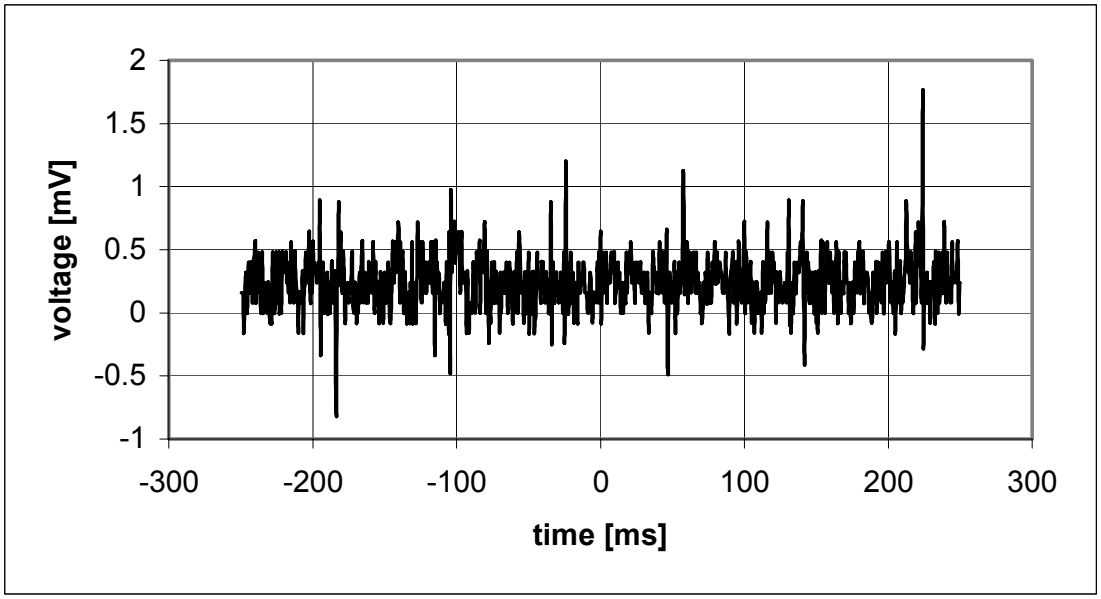

Figure 4.25: Recorded signal from neonatal rat ventricular cardiomyocytes without external amplification (unity gain mode). No evidence of biological activity.

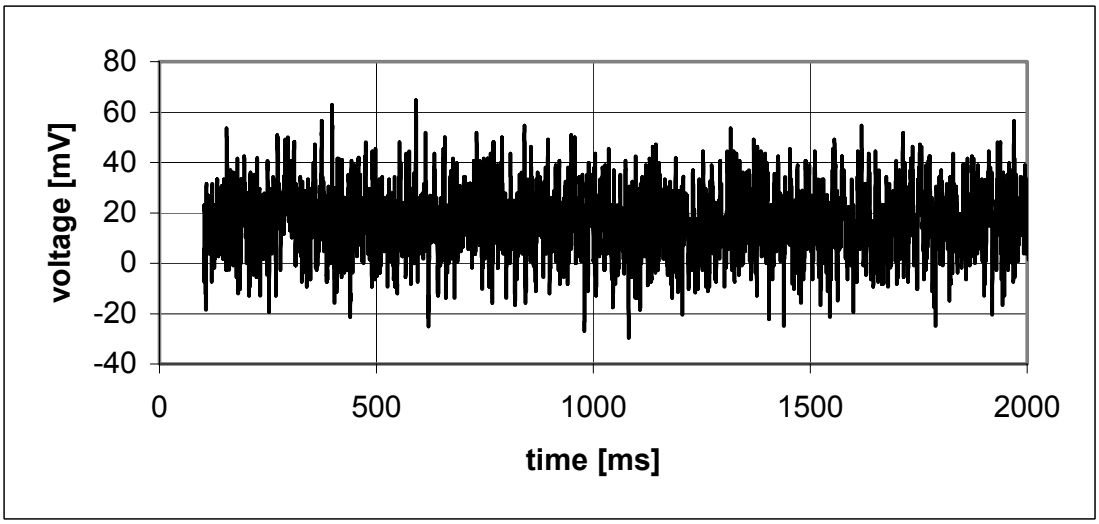

Figure 4.26: Recorded signal from neonatal rat ventricular cardiomyocytes with an external 100 times amplification (unity gain mode, sampling at 20 kHz). The noise is higher than that recorded during the electrical characterisation.

This seems contradicting the electrical tests performed in a phosphate solution where it has been seen that at least the close-loop mode should allow the recording. However, signals may be smaller than expected (1 mV_{p-p} as described for conventional MEAs), resulting from a loose sealing of the culture. A smaller sealing resistor directly affects the signals amplitude as described in chapter 2. In parallel to improving the cellular adhesion, the total set-up noise has also to be reduced.

Additionally, the system may not behave exactly in the same way as in electrical tests. The reason may be found in the differences between the applied AC signal (for electrical tests) and the one generated by the cardiomyocytes. The current density relevant for the signal recorded by the MEA is generated predominantly by the sodium inward current. In cardiomyocytes, the peak density of this current is in the order of 0.5 $pA/\mu m^2$, which rises to a maximal current of 200 pA for a 20 x 20 μm^2 microelectrode. This value is much lower than the measured I_{AC} current of 0.22 μA generated by the stimulus signal applied to a single microelectrode during the electrical tests in a phosphate solution.

Electrical tests in the unity gain configuration have been performed introducing a resistor for limiting the current of the AC signal. These results showed the lowering of the cut-off frequency (Table 4.4). The reasons for this behaviour are still under study.

resistor	$I_{AC, max}$	cut-off frequency
~0 Ω	0.22 μA	1 MHz
10 MΩ	~10^6 times smaller	700 Hz
100 MΩ	~100^6 times smaller	400 Hz

Table 4.4: Measured cut-off frequencies introducing a resistor lowering the AC injected current (V_{DC} = 1.4 V, I_{DC} = 8 nA for R = ~0 Ω).

For these reasons a second chip interface has been recently redesigned including an internal DC polarisation on the interface and taking care of limiting the injected current with a 1 MΩ resistor. This new interface is currently under evaluation and the schematic is reported in Annexe IV.

4.7 Discussion and future developments

From the beginning, it has been very clear that the development of high density MEAs based on the active pixel technology was a highly challenging, i.e. risky project. The developments carried out so far constitute the first essential steps for evaluating the feasibility of this approach. The prototype device allowed to clarify several issues and the results obtained constitute the basis for the future developments.
In particular, an original electroless technique has been developed to deposit gold microelectrodes on a large and dense active area. This allows the simple post-processing of electrode arrays based on CMOS devices The quality and the biocompatibility of the electrode material have been established electrochemically and with tests on cardiomyocytes cultures.
A simple analogue pre-amplifier based on a differential amplifier has been developed and evaluated. The circuit was designed to provide several working modes for evaluating the best configuration. As previously discussed, the open-loop mode is too sensitive to the noise of the DC polarisation on the differential pair and rises to an unstable gain. The feedback option seems to be a preferable choice in terms of the gain stability. However, the best solution would be to avoid the DC polarisation via the culture media by, for example, the symmetrical powering of the pre-amplifier, i.e. between $-V_{DD}$ and V_{DD} (keeping the culture media grounded).
Additionally a solution for lowering the pre-amplifier noise should be investigated, in particular for the recordings from neuronal networks. Also the chip interface has an important influence on the resulting total noise and has to be designed with particular care. In particular, the DC polarisation realised via an external power supply is not an

adequate choice. For these reasons a second version of this interface has been designed and is currently under evaluation (see Annexe IV).

4.8 Bibliography

Honma, H., *Plating technology for electronics packaging.* Electrochimica Acta, 2001. **47**: p. 75-84.

Krasopoulos, A.V., et al., *Rapid substitution of cold for aluminum metallization on integrated circuits.* Journal of the Electrochemical Society, 1997. **144**(3): p. 1070-1072.

Kucera, J.P., et al., *Power-law behaviour of beat-rate variability in monolayer cultures of neonatal rat ventricular myocytes.* Circulation research, 2000. **86**(11): p. 1140-1145.

Okinaka, Y., *Significance of inclusions in electroplated gold films for electronics applications.* Gold Bulletin, 2000. **33**(4): p. 117-127.

Okinaka, Y. and M. Hoshino, *Some recent topics in gold plating for electronics applications.* Gold Bulletin, 1998. **31**(1): p. 3-13.

Overstolz, T., *CMOS active pixel sensor (APS) for in vitro nerve signal recording*. 2000, Inst. de Microtechnique: Neuchâtel.

Pournaghi-Azar, M.H. and H. Razmi-Nerbin, *Voltammetric behaviour and electrocatalytic activity of the aluminum electrode modified with nickel and nickel hexacyanoferrate films, prepared by electroless deposition.* Journal of Electroanalytical Chemistry, 1998. **456**(1-2): p. 83-90.

Rohr, S., D.M. Schölly, and A.G. Kleber, *Patterned growth of neonatal rat heart cells in culture. Morphological and electrophysiological characterization.* Circulation research, 1991. **68**: p. 114-130.

Seitz, P., et al., *Smart Sensing Using Custom Photo-Application-Specific Integrated-Circuits and Charge-Coupled-Device Technology.* Optical Engineering, 1995. **34**(8): p. 2299-2308.

Strandjord, A.J.G., S. Popelar, and C. Jauernig, *Interconnecting to aluminum- and copper-based semiconductors (electroless-nickel/gold for solder bumping and wire bonding).* Microelectronics Reliability, 2002. **42**(2): p. 265-283.

Vanderputten, A.M.T. and J.W.G. Debakker, *Geometrical Effects in the Electroless Metallization of Fine Metal Patterns*. Journal of the Electrochemical Society, 1993. 140(8): p. 2221-2228.

Willemin, M., et al., *Optical characterization methods for solid-state image sensors.* Optics and Lasers in Engineering, 2001. **36**(2): p. 185-194.

5 THE NEUROBIT PROJECT

5.1 Introduction – context of the EU project

Following the Hebb's proposal (1949), it is generally believed that the information is processed by distributed neuronal networks and not by the features of single neurons. However the "decoding" of the neuronal network activity is still today a challenge. In previous chapters two directions for improving the current MEAs technology towards higher spatial and temporal resolution have been investigated.

Compared to artificial systems, a unique property of the brain is the plasticity, i.e. the capability of the brain to modify itself in terms of neuronal circuits. The ability of the nervous system to learn and to adapt its performance to previous experience, to integrate high-resolution multi-modal sensory information and extremely precise motor control, is nowadays far from the capabilities of artificial systems. These considerations are the main motivations of the Neurobit EU project, where the challenging objective is:

"take advantage of these unique plasticity properties to control the sensorimotor behaviour of an artificial body – a mobile robot – moving in a changing environment. As living and highly adaptable systems, we will use networks of neurons kept alive *in-vitro*, out of the brain of mammalian embryos. The living network will be real-time connected to an autonomous robot".

The contribution of the IMT to this project concerns the development of a neurophysiological mini laboratory (NML) integrating all features required for monitoring activity-dependent changes of synaptic plasticity of neurones. The final microsystem will include a mini incubator, local delivery features for biochemical modifications and a microelectrode array (MEA) for electrical stimulation and recording. A complete NML will be designed for operating with perfusion or under static conditions. The first module consists of a chamber

accommodating a heating element with a feedback temperature control, a pH sensor and a transparent top cover with ports for liquid medium perfusion and gas in and outlets. The second module is a micro-transducer-array (MTA), i.e. the bottom part of the mini-incubator. It comprises i) a microelectrode array (MEA) embedded on a planar substrate and ii) interconnected open structures delineating the clustering regions of the neuronal network. A priori, the neuronal network will be considered as a “black-box” and the clustering structures, i.e. open-wells, will allow the definition of input-output connections. The next paragraphs present the developments realised at the IMT during the first year of this ongoing project.

5.2 Functional block diagram of the NML microsystem

The final microsystem will integrate several functionalities in order to incubate the neuronal network for several months, to optically and electrophysiologically monitor the network activity and to electrically and chemically stimulate it. The functions block diagram of the final device is reported in Figure 5.1.
During the first year the basic elements of the NML have been developed and their functionality evaluated. In the design phase, different technological options were assessed with respect to the most convenient system assembly. Next, the development of the following NML elements is described:

- the clustering structures
- the microelectrode array (stimulation / recording)

} MTA

- temperature sensor (temperature control)
- heating element (temperature control)
- pH sensor (pH monitoring)

} NML

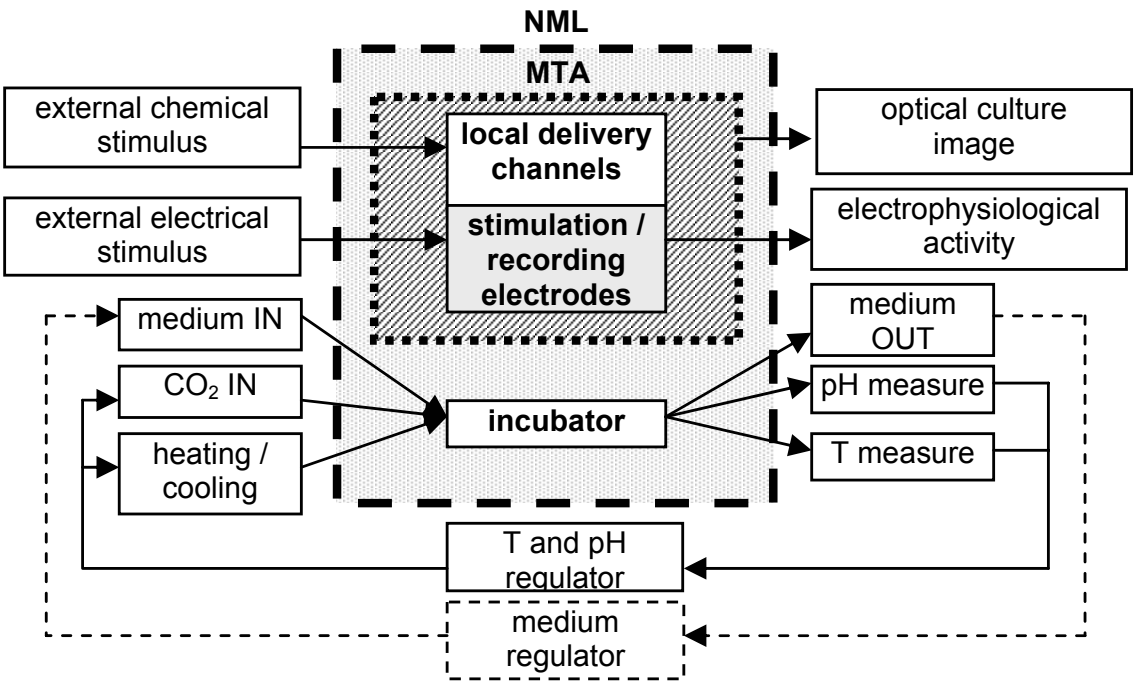

Figure 5.1: Functions block diagram of the complete mini neurophysiological laboratory (NML)

5.3 The micro-transducer-array (MTA)

The first generation of the MTA (Figure 5.2) provides the network-clustering structures defined on a MEA without integrating a micro-fluidics system for changing the culture medium or for the chemical stimulation.

The packaging of the device on an adapted PCB provides the compatibility with the MCS preamplifier as well as an optical window for back side optical microscopy. A total of 60 microelectrodes will be integrated.

The culture reservoir has to provide a sufficient volume of culture media for neuronal survival of at least one week (about 3 cm^3) limiting the need of replacing the culture media and thus the risk of infections.

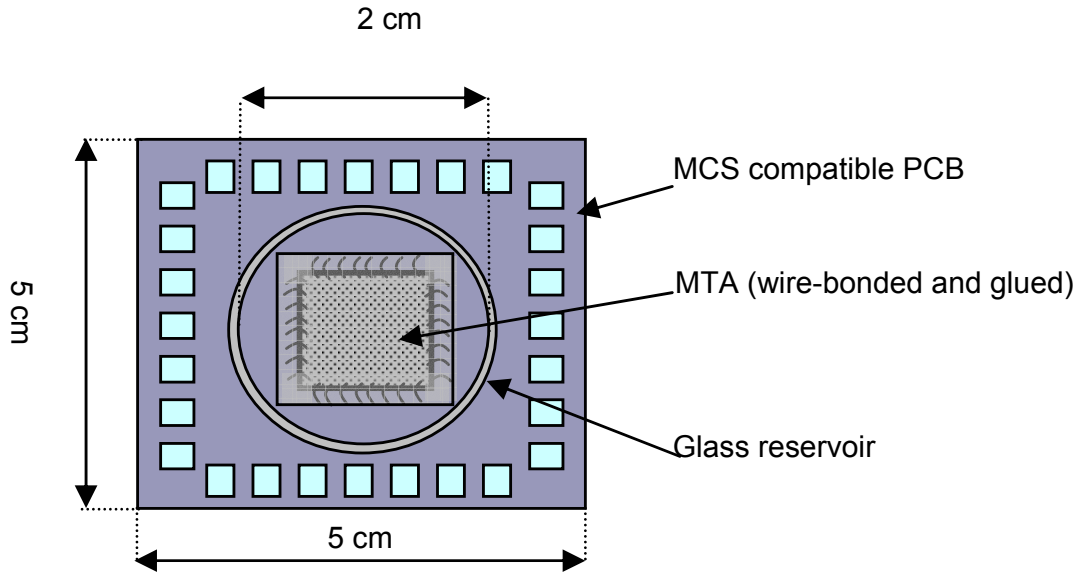

Figure 5.2: Schematics of the packaged MTA

5.3.1 The clustering structure

The first layout of the clustering structures provides five open, interconnected chambers for plating and growth of five distinct neuronal networks.

The dimensions of the open chambers should define a volume of at least 1 μL in order to be able to locally plate the neurons. This requires a chamber diameter of 2 mm for a minimal height of 300 μm.

The open-channel width has been fixed to 300 μm. Different channels lengths have been designed to investigate the ability of the networks to interconnect. The geometry and the dimensions are summarised here below (Figure 5.3).

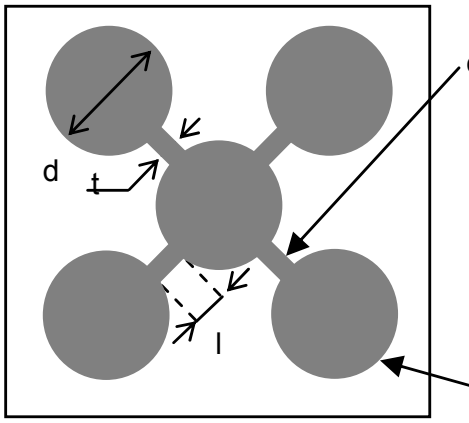

	dimensions
open-chamber diameters (d)	between 2 and 3 mm
open-channels width (t)	300 μm
open-channels length (l)	between 0.5 and 1 mm
height (h)	> 300 μm

Figure 5.3: Geometry and dimensions of the clustering structure

The main prerequisite for the material of the clustering structures is the biocompatibility. Considering this condition as well as the manufacturability criteria, possible materials and techniques for fabricating the clustering structure are:

- glass by US drilling or by electrochemical discharge machining (ECDM)
- plastics (PDMS, PMMA, PS) using micro-moulding technologies
- SU-8 by photolithography
- polysiloxane patterned by photolithography
- silicon by etching the structure by DRIE or KOH

The patterning of the structure directly on the MTA using SU-8 or polysiloxane presents the advantage of a precise alignment and of no additional assembly e.g. gluing or anodic-bonding. Moreover, both polymers have proved their biocompatibility [Heuschkel, 2002; Weisenberg, 2002; Arquint, 1994]. In particular, SU-8 has been previously used as a passivation material for MEAs. Its thickness can be controlled by the spinning rate and a typical aspect ratio of 1:20 can be obtained [Zhang, 2001; Zhang, 2001; O'Brien, 2001; Feng, 2001; Lorenz, 1998; Dellmann, 1998].

All these considerations have motivated the design and the fabrication of the first series of clustering structures in SU-8.
The SU-8 clustering structures have been fabricated on a pyrex substrate covered with a 4000 Å thick Si_3N_4 (PECVD) layer. These devices allow evaluating:

1) the SU-8 technology with respect to the sterilisation and the stability in the culture media.
2) the structure dimensions and geometry, namely channel length, chamber diameter and SU-8 thickness for clustering.

Clustering structures based on SU-8 technology

The SU-8 is an epoxy-based photo-structurable polymer (negative). The series from Microchem is available with several viscosities allowing layer thicknesses, in one spin, from a few microns up to 300 μm. Thicker layers are possible with a multiple spinning.
The scheme of the device is shown in Figure 5.4. To comply with the requirement of a minimum volume of 1 μl, the SU-8 layers of respectively 300 μm and 550 μm thick have been realised. A two layer technique has been developed for the structuring of 550 μm thick SU-8.

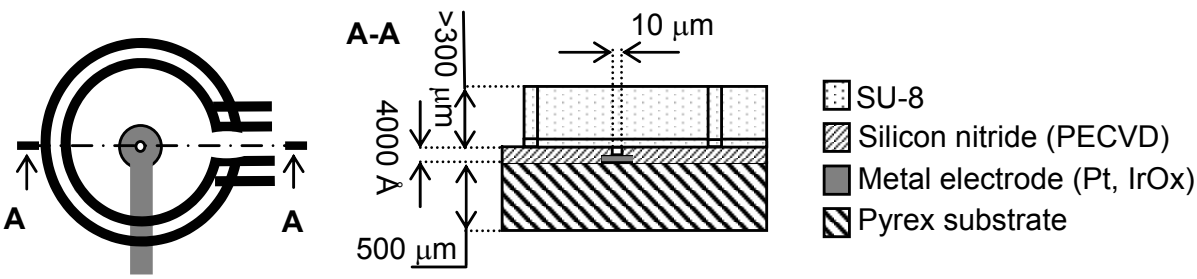

Figure 5.4: Schematics of the MTA realised with SU-8 clustering structures

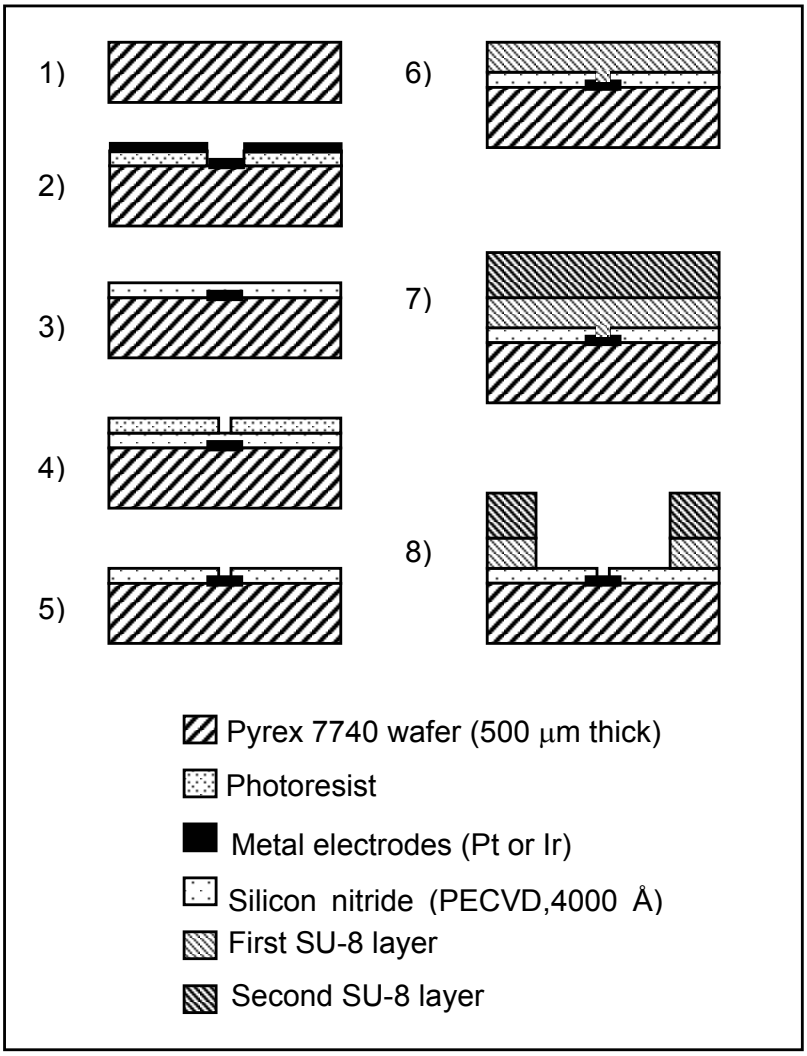

Figure 5.5: Fabrication process for MTAs with 550 μm thick SU-8 clustering structures. 1) substrate cleaning; 2) metal electrode lift-off; 3) silicon nitride deposition (PECVD); 4) and 5) opening of the electrodes (photolithography and dry plasma etching); 6) coating of the first SU-8 layer; 7) coating of the second SU-8 layer; 8) UV exposure and development of the two SU-8 layers.

The fabrication process of MTAs featuring a microelectrode array and SU-8 clustering structures is shown in Figure 5.5. The microelectrodes arrays are fabricated on Pyrex, 7740, wafers 500 μm thick (Sensor Prep Services, Elburn) following the process described in chapter 3. After cleaning in a piranha solution (5 min. in H_2SO_4 and 5 min. adding a drop of H_2O_2), the wafers are processed

with one of the following SU-8 technologies, i.e. 300 μm or 550 μm thick.

300 μm thick SU-8

The substrate is dehydrated at 200°C during 30 min. Then, the SU-8 100 (Microchem) is spinned at 500 rpm for 10 seconds and at 1100 rpm for 30 seconds. This is followed by a pre-bake on a hot-plate (ramp temperature from 35°C to 95°C, total time of 105 min.). The UV-exposure (650 mJ/cm^2) is performed in a proximity mode (separation of 50 μm) on a mask aligner (AL-6, Electronic Vision). The exposed layer is post-baked (65°C for 10 min. and at 95°C for 15 min), developed in PGMEA (15 min.) and rinsed in isopropanol.
After processing, the average thickness of the SU-8 layer is 328 μm ± 28 μm and the error in dimensions referred to the designed one is 3% (measurements collected on 6 wafers)

550 μm thick SU-8

The 550 μm thick layer of SU-8 is fabricated with two layers of SU-8, one UV exposure and one development. The wafer is at first dehydrated for 30 min. at 200°C and then coated with a first layer of SU-8 50 (500 rpm for 3 s. and at 700 rpm for 40 s). The first layer is pre-baked at 65°C for 5 min. and at 95°C for 5 min. A second layer of SU-8 100 is then spinned at 500 rpm. for 10 s. and at 1100 rpm. for 30 s. The two layers are baked at 65°C for 30 min. and at 95°C for 100 min. and UV-exposed (1700 mJ/cm^2) in a proximity mode (separation of 50 μm). The exposed layers are post-baked (65°C for 10 min. and at 95°C for 15 min), developed in PGMEA (21 min.) and rinsed in isopropanol.
After processing the average thickness of the SU-8 layer is 537 μm ± 22 μm and the error in dimensions referred to the designed one is 2% (measurements collected on 6 wafers).

Evaluation of the SU-8 clusters

The resulting 550 μm clustering structure is shown in Figures 5.6 and 5.7. The design has been realised with rounded edges, in particular for acute angles, to reduce the stress accumulation. The resulting devices show a good adhesion after processing without any stress effects.

A series of these clustering structures has been send to the partners for evaluation in culturing conditions and in particular for:

- defining a sterilisation protocol.
- evaluate the biocompatibility of the device
- evaluate the stability of the SU-8 clusters.
- evaluate the convenience of the chosen geometry

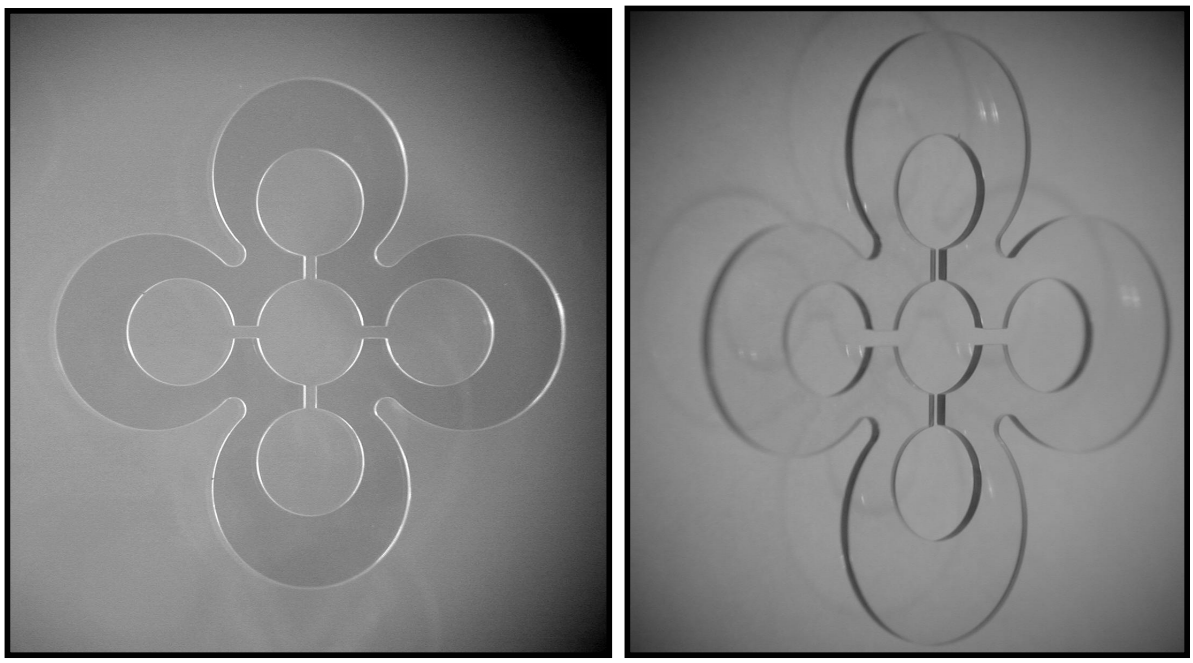

Figure 5.6: Optical picture of 550 μm thick SU-8 clustering structures on a pyrex substrate with 4000 Å of silicon nitride (PECVD).

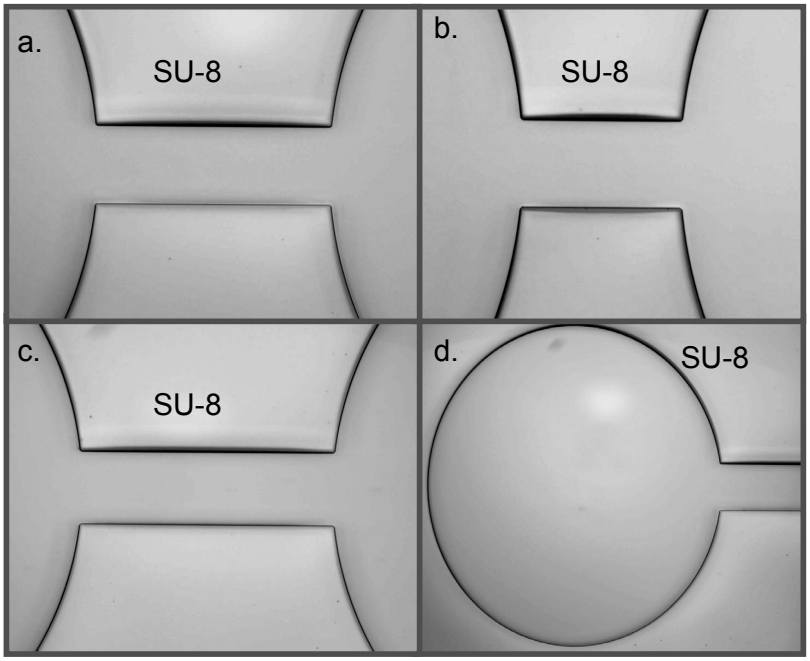

Figure 5.7: Details of the SU-8 550 μm thick structures. (a) open-channel of 800 μm, (b) open-channel of 500 μm, (c) open-channel of 1 mm, (d) open-well of 3 mm in diameter.

At first, the devices were sterilised at 120°C, dry or in autoclave, treated with an adhesion promoter, i.e. polylysine, laminine, and plated with hippocampal rat neurons. The neurons attached well and after a few days in culture produced some neurites. However, two problems have been encountered: the low cellular viability and the loss of the SU-8 adhesion in a humid environment.

At first, it has been observed that after about 5 days in culture most of the neurons had died. Moreover, in comparison with parallel cultures on coverslips, the neurites were much shorter (about 25 μm compared to hundreds of μm in parallel cultures).

This may have resulted from a toxic effect of the SU-8 or from an insufficient adhesion of the neurons on the substrate. Thus, the processing of the devices and their sterilisation have been modified to avoid any potential toxic effect resulting from degradation of the SU-8 at 120°C and/or from solvent contamination (PGMEA). In particular, the processing of the SU-8 has been modified by over-

developing the structures with 5 additional minutes in PGMEA. Also the wafers have been rinsed three times in isopropanol and DI water. Different surface treatments, reported in Table 5.1, were also investigated in order to improve the adhesion and prevent the surface contamination. Additionally, a conditioning of one week in PBS solution has been systematically performed at the end of the process before sending the devices to the partners.

Instead of sterilising the structures in the autoclave, the devices were sterilised in ethanol:

- conditioning in a phosphate buffered solution (PBS) for 1-2 days
- sterilisation in ethanol for 30 min.
- treatment with an adhesion promoter, i.e. polylysine, laminine to improve the culture adhesion on the substrate.

Pyrex (7740) roughness	treatment after SU-8 development
< 20 Å	none
< 20 Å	2 min. in gamma-butyrolactone
< 20 Å	10 min. Plasma O_2
< 20 Å	5 min. BHF

Table 5.1: Different treatments introduced at the end of the SU-8 processing for the cleaning of the devices. All the devices were treated in PBS solution for one weak after processing. No differences have been observed during culturing of hippocampal neurones.

Using these devices, it has been possible to grow hippocampal rat neurons as shown in Figures 5.8 – 5.10. No evident difference in the biocompatibility has been observed for the different surface treatments of the devices, suggesting that mainly the sterilisation and the SU-8 development seem to be responsible for the previously observed low cellular viability.
In parallel, the adhesion of the SU-8 clusters in PBS solutions was investigated at room temperature. It has been found that after a few

days, the structures (300 μm or 550 μm) loose their adhesion and lift-off. This may be caused by the penetration of the liquid, by capillarity, at the SU-8 and the silicon nitride interface. Another reason might be the swelling of the SU-8. In the literature, no experimental data concerning the loss of the adhesion with time have been reported.

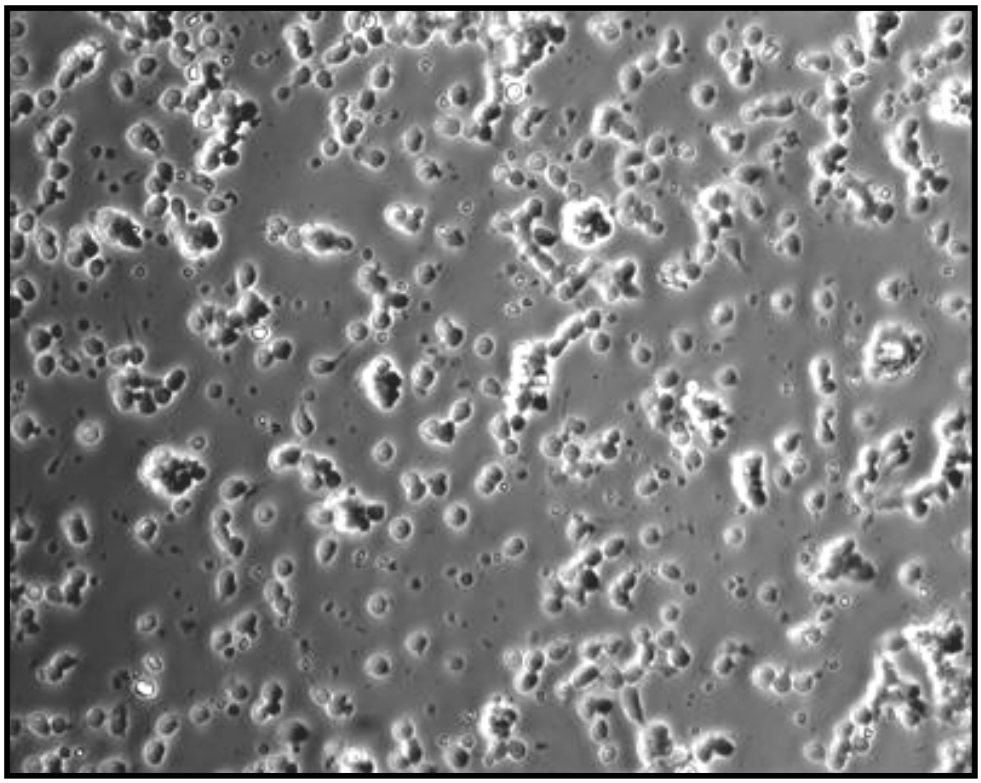

Figure 5.8: Rat hippocampal neurons after 4 hours in culture in the center of a SU-8 clustering well (photography performed at KNAW, Amsterdam, NL)

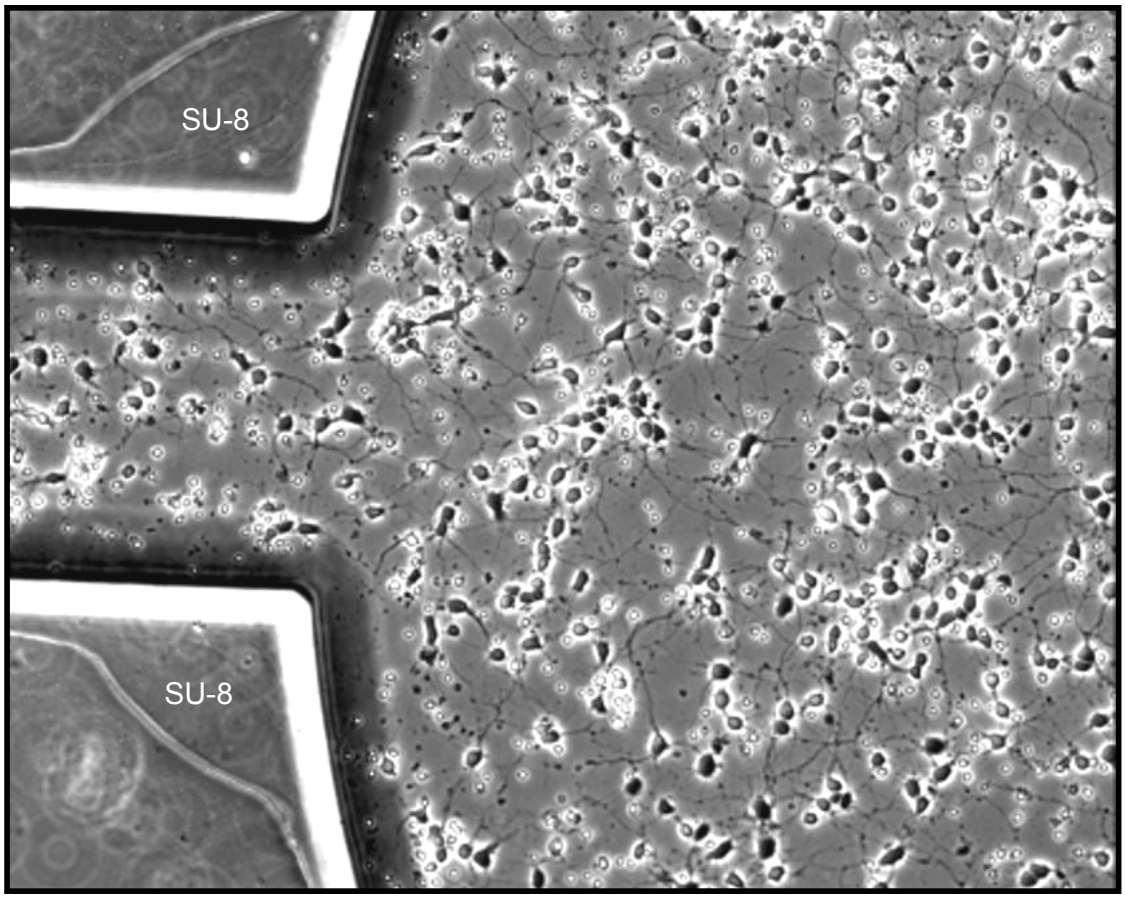

Figure 5.9: Rat hippocampal neurons after 3 days in culture into a SU-8 300 μm thick clustering well (photography performed at KNAW, Amsterdam, NL)

To improve the long-term adhesion, two approaches are being investigated: the mechanical stabilisation of the SU-8 structures by surrounding them with photosensitive glue and the development of an adhesion layer ensuring a chemical adhesion between the silicon nitride and the SU-8.

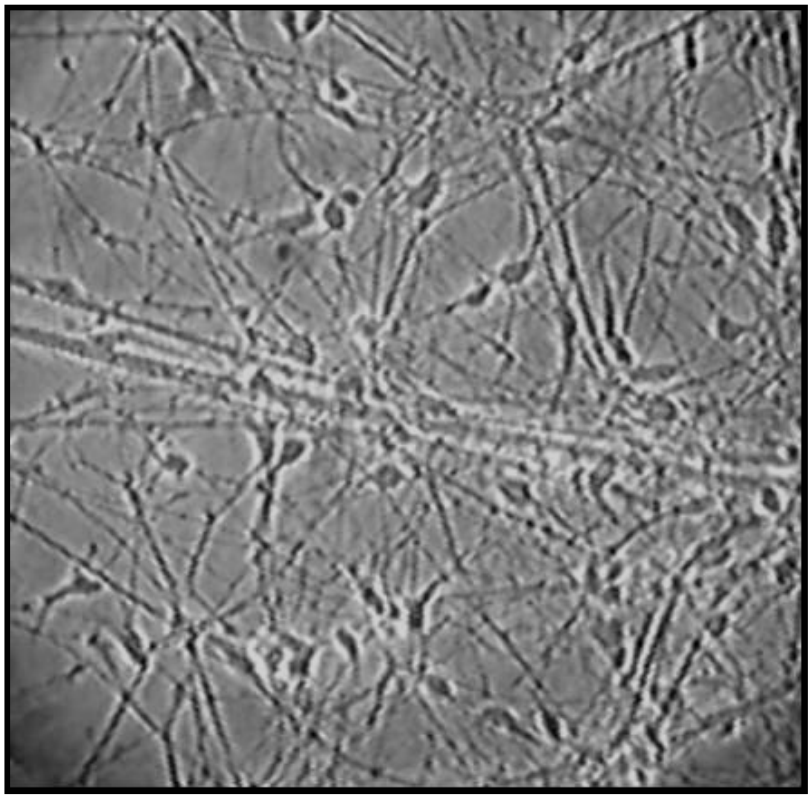

Figure 5.10: Rat hippocampal neurons after 9 days in culture on the center of a clustering well. (photography performed at INSERM, Bordeaux, F)

In the first approach, the SU-8 mechanical stability has been improved using UV glue (UVO 114, from Epotek). Although somewhat longer lifetimes could be obtained, this approach does not seem to be efficient enough for the envisaged use of two to three months.

In the second approach, an EPON 825 based photostructurable adhesion layer is currently under evaluation in collaboration with P. van der Wal. Preliminary adhesion tests in PBS show an excellent adhesion so far up to one month. Additionally, after mechanically removing the structures, residues resulting from a strong chemical adhesion are clearly visible.

5.3.2 The MEA

Arrays of microelectrodes with diameters of 10 μm, in platinum (planar), electrodeposited platinum (hillocks) and iridium-oxide were fabricated on pyrex substrates following the technologies and the layout described in chapter 3. The aim was to evaluate the biocompatibility and the recording/stimulation properties of different electrodes before integrating them in the final MTA structure.
After packaging (see chapter 3), the devices were sterilised in ethanol and conditioned in PBS solution as described previously. The results obtained confirmed that the growth of the hippocampal neurons on these structures was comparable to that, performed in parallel, with coverslip cultures (Figure 5.11).

Additionally, a new MEA has been designed in order to fit the clustering structure and provide a total of 60 microelectrodes divided in:

- 11 microelectrodes per lateral open-chamber
- 1 microelectrode per open-channel
- 12 microelectrodes in the central open-chamber.

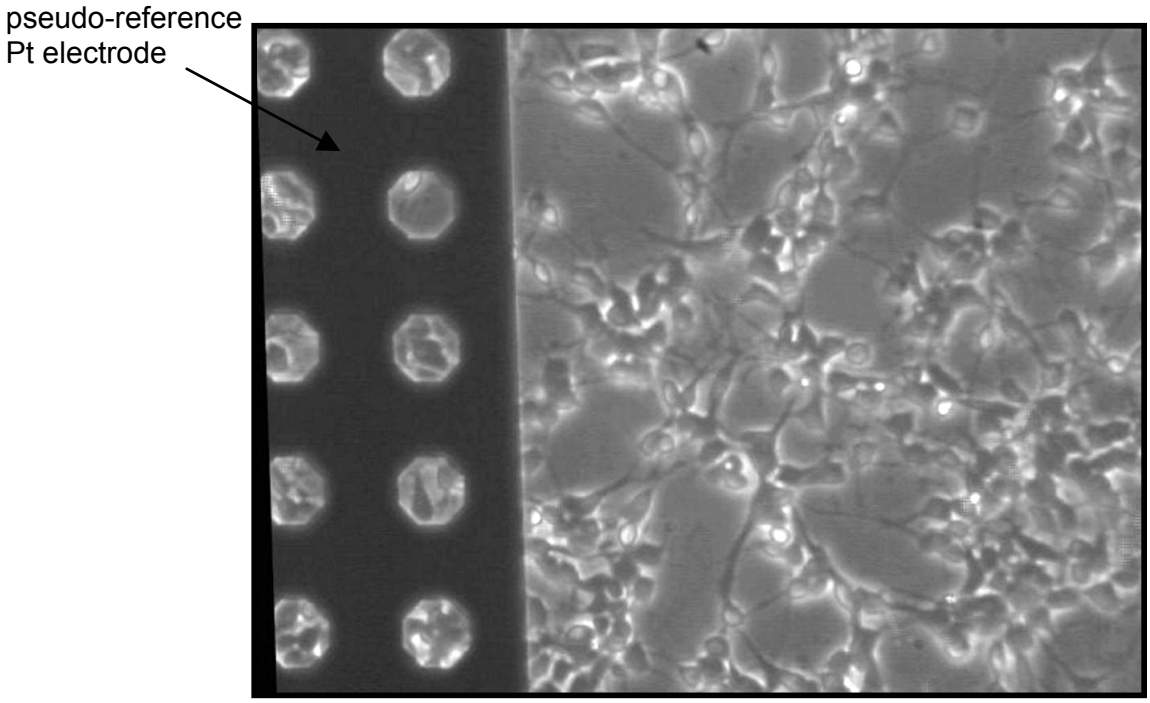

Figure 5.11: Rat hippocampal neurons on MEA after 18 hours in culture.
(photography performed at DIBE, Genova, It)

The repartition of the microelectrodes in the lateral (a) and central (b) open chamber follows the geometry shown in Figure 5.12.

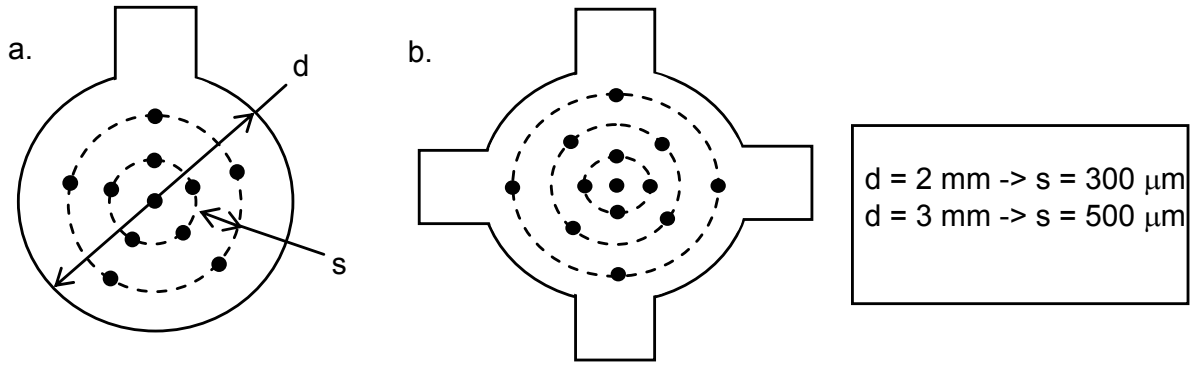

Figure 5.12: Disposition of the microelectrodes in (a) the lateral and (b) the central open-chamber for two chamber diameters, i.e. 2 mm and 3 mm.

Two types of MTAs with microelectrode diameters of respectively 10 μm and 30 μm were developed. This will allow to compare the characteristics of the microelectrodes diameters for both recording and stimulation.

5.4 The neurophysiological mini-incubator

The aim is to develop a stand-alone mini incubating system for neuronal cells allowing the long-term monitoring and stimulation of the network activity. Different portable incubation systems are reported in the literature for biosensor applications culturing embryonic chick cardiac myocytes [DeBusschere, 2001; Gray, 2001; Pancrazio, 1998]. They have been reviewed in [Pancrazio, 1999]. Recently, for neuronal cultures, the sealing of the culture dishes with a semi-permeable membrane (Teflon Fep) allowed neuronal survival up to one year [Potter, 2001]. The membrane prevent the culture media evaporation (and thus stabilizes its osmolarity) and allow cell culturing in a dry incubator limiting the risk of infections[13].

The first generation of the mini neurophysiological incubator (Figure 5.13) is a simplified version of the final system, and features :

1. cell culturing without perfusion of the media and without gas in and outlets
2. semi-permeable membrane (Teflon FEP) to prevent evaporation but ensuring O_2 permeability
3. temperature control :
   measurement in the culture media
   heating of the air in the surrounding chamber
4. no pH measurement (phenol red in the culture media can be used)

[13] The conventional cell culturing is performed in a humid incubator (95% RH) at 37°C where bacteria can easily proliferate.

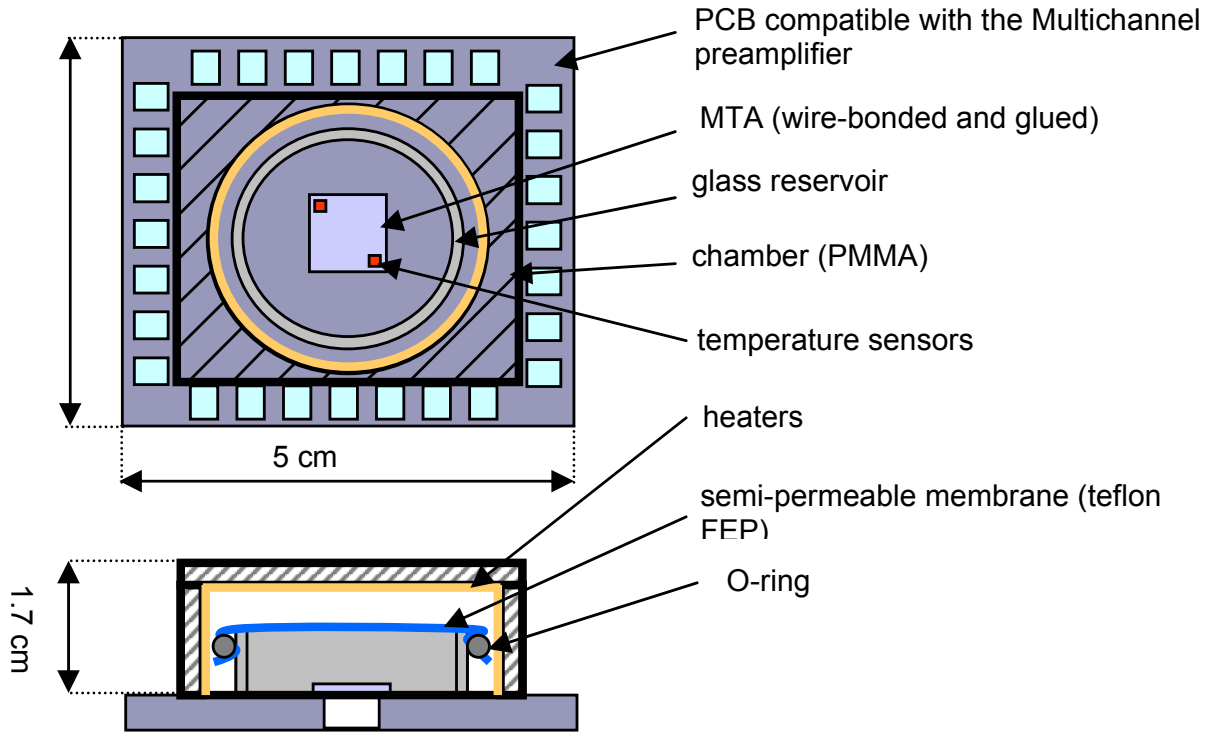

Figure 5.13: Scheme of the first generation of *NML*. The O-ring keeps the PMMA chamber in position allowing an easy assembling and dismantling of the top part.

The design and realisation of the heating elements and of the temperature sensor are described next. Additionally, even though this first design does not include the pH measurement, pH sensors based on iridium oxide have been evaluated.

5.4.1 Heating and temperature sensors

The temperature of the culture media has to be controlled with a precision of ± 0.1°C in the range between 30°C and 40°C. This control will be performed by a feed-back system. In the first investigated approach, the temperature is measured with two sensors integrated on the MTA (in contact with the culture media) and heating of the surrounding air is provided by two heaters placed on the PMMA chamber walls.

The heating system

Commercially available heating elements (thermal-clear heating, MINCO) have been fixed on the internal side of the PMMA chamber as well as on the top cover of the chamber in order to avoid vapour condensation (Figure 5.14). They have been selected considering the minimal power needed for keeping the internal chamber air at 37°C and compensate an external environment temperature of 25°C. In this first system, the cooling is realised by the thermal dissipation. Thus, the system does not function with external temperatures higher than the regulated one.
In order to estimate the minimal thermal power of the heating system, it is necessary to calculate the dissipated power. The total thermal resistor of the microsystem is described as the sum of the thermal resistors of the chamber walls (resistors in parallel):

$$R_{th,TOT} = \left[\frac{4}{R_{th,Sides}} + \frac{1}{R_{th,Cover}} + \frac{1}{R_{th,PCB}} \right]^{-1} \tag{5.1}$$

with the thermal resistors R_{th} for the sides, the cover and for the PCB defined with:

$$R_{th} = \frac{t}{\lambda A} \tag{5.2}$$

where t is the thickness of the wall, A is the area and λ the thermal conductivity (λ_{PMMA} = 0.18 W/m°K; λ_{PCB} = 0.15 W/m°K).

Considering the worst case of a minimal walls thickness of 2 mm and 1.5 mm for the PCB, the resulting total thermal resistor is 2.6 °K/W.

Thus, the thermal current I_{th} defined as:

$$i_{th} = \frac{\Delta T}{R_{th,TOT}} \tag{5.3}$$

results in 4.65 W for a ΔT of 12 °C. The minimal thermal power that the heating system has to provide is thus 4.65 W, and the heating elements have been dimensioned following the specifications of the provider.

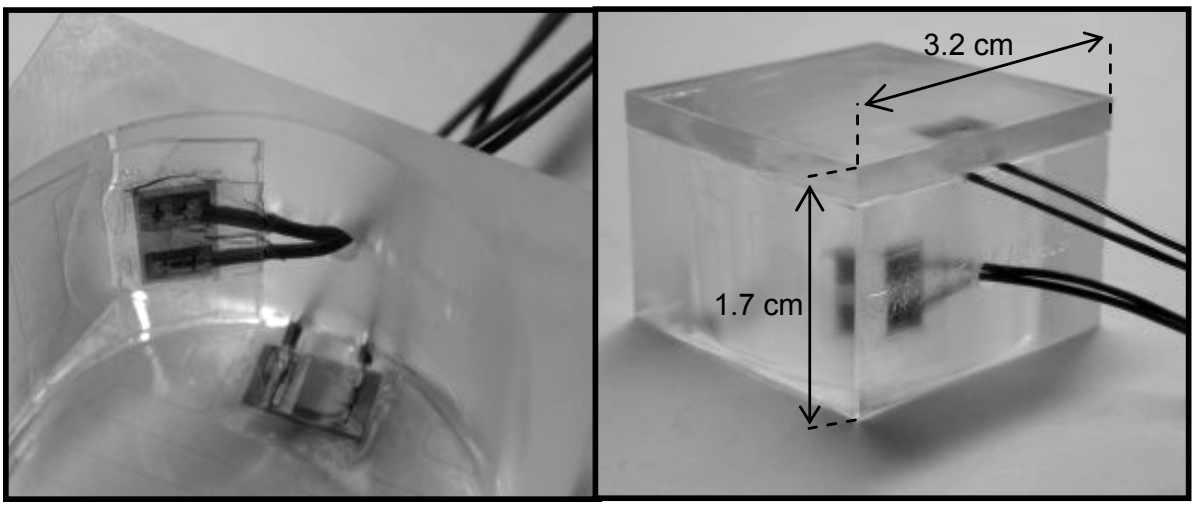

Figure 5.14: First prototype of the heating chamber. Two thermal-clear heating elements (from MINCO) have been fixed on the PMMA chamber.

The temperature sensor

There are different types of temperature sensors that could be integrated in the NML, i.e RTD (resistive temperature detector), thermistor, thermocouple and bipolar transistor. The RTD presents the advantage of being realisable on the MTA with the same technology used for the microelectrodes. We have therefore started by investigating Pt- RTDs with a metal thickness of 1500Å.

The principle of an RTD is based on the variation of the resistivity as a function of temperature, and the resistor towards the temperature can be calculated with:

$$R_T = R_0(1 + \alpha \cdot \Delta T) \tag{5.4}$$

where R_0 is the resistance at a reference temperature T_0, α is the temperature coefficient of the resistance (or TCR) and ΔT is the temperature difference towards T_0.

Materials showing a high TCR like Pt are thus preferred for a higher sensitivity. Thin film platinum has a TCR between $1.5.10^{-3}$ °C^{-1} and $2.5.10^{-3}$°C^{-1} and the resistivity ρ_{Pt}, of $1.06.10^{-7}$ Ωm (at 20°C).
Two line widths, 5 μm and 10 μm, and an area of 1 mm x 1 mm are considered for the RTD design. In order to achieve a high sensitivity (10 mV/0.1°C) and to limit the current applied to the resistor to a few mA, the integrated resistor has been maximised with a serpentine geometry. This gives for the theoretical resistors 3.5 kΩ for the 10 μm line sensor and 14.2 kΩ for the 5 μm line for a current of 7.2 mA and 1.8 mA respectively.

The devices have been realised by lift-off (see Chapter 3), with 200 Å of Ti and 1300 Å of Pt (Figures 5.15). The sensors behaviour has been evaluated in the temperature range between 22°C and 140°C (measured with a thermocouple). The resulting R(T) behaviour for the two layouts of the sensors is shown in Figure 5.16. The resulting specifications of the sensors are summarised in the Table 5.2. Experimentally, an average TCR value of 2.8 10^{-3} °$C^{-1}$and an average resistivity at 22.4°C of $1.78.10^{-7}$ Ωm have been obtained.

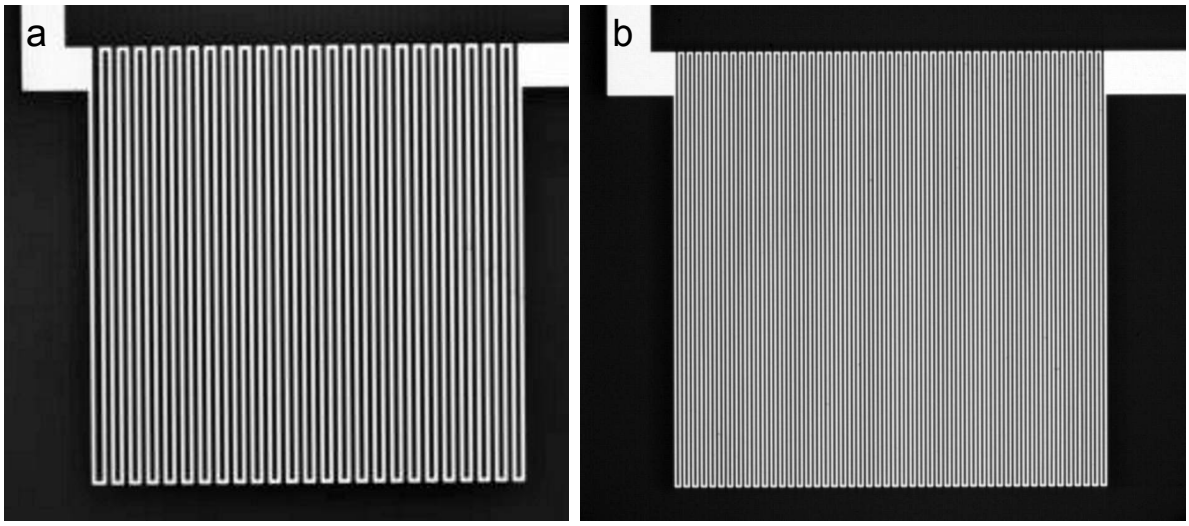

Figure 5.15: Pt RTD on 1 mm^2 surface area with (a) metal line of 10 μm and (b) metal line of 5 μm

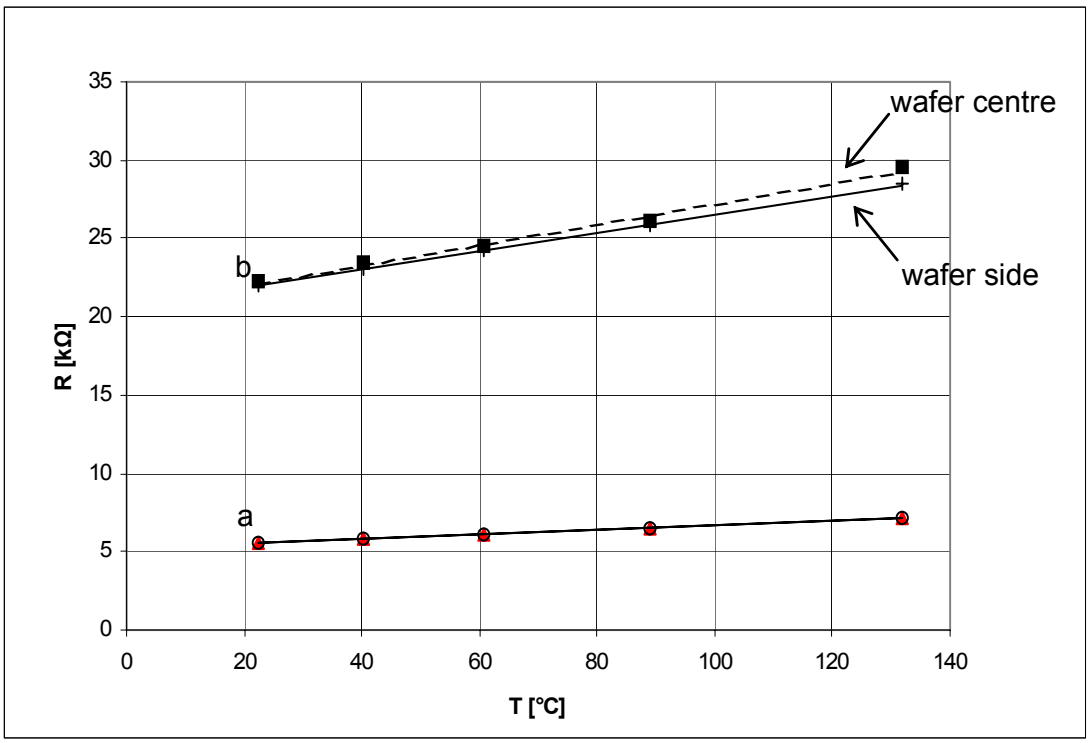

Figure 5.16: Measured resistance against the temperature for (a) Pt devices with 10 μm lines and (b) Pt devices with 5 μm lines.

Resistor line width [μm]	Resistor at 24°C ($R_{24°C}$)	Sensitivity Ω/°C
10 μm	6.7 kΩ	14.8
5 μm	25 kΩ	64.8

Table 5.2: Summary of the temperature sensitivity (experimental).

5.4.2 pH sensing

A healthy culture of neurons typically shows a pH of 7.3. An acidification of the media is observed when an infection occurs in the culture. For these reasons, the monitoring of the pH is an important indication of the culture health and its monitoring is thus necessary for long-term culturing.

In MEAs technology, a commonly used method for monitoring the pH is by optical observation of the colour changing of the culture media. In fact, the culture media contains phenol-red which, reacting with the CO_2 in the culture chamber (95%) results in a red colour for a pH of about 7. Lower pH tend to a yellowed colour. The first prototype of NML will not include pH sensors. However, for monitoring the monitoring of several MEAs in parallel, it would be preferable to include a pH sensor on the device.

The integration of iridium oxide pH sensors is a preferable choice for this application compared to other techniques, i.e. ISFETs due to the simplicity of their fabrication. In fact, as described in chapter 3, iridium oxide electrodes can be integrated structuring at first iridium electrodes by lift-off and secondly, electrochemically oxidising them in H_2SO_4. This motivated the preliminary characterisation of IrO_x electrodes towards pH in a range between 6 and 8. The potential referred to a Ag/AgCl reference electrode has been measured using a potentiostat and the resulting voltage versus pH behaviour is shown in Figure 5.17. A pH sensitivity of 67 mV/decade was obtained. Ongoing tests on different thicknesses of the oxide layer will allow to further optimise the Ir/IrO_x pH sensing behaviour.

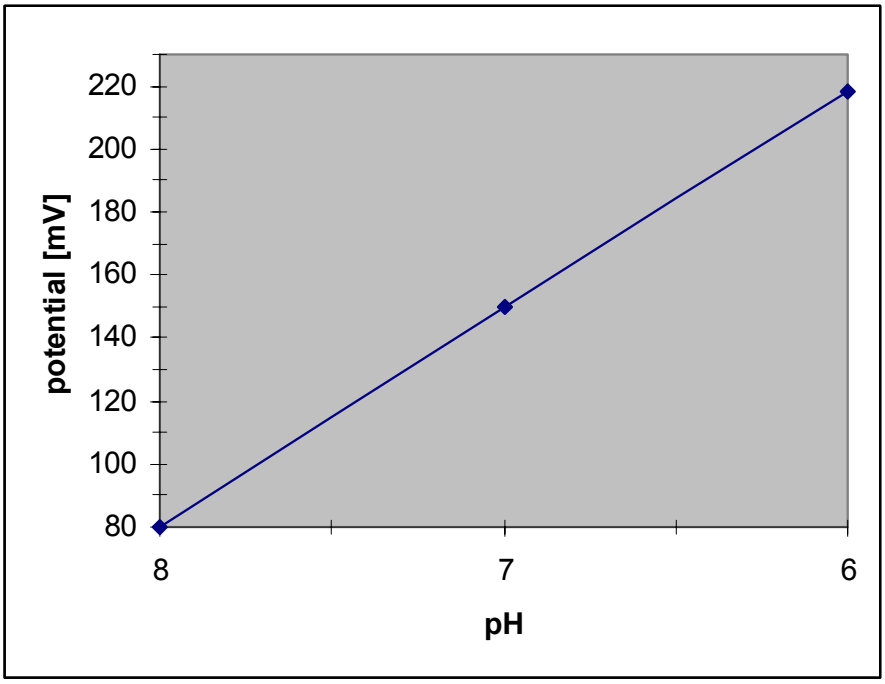

Figure 5.17: Measured pH sensitivity of IrO_x microelectrodes (67 mV/decade).

5.5 Outline and future work

Accordingly to the first year work plan of this EU project, all individual elements of the first generation of NML i.e. without media perfusion, have been realised and evaluated. This development includes several aspects, e.g. the network clustering, the MEAs and the culture incubation (temperature, pH).

SU-8 clustering structures of 300 μm and 550 μm thick have been developed with single and double layer technologies. However, the adhesion of the SU-8 in humid environment has not been adequate in the first series of devices. The lifting-off of the SU-8 structures after a few days in PBS solution (or in water) was not previously reported in the literature. Even though this is a problem for this project, this effect could be exploited in applications where the removal of SU-8 structures is required. Different ways of improving the longer-term stability have been investigated. Currently, SU-8 clustering structures with an EPON 825 based adhesion inter-layer

show a reasonable stability up to one month in PBS solution. The biocompatibility of these devices is currently under evaluation.
In parallel to fabricating the clustering structures in SU-8, a Si-glass device has already been designed and will be fabricated. These devices are intended to be complementary to the SU-8 ones.
MEAs featuring 60 microelectrodes are currently under fabrication and their evaluation for the stimulation and the recording will contribute to improve our today knowledge of the neuronal-interface.
The presented development of the first prototype of NML is a simplified version of the final one. The originality of the final system is the fabrication of a stand-alone system for both culturing and electrophysiology. This will allow the monitoring of parallel cultures.

5.6 Bibliography

Arquint, P., et al., Organic Membranes for Miniaturized Electrochemical Sensors - Fabrication of a Combined Po2, Pco2 and pH Sensor. Journal of Electroanalytical Chemistry, 1994. **378**(1-2): p. 177-183.

DeBusschere, B.D. and G.T.A. Kovacs, Portable cell-based biosensor system using integrated CMOS cell-cartridges. Biosensors & Bioelectronics, 2001. **16**(7-8): p. 543-556.

Dellmann, L., et al., Two steps micromoulding and photopolymer high-aspect ratio structuring for applications in piezoelectric motor components. Microsystem Technologies, 1998. **4**(3): p. 147-150.

Dellmann, L., et al., Fabrication process of high aspect ratio elastic and SU-8 structures for piezoelectric motor applications. Sensors and Actuators a-Physical, 1998, **70**(1-2): p. 42-47.

Feng, R. and R.J. Farris, Investigation of thermal and mechanical properties of SU8 negative photoresist coatings. Abstracts of Papers of the American Chemical Society, 2001, **222**: p. 228-PMSE.

Gray, S.A., et al., Design and demonstration of an automated cell-based biosensor. Biosensors & Bioelectronics, 2001. **16**(7-8): p. 535-542.

Griscom, L., et al., Cell placement and neural guidance using a three-dimensional microfluidic array. Japanese Journal of Applied Physics Part 1-Regular Papers Short Notes & Review Papers, 2001. **40**(9A): p. 5485-5490.

Heuschkel, M.O., et al., A three dimensional multi-electrode array for multi-site stimulation and recording in acute brain slices. Journal of Neuroscience Methods, 2002, **114**: p. 135-148.

Lorenz, H., et al., High-aspect-ratio, ultrathick, negative-tone near-UV photoresist and its applications for MEMS. Sensors and Actuators a-Physical, 1998, **64**(1): p. 33-39.

Lorenz, H., et al., SU-8: a low-cost negative resist for MEMS. Journal of Micromechanics and Microengineering, 1997, **7**(3): p. 121-124.

Lorenz, H., et al., Fabrication of photoplastic high-aspect ratio microparts and micromolds using SU-8 UV resist. Microsystem Technologies, 1998. **4**(3): p. 143-146.

O'Brien, J., et al., Advanced photoresist technologies for microsystems. Journal of Micromechanics and Microengineering, 2001. **11**(4): p. 353-358.

Pancrazio, J.J., et al., Portable cell-based biosensor system for toxin detection. Sensors and Actuators B-Chemical, 1998. **53**(3): p. 179-185.

Pancrazio, J.J., et al., Development and application of cell-based biosensors. Annals of Biomedical Engineering, 1999. **27**(6): p. 697-711.

Potter, S.M. and T.B. DeMarse, A new approach to neural cell culture for long-term studies. Journal of Neuroscience Methods, 2001. **110**(1-2): p. 17-24.

Tay, F.E.H., et al., A novel micro-machining method for the fabrication of thick- film SU-8 embedded micro-channels. Journal of Micromechanics and Microengineering, 2001, **11**(1): p. 27-32.

Thiebaud, P., et al., PDMS device for patterned application of microfluids to neuronal cells arranged by microcontact printing. Biosensors & Bioelectronics, 2002. **17**(1-2): p. 87-93.

Weisenberg, B.A. and D.L. Mooradian, Hemocompatibility of materials used in microelectromechanical systems: Platelet adhesion and morphology in vitro. Journal of Biomedical Materials Research, 2002. **60**(2): p. 283-291.

Zhang, J., K.L. Tan, and H.Q. Gong, Characterization of the polymerization of SU-8 photoresist and its applications in micro-electro-mechanical systems (MEMS). Polymer Testing, 2001. **20**(6): p. 693-701.

Zhang, J., et al., Polymerization optimization of SU-8 photoresist and its applications in microfluidic systems and MEMS. Journal of Micromechanics and Microengineering, 2001, **11**(1): p. 20-26.

6 SUMMARY AND OUTLOOK

The aim of this work was to contribute to the development of MEAs devices considering the ever increasing demands of current research in in-vitro neurophysiology, i.e. better recording / stimulation performances, higher electrode densities, large active areas.

This thesis can broadly be divided into four parts:

- “conventional” MEAs and their functional properties.
- a mix and match technology for fabricating nanoelectrodes.
- an approach for realising high-density arrays based on the APS, CMOS technology.
- the integration of the MEAs in a mini incubator for realising a complete electrophysiological microsystem.

Due to the high multi-disciplinarity of this field it has been necessary to introduce some basic concepts involved in MEAs technology (Chapter 1 and 2). The electrode-electrolyte-neuron interface has been discussed in order to highlight the critical aspects involved in recording and stimulation (Chapter 2). It has to be pointed out that several of those parameters such as the sealing resistor, are dependent on the “biology” and introduce an additional complexity to the system. The electrode impedance plays an important role for recording, in particular for low frequency signals where it shows a mainly capacitive behaviour. It has thus to be compensated by the input impedance of the measuring circuit.

Thin-film and electrochemical technologies for fabricating and for modifying platinum and iridium microelectrodes arrays, on silicon or pyrex substrates, have been presented in Chapter 3. The lift-off of platinum or iridium electrodes has been improved with a two layers

photoresist technique towards the process repeatability, the wafer homogeneity and for solving the problem of metal wing tips. In these conditions a resolution down to 2 μm has been achieved (exposing at a wavelength of 365 nm).
The microelectrodes behaviour for recording / stimulation has been improved by platinum electrodeposition on planar MEAs. This leads to hillock-shaped electrodes showing lower electrode impedances, and better recording performances. This technique allows the precise control of the deposited metal thickness. The real electrode radius has been calculated with the diffusion limited current in a ferrocyanide solution.
The electrochemical oxidation of iridium electrodes allowed also to improve the electrode behaviour under stimulation by increasing the injection charge.
These arrays are exploited in the current Neurobit European project.

The electrodes have been scaled down to nanometer dimensions with a mix-and-match approach (e-beam and conventional lithography). This method shows the main advantage of reducing the e-beam writing time. Such electrodes could allow the measurement in the nano-scale domain of cellular or sub-cellular physiology. The established technologies have been evaluated by fabricating nano-disk electrodes with diameters between 200 nm and 400 nm and nano-IDAs with a pitch of 785 nm and a gap of about 260 nm). A preliminary characterisation of these nano-devices has been realised with classical electrochemical methods. Contradicting the theory, the diffusion limited current of nano-disk electrodes with a passiviation of 2000 Å thick shows a behaviour comparable to that calculated for a non-embedded electrode with the same dimensions. However, more measurements are required to confirm this observation.
Nano-IDAs have been evaluated using ferrocyanide as the benchmark species, achieving a collection efficiency of 99 %.
Finally, the gap of nano-IDAs has been additionally reduced to ~100 nm by electroplating platinum on one electrode.

The concept, the design and the first generation of an APS based high density MEA (electrode pitch down to cellular dimensions) has been presented in Chapter 4 and electrically evaluated in a phosphate solution and under culture conditions. The realised device features 64 x 64 pixels on a surface of 2.56 x 2.56 mm^2. Each pixel has a dimension of 40 x 40 μm^2, a microelectrode of 20 x 20 μm^2 and an underneath pre-amplifier circuit. The analogue amplifier has been designed for providing different working modes for noise / signal trade-off. Simulation results show an open-loop programmable gain between 23 dB up to 50 dB with, respectively, a frequency bandwidth of 270 kHz to 14 kHz and an input referred noise of 79 μV_{rms}. In a phosphate solution, with a DC polarisation of 0.7 V, a gain between 29.5 dB and 30.8 dB on a bandwidth of 10 kHz has been obtained. However, due to the high sensitivity to DC offsets on the differential pair, this mode shows an unstable gain and is inadequate for measuring extracellular signals. The closed-loop mode, unity-gain, shows a better stability and provides a low-output impedance. However, even though the electrical functionality of the device has been demonstrated, it has not been yet possible to record the electrophysiological activity of cardiomyocytes culture. Ongoing work is focusing on redesigning the electrical interface for reducing its noise contributions.
An original gold electroless technique has been developed for rapidly post-processing the CMOS devices, since the standard CMOS aluminium layer is not usable as electrode material. The resulting gold electrodes have been evaluated electrochemically by cyclic voltammetry and with XPS measurements, showing an excellent quality. The biocompatibility has been confirmed with the preliminary tests on cardiomyocyte cultures.

In the context of the Neurobit project a mini neurophysiological laboratory is under development (Chapter 5). The results achieved after one year have been presented. SU-8 clustering structures of 350 μm and 550 μm have been fabricated improving the technology towards the biocompatibility and achieving thickness homogeneities

of 2-3 %. However, it has been observed that the SU-8 structures lift-off after a few days immersed in PBS. Alternative solutions have been developed. One of them is based on the use of an adhesion layer for promoting chemical bonding between the silicon nitride and the SU-8. Up to now, with this last approach, structures showing good adhesion for more than a month in PBS solution have been realised. Additionally, rat hippocampal neurons have recently shown a good viability on those devices. Finally, the first prototype of a mini incubator integrating Pt-RTD sensors, heating elements and pH IrOx sensors has been presented. The final challenge is to develop a stand-alone long-term mini incubator.

The materials, techniques and methods developed during this thesis constitute a large basis for future developments in Bio-MEMS and neuro-electrical interfaces.

ANNEXE I

Gain versus transistor dimensions

The relation between the open-loop gain and the input transistors dimensions (channel length and width) in the differential amplifier (Figure 4.2) is described considering the model of strong inversion of a MOS transistor in saturation.

The transistor is in saturation when:

$$U_{DS} \geq \frac{U_{GS} - V_{TH}}{n}$$

and the drain-source current is defined by the quadratic relation:

$$I_{DS} = \frac{\beta}{2n}\left(U_{GS} - V_{TH}\right)^2$$

where, U_{DS} is the drain-source voltage; U_{GS} is the gate-source voltage; V_{TH} is the threshold voltage; n [1, 2] and the parameter of transconductance is defined with:

$$\beta = \mu \cdot C_{ox} \cdot \frac{W}{L_{eff}}$$

with μ the electron mobility, C_{ox} defined as ε_{ox} / t_{ox} (gate oxide permittivity / gate oxide thickness) and W, L_{eff} the respective width and effective length of the gate channel.

The transconductance for a little AC signal is defined by

$$g_m = \frac{\Delta I_{DS}}{\Delta U_{GS}} = \sqrt{\frac{2 \cdot I_{DS} \cdot \beta}{n_0}} = \sqrt{\frac{2 \cdot I_{DS} \cdot \mu \cdot C_{ox} \cdot W}{n_0 \cdot L_{eff}}}$$

and the output conductance (between drain and source) is defined by:

$$g_o = \frac{\Delta I_{DS}}{\Delta U_{DS}} = \frac{I_{DS}}{V_{early} \cdot L_{eff}}$$

To calculate the gain, it is possible to propagate the signal from the input to the output exploiting the symmetricity of the circuit as shown in next figures.

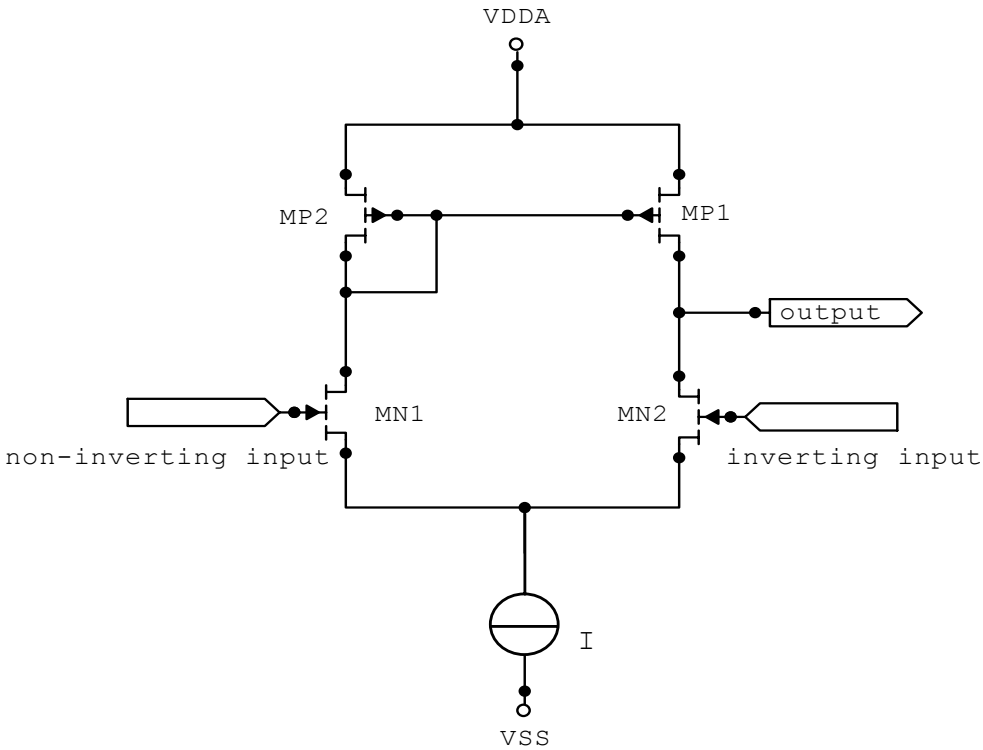

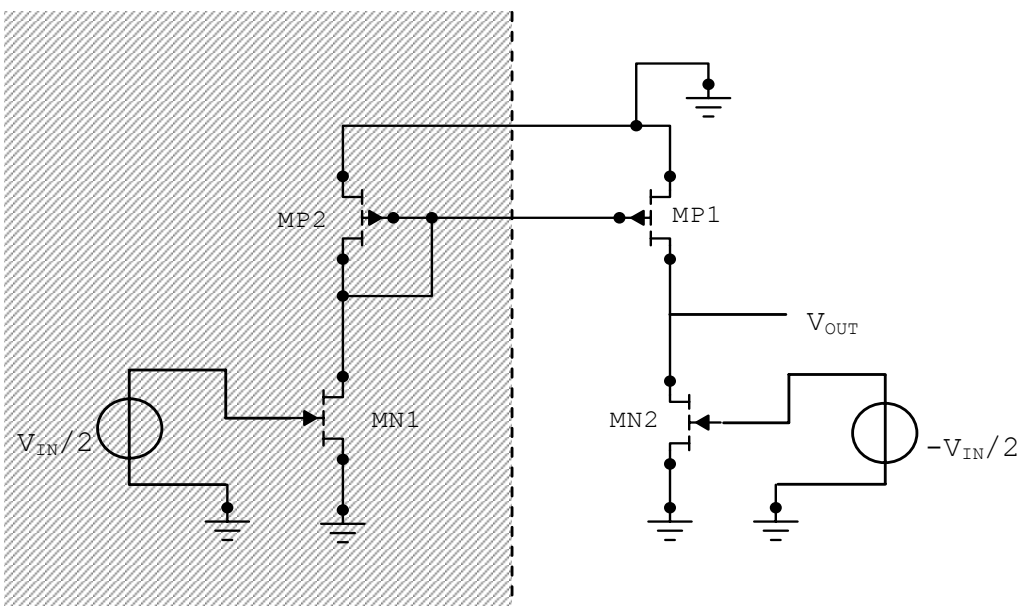

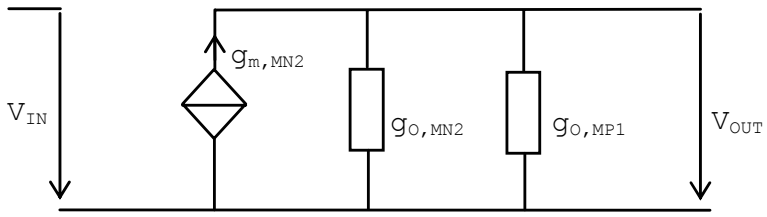

The gain results in:

$$G = \frac{V_{out}}{V_{in}} = \frac{g_{m,MN2}}{g_{o,MN2} + g_{o,MP1}}$$

Note that the transistors MN2-MN1 and MP2-MP1 are identical in dimensions.
Using the expression for g_m and g_o calculated above, the formula for the gain becomes:

$$G = \frac{V_{out}}{V_{in}} = \frac{g_{m,MN2}}{g_{o,MN2} + g_{o,MP1}} = \sqrt{\frac{2\mu C_{ox,MN2} W_{MN2} V_{early}{}^2 (L_{eff,MN2} + L_{eff,MP1})^2}{n_0 I_{DE} L_{eff,MN2}}}$$

From this expression it is observed that:

1. *the gain increases with the square root of the width of the input transistor.*
2. *the gain increases with the square root of decreasing drain-source current.*

Additionally considering relation of C_{ox}:

$$G \propto \sqrt{L_{eff,MN2} + 2L_{eff,MP1} + \frac{(L_{eff,MP1})^2}{L_{eff,MN2}}}$$

depending on the relation between $L_{eff,MN2}$ and $L_{eff,MP1}$ the gain results in three possible cases:

$L_{eff,MN2} = L_{eff,MP1}$ $\qquad G_{1=4} \propto \sqrt{4L_{eff,MN2}}$

$L_{eff,MN2} > L_{eff,MP1}$

e.g. $L_{eff,MN2} = 0.5\ L_{eff,MP1}$ $\qquad G_{1=4} \propto \sqrt{2.25L_{eff,MN2}}$

$L_{eff,MN2} < L_{eff,MP1}$

e.g. $L_{eff,MN2} = 2\ L_{eff,MP1}$ $\qquad G_{1=4} \propto \sqrt{9L_{eff,MN2}}$

and thus,

$$G_{1<4} > G_{1=4} > G_{1>4}$$

With regard to the gain, this results in:

3. the gain increases for long transistors in the current mirror and shorter transistors in the differential pair.

ANNEXE II

Evaluation of the amplifier noise

In general, the noise in a MOS transistor is modelled by three different noise sources which are not correlated: the thermal noise, shot noise and flicker noise.

Thermal noise

The variance i^2 of a current flowing through a conductor characterised by a resistance R is given by the Johnson noise:

$$i^2 = \frac{4KT}{R} B$$

where K is the Boltzmann constant, T the temperature, R the resistance and B the bandwidth.

In the case of a MOS transistor, the resistance R is represented by the channel created between source and drain. For a saturated MOS transistor in strong inversion and considering the transistor transconductance g_m it results:

$$i^2 = \frac{8}{3} KTg_m B$$

The thermal noise is a white noise which means that the power spectral density is frequency independent and constant over the bandwidth.

Shot noise

Physically it is not possible to create an ideal current source. A variance i^2 is always associated with a current I for a pure statistical reason. The variance i^2 associated with a current I is known as shot noise and occurs at the interface of the source-bulk junction of the MOS transistor. The shot noise is also a white noise. Its variance i^2 is given by:

$$i^2 = 2qIB$$

where B represents the bandwidth and q the elementary charge.
For a MOS transistor in strong inversion and considering the transistor transconductance g_m, after development it results:

$$i^2 = 4KT \cdot \frac{n}{2} \cdot g_m \sqrt{1 + UPLIM} \cdot B$$

Flicker noise (1/f noise)

Flicker noise is generated by the charge carrier density fluctuations within the channel of the MOS transistor. The flicker noise shows a typical 1/f noise power spectrum, given by:

$$u_{n,f}^2 = K_{n,p} \cdot \frac{1}{W \cdot L_{eff}} \cdot \frac{1}{f}$$

The technological parameter $K_{n,p}$ is different for n- and p-transistors, i.e. $K_n \approx 10 \cdot K_p$ which implies that n-transistors produce about 10 times more flicker noise than p-transistors do.
The fact that the flicker noise is inverse proportional to the device dimensions explains why MOS transistors are never designed with minimum gate area for optimum noise performance in amplifier structures.

Total referred input noise

A common method when analysing noise in a transistor consists in placing the different noise sources outside the transistor and to consider the transistor itself to be noiseless. Hence the noise sources at the transistors output can be referred to its input, as illustrated next.

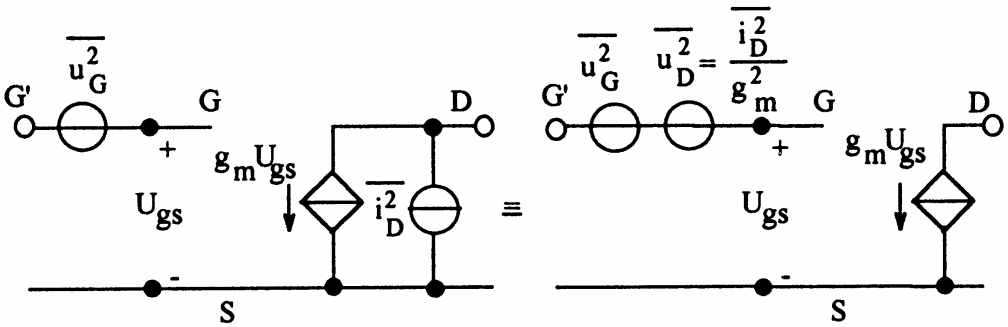

The concept of calculating the referred input noise enables to compare the contributions of the different noise sources since the overall noise is written as the sum of the single contributions. Since the drain current of a MOS transistor is commanded by a voltage source, thermal noise and shot noise are expressed in terms of voltage sources when referred to the transistors input considering:

$$U = \frac{I}{g_m}$$

The overall input referred noise results in:

$$u_{n,eq}^2 = \frac{K_{n,p}}{W \cdot L_{eff} \cdot f} + 4KT\frac{2}{3g_m} \qquad \text{(strong inversion)}$$

$$u_{n,eq}^2 = \frac{K_{n,p}}{W \cdot L_{eff} \cdot f} + 4KT\frac{n}{2g_m} \qquad \text{(weak inversion)}$$

The first term describes the flicker noise and is dominant at low frequencies. For higher frequencies white noise (thermal or shot noise) dominates flicker noise and the power spectral density gets constant and frequency-independent. In the case of the strong inversion the second term represents the thermal noise which dominates the shot noise. However, in weak inversion, shot noise dominates thermal noise.

Noise reduction by design optimisation

The noise contribution of the input stage is the most important to the overall noise production, because noise already present at the input stage will be amplified by the following stages.

In the case of the 5-transistor OTA, the transistors of the differential pair contribute directly to noise production whereas the transistors in the current mirror contribute to noise production accordingly to the relation between the transconductance of the transistors in the differential pair and in the current mirror, respectively. In order to minimise noise, the transistors of the differential pair must be wide to increase theirs transconductance whereas the transistors in the current mirror must be long to decrease their transconductance.

ANNEXE III

Simulation results

Simulations of the gain (G), of the bandwidth (B) and of the noise have been performed in function of the transistor dimensions, i.e. the input transistors (MN1,2), the transistors in the current mirror of the input pair (MP1,2), and the transistors of the biasing current mirror (MN3,4). The technology parameters of the CMOS technology Alcatel 0.5 μm have been used.
The calculated values allow to roughly estimate the amplifier characteristics and optimise the design.

MN1,2		MP1,2		MN3,4		G	B	Noise
w [μm]	l [μm]	w [μm]	l [μm]	w [μm]	l [μm]	[dB]	[kHz]	[μV]
6	9	1	9	1	4	48.621	18.266	78.141
6	9	1	9	2	4	43.515	33.829	78.632
6	9	1	9	2	2	41.718	42.098	78.916
6	11	1	9	0.9	1.3	43.685	30.072	79.085
6	9	1	9	3	3	41.226	44.277	79.207
6	9	1	9	1.5	1.5	42.212	40.026	79.324
6	10	1	9	0.9	1.3	43.44	32.71	79.351
6	10	1	9	1.1	1.3	42.965	34.403	79.374
6	10	1	9	1.3	1.3	42.644	35.588	79.411
6	11	1	9	0.9	1.1	43.591	30.582	79.536
6	9	1	9	0.9	1.3	43.221	34.987	79.544
6	9	1	9	1.1	1.3	42.8	36.798	79.577
6	9	1	9	1.3	1.3	42.515	38.702	79.622
5	**10**	**1**	**10**	**1.1**	**3**	**40.619**	**39.804**	**79.636**
6	11	1	9	1.1	1.3	43.152	32.164	79.721

6	11	1	9	1.3	1.3	42.791	33.625	79.752
6	10	1	9	0.9	1.1	43.406	32.71	79.822
6	10	1	9	1.1	1.1	43.057	33.829	79.873
6	10	1	9	1.3	1.1	42.813	34.987	79.928
6	9	1	9	0.9	1.1	43.238	34.87	80.028
6	9	1	9	1.1	1.1	42.925	36.798	80.085
6	9	1	9	1.3	1.1	42.704	37.422	80.144
6	11	1	9	1.1	1.1	43.203	32.164	80.217
6	11	1	9	1.3	1.1	42.934	32.71	80.269
5	10	1	9.5	1.1	2	40.56	40.475	80.315
6	11	1	9	1.1	0.9	43.518	30.582	80.422
5	10	1	9.5	2	2	37.146	60.723	80.455
5	10	1	9	2	2	41.927	35.58	80.534
5	10	1	9.2	2	2	40.204	43.272	80.572
6	10	1	9	0.9	0.9	43.641	32.614	80.656
5	10	1	9.3	2	2	39.251	47.834	80.701
6	10	1	9	1.1	0.9	43.397	32.71	80.729
5	9	1	9	2	2	41.705	38.702	80.765
6	10	1	9	1.3	0.9	43.22	33.265	80.798
6	11	1	9	0.9	0.9	43.785	29.963	80.835
6	9	1	9	0.9	0.9	43.506	33.829	80.87
6	9	1	9	1.1	0.9	43.282	34.987	80.946
6	9	1	9	1.3	0.9	43.12	35.58	81.02
6	11	1	9	1.3	0.9	43.326	31.628	81.148
6	9	2	11	1.1	1.1	53.648	10.89	81.327
6	10	2	10	1.1	1.1	53.967	9.968	81.545
6	11	2	11	1.1	1.1	53.636	9.838	81.556
5	10	1	10	2	2	30.673	121.91	81.561
5	10	1	9	1.1	1.1	43.087	25.416	81.644
5	10	1	9	1.3	1.1	42.796	32.164	81.689
6	9	2	10	1.1	1.1	53.995	10.418	81.712
5	10	1	9.2	1.1	1.1	41.55	36.615	81.743
5	10	1	8	1.1	1.1	48.18	17.368	81.752

5	11	1	9	1.1	1.1	43.321	28.499	81.817
6	10	2	11	1.1	1.1	53.646	10.351	81.85
5	11	1	9	1.3	1.1	42.991	29.963	81.855
6	11	1	10	1.1	1.1	32.384	104.89	81.881
5	9	1	9	1.1	1.1	42.878	33.265	81.883
5	9	1	9	1.3	1.1	42.621	34.403	81.932
6	11	2	10	1.1	1.1	53.933	9.4	81.992
6	10	2	9	1.1	1.1	54.103	9.838	82.042
6	9	2	9	1.1	1.1	54.158	10.177	82.124
5	10	1	7	1.1	1.1	50.567	13.274	82.366
6	11	2	9	1.1	1.1	54.044	9.351	82.537
6	10	1	10	1.1	1.1	31.591	115.5	82.801
6	9	1	10	1.1	1.1	31.543	127.77	82.894
6	9	3	11	1.1	1.1	55.05	9.351	83.128
5	10	2	11	1.1	1.1	53.15	9.838	83.13
5	11	1	10	1.1	1.1	33.534	84.416	83.204
5	11	2	11	1.1	1.1	53.148	9.351	83.284
6	11	3	11	1.1	1.1	54.937	8.352	83.365
5	10	1	10	1.1	1.1	32.952	94.889	83.376
6	11	3	10	1.1	1.1	54.837	6.553	83.442
5	10	2	10	1.1	1.1	53.317	9.695	83.469
6	10	3	10	1.1	1.1	54.911	8.888	83.631
6	10	3	9	1.1	1.1	54.752	8.962	83.691
6	9	3	10	1.1	1.1	54.985	9.194	83.695
6	10	3	11	1.1	1.1	54.995	8.738	83.757
5	11	2	10	1.1	1.1	53.435	9.084	83.774
4	11	1	9	1.1	1.1	43.747	24.242	83.799
5	9	2	11	1.1	1.1	53.147	10.527	83.799
4	11	1	9	1.3	1.1	43.305	25.478	83.807
5	9	2	10	1.1	1.1	53.491	10.006	83.835
4	11	1.1	10	1.3	1.1	42	29.578	83.848
5	10	2	9	1.1	1.1	53.596	9.351	83.966
5	9	1	10	1.1	1.1	32.415	106.25	84.033

5	9	2	9	1.1	1.1	53.652	9.838	84.064
4	10	1	9	1.3	1.1	42.958	27.722	84.094
4	10	1	9	1.1	1.1	43.341	26.656	84.138
6	11	3	9	1.1	1.1	54.659	8.661	84.271
5	11	2	9	1.1	1.1	53.539	8.934	84.338
4	9	1	9	1.3	1.1	42.654	30.772	84.508
4	9	1	9	1.1	1.1	42.982	29.57	84.564
4	9	1	9	1.1	1.1	42.982	29.57	84.564
4	11	1	10	1.1	1.1	35.436	61.341	84.591
4	11	1	10	1.1	1.1	35.436	61.341	84.591
5	10	2	8	1.1	1.1	53.561	9.502	84.725
4	10	1	10	1.1	1.1	34.552	71.211	84.783
4	10	1	10	1.1	1.1	34.552	71.211	84.783
6	9	3	9	1.1	1.1	54.845	9.51	85.179
5	11	3	11	1.1	1.1	54.453	8.076	85.2
5	10	3	10	1.1	1.1	54.424	8.494	85.42
5	10	3	11	1.1	1.1	54.512	8.494	85.442
5	9	3	10	1.1	1.1	54.502	8.888	85.639
5	9	3	11	1.1	1.1	54.57	8.888	85.714
5	9	3	9	1.1	1.1	54.357	9.039	85.786
4	11	2	11	1.1	1.1	52.599	8.888	85.806
5	11	3	10	1.1	1.1	54.347	8.213	85.973
4	9	1	10	1.1	1.1	33.754	82.31	86.086
4	9	1	10	1.1	1.1	33.754	82.31	86.086
4	10	2	11	1.1	1.1	52.576	9.351	86.148
5	11	3	9	1.1	1.1	54.163	8.352	86.244
5	10	3	9	1.1	1.1	54.258	8.638	86.349
4	10	2	10	1.1	1.1	52.873	8.947	86.383
4	11	2	10	1.1	1.1	52.861	8.629	86.403
4	9	2	11	1.1	1.1	52.554	12.26	86.426
4	11	2	9	1.1	1.1	52.946	8.447	86.614
4	10	2	9	1.1	1.1	52.991	8.888	86.806
4	9	2	10	1.1	1.1	52.887	9.563	86.917

4	9	2	9	1.1	1.1	53.04	9.351	86.94
4	11	3	11	1.1	1.1	53.878	7.663	87.883
4	10	3	10	1.1	1.1	53.834	8.057	87.966
4	11	3	10	1.1	1.1	53.763	7.792	88.104
4	10	3	11	1.1	1.1	53.93	8.057	88.154
4	9	3	11	1.1	1.1	53.984	8.494	88.313
4	11	3	9	1.1	1.1	53.567	7.923	88.57
4	10	3	9	1.1	1.1	53.659	8.213	88.638
4	9	3	9	1.1	1.1	53.758	8.592	88.786
4	9	3	10	1.1	1.1	53.91	8.482	88.837
4	11	1	11	1.1	1.1	22.055	191.56	106.639
4	10	1	11	1.1	1.1	20.551	308.34	117.199
4	9	1	11	1.1	1.1	19.165	367.6	129.637
5	11	1	11	1.1	1.1	18.501	393.49	133.534
5	10	1	11	1.1	1.1	17.462	448.44	146.321
5	9	1	11	1.1	1.1	16.457	512.04	159.271
6	11	1	11	1.1	1.1	16.29	511.81	161.497
6	10	1	11	1.1	1.1	15.455	565.29	175.272
6	9	1	11	1.1	1.1	14.615	624.74	191.238

ANNEXE IV

Chip interface v.1.0 and v.2.0

The amplifier (v.1.0)

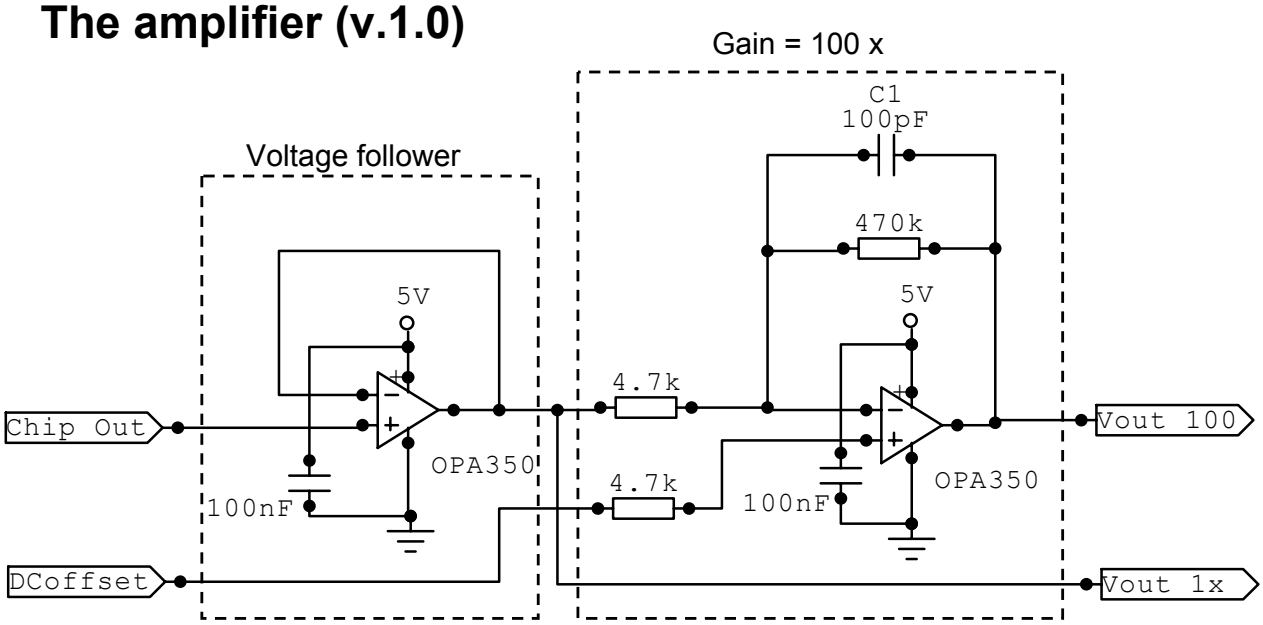

The biasing (v.1.0)

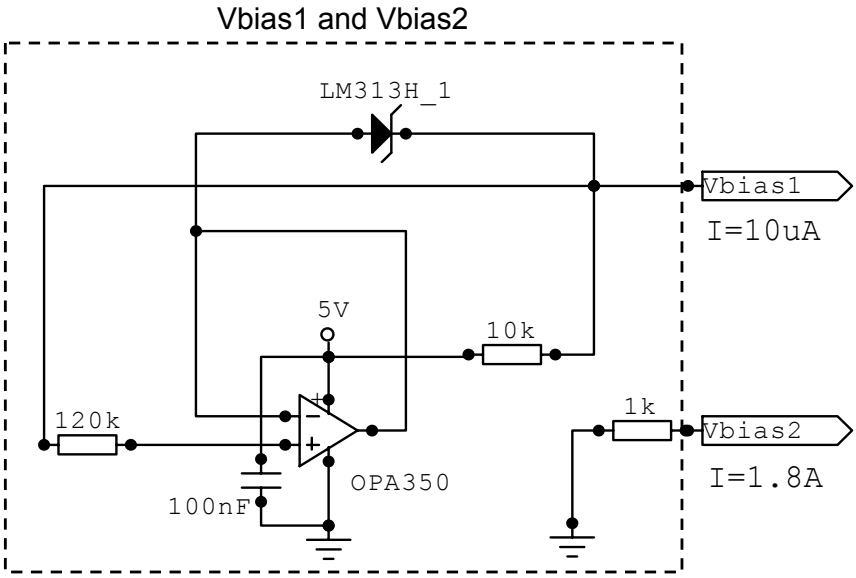

The power supply (v.1.0)

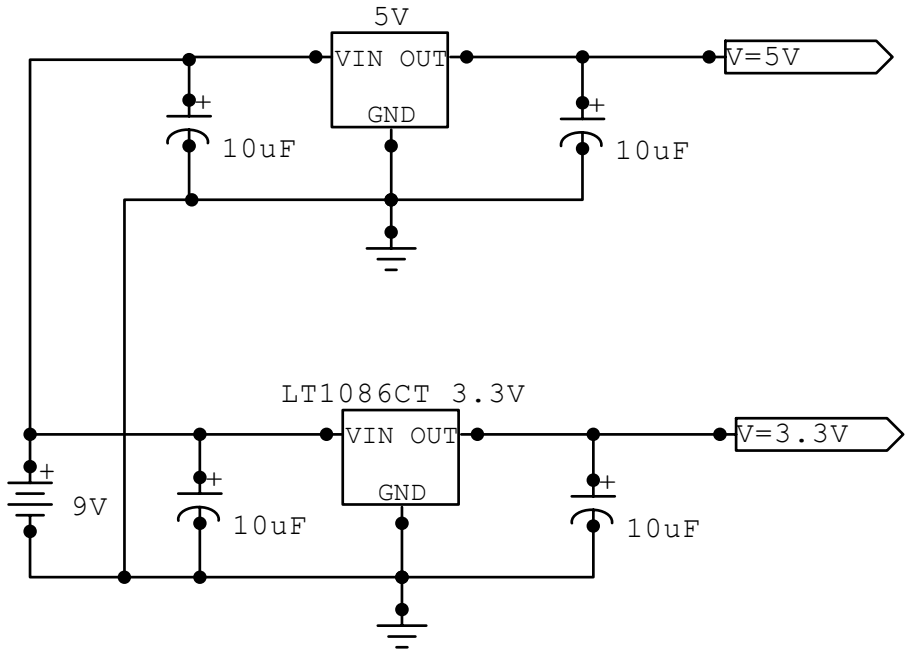

Chip interface v.2.0

The amplifier (v.2.0)

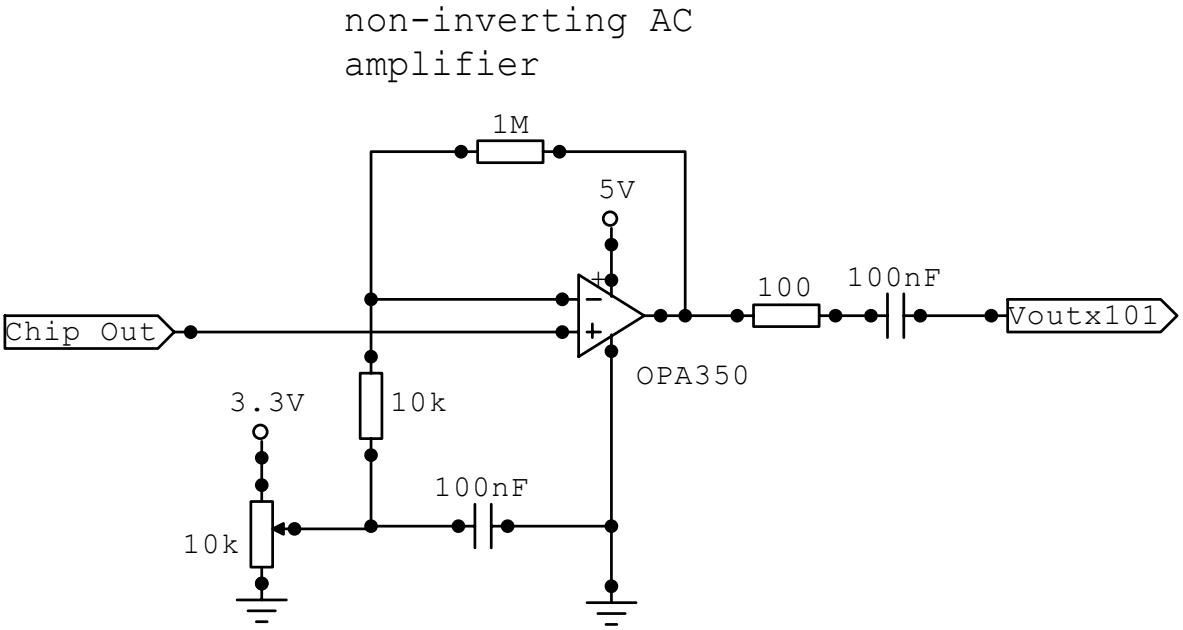

The biasing (v.2.0)

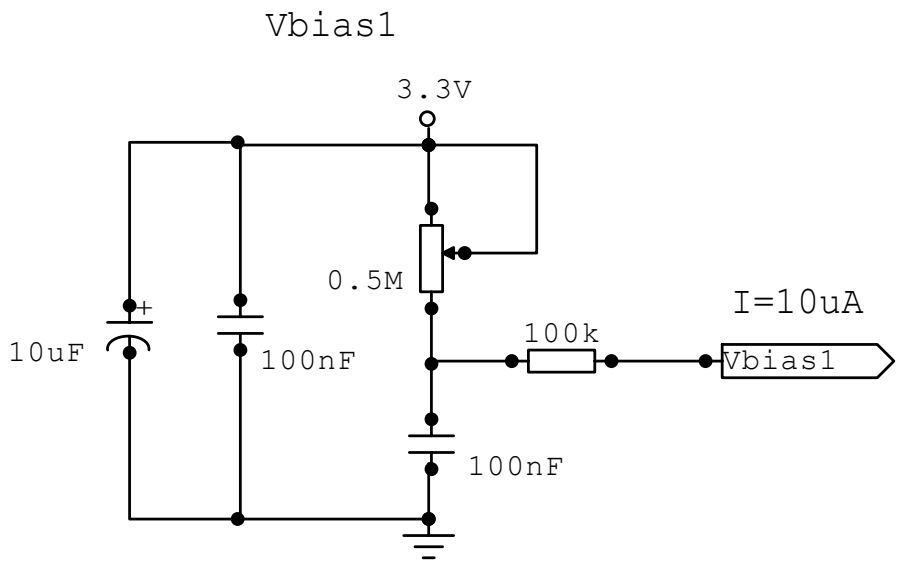

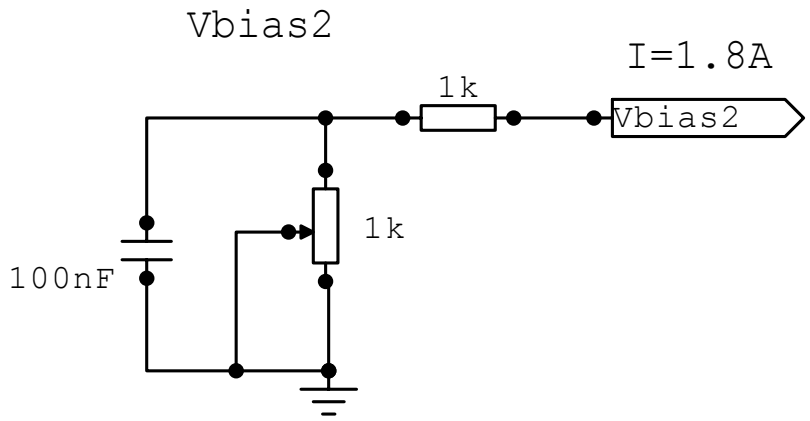

The power supply and the DC polarization (v.2.0)

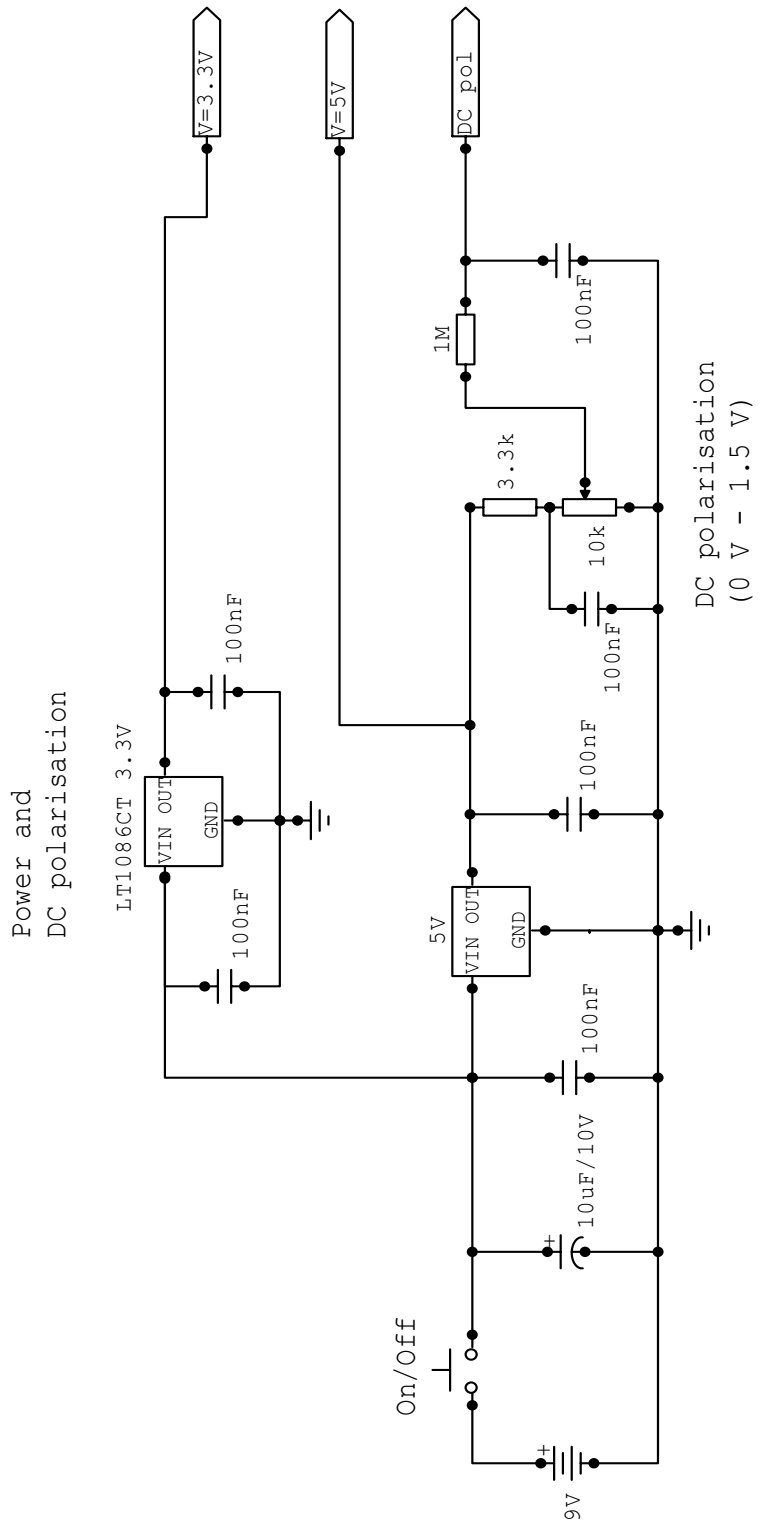

ACKNOWLEDGMENTS

My gratitude goes to my supervisor, Prof. Milena Koudelka-Hep, for her encouragement and guidance during my Ph.D. studies. Her expertise, understanding, and patience, added considerably to my research experience. I have also appreciated her management capabilities and her assistance in writing reports and for correcting the english of this thesis.

I thank the members of my thesis committee, Prof. Nico de Rooij, Prof. Peter Seitz, Dr. Nicolas Blanc and Prof. Sergio Martinoia, for their counsel and assistance. I acknowledge Prof. Nico de Rooij for the opportunity he gave me to realize this work in his group at the IMT; Prof. Peter Seitz and Dr. Nicolas Blanc for contributing and allowing the realisation of the first high density chip; and Prof. Sergio Martinoia for his friendship and for the interesting discussions about MEAs and neurophysiology.

I cannot think of Sergio without remembering Prof. Massimo Grattarola who left us prematurely. It has been an honour for me meeting him and working with him.

I am grateful to Prof. Stephan Rhor and his team at the University of Bern for his help with cardiomyocyte cultures; and to Dr. Rolf Kaufmann and Peter Metzler at the CSEM in Zürich for their contribution in the development of the high density array.

I would like to acknowledge the financial support and thank the partners of the “Slice array” and “Neurobit” european projects where I had the opportunity to contribute with my work.

I spent a wonderful time at the Sensors, Actuators and Microsystems Laboratory of the Institute of Microtechnology, in a stimulating, multi-disciplinary team and friendly atmosphere. I sincerely thank all of the current and former members of the group for their help and friendship over the last three and a half years. I especially wish to express my gratitude to Dr. Pierre Thiébaud, who introduced me in the art of the micromachining and directly contributed to my interest in the field of MEAs. I deeply thank Dr. Olivier Guenat, Dr. Peter van

der Wal, Vincent Auger for their helpful suggestions and the highly skilled technical team: Sylvain Jeanneret, Gianni Mondin, Edith Millotte, Pierre-André Clerc, Nicolle Hegelbach-G., Sabina Jenny, José Vaquera for their important support in technology. In particular, “Thank you Sylviane for dicing and packaging my devices !”.
I wish to recall with immense pleasure the scientific and unscientific discussions and events with Alexandra Homsy, Laure Aeschimann, Laura Ceriotti, Mireille Leboeuf, Eva l’Hostis, Fabienne Marquis-Weible, Sabeth Verpoorte, Phuong Quyên Pham, Florence Rohrbach, Rüegg Margrit, Anna Maria Spehar, Schahrazede Mouaziz, Cynthia Beuret, Isabel Rodriguez, Jean-Charles Fiaccabrino, Sebastien Gautch, Gian-Luca Lettieri, Patrick Carazzetti, Fernando Herrera, Akiyama Terunobu, Giovanni Bergonzi, Marc Boillat, Danik Briand, Dadras Massoud, Philippe Dubois, Giovanni Egidi, Teruo Fujii, Anpan Han, Thomas Hug, Raphaël Imer, Sander Koster, Pierre-André Künzi, Andreas Kuoni, Conel Marxer, Wilfried Noell, Claudio Novelli, Yves Petremand, Urs Staufer, Wilston Sun, Kaspar Suter (and Silvia), Bart van der Schoot, Peter Vettiger, Michael Zickar, Sasaki Minoru, Jan Lichtenberg, Benedikt Guldimann, Grégoire Genolet, Arash Dodge, Laurent Dellmann, Philippe Luginbuhl, Philippe Michel, Georges-André Racine, Sylvain Roth, Schürmann Grégor, and Antoine Daridon.
I would also acknowledge the students that I had the pleasure to supervise during their semester or diploma works: Thomas Overstoltz for his work on IrOx tips and the design of the high-density chip, Maurizio Gullo for his work on nano-electrodes and Gregory Choong for his contribution on the mini-incubator. You have significantly contributed to this work and I hope that working together has been a pleasure as it has been for me.
Outside the context of the IMT I would like to thank for their special friendship Roger Meier and Giselle, Alexis Boletis and Yvonne, Aline Baù, Francesco Minghetti, Sebastien and Florence Robyr, Ronny Maggini and Flavia. We know each other since a long time and I hope that the future will keep our friendship as strong as it is today.

Travelling each day from Lausanne to Neuchâtel I met a lot of people in what it has become the “Club of the train”. Meeting some of you in the early morning or in the evening gave another colour to my journey.
I am grateful to my parents and family, for understanding my absence from home during my studies, and for their precious support.
And finally to my wife, Anja, who suffered through each paragraph along with me, I acknowledge a debt, an appreciation that extends beyond any words: thank you for your love, your patience and understanding during my studies and during the writing of this thesis.

LIST OF PUBLICATIONS

Conferences and Proceedings

2003

L. Berdondini, T. Overstolz, N. F. de Rooij, M. Koudelka-Hep, P. Seitz, N. Blanc, "High density electrode arrays for in-vitro electrophysiology", SIMEA 2003, Denton, Texas, USA, March 5-8 2003.

P. Salaun, O. Guenat, L. Berdondini, J. Buffle, M. Koudelka-Hep, " Voltammetric microsystem for trace elements monitoring", Analytical Letters, Vol. 39, No. 9, pp. 1835-1849, 2003.

L. Berdondini, T. Overstolz, N. F. De Rooij, M. Koudelka-Hep, P. Seitz, N. Blanc, "Gold electroless deposition for active electrode arrays", KAIST: Kore-Switzerland Workshop on Materials for Medical Diagnostic and Bio Applications, Daejeon, Korea, October 5-7, 2003.

V. Auger, L. Berdondini, S. Gautsch, O. Guenat, N. F. De Rooij, P. van del Wal, M. Koudelka-Hep, "Implementation of new materials and technologies in (Bio)electrochemical microsystems", KAIST: Kore-Switzerland Workshop on Materials for Medical Diagnostic and Bio Applications, Daejeon, Korea, October 5-7, 2003.

L. Berdondini, M. Kalbac, S. Gautsch, M. Gullo, U. Staufer, M. Koudelka-Hep, N.F. de Rooij, “Fabrication of nano interdigitated electrodes”, Smart Sensors, Actuators, and MEMS, Proceedings of SPIE, Maspalomas, Gran Canaria, Spain, May 19-21, 2003.

L. Berdondini, T. Overstoltz, N.F. de Rooij, M. Koudelka-Hep, "Microelectrode arrays for electrophysiological monitoring of neuronal networks", CMI-COMMLAB meeting, EPFL, Switzerland, May 2003.

2002

L. Berdondini, T. Overstolz, N. F. de Rooij, M. Koudelka-Hep, S. Martinoia, P. Seitz, M. Wäny, N. Blanc, "High resolution electrophysiological activity imaging of in-vitro neuronal networks", IEEE-EMBS Proceedings, Madison, May 2-4 2002, pp. 241-244.

L. Berdondini, N. F. de Rooij, M. Koudelka-Hep, "Micro and nano-technologies for electrophysiological neuronal applications", NEWS 2002, Genova, June 10-13, 2002. (invited)

L. Berdondini, T. Overstoltz, N.F. de Rooij, M. Koudelka-Hep, "Microelectrode arrays (MEAs) for cellular physiology", CMI-COMMLAB meeting, EPFL, Switzerland, June 2002.

V. Auger, L. Berdondini, T. Akiyama, M. Kalbac, S. Gautsh, O. T. Guenat, U. Staufer, N. F. de Rooij, M. Koudelka-Hep, “Nanostructures for electrochemical applications”, IMCS 2002, 9th International meeting on chemical sensors, Boston, USA, 7/10 July, 2002.

2001

L. Berdondini, T. Overstolz, N.F. de Rooij, M. Koudelka.Hep, M. Wäny, P. Seitz, “ High-density microelectrode arrays for electrophysiological activity imaging of neuronal networks”, ICECS: The 8th IEEE International Conference on Electronics, Circuits and Systems, Malta, September 2- 5, 2001, pp. 1239-1242.

L. Berdondini, V. Auger, P. van der Wal, N. F. de Rooij, M. Koudelka-Hep, “Thin-film microelectrode arrays”, Materials 2001, Coimbra, Portugal, April 9-11, 2001. (invited)

V. Auger, L. Berdondini, P. van der Wal, N. F. de Rooij, M. Koudelka-Hep, “ Thin-film technology for the development of electrochemical microsystems”, E-MRS 2001 spring meeting, Strasbourg, France, June 5-8, 2001. (invited)

L. Berdondini, P. Thiébaud, N. F. de Rooij, M. Koudelka-Hep, M. Grattarola, S. Martinoia, M. Bove, M. Balestrino, J. Zimmer, H. Jahnsen, R. Köhling, “Technological aspects of the MEAs development”, Cell-substrate interactions, Münich, June 17-30, 2001. (invited)

2000

L. Berdondini, P. Thiébaud, N.F. de Rooij, M. Koudelka-Hep, R. Kohling, E-J. Speckmann, H. Jahnsen, J. Zimmer, B. Kakobsen, B. Kristiansen, M. Grattarola, S. Martinoia, M. Bove, M. Balestrino, “Three-dimensional microelectrodes arrays (MEAs) for in-vitro brain slices recording and stimulation”, International meeting on Substrate-Integrated MEAs, Reutlingen, Germany, June 21-23, 2000.

Patents

L. Berdondini, T. Overstolz, M. Koudelka.Hep, P. Seitz, “High-density microelectrode arrangement ", EP1278064, 2003-01-22.

BIOGRAPHY

Luca Berdondini was born in 1974 in Locarno, Switzerland. He received in 1999 the M.Sc. degree in micro-engineering from the Swiss Federal Institute of Technology of Lausanne (EPFL), Switzerland. During his “diploma work” he was visiting the Pine Lab at Caltech, California, USA, where he worked with S. Potter and J. Pine.

After few months in the industry, K-team (Switzerland), working on robotics, in November 1999 he joined the Sensor, Actuator and Microsystems Laboratory (SAMLAB), headed by Prof. Nico de Rooij, at the Institute of Microtechnology (University of Neuchâtel, Swizerland). His research activities in the “Micro- (bio) electrochemical systems” group of Prof. Milena Koudelka-Hep focus on the development of micromachined devices for bio-electrochemistry and neurophysiology.